Deposition & Characterisation of Silicon and Conductive Layers on Woven Polyester

<Anna Helena Nilsdotter Lind>

Submitted for the degree of Doctor of Philosophy

Heriot-Watt University

<The School of Engineering and Physical Science>

<January> <2013>

The copyright in this thesis is owned by the author. Any quotation from the thesis or use of any of the information contained in it must acknowledge this thesis as the source of the quotation or information.

Abstract

Textile and semiconductor processes were combined to produce a flexible solar panel by depositing silicon thin film onto woven polyester. Semiconductor processes such as evaporation, Plasma Enhanced Chemical Vapour Deposition (PECVD) and RF-sputtering were done under vacuum conditions. Microwave PECVD proved difficult for textile substrates as the weave was damaged using parameter settings commonly used for conventional substrates such as silicon wafers and glass. PECVD parameters such as temperature, gas flow-rate, mixture, pressure and power were adjusted to allow the textile to be processed and a good quality silicon thin film to be deposited. An extra conductive layer was introduced between the textile and metal back-contact to support the cell. The silicon film structure changed from amorphous to mixed crystal growth in an amorphous matrix, as revealed by Raman spectroscopy and light transmission. The silicon Raman spectrum often had three peaks with the middle one, a fingerprint for nanocrystal growth with a hexagonal wurtzite structure in between the amorphous and crystalline peaks. Process conditions for pure amorphous and microcrystalline structures were also established, requiring two peaks to fit the Raman spectrum. Different structures have different band-gap energies and these were determined by measuring the variation in light transmission. An amorphous structure has a band-gap energy of 1.8eV while a crystalline silicon structure has a band-gap of 1eV and a mixed nanocrystalline content has an intermediate value which depends on the crystal size. A microcrystalline structure has a band-gap of 1.6eV.

ACKNOWLEDGEMENT

Thanks………………

To all of you, who made this thesis possible and especially:

John Wilson and Robert Mather, who guided me through my PhD work and with their feedback and knowledge, helped me to complete the chapters of my thesis.

Family and friends, who supported and encouraged me through this on-going "saga" of thesis writing and with their great understanding of me being unsociable for the last years.

Without all these people's help and support, I would not gotten this far.

Thanks……………….

ACADEMIC REGISTRY
Research Thesis Submission

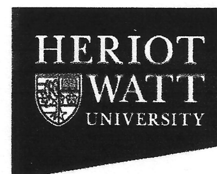

Name:	Anna Helena Nilsdotter Lind		
School/PGI:	The School of Engineering and Physical Science		
Version: *(i.e. First, Resubmission, Final)*	First	Degree Sought (Award **and** Subject area)	Doctor of Philosophy

Declaration

In accordance with the appropriate regulations I hereby submit my thesis and I declare that:

1) the thesis embodies the results of my own work and has been composed by myself
2) where appropriate, I have made acknowledgement of the work of others and have made reference to work carried out in collaboration with other persons
3) the thesis is the correct version of the thesis for submission and is the same version as any electronic versions submitted*.
4) my thesis for the award referred to, deposited in the Heriot-Watt University Library, should be made available for loan or photocopying and be available via the Institutional Repository, subject to such conditions as the Librarian may require
5) I understand that as a student of the University I am required to abide by the Regulations of the University and to conform to its discipline.

* *Please note that it is the responsibility of the candidate to ensure that the correct version of the thesis is submitted.*

Signature of Candidate:	Helena Lind	Date:	6/1-2013

Submission

Submitted By *(name in capitals)*:	
Signature of Individual Submitting:	
Date Submitted:	

For Completion in the Student Service Centre (SSC)

Received in the SSC by *(name in capitals)*:			
Method of Submission *(Handed in to SSC; posted through internal/external mail)*:			
E-thesis Submitted ***(mandatory for final theses)***			
Signature:		Date:	

Abbreviation

a-	Amorphous
a-Si-	Amorphous silicon
a-Si:H-	Hydrogenated amorphous silicon
Ar-	Argon
B_2H_6-	Diborane
BOS-	Balance of system
c-	Crystal
CdTe-	Cadmium Telluride
CIS-	Copper indium Diselenide
CIGS-	Copper indium Diselenide with gallium
DEFRA-	Department of Environment, Food and rural Affairs
DSC-	Differential Scanning Calorimetry
Dtex-	Decitex (g/10km)
E_g-	Band-gap energy
EPBT-	Energy payback time
EPIA-	European photovoltaic Industry associations
EYR-	Energy yield ratio
EPE-	Electricity production efficiency
GA-	Gallium
GHG-	Greenhouse gases
GWP-	Global warming potential
H_2-	Hydrogen
i-layer-	Intrinsic, undoped silicon between doped silicon.
ITO-	Indium Tin Oxide
ISO-	International Organisations of Standardisation
LCA-	Life-cycle assessment
LCI-	Life-cycle impact
LCI-	Life-cycle inventory
LA-	Longitudinal acoustics
LO-	Longitudinal optical
MW-	Microwave
n-layer-	Negative layer (dopent) with increased number of negative electrons
ηc-	Nanocrystal

NREAP-	National renewable energy action plans
p-layer	Positive layer (dopant) with increased number of holes (positive charged)
PECVD-	Plasma enhanced chemical vapor deposition
PET-	Polyethylene Terephthale (polyester)
PH_3-	Phosphine
PID-	Proportional- integral- derivative controller
PV-	Photovoltaic
QCE-	Quantum confinement effect
R2R-	Roll-to-Roll
RF-	Radio frequency
sccm-	Standard cubic centimeter per minute
Si-	Silicon
SiH_4-	Silane
SO-	Surface optical
T_g-	Glass transition
T_m-	Melting point
TPB-	Three phase line
TPL-	Triple phase line
TA-	Transverse acoustic
TCO-	Transparent conducting oxide
TO-	Transverse optical
μc-	Microcrystal

TABLE OF CONTENTS

1. Introduction page 1

2. Brief history of silicon thin film and its process on textile substrate

2.1. Introduction page 6
2.2. Photovoltaic, PV and the market page 6
2.3. Solar cell operation page 13
2.4. Process to manufacture thin film flexible solar cells page 17
2.5. Thin film silicon growth, amorphous and crystal content page 21
2.6. Textile material page 30
2.7. References page 39

3. Nanocrystal structure and properties

3.1. Introduction page 46
3.2. Silicon crystal (crystal growth) page 47
3.3. Raman spectroscopy of silicon page 50
3.4. Raman spectrum for amorphous and crystal silicon page 55
3.4.1. Phonon modes for wurtzitesilicon page 57
3.4.2. How crystal size influences Raman spectra page 59
3.4.3. Raman peaks regarding nanocrystalline structure page 61
3.5. Properties of nanocrystal structure page 64
3.6. Conclusion page 66
3.7. References page 67

4. Environmental assessment & impact of silicon thin film on woven polyester

4.1. Introduction page 72
4.2. Standards and regulations page 78
4.3. Energy emission page 80
4.3.1. Energy returns related to design of device and location page 80
4.3.2. Design of solar device and its manufacturing process page 82

4.3.3. Thin film process page 84
4.4. Energy use and waste in textile and semiconductor process page 87
4.4.1. Waste related to process of silicon thin film on to woven polyester page 87
4.4.2. Recycling of photovoltaic device page 90
4.4.3. Energy use related to photovoltaic device page 92
4.4.4. Manufacturing steps regarding silicon thin film on polyester weave page 92
4.5. Energy use related manufacturing silicon thin film onto woven polyester page 95
4.5.1. Energy use required for woven polyester page 96
4.5.2. Coating and deposition on textile substrate page 97
Polyester weave page 97
Plasma process page 97
4.6. Discussion and conclusion page 100
4.7. References page 101

5. Processes and parameters influencing the textile substrate

5.1. Introduction page 104
5.1.1. Cell design page 104
5.1.2. Substrate page 105
5.1.3. Process methodology page 106
5.2. Experimental methodology for thin film on textile substrate page 107
5.2.1. Preparation of textile substrate page 107
Washing page 107
Calendering (heat-treatment) page 108
Instrument and method page 108
Experimental page 109
5.2.2. Conductive backcontact and substrate page 110
Polyaniline mix, Panipol page 112
Coating procedure for polyaniline page 112
Experimental page 113
Metal contacts, aluminium page 114

5.2.3. Plasma deposition page 116
Plasma deposition with microwave and radio frequency powered source page 116
Preparation of process page 116
Process parameters influencing a plasma process page 117
Plasma enhanced CVD with Radio Frequency- RF page 118
Plasma enhanced CVD with Microwave- MW page 119
5.2.4. RF- sputter, ITO- Indium Tin Oxide page 121
Magnetron sputter technology page 121
Experimental page 122
5.2.5. Experimental design for N-I-P-layer page 123
Intrinsic silicon films with Microwave powered plasma page 123
Taguchi model page 126
Interface between n- and i-layer page 128
Doped layers page 130
N-I-P- layers, combinations page 132
5.2.6. RF- powered plasma run page 134
5.3. Introduction to analytical instruments page 135
5.3.1. Scanning Electron Microscopy, SEM page 136
The instrument and method page 136
5.3.2. Raman spectroscopy page 136
Raman parameter's influence on thin film page 137
5.3.3. Thermal analysis, Differential Scanning Calorimetry, DSC page 138
The instrument and method page 138
Experimental page 141
5.3.4. Electrical properties page 141
The instrument and method page 141
Experimental page 143
5.3.5. Optical properties page 143
The instrument and method page 144
Experimental page 148
5.4. Summary page 148
5.5. References page 150

6. Results and discussion

6.1. Introduction page 154

6.2. Textile for plasma process page 154

6.2.1. Introduction page 154

6.2.2. Different textile substrate page 155

6.2.3. Calendering of textile substrate page 156

6.2.4. Heat evaluation of textile substrate page 158

6.3. Conductive option to support the back contact page 160

6.3.1. Introduction page 160

6.3.2. Conductive substrate, material page 160

6.3.3. Conductive substrate, coating page 162

Evaporation page 164

Plasma Process page 165

6.4. Plasma process on textile substrate page 165

6.4.1. Plasma process, chamber pressure page 165

6.4.2. Initial plasma process of intrinsic layer page 165

6.4.3. Plasma process, intrinsic layer, Taguchi model page 168

Taguchi model, process page 168

Analysis of the Taguchi thin film page 170

Visual page 170

Raman spectroscopy page 171

Raman peaks related with different process parameters page 176

Structure development page 179

Raman peak width page 181

6.4.4. Plasma process, intrinsic silicon, after the Taguchi Model page 182

Deposition time page 182

6.4.5. Plasma process, interface between doped and undoped layers page 186

6.4.6. Plasma process, doped layers page 188

Plasma process, p-layer page 189

6.4.7. *N-I-P- layers, introduction* page 192

6.4.8. Radio frequency powered plasma page 194

6.5. Results from the analytical instruments page 195

6.5.1. Raman spectroscopy page 195

Raman spectra from wurtzite silicon structure page 195

Raman spectroscopy and its laser power page 196

6.6. Optical properties page 198

6.6.1. Transmission measurement page 199

6.7. Electrical properties page 203

6.7.1. I-V & four-point probe page 203

6.8. RF- sputtering of ITO and analysis page 204

6.9. Thermal properties and analysis page 205

6.9.1. Differential Scanning Calorimetry, DSC page 205

6.10. Summary page 208

6.11. References page 211

7. Summary and conclusion

7.1. Introduction page 214

7.2. Silicon thin film on woven polyester page 214

7.2.1. Textile substrate and preparation page 215

7.2.2. Process settings for silicon thin film on woven polyester page 215

7.3. Evaluation of deposited silicon thin film on woven polyester page 217

7.4. Environmental assessment regarding energy use page 219

7.5. Future thoughts page 219

Encapsulation page 220

Flatter yarn page 220

Wet-coat page 221

7.6. Final conclusion page 221

7.7. References page 221

8. Appendix

8.1. Product data sheet

8.1.1. Panstat W Appendix I

8.1.2. Cognis DSX Appendix II

8.2. Process procedure

8.2.1. Wet coat application with polyaniline Appendix III

8.2.2. Evaporation Appendix IV

8.2.3. Plasma enhanced chemical vapor deposition, PECVD Appendix V

8.2.4. RF- sputter Appendix VI

8.3. Posters and article

8.3.1. Posters

TPW, Technological Plasma Workshop 07 Appendix VII

TPW, Technological Plasma Workshop 09 Appendix VIII

SISER- 2010 Appendix IX

CMMP 2010 Appendix X

8.3.2. Articles published

CMMP 2010, extended abstract Appendix XI

Physica Status Solidi A 208 (12), p. 2765–71 (2011) Appendix XII

8.4. Raman spectrum

8.4.1. Additional Raman spectrum from Results and discussion Appendix XIII

LIST OF FIGURES AND TABLES

Figures

2. Brief history of silicon thin film and its process on textile substrate

Figure 2.1. *"forecast for 2020 based on EPIA's three scenarios"* page 8
Figure 2.2. *"different generations of cell design".* page 11
Figure 2.3. *"flexible panels integrated into a garment"* page 13
Figure 2.4. *"p-i-n solar cell and electrons and holes separate"* page 14
Figure 2.5. *"silicon layers (n-i-p or p-i-n) depend on substrate"* page 15
Figure 2.6. *"spectral response of an a- and µc- Si cell"* page 16
Figure 2.7. *"a plasma chamber and the main factors"* page 18
Figure 2.8. *"production line for the 5 chambers from Roth& Rau"* page 19
Figure 2.9. *"two different power sources in a roll-to-roll system"* page 20
Figure 2.10. *"difference between a crystal and amorphous structured silicon lattice"* page 21
Figure 2.11. *"a silicon structure with dangling bonds"* page 22
Figure 2.12. *"development of crystal size in relation to ratio of silane and hydrogen"* page 23
Figure 2.13. *"mixed growth structure with small crystals"* page 24
Figure 2.14. *"different growth stages"* page 25
Figure 2.15. *"the electron energy (eV) for the different silane, SiH_4 radicals"* page 26
Figure 2.16. *"growth procedure with SiH_3"* page 27
Figure 2.17. *"ratio of argon dilution against silane"* page 29
Figure 2.18. *"differences between multifilament and monofilament yarn"* page 31
Figure 2.19. *"chemical structure of Polyethylene Terephthalate, PET"* page 32
Figure 2.20. *"weave structure with continuous filaments in the yarn"* page 34
Figure 2.21. *"woven fabric contains a higher surface area"* page 35
Figure 2.22. *"possible plasma penetration in a tight weave"* page 35
Figure 2.23. *"a mean free path changes by pressure"* page 36
Figure 2.24. *"fibres with different water content"* page 38

3. Nanocrystal structure and properties

Figure 3.1. *“difference between wurtzite hexagonal structure and zinc blende cubic structure”* page 48

Figure 3.2. *“different stacking orders”* page 49

Figure 3.3. *“compare with and without twin defect”* page 49

Figure 3.4. *“a typical Raman layout”* page 51

Figure 3.5. *“how the incident light penetrates through a sample”* page 52

Figure 3.6. *“a comparison between laser sources”* page 53

Figure 3.7. *“how atoms move during vibrations”* page 54

Figure 3.8. *“a typical graph for the four modes in crystalline Si”* page 55

Figure 3.9. *“spectra with structure content of small crystals”* page 56

Figure 3.10. *“peak change both in shape and location”* page 57

Figure 3.11. *“change in peak width and location due to crystal size”* page 60

Figure 3.12. *“correlations between crystal size, peak shift and width”* page 61

Figure 3.13. *“typical peaks, location and shape”* page 62

Figure 3.14. *“peak locations depended on the number of peaks and type of peak fit”* page 62

Figure 3.15. *“how increased silicon film thickness reduces the carrier mobility”* page 65

4. Environmental assessment & impact of silicon thin film on woven polyester

Figure 4.1. *“total primary energy (MJ) input for amorphous silicon thin film”* page 75

Figure 4.2. *“suggestion of a life-cycle model”* page 77

Figure 4.3. *”different solar designs available today”* page 82

Figure 4.4. *“a process chart of silicon process of conventional solar cell, material use”* page 83

Figure 4.5. *“a process chart of silicon process of conventional solar cell, energy use”* page 84

Figure 4.6. *“the process stages involved for wet-coat of textile”* page 88

Figure 4.7. *“water during recycling process for material and energy use”* page 90

Figure 4.8. *"recycling of a complete PV- system"* page 91
Figure 4.9. *"LCA diagram for a PV-system"* page 92
Figure 4.10. *"LCA with energy use for silicon thin film through its life-cycle"* page 93
Figure 4.11. *"different stages involved in extrusion of polyester filament, fibre"* page 94
Figure 4.12. *"the stages involved in a weaving process"* page 94
Figure 4.13. *"the different process stages, maintenance and recycling to consider"* page 95

5. Process and parameters influencing the textile substrate

Figure 5.1. *"cell structure"* page 105
Figure 5.2. *"different stages in developing a solar device"* page 106
Figure 5.3. *"the principle of calender process"* page 108
Figure 5.4. *"direct coating in industrial scale"* page 113
Figure 5.5. *"a typical RF plasma process with parallel plate system"* page 119
Figure 5.6. *"the layout of the Quartz Cylinder"* page 121
Figure 5.7. *"sample and reference to analyse in a DSC"* page 140
Figure 5.8. *"the principles with four-point-probe"* page 142
Figure 5.9. *"change of incident light by it being split into different directions"* page 144
Figure 5.10. *"transmission spectrum and development of interference fringes"* page 145
Figure 5.11. *"optical absorption and band-gap energy"* page 147
Figure 5.12. *"optical absorption can be divided into three areas"* page 148

6. Results and discussion

Figure 6.1. *"applied hot-air from below and above"* page 159
Figure 6.2. *"fabrics damaged during a plasma process"* page 159
Figure 6.3. *"burned area and non-damaged aluminium"* page 164
Figure 6.4. *"deposition in relation with silane rate"* page 170
Figure 6.5. *"Amorphous fraction of deposited film on aluminium"* page 173
Figure 6.6. *"Crystal fraction of intermediate peak (C1) of deposited film on aluminium"* page 173

Figure 6.7. *"Crystal fraction of crystal peak (C2) of deposited film on aluminium"* page 174
Figure 6.8. *"Amorphous fraction of deposited film on textile"* page 174
Figure 6.9. *"Crystal fraction of intermediate peak (C1) of deposited film on textile"* page 175
Figure 6.10. *"Crystal fraction of crystal peak (C2) of deposited film on textile"* page 175
Figure 6.11. *"structure content and peak location for the different silane rates"* page 177
Figure 6.12. *"the runs which became most amorphous"* page 177
Figure 6.13. *"the effect of power"* page 178
Figure 6.14. *"peak location and width related with silane, SiH_4 rate for aluminium"* page 181
Figure 6.15. *"peak location and width related with silane, SiH_4 rate for textile"* page 182
Figure 6.16. *"how argon purges in relation with H_2/Ar ratio of 17/3 and 14/6 influences the structure outcome"* page 188
Figure 6.17. *"the two process options with highest crystal content"* page 191
Figure 6.18. *"the different structures such as a-Si, μ- and η-crystal"* page 195
Figure 6.19. *"different vibration modes"* page 196
Figure 6.20. *"Raman spectra with laser power cycle of 10-50-10%"* page 197
Figure 6.21. *"Raman spectra with laser power cycle of 50-10-50%"* page 198
Figure 6.22. *"how absorption was influenced by process time and temperature"* page 199
Figure 6.23. *"comparing square and cube root calculation"* page 201
Figure 6.24. *"polyaniline coated textile"* page 206
Figure 6.25. *"increased numbers of peak after polyaniline coated substrate"* page 207
Figure 6.26. *"peaks of polyaniline become reduced after evaporate aluminium"* page 207
Figure 6.27. *"the melting point after plasma process of silicon increases by 10°C"* page 208

Tables

2. Brief history of silicon thin film and its process on textile substrate

Table 2.1. *"an estimate of installed photovoltaic to 2025"* page 9

3. Nanocrystal structure and properties

Table 3.1. *"how beam penetration through a crystalline silicon material vary"* page 52

4. Environmental assessment & impact of silicon thin film on woven polyester

Table 4.1. *"explains how location and different PV-system reflects on the EPBT"* page 81
Table 4.2. *"electricity output in relation with device design and location"* page 81
Table 4.3. *"energy generated during a period of 20 years"* page 81
Table 4.4. *"estimated value for growth rate"* page 85
Table 4.5. *"different values of energy use for plasma process"* page 85
Table 4.6. *"summary of process stages"* page 89
Table 4.7. *"waste and emission within process of silicon thin film on woven polyester"* page 89
Table 4.8. *"energy input became less with a polymer layer"* page 99

5. Process and parameters influencing the textile substrate

Table 5.1. *"process settings used to calender textile substrate"* Page 109
Table 5.2. **"***Calender process of Conductive material"* Page 111
Table 5.3. *"different runs and their settings used in the Taguchi model"* page 126
Table 5.4. *"Silane rate, process time and increased power against H_2/ Ar ratio of run 10 and 11"* page 127
Table 5.5. *"combinations with temperature and time against fixed parameters"* page 127
Table 5.6. "*trial "clean break" between doped and intrinsic"* page 129

Table 5.7. “*different flow-rates used to optimise the p-layer*” page 131
Table 5.8. “*the settings for the n-i-p- layers*” page 133
Table 5.9. “*altered time and temperature of n-i-p- layers*” page 134
Table 5.10. *“RF-powered trials”* page 135

6. Results and discussion

Table 6.1. *“Calender settings for polyester weave”* page 157
Table 6.2. *“Calender settings for conductive material”* page 161
Table 6.3. *“conductive substrate during plasma process”* page 162
Table 6.4. *“Taguchi model and its parameter”* page 169
Table 6.5. *“amorphous and crystal content for aluminium and textile substrates”* page 172
Table 6.6. *“process parameters, which led to same structure content”* page 179
Table 6.7. *“process parameters resulting in different structure content”* page 180
Table 6.8. *“possible development routes for crystal growth”* page 180
Table 6.9. *“silane rate and time were altered to increase crystal content”* page 183
Table 6.10. *“time and temperature were altered to compensate for low process power”* page 184
Table 6.11. *“process power was evaluated against time and temperature”* page 185
Table 6.12. *“how the amorphous content changed by time and temperature”* page 186
Table 6.13. *“use “clean break” between doped and Intrinsic”* page 187
Table 6.14. *“amorphous and crystal fraction in the p-layer”* page 190
Table 6.15. *“summary of process settings of N-I-P-layer”* page 193
Table 6.16. *“how argon purges influenced optical properties”* page 200
Table 6.17. *“how the p-layer trial influenced optical properties”* page 202
Table 6.18. *“how the band-gap values changes regarding to structural phase”* page 202

1. Introduction

The intention of this study was to clarify and improve earlier efforts to construct flexible solar cells on a fabric base, by using a microwave plasma process to form thin-film silicon and then to determine the dependence of the silicon structure on process conditions.

This research work has focused on depositing silicon thin film directly onto woven polyester, a product design which combines traditional textile processing with known semiconductor processes. The semiconductor processes for the cell structure were done in vacuum, which was not a common way of processing textile material. Woven polyester being more textured than conventional substrates for solar cells, made it necessary to establish process settings, which provided a good quality silicon thin film without changing the textile performance.

Objective: prepare the textile weave to a condition necessary to withstand the thin film process based on vacuum and reactive gases.

Objective: establish process settings for the semiconductor processes and especially the plasma enhanced chemical vapor deposition, PECVD for n-i-p- layers to get the thin film properties such as electrical, optical, physical and mechanical required necessary for a solar cell on flexible substrate.

Objective: identify methods to measure and analyse the thin film properties on textile substrates, which are more textured than conventional substrates such as glass or silicon wafers.

Objective: design a process route, which combines conventional process techniques from both the textile and semiconductor industries, but also to have a low impact on the environment such as the carbon footprint.

Different solar cell structures have been developed through the years and the work can be divided into three generations: the 1st regards crystal silicon panels (based on silicon wafer) followed by thin film (2nd) with flexible and cheaper substrate. Regarding 2nd generation solar cells, these still require higher cell efficiency and a 3rd generation

solar cell design has been developed with focus on enhanced cell efficiency of thin films by using mixed content such as amorphous and crystal, organic and inorganic materials, and combined semiconductor layers in a tandem- or triple- junction. Even though crystal silicon has a good efficiency and is difficult to replace, the flexible thin film panels will find a new niche market for applications and designs such as buildings, construction, outdoor equipment and clothing. Thin films available today are often deposited directly onto a polymer sheet, which is either laminated or stitched onto a flexible support such as a textile. The work reported in this thesis has deposited silicon thin film directly onto a woven textile with the aim of the flexible solar panel gaining the textile's physical properties.

The process methods used were both from the textile and the semiconductor industries. Preparation of the substrate was based on textile process, whereas the vacuum based depositions of the cell structure were common semiconductor processes. A plasma process based on microwave powered plasma deposition at vacuum pressure with reactive gases such as silane, hydrogen, diborane and phosphine was unusual for textile substrates and therewith very little information published.

However, depositing silicon thin film directly onto woven polyester proved difficult after the textile substrate was found to become damaged. With no information regarding thin film cells deposited directly onto the textile and it being an unknown material for vacuum based processing with microwave powered plasma, much time was spent on understanding and establishing process methods, parameters and their settings. (This is discussed in *chapter 5 Processes and parameters influencing the textile substrate and chapter 6 Results and discussion).*

Plain weave structure with filament yarn in both warp and weft was chosen to avoid the substrate influence on the outcome of the process and deposition. Plasma penetration through the fabric structure was to be avoided and process pressure was carefully adjusted. Textured and denser fabric could influence the outcome by encouraging increased reaction rate on the fabric surface, which could give temperature rise and damage the substrate. The textile was heated on the substrate plate and proved very sensitive to heat in a vacuum process, which led to a process temperature of maximum 200°C.

During the work with process parameters and conditions, additional substrates such as

aluminium sheet and microscope-slide glass were treated together with the textile to understand how each substrate behaved during the process. Comparison of the three substrates helped to conclude, that performance during the process and the quality of deposition depended on substrate quality and surface. Both aluminium sheet and microscope-slide glass gave similar structure content and growth rate compared with the textile substrate.

The first cell structure was built directly onto the textile substrate by starting with a back contact of evaporated aluminium followed by the semiconductor layers (n-i-p) deposited by Plasma Enhanced Chemical Vapor Deposition from silane, PECVD in the order of n-type (phosphine doped), intrinsic and p-type (diborane doped). A protective layer and top contact of Indium Tin Oxide, ITO was RF-sputtered. Encapsulation of the complete cell was considered too by using lamination or coating to apply a protective film and avoid the cell being damaged. It is important to deposit a uniform film onto the textile surface to gain required film quality, which can withstand flexing without deteriorating electrical or optical properties. With the back contact of aluminium being poor due to an uneven distribution, additional conductive support such as conductive substrates based on carbon fibre, or a conductive coating such as polyaniline, were considered. Polyaniline was coated directly on the textile and had the advantage of being water-based and already successfully applied on textile substrates. *(See chapter 5 Processes and parameters influencing the textile substrate and chapter 6 Results and discussion)*

The process conditions for plasma enhanced CVD were based on low pressure and reactive gases with a microwave powered plasma source. The project prior to this had suggested process parameters for a working solar cell based on amorphous silicon (based on a gas mixture of silane and hydrogen). The textile substrate proved sensitive to plasma process powered by microwave energy and with an increased quantity of hydrogen became damaged. This led to hydrogen being limited to the silane dilution and instead argon was tried with silane. A gas mixture of silane and argon resulted in an amorphous rich structure with no crystal growth. In an attempt to introduce the needed hydrogen into the intrinsic recipe, an orthogonal statistical design “Taguchi model” (see *chapter 5 Processes and parameters influencing the textile substrate*) was used. Hydrogen was added into the process through a ratio of argon/ hydrogen combined with altered microwave power and silane rate. After possible combinations with hydrogen were found (see *chapter 6 Results and discussion*), further work (see *chapter 5 Processes and parameters influencing the textile substrate*) was carried out

to improve crystal growth in the amorphous structure. The different process settings and experimental approaches were analysed, evaluated and discussed (see *chapter 6 Results and discussion*).

Raman spectroscopy was the main technique used to analyse structure content and film quality and how the structure changed by altering process parameters (see *chapter 3 Nanocrystal structure and properties*). Knowledge was gained how process parameters influenced the film structure and which parameter settings to use for different crystal growth in the amorphous matrix, which led to further examination of the parameters required for nano- and micro- crystal silicon. The crystal growth within the size of nanocrystals was later identified as having the hexagonal wurtzite structure. Wurtzite structure had an additional Raman peak ("intermediate peak"), a specific fingerprint appearing at 500/ 505cm^{-1} between the amorphous peak at 480cm^{-1} and the crystal peak at 520cm^{-1}. Raman spectra of wurtzite structure films did not only contain the three peaks of amorphous, intermediate and crystal silicon, but also several smaller peaks due to additional phonon vibrations. The structure of the known hexagonal Si-IV phase and its features are discussed in *chapter 3 Nanocrystal structure and properties*, and the typical Raman peak shape and location related to the hexagonal structure and the phonon vibrations typical for wurtzite. It was also found that using Raman spectroscopy on nanocrystal silicon thin film required careful settings of the power for the laser-beam, when increased power changed peak location and shape.

An expected advantage with crystal growth in the amorphous matrix is improved physical properties, because amorphous silicon has high light-degradation known as the "Staebler-Wronski" effect. The measurement of optical transmission and band-gap energy gave different values according to the content of amorphous and crystalline components and crystallite size. The Tauc plot of optical absorption coefficient based on traditional square root dependence was not always applicable in a structure with nanocrystal content and instead cube root dependence was used to get a more linear fit for the crystal phase. The square root value proved a good fit with the amorphous band-gap energy value at ~1.8eV, while cube root was more applicable for crystal growth with band-gaps of ~1.1eV and ~1.6eV depending on crystal size. (see *chapter 5 Processes and parameters influencing the textile substrate*)

After experiencing that the polyester weave could melt far below 200°C and its melting point at ~256°C, thermal analysis was tried to check the content of polyester. Differential Scanning Calorimetry, DSC helped to identify a slight modification of the

polymer chain, shown by glass transition, T_g and melting point, T_m changing slightly in temperature after the calendaring and conductive coating, whilst a greater change took place after the PECVD process. Settings of the process parameters became very important too, to gain a stable process condition and to avoid fluctuation of process and substrate temperature. (See chapter *5 Processes and parameters influencing the textile substrate*)

In work with renewable energy, it is important to consider a product's carbon footprint, which is based on the emission of carbon dioxide, CO_2 coming off the quantity of consumed energy used in manufacturing the product. The awareness of carbon footprint has led to many European countries agreeing to reduce the emission of CO_2 by 2020. More common in larger companies is to map the energy emission related with the product and its manufacturing. Energy emission refers to the total energy use related to a product such as silicon thin film on woven polyester. To get a value of carbon footprint, both Life-cycle assessment, (LCA) and Life-cycle impact, (LCI) were used to calculate the total energy use from manufacturing to recycling of the device. Studies from both the semiconductor and the textile industry have been used, which helped to estimate the energy use for the silicon thin film on woven polyester. *(See chapter 4 Environmental assessment& impact of silicon thin film on woven polyester)*

Finally *chapter 7 Summary and conclusion* emphasizes that knowledge gained from published material and the results from this experimental work have helped to conclude a possible way of depositing silicon thin films with nanocrystal growth in an amorphous matrix on a textile substrate. Silicon thin film on a polyester weave is an unusual product and a cross-discipline between semiconductor and textile industries: their process technologies require research in areas such as thin film markets, processes and structures related to silicon thin films, and textile materials. These different topics are found in the review that follows this present chapter, *chapter 2 Brief history of silicon thin film and its process on textile substrate*, together with underlying science and technology.

2. Brief history of silicon thin film and its process on textile substrate

2.1. Introduction

This chapter gives a brief review of the topics related to this work "silicon thin film on textile substrate, woven polyester", which refers to the photovoltaic, semiconductor and the textile industries. The subjects considered are the photovoltaic market with focus on development of silicon thin film, process methods and structure content regarding silicon thin film and the performance and properties by using a textile substrate such as woven polyester. The photovoltaic market contains a brief overview of the development from conventional crystal silicon to thin film (silicon) and the new niche markets developing with the introduction of flexible solar cell design. The necessity of developing alternatives to conventional crystal silicon cells comes with an increased shortage of silicon and the higher manufacturing cost related with silicon wafer. Thin film became an option by using limited resources and even though thin film cells have less efficiency than crystal silicon, the flexible solar cell offers design options, the rigid crystal cell can't compete with. With development of silicon thin film, different process and structure options are being discussed to optimize manufacturing and the cell capacity.

2.2. Photovoltaic, PV and the market

An increasing awareness, how the use of fossil fuel damages the environment, has led to the development of renewable energy sources such as hydro, wind and solar. Photovoltaic technology is one of the renewable energy sources developed as an alternative to fossil fuel. This alternative source was highly considered after the oil crisis in 1974 and at the beginning of 1980 photovoltaics was discussed as a possible energy source. The advantage of using photovoltaics was no limitation of the source, solar energy. Countries such as Germany and Japan introduced programs to support growth of solar sourced energy for residential use. The policy driven programs have proven a success after these countries have become the leading nations in use of photovoltaics as an energy source. [1,2,3,4,5]

The European Governments have established programs and given financial support to develop renewable energy and especially photovoltaics as a future energy source. The positive development of photovoltaics in Germany and the support from the European Union, EU has led to other European countries such as Belgium, Spain, Italy and France introducing similar programs. [1,2,6,7,8,9] Other nations such as China, India and South Korea are supporting a fast progress through photovoltaic research, to establish PV production. [1,6,9,10] The USA has used a policy driven program to increase solar power supply and is forecast to get a similar or greater growth than Germany, however this depends on choice of policy. [6] The leading countries with installed photovoltaics are all policy driven by programs from the government and it is found that policy driven programs are five times more effective than having no policy. [6,8,9]

The European countries are ahead with installation of photovoltaics compared with other nations around the globe such as Japan, USA, China and India. The global investment in PV installation rose from 23GW in 2009 to 40GW in 2010 and 69GW in 2011. [8,9,10] A prediction (figure 2.1.) for possible installation of photovoltaics by 2020 was carried out by European photovoltaic Industry Association, EPIA. [10] This study considered three scenarios such as *baseline*, *advanced* and *paradigm shift* with forecast for 2020 together with earlier studies from 2009 by EPIA, which discussed development to 2016 by using scenarios such as *moderate* and *policy-driven*. This prediction by EPIA was combined with the target values given by National Renewable Energy Action Plans, NREAP. The three scenarios from 2009 related to different rates of installment of photovoltaic for electricity supply by 2020. *Baselin*e related to 4% of the total electricity supply being photovoltaic, which resulted in 130GW by 2020. *Advanced* had an increase of 6% giving a total of 200GW at 2020. Both scenarios involved no or very little change to the infrastructure of electricity supply. While the *paradigm shift* scenario related to change in infrastructure and an increase by 12% and a total of 390GW by 2020. The moderate and policy-driven forecast for 2016 could be linked to the prediction for 2020, when *moderate* with 4% growth is a shorter version of the baseline, while *policy-driven* with 8% is halfway between advanced and paradigm shift. [10]

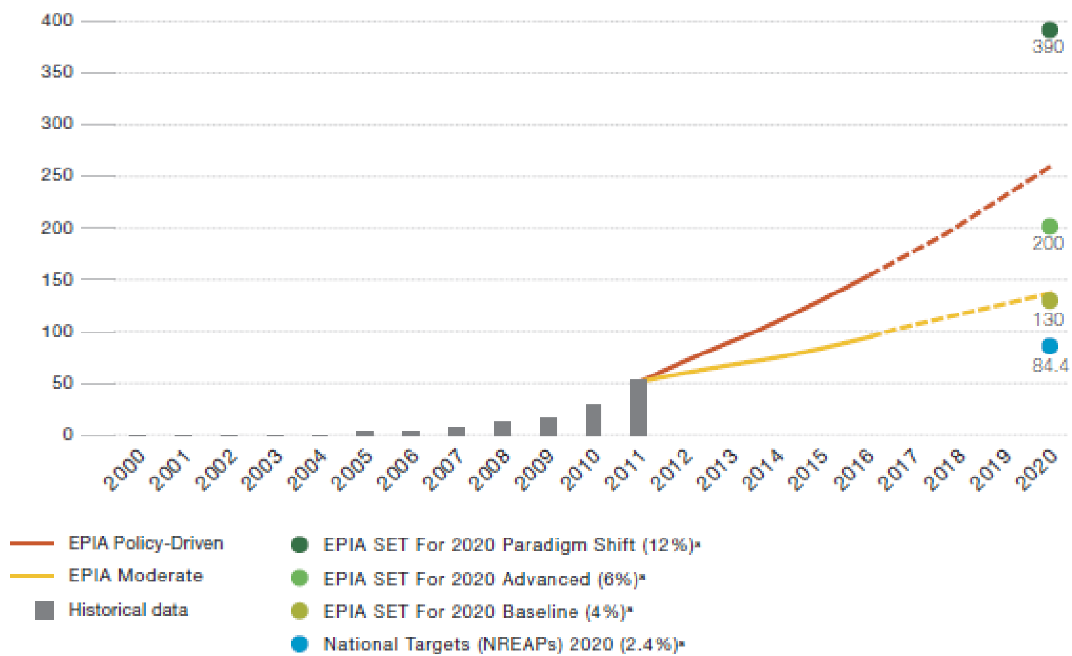

Figure 2.1. forecast for 2020 by different references such as EPIA's three different scenarios (baseline, advanced and paradigm shift), NREAP, National Renewable Energy Action Plans value with earlier EPIA prediction for 2016 with a moderate and policy-driven scenarios. [10]

However countries with an established PV market such as Germany are facing new challenges, how to maintain strong manufacturing and service at a low cost after experiencing reduced demand. The prices today for a PV-system are set according to a high manufacturing rate. One option has been to start taking a market share outside Germany, which allows them to keep a high manufacturing rate and to be able to provide a good service at low cost. [4,6] Discussion between European countries, the member states and European Photovoltaic Industry Association, (EPIA) has led to a strategy to increase the growth of photovoltaics. The main target is to improve manufacturing processes by new technologies, reduced costs in relation to manufacturing and increased generated energy, as well as developing building integrated PV-devices. For a strong increase in PV investment and installation in the future, government policy is required such as feed-in-tariff systems and financial support to R&D, plus manufacturing investment to allow continuous growth of the overall PV-market during a time with strong financial uncertainty. [2,5,9,11,12]

A new PV market is to be developed within the countries in the sunbelt region (75% of the global population) after starting to appreciate the advantage with photovoltaics and potential as an energy source both domestic and for export. [8] With the highest solar irradiation in this area, the investment in photovoltaics is soon paid back due to the high energy generated and this has resulted in a high interest for investment. It has been forecast that PV will be the main electricity supply by 2030. [13] Export of photovoltaics today refers mainly to the energy generated by solar concentrators on a large scale in countries such as Spain and USA, who are the leaders. However this kind of technique is facing challenges by having high installation costs, which reflects on the energy cost. Other issues for this kind of system are the location of the plant, which is often outside the infrastructure of grid-connection. Due to the large scale of the PV-plant with solar collectors a discussion has arisen as to how it affects the environment around the plant.

For photovoltaics to become one of the main energy sources three key areas need to be addressed such as "*Government incentives*", "*energy and solar cells costs*" and "*portable and flexible electronics*". Government support through policy driven programs is important to gain a growing market, together with the cost and efficiency of a cell, and the applications, when part of the future market will be portable and flexible solar devices. For the future and the growth of thin film PV this technique and devices need to be grid-connected, which depends on the government. [5]

A forecast (table 2.1.) for photovoltaics to 2025 was carried out [2], which addressed the concerns of carbon dioxide in relation to manufacturing and the device and the amount of jobs predicted with an increase in manufacturing of PV-devices.

Table 2.1. an estimate of installed photovoltaics and the power it generates. [2]

Estimated global growth of photovoltaic to 2025

Year	Annual Installed Capacity [MW]	Annual Growth Rate [%]	Estimated Annual Electricity Production [MWh]	Estimated Reduction of COc [COc]	Estimated Jobs
2010	5.609	26,0	28.746.819	17.248.092	228.714
2012	8.425	26,0	48.344.329	29.006.597	347.162
2015	16.765	26,0	102.433.996	61.460.398	650.629
2020	34.079	19,0	275.689.801	165.413.881	1.892.736
2025	55.343	11,0	588.997.967	353.398.780	3.249.004

First generation crystal silicon PV (figure 2.2.) has a strong advantage with good efficiency, which makes it difficult for newcomers. However crystal silicon cells have had the disadvantage of using a large quantity of high purity silicon for the substrate wafers. An increased demand for crystal silicon from both the photovoltaics and semiconductor industries in 2009 led to a shortage of high purity silicon, predominantly in Europe. The shortage of silicon raised manufacturing cost and increased the lead-time, which made it clear, that a cell structure with less purity and quantity of silicon was necessary such as thin film. [14,15,16] The need of a cheaper cell design supported development of second and third generation solar cells (figure 2.2.) with focus on developing a cell with reduced silicon use, but with the same good efficiency as crystalline silicon solar cell. The third generation solar cell (figure 2.2.) focuses on cell efficiency by changing the cell design and its content such as integrating crystal growth into an amorphous structure, combining several junctions such as tandem and triple junctions or using organic and inorganic material in the same cell. [1,14,16] The most important and strongest option predicted within the third generation of solar cells is different band-gap materials, either by stacked cells or integrated quantum effects/ confinements with silicon nanocrystals (2-5nm). [17]

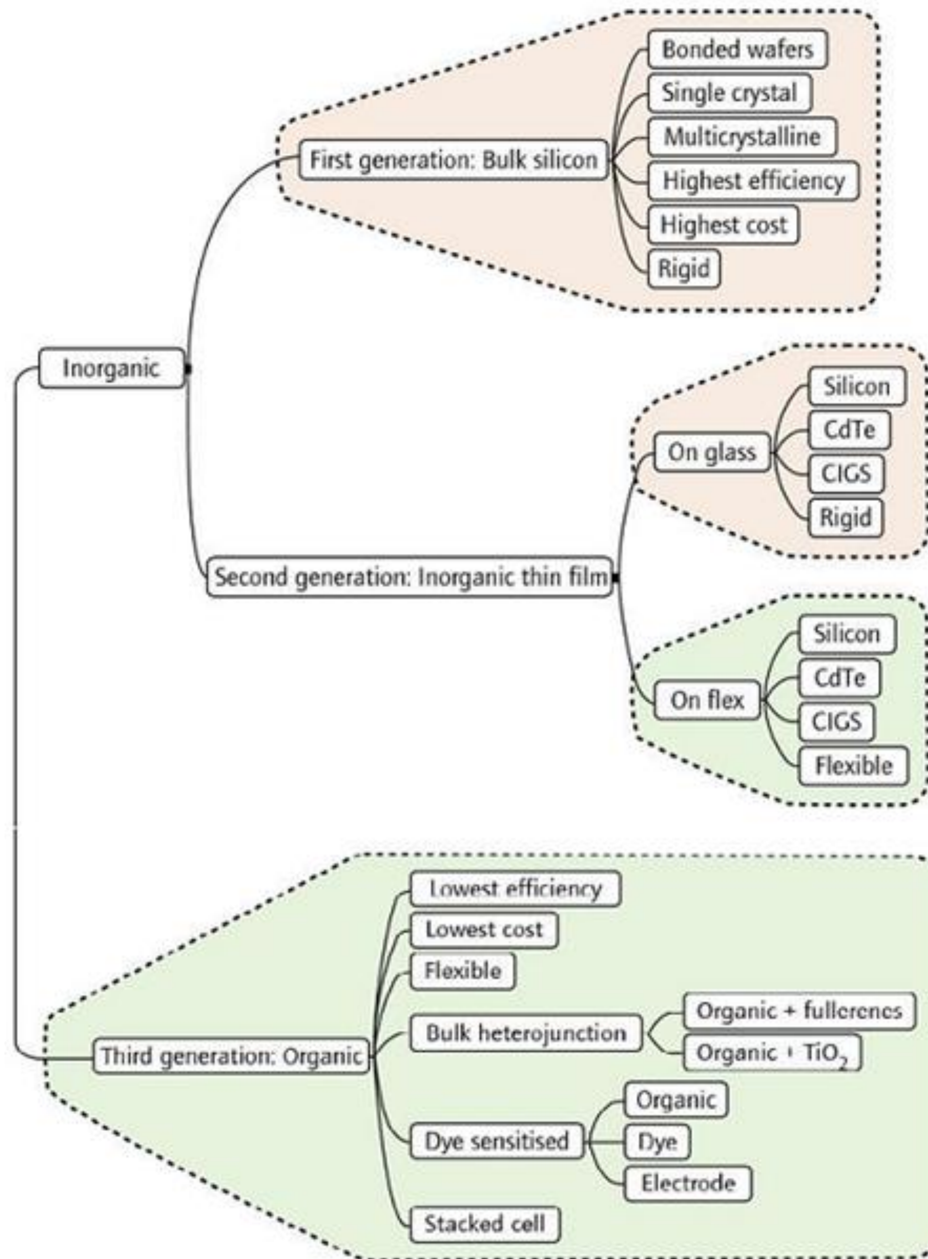

Figure 2.2. shows the different generations of cell design and the content. [4]

Thin film cells had the advantage of much lower manufacturing and installation costs, larger manufacturing capacity, less material use and reduced number of process stages than manufacturing of high purity silicon wafer. The increased choice of low-cost substrate such as foil, polymer film, paper etc., is the main factor to lessen the manufacturing cost of thin film. The choice of substrate for thin film has allowed the solar panels being lightweight, flexible and portable, which increased the number of applications due to being easier to integrate into different designs. [4,18]

This has made flexible solar panels competitive in certain niche markets, when the conventional solar panel of crystal silicon is too stiff and heavy framed, which often limited the use to roof-fitted panels. [1]

Silicon is the most common material used in photovoltaic devices. [9] Amorphous silicon (a-Si) thin film cell has the advantage of a relatively low production cost compared to other thin film technologies. [16,19,20] A-Si thin film is actually a hydrogenated amorphous silicon alloy (also known as a-Si:H): it has good mechanical and physical properties, which makes it durable and possible to deposit on flexible substrate. This film quality can be processed at a low temperature and still have high heat-resistance in air and withstand direct sunlight. [21] A disadvantage of amorphous silicon thin film PV is the low efficiency (5-7%) compared to crystal silicon PV with a typical cell efficiency of 20%. [16,19,20] For thin film to compete against conventional crystal silicon (which offers >25 years life-time) an efficiency of more than 10% is needed, with a life time above 20 years. [18] By targeting a higher cell efficiency with reduced costs, other cell options (figure 2.2.) have been developed such as Cadmium Telluride, CdTe and Copper Indium Diselenide, CIS, which has been modified by adding gallium, Ga known as Copper Indium Diselenide with Gallium, CIGS. [2,3,16,19]

The capacity from installed thin film cell increased by 50% to 2GW between 2009 and 2010 and CdTe stood for 90%, while a-Si and CIGS shared the remaining 10%. [5] However CIGS cell has shown a better cell efficiency and performance than first expected, after introducing large scale manufacturing and with continuous improvement in efficiency, the CIGS cell is forecast a strong future. [4,22] It is predicted that thin film will represent 25% of the total PV market in 2013. [17] However, a higher efficiency is still required before the thin films option can replace crystal silicon (C-Si) solar cell.

Light-trapping techniques have lately been applied by working with a textured backing to a conventional crystal silicon or thin film. This has led to crystal silicon wafer becoming thinner and textured, which helped to reduce material use and cost, manufacturing and installation cost, with an increased cell efficiency per square meter. [15,16,17,19,22,23] Textured back surface increased the light scattering back through the cell, which gave an optical thickness 50 times of its actual thickness and an enhanced cell efficiency of 25% without modifying the cell structure. [17,24]

Thin film deposited directly onto a flexible substrate can operate either as a solar module (panel) by itself or attached to a flexible material such as textile either by lamination or stitching etc. The flexible solar panels commercially available are based on a polymer film either operating on its own or being laminated to a flexible material such as a textile material (figure 2.3.). The laminated panels are often used for outdoor garments and accessories. [25,26] An example is from O'Neill [27] with powered jackets and rucksack. The flexible panels attached to the garments and accessories are often fitted in such a way, that they can be easily detached during washing. Portable solar panels can often supply enough energy to power electronic items such as mobiles, iPods etc. [25,26,27,28,29] Flexible solar cells have also been tried in interior design such as curtains, wall paper etc. [30] Thin film onto textile material requires a product solution, which allows the use of existing process methods to avoid new investment, when this is a niche market with presently low return. [4]

Figure 2.3. an example of flexible panels integrated into a garment. [25,29]

2.3. Solar cell operation

"Photovoltaics" comes from "photo" as light and "voltaic" as voltage, which means light converts into electricity. [31] A working solar cell needs semiconducting materials with opposite built-in charge in a diode structure to control the separation of electrons and holes. The most basic diode contains two oppositely charged materials, known as n-

layer and p-layer. The n-layer has an increased number of negative electrons and the p-layer has a higher number of positive holes, from the intentional addition of small amounts of impurities (donors and acceptors, respectively). The two layers produce an electric field between them and cell activity depends on the light striking the cell, when increased light generates pairs of electrons and holes. The electrical properties of a device depend on the creation and motion of electrons and holes. [31] In a conventional photovoltaic cell having a simple pn diode structure, there is a built-in electric field at the pn junction which separates the oppositely charged electrons and holes, driving them to opposite sides of the junction. This field region is relatively narrow and cannot separate electrons and holes created in the rest of the device. Amorphous silicon thin film solar cells have taken this a step further by introducing an undoped layer between the two charged layers (doped) known as the intrinsic, i-layer (figure 2.4.). The intrinsic layer improves the separation of electrons and holes by providing a wider electric field, which helps to increase the volume of captured photons. [32,33,34,35]

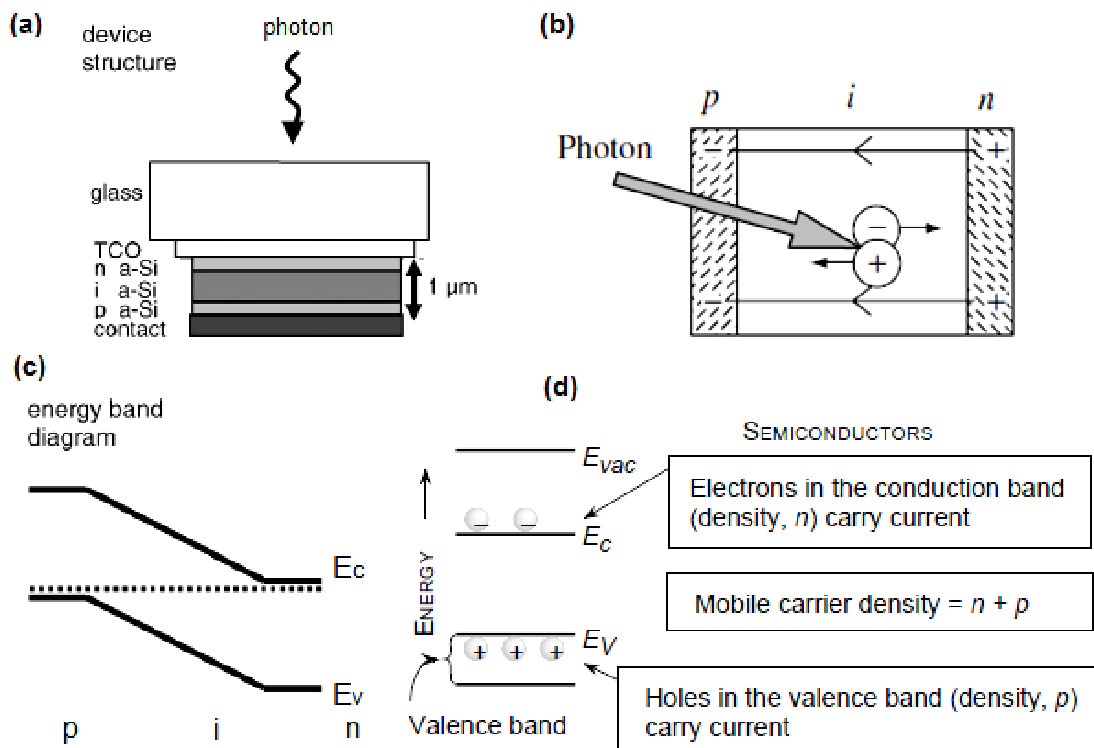

Figure 2.4. (a) [34] illustrates how the light enters a p-i-n solar cell, while (b) [33] explains a separation of charges due to the photon energy. How electrons and holes separate into each area is often explained by an energy band diagram (c) [34], which explains (d) [35] how the valence band becomes positive charged (holes) by increased number of electrons becoming excited and moving to the conduction band. [33,34,35]

As the light strikes the cell, the photon energy is transferred to a bonded electron. The extra photon energy makes the electron excited in the valence band and if enough energy is gained the electron will jump out of its bonded position into the conduction band and drift freely in the semiconductor. When the electron leaves the valence band, it creates a hole, which is positively charged and can attract a negatively charged electron. The electron-hole pair can only be generated when the photon has higher energy than the band-gap energy, E_g which separates conduction and valence bands. [32,34,35] The light source discussed does not need to be direct sunlight, as the photovoltaic cells are still efficient in normal diffuse daylight. [22,34]

The order of thin film silicon cell of n-i-p or p-i-n layers depends on the type of substrate in use such as transparent glass or opaque metal (figure 2.5.). In the “substrate” configuration the light comes through a transparent contact into the p-layer continuing through i-layer into the n-layer, which is connected to the back contact of the cell. The fabrication of a cell-design needs attention to the structure and film thickness for each layer to obtain a high efficiency with optimum light-scatter through the cell. The right thickness and band-gap are important and especially for the p-layer, when a too thick layer and narrow band-gap would trap the light in the p-layer and prevent it reaching through to the i-layer. The top layer (p-layer) needs high optical transmission and should avoid light being reflected. [18,22]

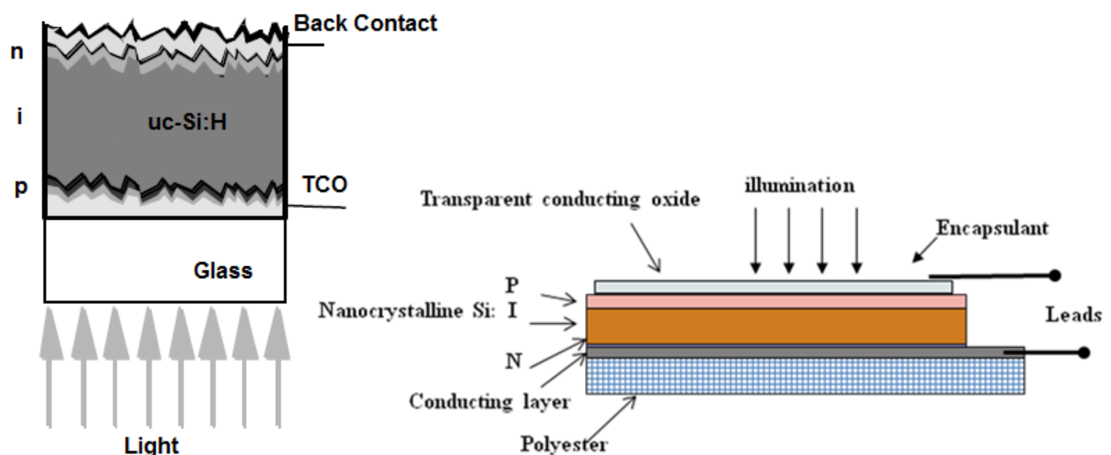

Figure 2.5. the order of the silicon layers such as n-i-p or p-i-n depends on the substrate, when glass will start with p-layer (left) compared to textile with n-layer (right). [36,37]

A silicon thin-film cell (n-i-p-layer) with mixed phase of crystal growth in an amorphous structure needs less cell thickness than a completely micro-crystal structure, which required increased thickness (1μm) to gain the right optical and electrical properties. [38,39] The increased thickness of a crystalline film was to compensate for a low optical absorption coefficient. [38]

In a combination crystal phase in amorphous matrix, a balance of deposition time was necessary to allow enough crystal growth without the structure becoming 100% amorphous. The ratio of crystal against amorphous phase, and crystal size, reflected on cell performance, when increased amorphous phase gave a higher risk of light-degradation. Larger crystals produced voids in the deposition and small crystals increased the optical and electrical performance of a thin film. [38,40,41,42] The advantage with nanocrystals (1-10nm) and quantum confinement effect is absorption of light at long wavelength, which increases the overall absorption of a mixed cell structure. Another advantage with small size crystals is the increased scattered light and emitted light through the cell layers due to the spherical particles. [43,44] The optical absorption becomes enhanced with mixed structure by having a broader waveband response (figure 2.6.). [31,38] The effective threshold wavelength for crystal silicon is 1100nm compared with 700nm for hydrogenated amorphous silicon. However with a thin amorphous layer, the maximum absorption has been found at 550nm. [44]

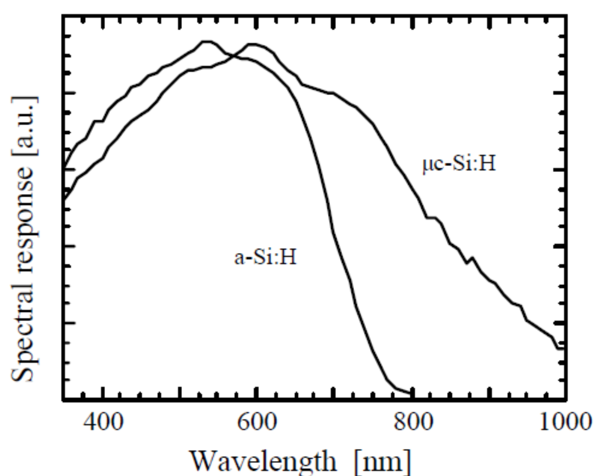

Figure 2.6. comparing spectral response of an amorphous and microcrystal silicon cell, both designed with p-i-n. [36]

The advantage with a mixed structure of small crystals (micro) embedded into the amorphous matrix was increased spectral absorption by having two band-gap values, E_g, where nanocrystal responds to long and amorphous to short wavelength. Absorption curve of nano- and micro- crystal silicon follows crystal silicon to a great extent, which is discussed more in *chapter 3, section 3.6.*. [32,33,34,35,36,38,45]

2.4. Process to manufacture thin film flexible solar cells

Plasma comes from an electrical discharge produced by a combination of power and gas, and a plasma process can be divided into three distinct areas: plasma bulk, plasma sheath and substrate. Plasma sheath is important in relation to surface activation and deposition, especially at low process pressure, when the process parameters will control the plasma sheath's thickness. [46]

Plasma polymerization [47] and its parameters influencing plasma reaction was applicable also to vacuum based plasma enhanced chemical vapor deposition, PECVD system for silicon thin film. Reaction rates were strongly dependent on power, process pressure and gas-flow, which influence plasma distribution. The chamber geometry such as location of the electrodes (electric field), the substrate plate combined with flow rate would determine the size of a plasma's sheath distribution and the deposition rate and quality. A plasma distribution can either become asymmetric or symmetric. A non-uniform plasma can be due to too much gas-flow compared with energy input, which would allow gas to pass the plasma without being activated. A uniform plasma distribution was necessary, to gain a deposition with even rate and distribution. [47] A plasma process can either be heterogeneous or homogenous depending on plasma configuration, when a heterogeneous reaction is between the gas phase and a surface compared with a homogeneous, which reaction is mainly in the gas phase. Homogenous deposition often has a poor bond to the substrate and can appear as a white powder, while heterogeneous reaction contains a strong bond between deposit species and the surface. [33,37]

Reactions between radicals can take place in the plasma, but also at the substrate surface between radicals and bonded species. [48] Radicals (formed in the plasma zone) travelling towards the substrate can react and transform several times before reaching the surface and bonding with deposit species on the substrate. In plasma with

silane mixtures, most formations of radicals come from silane to form amorphous growth. Additional gases will also take part depending on their response to a given plasma condition. [49,50] Plasma also contains electrons, ions and non-reacted species (figure 2.7.). [49]

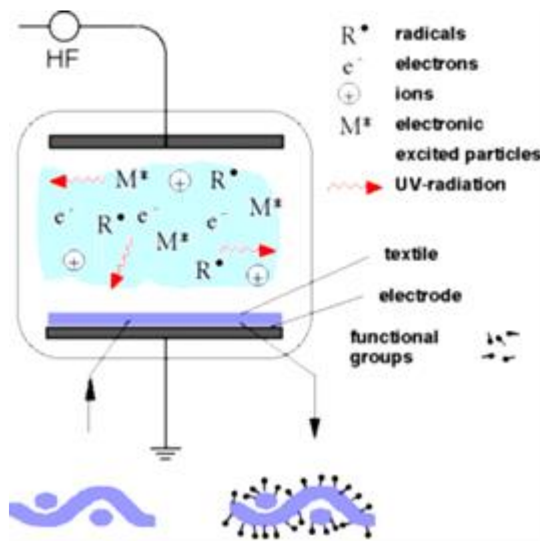

Figure 2.7. a plasma chamber and the main factors related to a plasma process. Depending on gas mixture and process settings there will be different kinds of radicals, electrons, ions etc. [49]

The electrons become excited in the plasma and start colliding with gas molecules and form species such as ions, radicals and more electrons. [51] The species formed depend much on pressure, power level and frequency of power source. Process pressure affects the collision rate and will alter the mean-free path either by shortening or increasing the travel distance of excited species. With low pressure the travel distance increases (figure 2.23.), while high pressure gives the reverse effect. Travel distance will affect reaction rate and distribution of the plasma in relation with substrate.

The difference between microwave- and radio-frequency- (RF) plasma is the energy and quantity of ions in the deposition, as the ions are too slow to respond to higher frequency. With RF plasma, ions can take part in the deposition and an ion rich deposition makes it more difficult for smaller radicals to bond, when often an ion has only one electron missing before reaching steady state. [47,52] Plasma from microwave energy gave less risk to ion bombardment of surfaces due to the higher frequency producing little ion energy. [36,53] Electron energy is also affected by plasma

energy, when increased power excites the electrons more. The level of gas excitation depends also on gas- mix and rate together with process pressure and temperature.

Common process method for thin film production with flexible substrate is roll-to-roll (R2R) [54], which allows thin film deposition being applied continuously without interruption. Continuous and closed process avoids breaks due to batch or machine change, which helps to prevent exposure of oxygen and sudden temperature drops during the film process and avoids damaging the film quality. Other advantages with continuous production are increased throughput, reduced handling cost and a more environmentally friendly process by less loss of heat, gas etc. [55] The roll-to-roll system (figure 2.8.) contains several chambers with individual settings such as vacuum pressure, plasma-power and gas mixture and rate. [56,57] One of the more known machine manufacturers of roll-to-roll systems is Roth & Rau AG and they together with the research institute, ECN Solar Energy have designed and studied the process capacity of roll-to-roll process. Jointly they have published [57,58,59,60,61] regarding the machine layout, process parameters for different silicon cell designs (p-i-n or n-i-p), film qualities and structure content such as amorphous, nano- and micro- crystalline silicon.

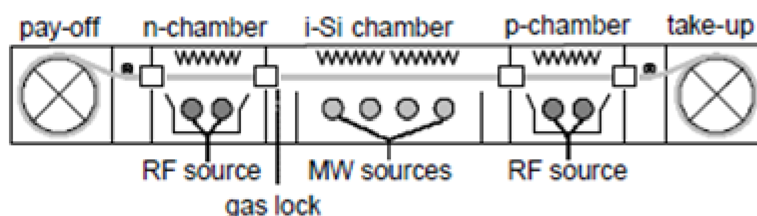

Figure 2.8. production line for the 5 chambers from Roth& Rau, which illustrate input of material and the different processes used to the finished panel. [58,61]

One roll-to-roll system (Flexicoat 300, Roth& Rau AG) contained five chambers (figure 2.8.) divided into substrate load and unload and three process chambers, two for doped layers and one intrinsic. [55] Pressure and gas supply were individually controlled in each chamber and between the chambers. Argon was often used as a cleaning and transport gas in areas of load and unload and between the deposition chambers. Argon has the advantage of being a stable gas compared with hydrogen, which easily can be explosive in air and therefore restricted to limited quantity and use. [62,63] The deposition chambers are equipped to control parameters such as power,

pressure, gas rate and mixture for each chamber and between each chamber are pumps to avoid contamination carry-over from the substrate and the chambers. A set vacuum through the machine and chambers allows a more stable process condition and avoids variation in pressure and temperature and repeated degassing of the substrate. [59,62,63]

Deposition chambers (doped and intrinsic) were equipped with linear power sources (figure 2.9.), which allowed a continuous deposition through the chamber and a more uniform plasma distribution. [64] The plasma enhanced chemical vapor deposition, PECVD was powered both by microwave and radio-frequency (RF), when it helped to tune the different thicknesses required for each layer. Doped layers required being thinner and RF-powered plasma was used compared with intrinsic layer that used a microwave powered plasma. [55,56,58,61] The microwave based linear source (figure 2.9.) had restrictions in width and length by a maximum of 20cm wide and a length between 50 and 150cm. The substrate transport speed was between 5 and 25cm/ minute depending on process parameters (gas mixture and rate, power and pressure, from 0.001 to 0.1mbar), when high deposition rate gave less uniform film and poorer reproducibility of the film quality. [56,57,59]

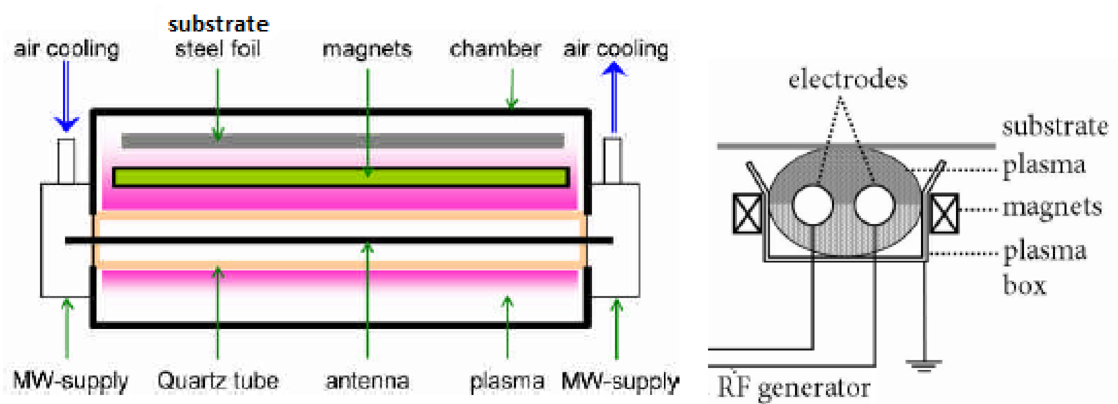

Figure 2.9. the diagram shows the two different power sources used in the roll-to-roll system, see figure 2.8. The plasma unit to left is a microwave source, while the image to right is a cross-section image of a linear radio-frequency based plasma source. [55]

2.5. Thin film silicon growth, amorphous and crystal content

Microcrystal silicon was first discussed and developed back in 1960 by Veprek [36,65], but not seriously considered as a structure in silicon based photovoltaics until 1980. [66] The interest for microcrystal structure came as an option to avoid light-degradation, when integrating crystal growth into the amorphous structure reduced the effect. [65,67] Amorphous silicon (a-Si:H) thin film was developed as a possible “replacement” for conventional crystalline silicon. [22] The drawback with hydrogenated amorphous silicon, a-Si:H was the low cell efficiency after exposure to light, known as the Staebler-Wronski effect. The light-degradation (Staebler-Wronski effect) comes from hydrogen bonds breaking over a period of time. [31,33,68]

The silicon atoms in an amorphous structure have the same basic position as in a crystal structure with covalent bonds between four silicon atoms with Si-Si bonds repeated through the lattice but without long-range order (figure 2.10.). [69]

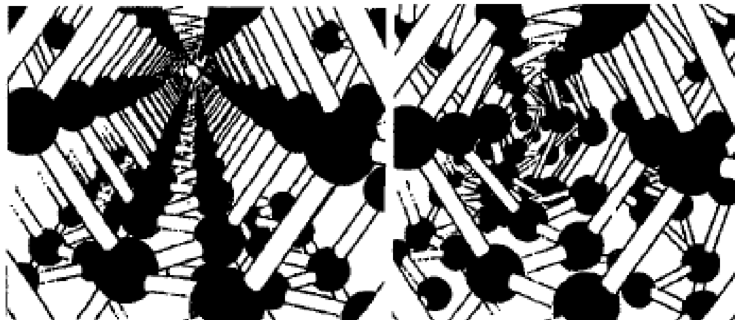

Figure 2.10. the difference between a crystal (left) and amorphous (right) structured silicon lattice, amorphous having a random bonding pattern compared with crystal. [69]

Amorphous structure is made up of an interrupted/ non-repeated chain (figure 2.10.) and with silicon not always bonded to another silicon, loose bonds are produced, which makes it possible for hydrogen to bond (figure 2.11.) known as hydrogenated amorphous silicon (a-Si:H). The bond between hydrogen and a silicon atom is weak and easy to break, which leaves a dangling bond (figure 2.11.). Dangling bond is known as a defect with reduced electronic properties due to the charge carriers being trapped. [45,59]

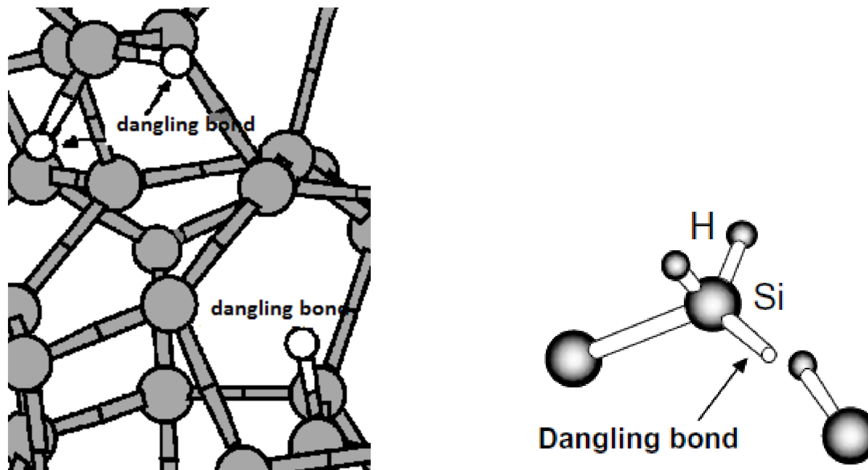

Figure 2.11. a silicon structure with dangling bonds (left) [18], while the right image is more detailed with silicon bond to silicon and hydrogen. [70]

Additional hydrogen, diluting the silane, SiH_4 influenced the growth mechanism by increasing the crystal content in the amorphous silicon structure. The concentration of hydrogen against silane reflected on the crystal growth, grain size and the quality and properties of deposit film/ structure. [31,45,46,66,71,72] The number of hydrogen bonded into a structure depended on the plasma and process conditions. When added hydrogen did not support crystal growth, the amorphous phase was enhanced followed by a higher number of hydrogen induced loose bonds, which gave problem with light-degradation. [73,74,75,76,77] The crystal growth and formation in a mixed structure and the quality of deposition depend much on process conditions such as high power, which encouraged a columnar growth with large crystals. [78,79]

Crystal nucleation as clusters appears in islands randomly through the amorphous matrix. [36,80,81] The clusters can change into spheres and columnar shape depending on crystal size and process condition (figure 2.12.). [46,66,82,83]

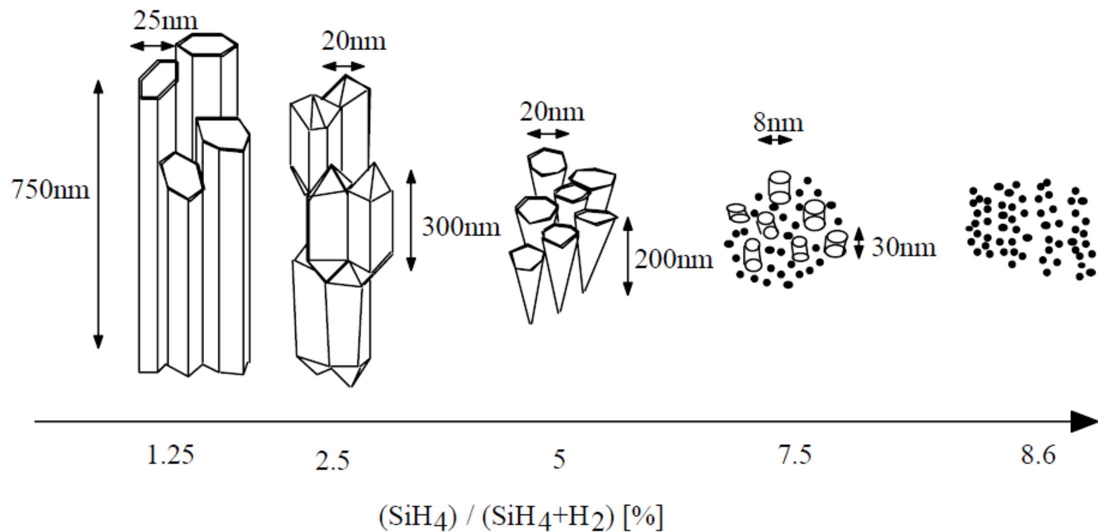

Figure 2.12. shows development of crystal size in relation to ratio of silane and hydrogen. The development of crystals starts by nucleation and continues into a mixture of crystal grains and larger crystals, where some continue growth into columnar shape. [36,80]

Crystal formation in an amorphous matrix is often described as a linear effect, which refers to the straight crystal formation in the random amorphous network. [84] By integrating crystal growth, the level of stress may be enhanced in the structure. The amount of stress depends on crystal size, when deposits with smaller crystals contain more stress. [82,85]

Mixed structure (figure 2.13.) starts with amorphous growth followed by crystal nucleation within the amorphous matrix, the crystal size increasing over time. Larger crystal size in the amorphous growth led to higher content of voids, cracks and defects etc., which gave reduced mechanical properties and increased number of cracks during flex and movement. (figure 2.13.), [46,66,86,87] Growth of smaller crystal grains created fewer columnar defects and voids, which were typical for microcrystal structure. [86]

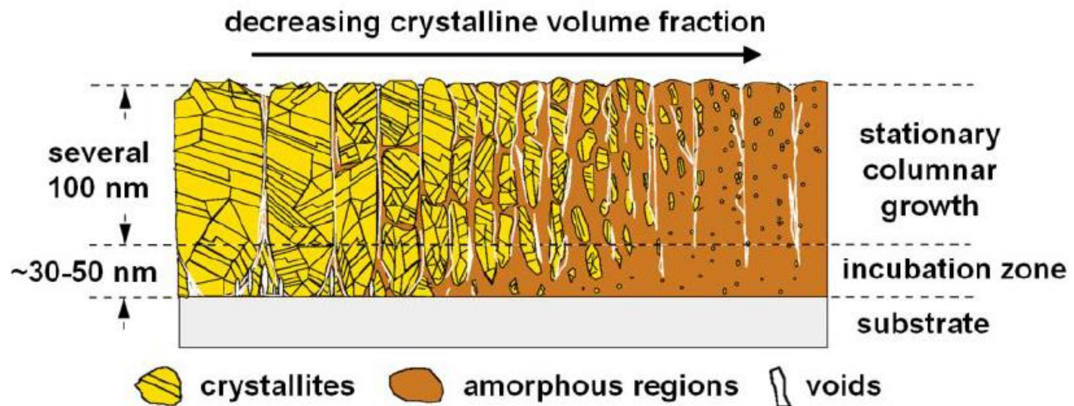

Figure 2.13. mixed growth structure with small crystals nucleating and developing in the amorphous matrix, some of the crystals stay small when others become larger by deposition time. [66]

Increased growth of small crystals resulted in large grain boundary areas between the crystal and the amorphous structures and the best cell efficiency was gained at the threshold between the crystal and amorphous phases with crystals of 1-2nm. [33,36,46] The small grains helped to support a stable structure and provided a good boundary between the phases, which reduced light-degradation and improved electrical and optical properties. [43,77,80,88,89] The nanocrystal phase showed no light-degradation, while the amorphous phase and the boundary between the phases did degrade. [38,74]

Nanocrystal structure can be produced in two ways, either by small particles (1-2nm) being produced by a reaction in the plasma and embedded into the structure or nano-particles (1-2nm) formed through a reaction with deposited radicals in the amorphous structure. Crystal growth (figure 2.14.) in an amorphous matrix can be described [50,80] in three phases:

1/ *Nucleation* by forming 2-10nm crystals embedded into the amorphous matrix.

2/ *Cluster formation/ coagulation*, larger crystals (20-40nm) are formed by coagulation.

3/ *Powder*, larger crystals merging, which depends on process temperature and time.

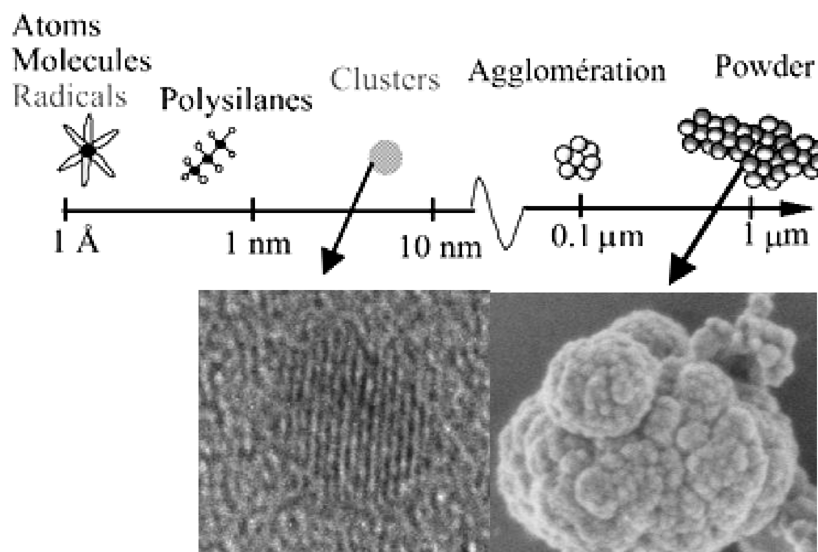

Figure 2.14. above different growth stages are given from initial nucleation through structural formation to cluster and merger into larger crystal and powder formation. The image to left refers to cluster formation, while the right picture is powder formation. [50]

When crystals merge into larger units they are conical shaped perpendicular to the substrate surface. [46] During the coagulation stage the temperature dropped, which partly caused powder formation, through embedded crystals of a few nm. [80] The crystals of cluster, sphere or columnar shape had the same atomic arrangement in the crystallites. [90]

Formation of crystals of different size depends on types of radicals available in the plasma chemistry. [78] The radicals generated from silane, SiH_4 were SiH_3, SiH_2, SiH, Si with additional species of higher silane such as Si_2H_6, Si_3H_8….Si_4H_{10} as well as H_2 and H. [70,78] The reaction route for SiH_4 decomposition depends on the electron energy (e),

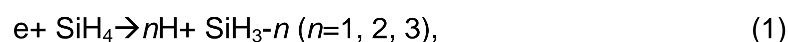

$$e + SiH_4 \rightarrow nH + SiH_{3-n} \ (n=1, 2, 3), \qquad (1)$$

and forming SiH_3 requires less energy than SiH_2 and SiH. [73] Available electron energy will determine the size of radicals, when larger radicals require less energy than small radicals (figure 2.15.). [78] However SiH_2, SiH and Si have a shorter reaction time than SiH_3 due to the fact that they are easier to bond. [70] The reaction route depends much on the energy available, when higher energy results in longer chain reactions. [71] The higher electron energy makes SiH_2 more active and easier to form larger molecules such as Si_2H_6 followed by Si_3H_8....Si_4H_{10} and formation of crystals larger than 10nm is often linked to SiH_2. [78]

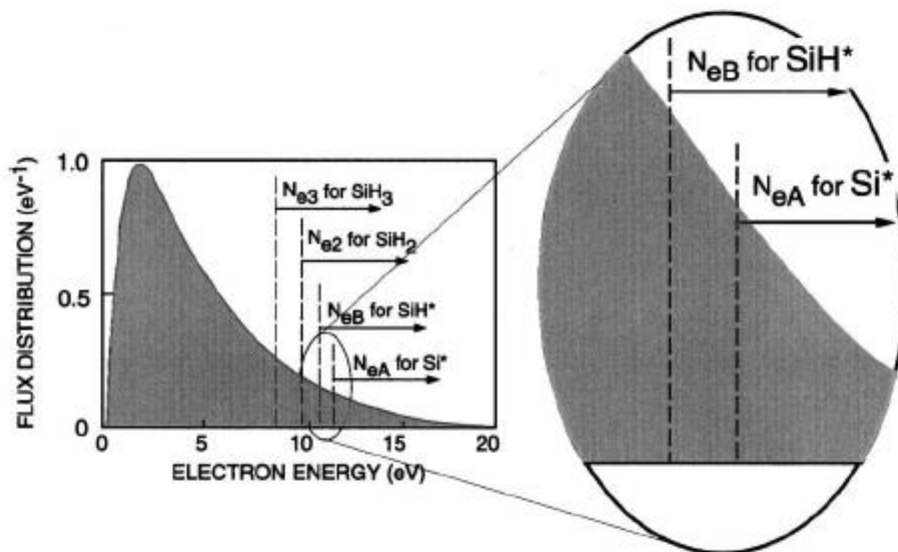

Figure 2.15. The electron energy (eV) for the different silane, SiH_4 radicals such as SiH_3, SiH_2, SiH and Si vary in value. [78]

With larger radicals bonding to the substrate surface, a sufficient etch effect is necessary to optimize bonding options and encourage small radicals to bond into a more linear formation in the random amorphous structure. Larger radicals encourage a random bonding pattern such as amorphous and with an enhanced number of loose bonds encourage an increased number of hydrogen bonds in the amorphous silicon structure. However larger radicals such as SiH_3 often related to microcrystal growth. Process conditions which encourage larger radicals to form, often give fewer small crystals, which results in low etch and reaction rates. A plasma deposition with larger radicals such as SiH_3 has three possible growth scenarios (figure 2.16.);

(A) Surface diffusion,

(B) Etching,

(C) Chemical annealing.

Surface diffusion (**A**), a high quantity of hydrogen is bonded to the substrate surface and through reaction within the hydrogen, local heating area is formed. The additional heat encourages larger radicals to bond to the surface.

Etching (**B**), the hydrogen reaching the substrate surface is breaking the weak bonds of Si-Si and allows radicals such as SiH_3 to bond.

Chemical annealing (**C**), the hydrogen reaction and bombardment against the amorphous structured substrate surface form an etch effect. The excited hydrogen penetrates through to the sub-layers and supports crystal formation. [70]

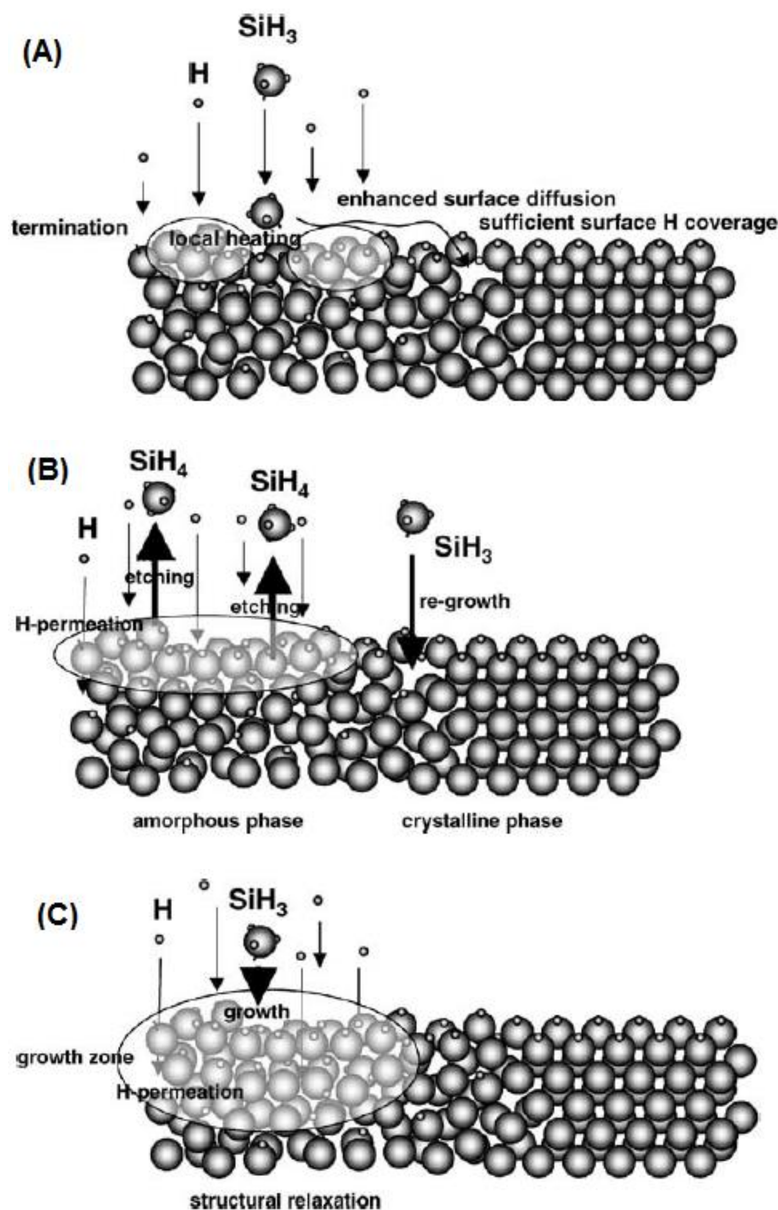

Figure 2.16. (**A**) growth procedure with SiH_3, then (**B**) illustrates etch effect and difference in structural order between amorphous and crystal growth, while (**C**) shows how larger crystals form through chemical-annealing. [70]

Plasma process with low process temperature has often higher concentration of SiH_3, which makes it important to have a good etch effect and supporting development and growth of both the crystals and amorphous phase. [70,76,91] However a careful balance was required between etch and deposition rates, when hydrogen affects both etch and deposition rates. [40,92] Balance between etch and deposition rates can be expressed by

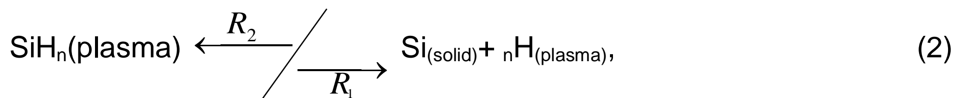

$$SiH_n(plasma) \underset{R_1}{\overset{R_2}{\rightleftarrows}} Si_{(solid)} + {}_nH_{(plasma)}, \quad (2)$$

where R_1 is deposition and R_2 is etching. [93]

A balance between good deposition rate and etch was necessary to clean off and reduce the number of poor and loosely bonded material, to get a good adhesion. [63,93] Low or no etch gives high deposition rate with powdery coat and poor bonding properties, while too high excitation gives high etch and cleaning with reduced growth rate. [92]

Historically argon has been regarded as a gas which enhances amorphous growth and not a gas usually used in thin film depositions. Later it was found that argon together with hydrogen diluted silane [63,72,81] supported microcrystal growth when using microwave powered plasma. [45,94] The ratio argon/ hydrogen was found important in relation to crystal growth, crystal size and film thickness, when high argon rate gave a thicker film by supporting growth rate with reduced etch effect, which led to amorphous dominance compared with low argon rate supporting crystal growth (figure 2.17.). [33,79,95]

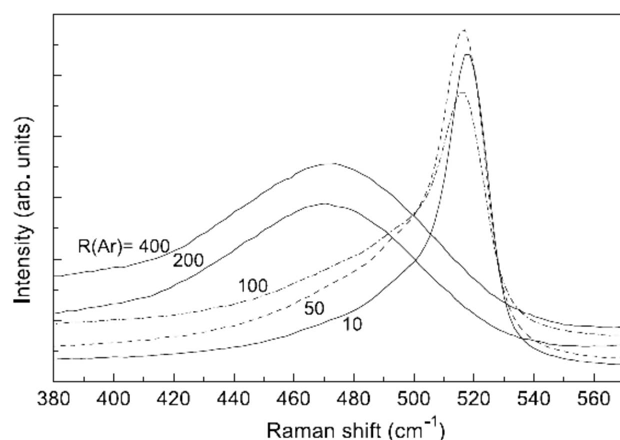

Figure 2.17. ratio of argon dilution against silane and how the Transverse optical, TO peak-width was reduced and shifted with increased crystal growth, when the argon quantity was reduced. [79]

The ratio of argon/ hydrogen against hydrogen diluted silane varied the crystal growth, when certain ratio of argon/ hydrogen gave microcrystal growth [96] and some nanocrystal growth [49] in the amorphous matrix. [79,94,96] Further reports [62,63,97] found how argon could influence etch effect and crystal growth. Argon showed more influence with microwave plasma at low pressure (below 0.1mbar) by influence on the electron energy [81] and the plasma configuration [94] and by stabilising the plasma condition. [59,62] Argon/ hydrogen mixture gave a more stable plasma process with less fluctuation compared to hydrogen alone. [59,62,63] The SiH_n radicals were changed by argon addition through the reduction in electron temperature. [62]

Process temperature proved important with argon/ hydrogen ratio, when deposition quality and crystal size and its density changed by substrate temperature. [98] It was reported, that crystal growth was experienced even with low process temperature at 200°C, but even as low as 150°C. [96,99] For a process with low substrate temperature, the gas mixture and flow-rate became more important to gain correct deposition quality and rate. [100] The advantage with low process temperature was increased growth of small crystals, which resulted in large grain boundary areas between the crystal and the amorphous structures. [33,36,46] Process temperature at 200ºC supported nanocrystal growth of wurtzite structure, hexagonal structure (Si-IV phase). [82,83]

2.6. Textile material

Textured backing for solar cells have become in focus, after experiencing improved cell efficiency by enhancing the optical reflection. Textile has proven interesting due to its texture and flexible properties and especially for the thin film solar cells. The advantage of using textile substrate is the variation of surface characteristics and a flexible substrate, which has a good mechanical performance with its high strength in relation to weight, structure and density. [101] Substrate surface has a great influence on thin film deposition, when increased surfaces roughness (texture) encouraged nucleation of crystal growth, rate and size. [33]

Textile can contain different yarn, filament/ fibre qualities, which reflect on the properties of a cloth. The yarn quality can be divided into groups of synthetic or natural materials and their performance and properties are very different. Natural fibres originate from nature from plants and animals such as cotton, linen, wool, silk etc., while man-made and synthetic fibres are manufactured by a cellulose or polymer based solution. Development of synthetic fibres has been carried out through the latter half of the twentieth century by focusing on qualities with easy care, lighter weight, increased strength in relation to its weight, to get a natural look, feel and performance. [102]

Polymer yarn and fibre have more options than natural fibres by being able to change chemical composition, morphology and fibre/ filament size and shape. [102,103] The performance of a polymer yarn can be modified after requirements by changing chemical structure and appearance of the filament by altering extrusion process and polymer content. The extruded filament comes from chips or powder, which transform by heat or solvent into a viscous solution, which is pushed through a spinneret. The spinneret contains a number of holes, which can vary in formation and the shape of a hole will reflect on a filament’s properties. The cross sectional design reflects on a filament's properties, surface appearance and morphology of the filament/ staple fibre. The extrusion process can be divided into three main methods: melt, dry and wet spinning, and the method used depends on the polymer type, when melting point will be determining how it transfers into a viscous state. Melt spinning refers to melting a polymer by heat, when dry spinning dissolves a polymer by mixing it into a solvent and after the spinneret drying the filament by heat. Wet process uses a solution to dissolve the polymer and the filament is produced and coagulated in a bath of liquid. After the spinneret the filament is drawn, which can alter the filament properties by influencing

the orientation of the polymer chain and the ratio of crystallinity and amorphous structure. [102]

Mono-filament refers to one single filament making the yarn, when multi-filament refers to several continuous filaments grouped either by being combined together or twisted into a yarn (figure 2.18.). Appearance of the filament can be altered by either texturing or twisting the filament during heat, which gives a permanent texture and a more natural look. [102]

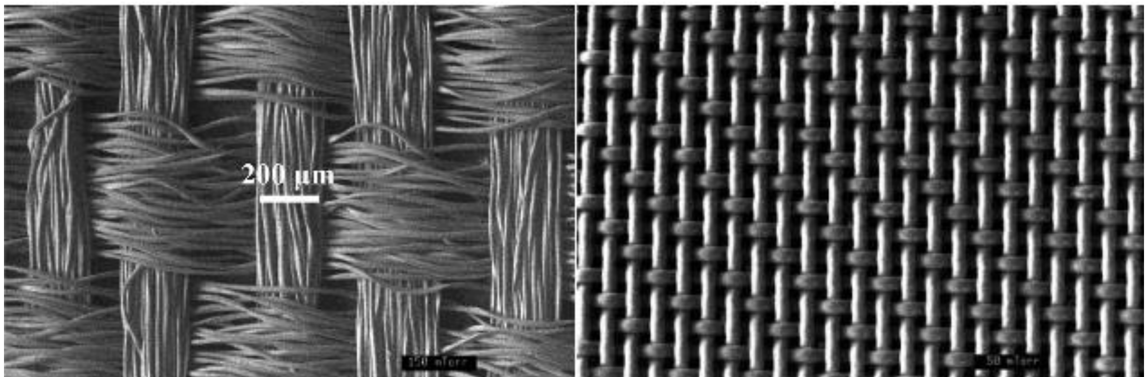

Figure 2.18. differences between a multifilament yarn (left) and a monofilament yarn (right). [104]

Another yarn type is based on cut filament known as “staple fibre” and the length of the filament often matches that of natural fibres. The staple fibres are spun together. The yarn quality of staple fibre gets a higher yarn density and appearance like a natural fibre yarn compared with filament. The polymer filament and fibre content and appearance can be matched to the required performance for a specific end-use. [102,103] Textured material refers to its yarn quality such as a filament's diameter, level of texture and type of weave/ knit structure. Filaments are classified by their dtex (g/ 10km), which is a unit based on a yarn's weight per 10km. [102,105] Thicker yarn diameter and textured yarn results in a higher fabric density and a more textured material. [106] The surface area of a fabric depends on thickness of a fibre/ filament, yarn and the weave/ knit structure. [99] Polymer based filaments provide more options regarding appearance and properties compared with natural fibre and yarn. The polymer based fabric can be manufactured to meet the need of a specific end-use more precisely than a natural fibre. The polymer based fabric can vary by weave/ knit structure, the yarn quality by choosing number of filaments such as mono- and multi-

filament or spun-yarn, and the yarn appearance such as being textured, heat-treated etc. and its polymer content, which all reflects on a material's properties. [101]

Polyester is the most manufactured fibre in the textile industry, which has a great knowledge of how to manufacture this polymer. Polyester has a high resistance to heat, chemicals, UV light and micro-organisms etc., which support a use of polyester in application of solar panels. [102] Polymers can not only vary in chemical content, but also in chain length, orientation and structure content of crystal and amorphous phase. Ratio of amorphous to crystalline regions depends on the extrusion and the drawing processes, although the most common ratio for polyester is 35% crystallinity and 65% amorphous. [102,103] The ratio reflects on a filament, a fibre's physical and chemical properties such as thermal stability, when the glass transition, T_g (~70˚C) and melting temperature, T_m (~260˚C) change depending on polymer content. Glass transition (T_g) is when the polymer becomes soft, which is followed by a rubber-like behaviour before transfer into a viscous phase and later into a liquid form at the melting point (T_m). The change in a polymer from solid to liquid comes with a steady increase in temperature. [103]

Polyester (generic name) belongs to the synthetic group, but can be named after its tradename such as Dacron and Terylene. The different brand names can have a slight change to the basic polyester chain so as to get a more suitable match for the specific end-use. The chemical name for polyester is Polyethylene Terephthalate, PET, whose chain contains carbon bonded to hydrogen and oxygen. Along the chain are different "chemical" groups formed such as ester group RCOOR (double bond to 1st oxygen), methylene CH_2, carbonyl CO and benzene ring C_6H_6, shown in figure 2.19.. [102,103]

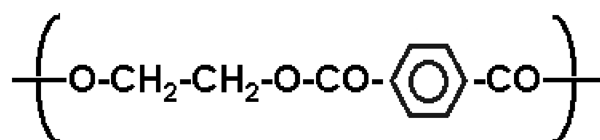

Figure 2.19. chemical structure of Polyethylene Terephthalate, PET known as polyester. [102]

Today, plasma treatment of textile is used to modify a fibre/ yarn's dye properties by becoming more hydrophobic or hydrophilic and having improved adhesion by cleaning a substrate surface. [107,108,109] These treatments were often done by RF-powered

plasma at atmospheric pressure with less reactive gases. Plasma treatment of textile is still limited to technical products, when more knowledge requires fully understanding and controlling the textile behaviour during the plasma process. [52] Plasma process to deposit a coat was not widely used on textile and a careful adjustment of process parameters was required to get a balance between good textile condition and deposition quality and rate. Plasma process in vacuum is generally sensitive to impurities, when this will change the process conditions. Clean vacuum process becomes a challenge for textile substrate, which contains species acting as contamination during the process. Textile is difficult to clean to the level required to avoid change of processing conditions during the plasma process. [108]

Textile substrate influenced the outcome in a process with vacuum and plasma enhanced chemical vapor deposition. This helped to address the importance of using the right textile to get as little influence as possible from the textile substrate. [48,108, 109] Plain weave (figure 2.18.) is the most simple structure with repeated position of the yarn, which is the same from both warp and weft directions. The image below (figure 2.20.) illustrates a woven substrate of a plain weave with the warp yarn cut in cross section and the weft yarn floating across the warp. The warp yarn comes along the machine (loom), when the weft crosses the warp yarn by travelling in the machine width (from side to side). Weft yarn crosses the warp in a repeated pattern known as a weave structure and the easiest structure is plain weave 1 x 1, which means every second weft yarn goes above and below the warp yarn. On the return of the weft yarn, the warp changes position to the opposite and the ones that have the weft above get it crossing below and vice versa. After each weft insert, the yarn gets packed close to the previous weft insert.

A structure of plain weave is shown below (figure 2.20) to help understand how the weft and warp threads cross. The space (figure 2.20.) in a woven structure and between the filament yarn can allow the plasma to travel through. [101,105]

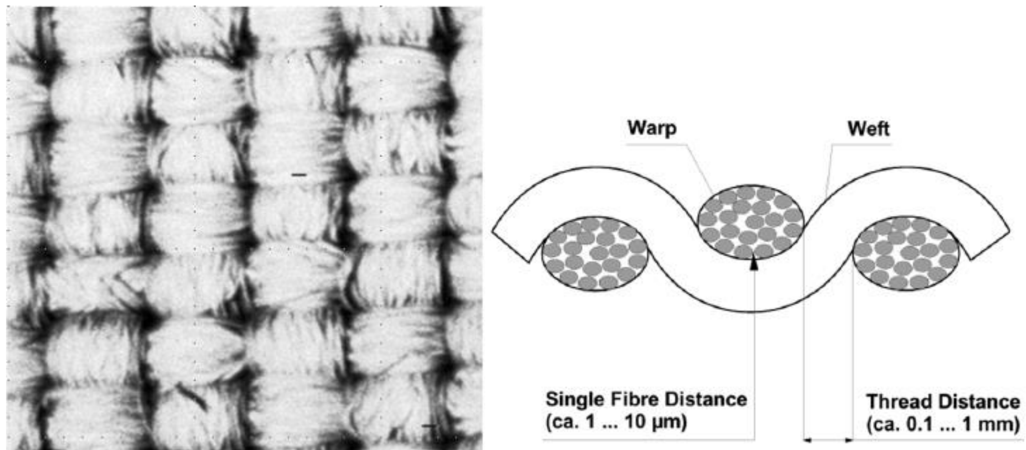

Figure 2.20. is a weave structure with continuous filaments in the yarn. Image to right [108] shows a plain weave 1x1, when left [109] gives more detailed picture of the space within the yarn and the bundle of filament.

Plasma distribution through the textile depended on the textile structure and its open space (distance) between fibre/ filament, yarn together with process parameters. Increased substrate density, textured surface and yarn could influence the plasma reaction and deposition quality. [21,48,109] A textile weave of 2D structure needs to be considered [108] as a 3D structure in a plasma process. This is due to the high density and large surface area the textile substrate has compared with conventional flat substrates of solar cells such as glass, silicon wafer etc. [101]

Density and surface area of a textile depends much on the type of structure, number of yarn and filaments/ fibres in each yarn (figure 2.21.). The total surface area of a woven material is given by number of yarns/ cm in both warp and weft and the diameter (μm) of the yarn (d_y) and the number of fibre/ filament (d_f) in the yarn. (figure 2.21.). [101]

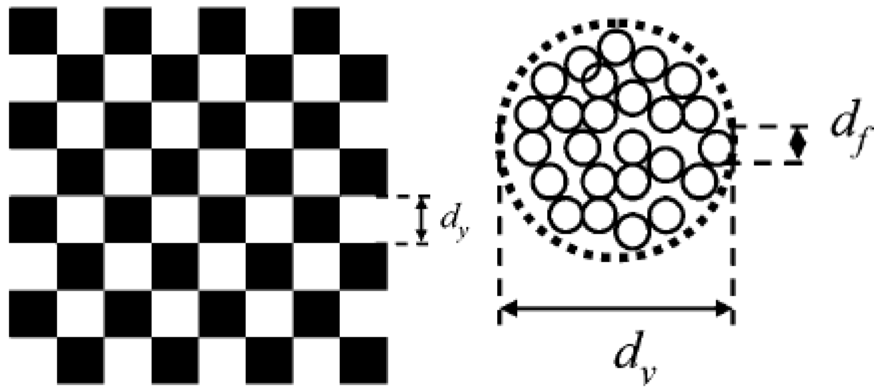

Figure 2.21. woven fabric contains a higher surface area than conventional solar cell substrates; considering the area of a filament, yarn within a specific square area helps to estimate the total area being exposed to a plasma. [101]

Plasma can theoretically deposit and etch a yarn, fibre, filaments in and around depending on process parameters. The area of a textile exposed to plasma can be calculated (figure 2.22.) by number of filaments (n) parallel along the width (W_P) of a surface exposed to plasma. The filament has a half-circumference of π d_f/ 2 or 1.57 d_f, which means the treated surface area is at least 1.57 times larger than area exposed to a plasma. [108]

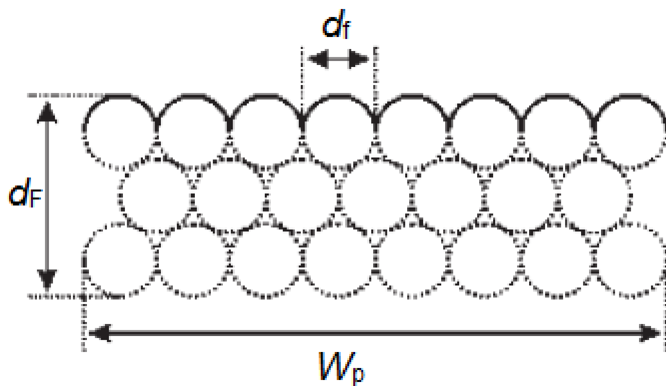

Figure 2.22. possible plasma penetration in a tight weave can be calculated by considering thickness, d_F and width W_p of filaments packed together and the diameter of a filament, d_f. [108]

Plasma distribution depended on the mean-free path of the gas species (radicals, electrons), which depended on settings of process parameters such as gas type, power and pressure. Consider a textile structure containing pores: the value of mean-free path exceeding the pore size helps to avoid plasma penetration and instead give a more uniform surface activation. A mean-free path below pore size will allow plasma to travel into a depth of the textile structure and filament, therefore a balance between mean-free path and open space in the structure is necessary to restrict the travel of gas species. [108] The plasma would unlikely penetrate through a space less than 10nm. [107] Another important factor regarding plasma penetration is molecular size of the gas species, when this affects the travel speed and distance too. [47]

Plasma penetration and mean-free path was considered by placing several layers of textile in a pile and thereafter determining the depth of plasma treatment on the textile. [48,101,107,108,109] Some of the aspects considered in these studies were process pressure [109], weight loss and fibre orientation [48] and sample size. [109,110] Depth of a plasma penetration depends on mean-free path (figure 2.23.), which relates to the uninterrupted distance gas species travel through the plasma. The mean-free path (λ) in a textile substrate with yarn, filament/ fibre can be calculated by assuming plasma penetration is equal to the mean-free path, (λ, μm) for radicals at a certain pressure (P, Pa). [107,109]

λ= gas data/ P (3) [109]

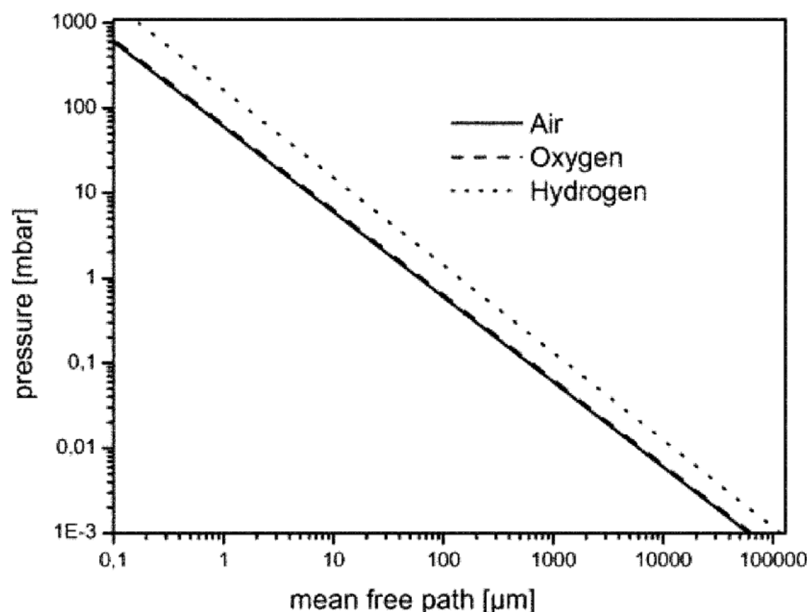

Figure 2.23. how a mean-free path changes by pressure. [107]

The process parameters and their settings and combination would determine plasma condition, number of active species (ions, electrons and radicals), deposition and etch rate. [48,107,108] Process pressure proved to be a key parameter to determine plasma treatment, when low pressure gave higher velocity and longer travel distance for radicals and electrons in textile material. [108] A certain pressure range supported a more homogenous plasma treatment than others. [109] Pressure less than ~1mbar has a mean-free path greater than a textile structure, which resulted in a low number of radicals and a very sufficient modification. Higher pressure than 1mbar gave less surface treatment. [108] Another source [107] suggested that at a pressure of ~0.1mbar, the deposit became uniform and flexible.

Textile with larger surface area showed higher weight loss, which was explained by the larger surface being more exposed to plasma with higher etch effect. [48] Structure of a material played a part too, when a tighter weave or smooth surface experienced less weight loss compared to a denser and more textured surface with more etch effect. Yarn direction proved important, when parallel yarn got more etched due to the plasma having an easier access to travel between yarn, filament, fibre and therewith the plasma density increased with a higher etch effect. The high etch effect was explained by gas being trapped in limited space, which resulted in the velocity of electron and radicals and the number of collisions being increased. [48,107] Even if the plasma penetration and etch effect was increased, the bulk properties of a fibre/ filament were not affected, due to plasma not travelling into spaces less than 10nm. [107] With increased plasma penetration, the plasma activation and energy becomes reduced, which gave an uneven plasma activation in both depth and location on the textured textile. Therefore depth of plasma penetration is very important to understand and how it will affect and react with the textile substrate. [107,108]

The drawback of using a textured and dense material is trapped moisture and air, which can increase actual substrate temperature during a plasma reaction. [101,110] All fibre contains some water even though synthetic has much less than natural fibre. The water content is given in percentage in relation to weight of dry fibre and typical values for natural fibres are between 7 and 17%, when synthetic fibres are from 0 to 5.5%. Polyester has 0.3%, but this figure can vary depending on the surface and the cross shape of the filament. The water content in a fibre will depend on the environment, when increased Relative Humidity, RH% gives a higher percentage due to the fibre absorption and swell. [105,108]

Textile substrate exposure in low process pressure proved difficult due to the water content, when some of it became trapped in the textile, which faced the substrate plate, when the rest was pumped out. Later, the remaining moisture during the process increased the substrate temperature, which led to damaged textile substrate. [108,110] The moisture in a plasma process will act as an impurity in a plasma process and extend the pumping down of a vacuum process and cause a weight loss to the fibre. Therefore, it was important to control and avoid unnecessary water/ moisture in the fibre and the textile substrate (figure 2.24.). The moisture/ water content in a fibre will reflect on time to pump down and release moisture from chamber and substrate (figure 2.24.). [108] Surface contamination in a textile is another problem, when the textile is difficult to clean to the level required to avoid change of process condition during the plasma process. [101]

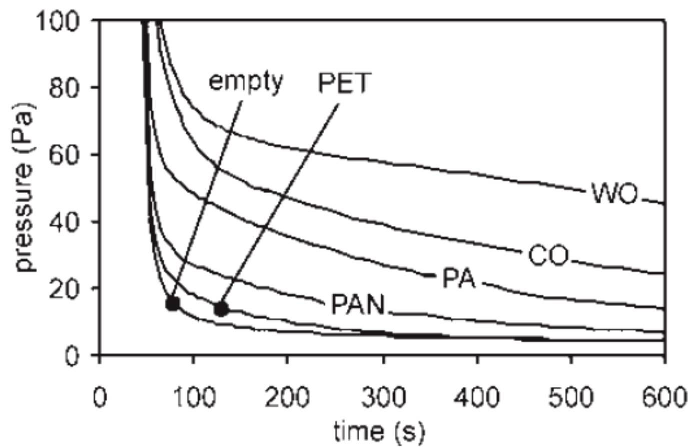

Figure 2.24. fibres with different water content will affect the time to pump down to process vacum required. [108]

2.7. References

1 M.A. Green, *Recent development in photovoltaics*, Sol. Energ. **76**, p.3-8 (2004)

2 J. Stierstorfer, K. McDonald, S. Teske and M. Cameron, *Solar Generation, Solar electricity for over one billion people and two million jobs by 2020*, EPIA- European Photovoltaic Industry Association and Greenpeace International, (pp.52) (2006)

3 A. Jager-Waldau, *PV Status, Research, Solar cell Production and market Implementation of Photovoltaics*, European Commission, DG JRC, Institute for Environment and Sustainable, Refocus **September** (2007) www.re-focus.net

4 K. Derbyshire, *The future of photovoltaics to 2015*, Pira international Ltd., Surrey, UK, (pp.15) (2006)

5 *Thin film technologies go mainstream*, European photovoltaic Industry association (November) (2010) www.epia.org

6 C. Wolfsegger, M. Latour, M. Annett and S. Sveninge, *Global Market outlook for Photovoltaic until 2012, Facing a sunny future,* European Photovoltaic Industry Association, EPIA. www.epia.org

7 A. Jager-Waldau, *PV Status*, Refocus **May**, p.20-3 (2005) www.re-focus.net

8 An Angle Business Communications Publication, *How long will Germany stay number one?*, Solar international A PV Management Magazine **VIII**, p.10-1 (2011)

9 J. Cielska et al., *Global Market Outlook for Photovoltaics until 2015*, EPIA- European Photovoltaic Industry Association **04/11**, (pp.44) (2011) www.epia.org

10 G. Masson, M. Latour and D. Biancardi, *Global market outlook for photovoltaics Until 2016*, editor C. Winnike EPIA, European Photovoltaic Industry Association, **May 2012**, (pp.76) (2012)

11 An Angle Business Communications Publication *Concentrated Growth*, Solar International A PV Management Magazine **IV**, p.22-3 (2011)

12 *The European solar photovoltaic industry is ready to co-finance 1,235 million euro in R&D in order to achieve competitiveness in all its market segments*, European photovoltaic industry association, (2010) www.epia.org

13 *Photovoltaic power poised to become mainstream source of energy in all sunbelt countries by 2030*, EPIA- European photovoltaic industry association **October (**2010) www.epia.org

14 Nano Markets reports, *Positioning thin film photovoltaics for success*, Photovoltaics **April**, p.36-8 (2008) www.euroasiasconductor.com

15 H. Wicht, *The highest hand wins*, Photovoltaics **April**, p.31 (2008) www.euroasiasconductor.com

16 M. Boreland and D. Bagnall, *Photovoltaics Technologies*, Energ. Policy **36**, p.4390-6 (2008)

17 Z. Barber, *Optimism reigns in solar circle*, Solar international a PV Management Magazine **X**, p.16-20 (2011)

18 X. Deng and E.A. Schiff, *Amorphous Silicon Based Solar Cells*, p.1-62 (2002)

19 C. Wolfsegger, J. Stierstorfer, S. Teske and M. Bitter, *Solar Generation IV- 2007,Solar electricity for over one billion people and two million jobs by 2020*, EPIA- European Photovoltaic Industry Association/ EPIA and Greenpeace*,* www.epia.org, www.greenpeace.org

20 R. Brendel, *Thin-Film Crystalline. Silicon Solar Cells*, Physics and Technology, Wiley-VCH Verlag GmbH & Co., ISBN: 3-527-40376-0, (pp.285) (2003)

21 Y. Zhao, X. Geng, W. Wang, X. Li and Y. Xu, *R&D activities of silicon- based thin film solar cells in china*, Phys. Status Solidi (a) **203** (4), p.714-20 (2006)

22 T. Surek, *Crystal Growth and Materials research in photovoltaics: progress and challenges,* J. Cryst. Growth **275**, p.292-04 (2005)

23 R.M. Swanson, *A vision for crystalline silicon photovoltaics*, Prog. Photovolt: Res. Appl. **14**, p.443-53 (2006)

24 H.C. Kim and V.M. Fthenakis, *Comparative life-cycle energy payback analysis of multi-junction a-SiGe and nanocrystalline/ a-Si modules*, Prog. Photovoltaics: Research and applications **19**, p.228-39 (2011)

25 M.B. Schubert and J.H. Werner, *Flexible solar cells on clothing*, Materials Today **9** (6), p.42-50 (2006)

26 F.C. Krebs, M. Biancardo, B. Winther-Jensen, H. Spanggard and J. Alstrup, *Strategies for incorporation of polymer photovoltaics into garments and textiles*, Sol. Energ. Mat. Sol. C. **90**, p.1058-67 (2006)

27 C. Borciani, *Underground hit, Christian Roos- The man behind O'neill's smartclothing for the IPod generation, is about to launch his biggest line yet*, Plastic Electronics **November& December**, p.20-8 (2007)

28 A. Wilson, *Imperfect partners, the gulf between electronics and textiles Appears even wider following the release of Apple's iPhone*, Smartech- Future Material **January& February**, p.7-8 (2008)

29 M. Schubert and M. Rainer, *Flexible solar cells and module*, Philos. Mag. & Phil. Mag. Lett. **89** (28-30), p.2623-44 (2009)

30 http://inhabitat.com/solar-harvesting-textiles-energize-soft-house/solar-textiles-kva-matx-soft-house-by-kva-matx-soft-house-soft-house-by-sheila-kennedy-sheila-kennedy-kva-matx-solar-textile-house-electricity-generating-textiles-solar-powered-house-4/ (04/11/12)

31 J. Portman and V. Arkhipov, *Thin Film Solar Cells, Fabrication, Characterization and Applications*, John Wiley& Sons Ltd, UK, ISBN-13:978-0-470-09126-5, (pp.463) (2006)

32 M. Pagliaro, G. Palmisano and R. Ciriminna, *Photovoltaics,* chapter 2, *Flexible Solar cells*, Wiley-VCH Verlag GmbH&CO KGaA, ISBN:978-3-527-32375-3, (p.31-54) (2008)

33 X. Deng and E.A. Schiff, *Amorphous Silicon Based Solar Cells*, edited by Antonio Luque and Steven Hegedus, Handbook of Photovoltaic Science and Engineering, John Wiley & Sons, UK, ISBN: 9780471491965, p.505–65 (2003)

34 A. Goetzberger, C. Hebling and H-W. Schock, *Photovoltaic materials, history, Status and outlook*, Mat. Sci.Eng. **R40**, p.1-42 (2003)

35 J. Singh, *Semiconductor bandstructure (chapter 3), Semiconductor devices basic principles*, John Wiley & Sons Inc., ISBN:978-0471362456, (pp.540) (2000)

36 A.V. Shah et al., *Material and solar cell research in microcrystalline silicon*, Sol. Energ. Mat.Sol. C. **78**, p.469-91 (2003)

37 S. Jardine, *Thin Film Silicon on Textiles by Microwave Plasma Chemical Vapour Deposition*, PhD Thesis, Heriot-Watt University, UK (2006)

38 B. Yan, G. Yue, X. Xu, J. Yang and S. Guha, *High efficiency amorphous and nanocrystalline silicon solar cells*, Phys. Status Solidi A **207** (3), p.671-7 (2010)

39 M. Kroll et al. *Employing dielectric diffractive structures in solar cells- numerical study*, Phys. Status Solidi. (a) **205** (12), p.2777-95 (2008)

40 B. Yan, G. Yue, J. Yang and S. Guha, *Hydrogen dilution profiling for hydrogenated microcrystalline silicon solar cells,* Appl. Phys. Lett. **85** (11), p.1995-7 (2004)

41 B. Yan et al., *On the bandgap of hydrogenated nanocrystalline silicon thin films*, photovoltaic specialists conference (PVSC) **2010 35th** IEEE, p.003755-60 (2010)

42 G. Yue, B. Yan, C. Teplin, J. Yang and S. Guha, *Optimization and characterisation of 1/p buffer layer in hydrogenated nanocrystalline silicon solar cells*, J. Non-Cryst. Solids **354**, p.2440-4 (2008)

43 G. Yue et al., *Material structure and metastability of hydrogenated nanocrystalline silicon solar cells,* Appl. Phys. Lett. **88**, (pp.3) (2006)

44 W.G.J.H.M. van Sark, A. Meijerink, R.E.I. Schropp, J.A.M. van Roosmalen and E.H. Lysen, *Enhancing solar cell efficiency by using spectral converters*, Sol. Energ. Mat.Sol. C. **87**, p.395-409 (2005)

45 S. Klein, F. Finger, R. Carius, T. Dylla and J. Klomfass, *Relationship between the optical absorption and the density of deep gap states in microcrystalline silicon*, J. Appl. Phys. **102**, 103501 (2007)

46 K. Ostrikov, *Colloquium: reactive plasmas as a versatile nanofabrication tool*, Rev. Mod. Phys. **77**, p.489-511 (2005)

47 D. Hegemann, M.M. Hossain, E. Körner and D.J. Balazs, *Macroscopic description of plasma polymerization*, Plasma Proc. Polym. **4**, p.229-38 (2007)

48 J. Verschuren and P. Kiekens, *Gas flow around and through textile Structures during plasma treatment*, AUTEX Research journal **5** (3), p.154-61 (2005)

49 C. Oehr, *Glow discharge treatments for Modification of Technical textile,* Fraunhofer IGB (2001) www.igb.fraunhofer.de/en/competences/interfacial-materials/plasma-processes/glow-discharge-treatments-textiles.html (06/11/12)

50 P.R. i Cabarrocas, A. F. i Morral, S. Lebib and Y. Poissant, *Plasma production of nanocrystalline silicon particles and polymorphous silicon thin films for large-area electronic devices*, Pure Appl. Chem. **74** (3), p.359–67 (2002)

51 W.G.J.H.M. van Sark, G.W. Brandsen, M. Fleuster and M.P. Hekkert*, Analysis of the Silicon Market: Will thin films profit?*, Energ. Policy **35**, p.3121-5 (2007)

52 B. Marcandalli and C. Riccardi, *Plasma treatments of fibres and textiles*, Chapter 11 Plasma technologies for textiles, edited R. Shishoo, ISBN: 978-1-4200-4450-8, p.282-98 (2007)

53 W.J. Soppe, C. Devilee, M. Geusebroek, J. Löffler, H.-J. Muffler, *The effect of argon dilution on deposition of microcrystalline silicon by microwave plasma enhanced chemical vapor deposition*, Thin Solid Films **515**, p7490–4 (2007)

54 S. Guha and J. Yang, *Progress in amorphous and nanocrystalline silicon solar cells*, J. Non-Cryst. Solids **352**, p.1917-21 (2006)

55 B.B. van Aken et al., *MW plasma enhanced CVD of intrinsic Si for thin film solar cells*, MRS Spring meetings, San Francisco, (pp.7) (2008)

56 N. Martins et al., *Performances of an inline PECVD system used to produced amorphous and nanocrystalline silicon solar cell*, Thin Solid Film **511-12**, p.238-42 (2006)

57 H. Schlemm et al., *Industrial large scale silicon nitride deposition on photovoltaic cells with linear microwave plasma sources*, Surf. Coat. Tech. **174-5**, p.208-11 (2003)

58 B.B. Van Aken et al., *Fabrication of a-Si solar cells with RF- and MW- PECVD*, Presented at the 23rd European Photovoltaic Sol. Energ. Conf., Valencia, Spain, 1-5 September, (pp.4) (2008)

59 W.J. Soppe et al., *High rate growth of micro-crystalline silicon by microwave- PECVD*, 3rd World Conference on Photovoltaic Energy Conversion, p.1655-8 (2003)

60 W.J. Soppe, B.B. Van Aken, C. Devilee and H. Schlemm, *A Novel Linear RF Source for PECVD of thin- film Silicon*, Proceedings of the 22nd European Photovoltaic Solar Energy Conference, Italy, p.1847-51 (2007)

61 B.B. Van Aken et al., *Pilot roll-to-roll PECVD system for fabrication of thin film Si solar cells*, The international conference on coating on glass and plastics, Netherland, (pp.4) (2008)

62 W.J. Soppe, C. Devilee, M. Geusebroek, J. Löffler and H-J. Muffler, *The effect of Argon dilution on deposition of microcrystalline silicon by microwave plasma enhanced chemical vapor deposition*, Thin solid films **515**, p.7490-4 (2007)

63 P. Chaudhuri, R. Meaudre and C. Longeaud, *Argon dilution of silane as an alternative to hydrogen dilution for stable and high efficiency silicon thin films solar cells*, J. Non-Cryst. Solids **338-40**, p.690-3 (2004)

64 H. Schlemm, M. Frizsche and D. Roth, *Linear radio frequency plasma sources for large scale industrial applications in photovoltaics*, Surf. Coat. Tech. **200**, p.958-61 (2005)

65 Z. Iqbal and S. Veprek, *Raman scattering from hydrogenated microcrystalline and amorphous silicon*, J. Phys. C: Solid State Phys. **15**, p.377-92. (1982)

66 S. Reynolds, *Carrier mobility, band tails and defects in microcrystalline silicon*, *16 ISCMP: Progress in solid state and molecular electronics, ionics and photonics*, J. of Phys.: Conf. Series **255**, (pp.12) (2010)

67 C.R. Wronski, J.M. Pearce, J. Deng, V. Vlahos and R.W. Collins, *Intrinsic and light Induced gap states in a-Si:H materials and solar cells effects of Microstructure*, Thin Solid Films **451–452**, p.470–5 (2004)

68 D.L. Staebler and C.R. Wronski, *Reversible conductivity changes in discharge-produced amorphous Si*, Appl. Phys. Lett. **31** (4), p.292-4 (1977)

69 C.R. Wronski, *Amorphous silicon Photovoltaics: Order From Disorder*, *Centre for*

Thin film Devices, The Pennsylvania State University, (pp.6) (2000)

70 A. Matsuda, *Microcrystalline silicon. Growth and device application*, J. Non-Cryst. Solids **338-40**. p.1-12 (2004)

71 W.B. Jackson and C.C. Tsai, *Hydrogen transport in amorphous silicon*, Phys. Rev. B **45** (12), p.6564-80 (1992)

72 P. Gogoi, P.N. Dixit and P. Agarwal, *Amorphous silicon films with high deposition rate prepared using argon and hydrogen diluted silane for stable solar cells*, Sol. Energ. Mat. Sol. C. **91**, p.1253–7 (2007)

73 M. Kondo and A. Matsuda, *Novel aspects in thin film silicon solar cells- amorphous, microcrystalline and nanocrystalline silicon*, Thin Solid Films **457,** p.97-102 (2004)

74 S. Mukhopadhyay, A. Chowdehury and S. Ray, *Nanocrystalline silicon: A material for thin film solar cells with better stability*, Thin Solid Films **516** (20), p.6824-8

75 H. Hao et al., *Light- induced changes in diphasic nanocrystalline silicon films and solar cells*, J. Non-Cryst. Solids **352,** p.1904-08 (2006)

76 S. Shimizu, M. Kondo and A. Matsuda, *A highly stabilized hydrogenated amorphous silicon film having very low hydrogen concentration and improved Si bond network*, J. Appl. Phys. **97**, 033522, (pp.4) (2005)

77 A. Chowdhury, S. Mukhopadhyay and S. Ray, *Fabrication of thin film nanocrystalline silicon solar cell with low light-induced degradation*, Sol. Energ. Mat. Sol. C. **93** (5), p.597-603 (2009)

78 M. Takai, T. Nishimoto, M. Kondo and A. Matsuda, *Chemical-reaction dependence of plasma parameter in reactive silane plasma*, Sci. Tech. Adv. Mat. **2**, p.495-503 (2001)

79 D. Das, *Structural studies in Si:H network by micro- Raman, micro-photoluminescence, electron microscopy and ultraviolet ellipsometry: effect of Ar dilution to the SiH4-plasma*, Thin Solid Films **476**, p.237-45 (2005)

80 G. Viera et al., *Atomic structure of the nanocrystalline Si particles appearing in nanostructure Si thin films produced in low-temperature radiofrequency plasmas*, J. Appl. Phys. **92** (8), p.4684-94 (2002)

81 G. Viera, S. Huet, M. Mikikian and L. Boufendi, *Electron diffraction and high- resolution transmission microscopy studies of nanostructured Si thin films deposited by radiofrequency dusty plasmas*, Thin solid films **403-4**, p.467-70 (2002)

82 K. Wu, X.Q. Yan and M.W. Chen, *In situ Raman characterisation of reversible phase transition in stress-induced amorphous silicon*, Appl. Phys. Lett. **91** (10) (pp.3) (2007)

83 G. Viera, S. Huet and L. Boufendi, *Crystal size and temperature measurements in nanostructured silicon using Raman spectroscopy*, J. Appl. Phys. **90** (8), p.4175-84 (2001)

84 I. Zardo, G. Abstreiter and A. Fontcuberta I Morral, *Raman spectroscopy on semiconductor nanowires*, chapter 12 Nanowires, edited by Paola Prete, ISBN 978-953-7619-79-4, p.227-54 (2010)

85 D.V. Tsu et al, *Effect of hydrogen dilution on the structure of amorphous silicon alloys*, J. Appl. Phys. Lett. **71**, p.1317-9 (1997)

86 J. Kocka, T. Mates, H. Stuchlikova, J. Stuchlik and A. Fejfar, *Characterization of grain*

growth, nature and role of grain boundaries in microcrystalline silicon- review of typical features, Thin Solid Films **501** (1-2), p.107-12 (2006)

87 H.B.T. Li, R.H. Franken, J.K. Rath and R.E.I. Schropp, *Structural defects caused by a rough substrate and their influence on the performance of hydrogenated nano-crystalline silicon n-i-p solar cells*, Sol. Energ. Mat. Sol. C. **93**, p. 338-49 (2009)

88 B. Yan, G. Yue, J.M. Owens, J. Yang and S. Guha, *Light induced metastability in hydrogenated nanocrystalline silicon solar cells*, Appl. Phys. Lett. **85** (11), 1925 (pp.3) (2004)

89 D. Gracin et al., *The structural ordering of thin silicon films at the amorphous to nano-crystalline phase transition by GISAXS and Raman spectroscopy*, Renew. Energ. **33**, p.326-30 (2008)

90 H. Aguas et al., *Large area deposition of polymorphous silicon by plasma enhanced chemical vapor deposition at 27.12MHz and 13.56MHz*, Jpn. J. Appl. Phys. **42**, p.4935-42 (2003)

91 L.H. Teng and W.A. Anderson, *Thin film transistors on nanocrystalline silicon directly deposited by a microwave plasma CVD*, Solid State Electron. **48**, p.309-14 (2004)

92 L. Cau, P. Fan, E.S. Barnard, A.M. Brown and M.L. Brongersma, *Tuning the colour of silicon nanostructures*, Nano Lett. **10**, p.2649-54 (2010)

93 C.C. Tsai, G.B. Anderson, R. Thompson and B. Wacker, *Control of silicon network structure in plasma deposition*, J. Non-Cryst. Solids **114**, p.151-3 (1989)

94 J. Löffler, C. Devilee, M. Geusebroek, W.J. Soppe and H-J Muffler, *Deposition of µc-Si:H by Microwave PECVD- influence of process conditions on layer properties*, The 21st European photovoltaic solar energy conferences and exhibition, Germany, (pp.4) (2006)

95 Y. Gogotsi, C. Baek and F. Kirscht, *Raman microscopy study of processing-induced phase transformations and residual stress in silicon*, Semicond. Sci. Technol. **14**, p.936-44 (1999)

96 D. Gracin, S. Bernstorff, P. Dubcek, A. Gajovic and K. Juraic, *Study of amorphous nanocrystalline thin silicon films by grazing- incidence small- angle X-Ray scattering*, J. Appl. Cryst. **40**, p.373-6 (2007)

97 M. Kondo, Y. Nasuno, H. Mase, T. Wada and A. Matsuda, *Low- temperature fabrication of microcrystalline silicon and its application to solar cells*, J. Non- Cryst. Solids **299- 302**, p.108-12 (2002)

98 A.T. Voutsas, M.K. Hatalis, J. Boyce and A. Chiang, *Raman spectroscopy of amorphous and microcrystalline silicon films deposited by low- pressure chemical vapor deposition*, J. Appl. Phys. **78** (12), p. 6999-06 (1995)

99 Q. Cheng, S. Xu K. Ostrikov, *Structural evolution of nanocrystalline silicon thin films synthesized in high-density, low-temperature reactive plasmas*, Nanotechnology **20**, 215606, (pp.8) (2009)

100 J.K. Rath, M. Brianza, Y. Liu, A. Borreman and R.E.I. Schropp, *Fabrication of thin Film silicon solar cells on plastic substrate by very high frequency PECVD*, Sol. Energ. Mat. Sol. C. **94**, p.1534-41 (2010)

101 G. Buyle, *Nanoscale finishing of textiles via plasma treatment*, Mater. Technol. **24** (1), p.46-51 (2009)

102 K.L. Hatch, *Textile science*, *West Publishing Company*, ISBN: 0-314-90471-9, (pp.472) (1993)

103 J.M.G. Cowie, *Polymers Chemistry & Physics of Modern materials 2nd Edition*, Black Academic & professional, UK, ISBN 075140134 (pp.436) (1991)

104 S. Guimond, B. Hanselmann, M. Amberg and D. Hegemann, *Plasma functionalization of textiles: Specifics and possibilities*, Pure Appl. Chem., **82** (6), p.1239–45 (2010)

105 J.E. McIntyre and P.N. Daniels, *Textile Terms and Definitions Tenth Edition*, The Textile Institute, UK, (pp.401) (1995)

106 A Pourmohammadi, *Thermal Bonding*, Chapter 6 Handbook of Nonwovens by S.J. Russell, Textile institute, UK, ISBN: 978-0-8493-2596-0, p.298-329 (2006)

107 H.U. Poll, U. Schladitz and S.Schreiter, *Penetration of plasma effects into textile structures*, Surf. Coat. Tech. **142-144**, p.489-93 (2001)

108 J. Verschuren, P. Kiekens and C. Leys, *Textile-specific Properties that Influence Plasma Treatment, Effect Creation and Effect Characterization*, Tex. Res. J. **77** (10): p.727–33 (2007)

109 N. De Geyter, R. Morent and C Leys, *Penetration of a dielectric barrier discharge plasma into a textile structures at medium pressure*, Plasma sources Sci. T. **15**, p.78-84 (2006)

110 C. A. Bishop, *Vacuum Deposition onto Webs, Films and Foils*, Material Science and Process Technology Series, ISBN: 978-08155-1536-4, (pp.650) (2006)

3. Nanocrystal structure and properties

3.1. Introduction

Initially, amorphous silicon thin film was produced as a replacement to the conventional solar cells of silicon crystal as an option to reduce the large quantity of silicon used per cell. The drawback with amorphous silicon was the high light-degradation known as Staebler-Wronski effect (*chapter 2 section 2.5*), which led to a permanent degradation of the cell performance. [1] Integration of crystal growth into the amorphous matrix was understood to stop this light-degradation. A mixed structure of crystal growth in an amorphous matrix gave a more stable cell structure in respect to light-degradation by reducing the hydrogen content and the number of dangling bonds. [1,2] Hydrogen bonds easily break by energetic photons, resulting in trapped charge carriers and reduced cell performance. [3]

Even though a mixed structure mainly contains amorphous material, the small crystals support a stable structure and a good boundary between the phases, which improve electrical and optical properties. [4,5,6,7,8,9] However, a careful balance of film thickness, ratio between crystal and amorphous phase and crystal size was required to gain enhanced electrical and optical properties. [5,10] Textured material encourages nanocrystal growth due to its unevenness, when local energy fields with higher energy were formed in the pits. [11,12] The local energy fields with higher energy favoured crystal growth of Wurtzite structure. [13]

The most known method to decide crystal growth in an amorphous structure is by Raman spectroscopy, even though the result is based on an average crystal size. [14] The crystal size will reflect on the peak location, width and shape, when increased crystal size produced a more narrow and sharp peak compared to smaller crystals. [15] The numbers of peaks and location required to fit a Raman spectra are known regarding conventional amorphous, crystal and pure microcrystal silicon, while nanocrystals are less understood. The ratio of amorphous and crystal structures and crystal size reflected on peak location and peak shape. Crystal growth could either contain one kind of crystal size or a mixture of small and large crystals. Raman spectrum made it possible to distinguish between nano- or micro-crystal growths in the amorphous structure. [12,16,17,18] Raman spectroscopy has the advantage of no

sample preparation or change to sample properties during measurement. Using Raman spectroscopy to analyse fabric or fibre surface is less common, when most published material regarding textile and Raman spectroscopy discusses analysis of bulk properties of a fibre/ filament.

3.2. Silicon crystal (crystal growth)

There are twelve silicon phases [19,20,21], although an additional phase, Si-XIII was recently reported. [22] All silicon phases originate from silicon Si-I which is of a cubic structure. Some of the silicon phases only transform by pressure, when others need a combination of pressure and temperature. A number of phases are metastable, which means they can easily reverse their phase transformation. [17] Each phase is unique with its specific structure and mass, which reflect on optical and electrical properties. [23]

Indentation (nano-) [22,24,25] and laser annealing [7,26,27,28] has helped to understand the possible transformation of silicon from the familiar cubic silicon crystal, Si-I by pressure and heat into different phases. Indentation experiments [22,24,25] started often with silicon crystal, Si-I and by applied pressure changed this to Si-II and Si-III etc. A quick pressure release gave increased amorphous content. [29] Laser annealing experiments [28,29] started either from Si-I or from amorphous silicon with phase transformation produced by heat. The annealing studies [7,26] with amorphous material on a silicon wafer reported how crystal growth was identified as a linear effect in the random network of amorphous silicon after heat had been applied.

Silicon phases such as Si-I, Si-III, Si-IV and Si-XII were of interest in relation to silicon thin film on woven textile [30] due to requiring less pressure for transformation. Si-IV phase could transform directly from Si-I without passing through other phases, [25,31] and the low pressure and peak locations/ wavenumber given [17] were applicable to the plasma process for silicon thin film. [22,32]

Si-IV was known as a nanocrystal structure of small crystallites, although development of larger crystals such as microcrystals had been experienced too. [33] The Si-IV phase was of a hexagonal structure known as wurtzite (WZ) structure and first addressed by Kobiliska. [34] Wurtzite structure was known for its typical vibrational

modes in three crystal directions, two in the hexagonal plane and one perpendicular to the plane. [18,34] It was discussed how the wurtzite structure in silicon, Si(2H-4) related to the more common cubic structure, (FC-2). [34] Wurtzite contains of 4 atoms/ unit cell and two types of monolayer, ABAB…., stacked in the direction of the c-axis [0001]. Wurtzite silicon, Si-IV can appear in two types of structure, A and B. [35] The slight difference between the options is that B had longer lattice distance (a=4.04, b=4.04 and c=6.60) than A (a=3.80, b=3.80 and c=6.60). Type of structure Si-IV_A or Si-IV_B, depended on crystal size. Larger crystals (above 10nm) contained a mixture of the two (Si-IV_A and Si-IV_B), although Si-IV_B dominated. This kind of mixture of A and B was typical for nanowire growth and wires of smaller radii showed a more frequent change, when the surface energy was very low. [35] Crystal growth was a mixture of cubic and wurtzite structures (Si-IV_A) and with increased size, the cubic phase increased. [35]

Wurtzite is similar to the zinc blende cubic structure, as both have the same atomic number per unit cell. [22,36,37,38] However, the cubic structure requires three mono-layers per unit cell, while wurtzite contains two (figure 3.1.). The two structures were found to have similar lattice distances and angles (figure 3.1.). [39] A mixture of the two phases was explained to be due to change in surface-energy, crystal size and unstable process conditions. [39]

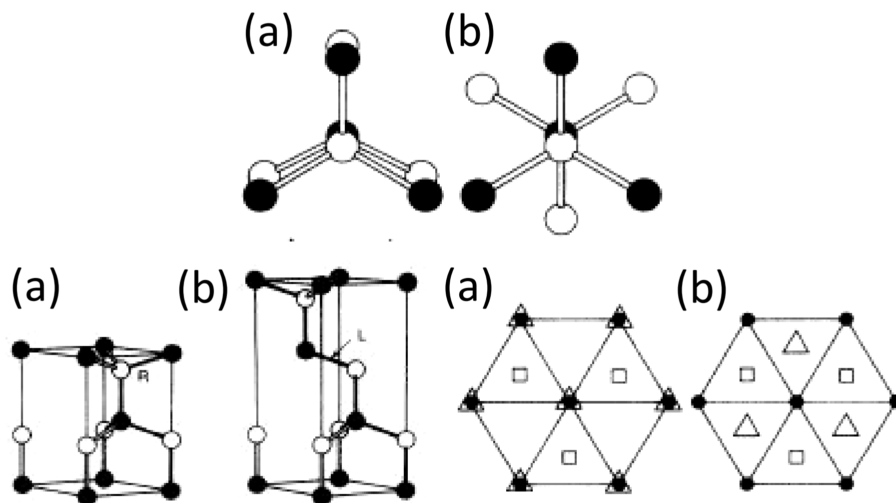

Figure 3.1. shows the difference between (a) the wurtzite hexagonal structure and (b) the zinc blende cubic structure. [40]

With the cubic zinc blende (ZB) and hexagonal wurtzite (WZ) structures have very similar stacking orders of AB,AB….for WZ and ABC,ABC… for ZB and with the two structures having similar cohesive energies they are easily mixed during growth. [36,38,41] Stacking faults can either occur as single or repeated entities and it may be common for wurtzite to interrupt the growth of zinc blende in this manner. The defect often occurs at edges, borders or in much textured areas (figure 3.2.). [38,41,42,43] Stacking disorder will reflect on phonon vibrations and a material's optical, electrical and thermal properties. [7,44] During nanocrystal growth twin formation AaBb is the most common defect due to a mixture of zinc blende and wurtzite phases, see figure 3.2. and figure 3.3.. [36,41,45] Transformation between WZ and ZB has two options named as Type I (BCBC) and Type II (ABAB) although Type II is less common. [36,45] The defect can be described by the total number of hexagonal layers, N_h related to the number of cubic layers, N_c in the structure. $H = N_h / N_{total} = N_h / N_h + N_c$. [43]

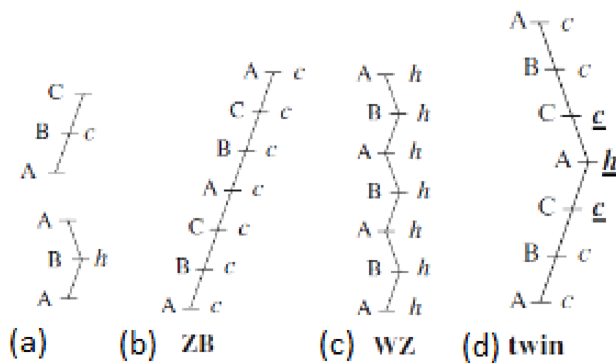

Figure 3.2. examples of different stacking orders (a) shows the order of a unit cell with hexagonal (h) and cubic (c) formation, (b) shows zinc blende and (c) shows wurtzite structures and in (d) the two are mixed in a twin defect. [38]

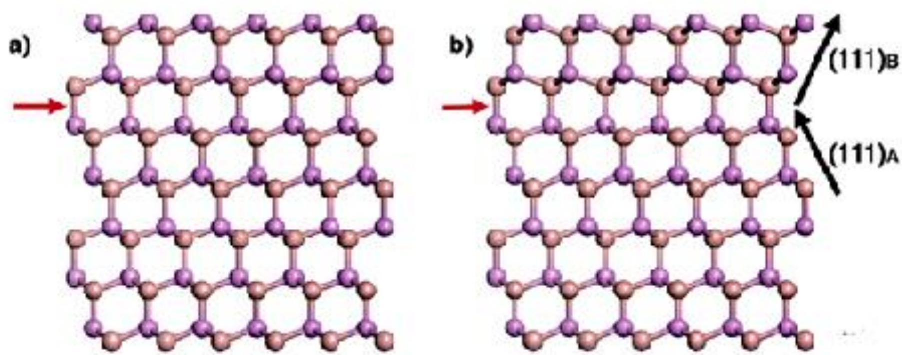

Figure 3.3. compares deposition without twin defect (a) and with twin defect (b). [41]

Crystal nucleation of wurtzite was found to favour growth at edges, borders or textured surfaces, due to a higher surface energy in these specific areas. The uneven (textured) surfaces produced local energy fields and with reduced overall energy for crystallization resulted in small-sized crystal growth. [12,29,45,46] The increased energy by local energy fields was produced either by being trapped into a textured surface or by a three phase boundary, TPB, sometimes known as triple phase line, TPL, which usually refers to solid-liquid-vapor meeting at one point. [29,36,45] Glas et al [36] studied the cause of phase mixture at borders and edges and concluded that the change of structure growth was due to altered energy level. The increased density led to higher energy, which gave a condition of "supersaturation". Nucleation of wurtzite related to higher vapor density at the TPL/ TPB, which initiated nucleation and spread of small crystals (wurtzite) at the interface of these three materials. Increased energy at the interface of the materials supported nucleus formation in form of islands. In circumstances with low energy it was found how some of the islands had not enough energy to activate a growth of wurtzite and instead encouraged the islands to grow in the cubic phase. After a monolayer of hexagonal growth, the energy dropped below saturation and a monolayer of cubic phase was allowed to form. With less energy during zinc blende formation, the energy level increased above saturation and made a monolayer of wurtzite possible to form followed by a zinc blende layer. The continuous change of energy supported a repeated growth pattern between wurtzite and cubic phases. [36]

The cohesive energy ($h\Delta_c$) between the two monolayers for a certain structure helps to stabilize the regular growth and prevent a defect forming in the stacking order. This is calculated by considering the cohesive energy per unit volume, Δ_c and distance, h between two monolayers, when the distances are too small to be measured. The energy required for a crystal structure to nucleate depends on number of atoms per unit cell. [38]

3.3. Raman spectroscopy of silicon

Raman spectroscopy uses electromagnetic radiation, which makes the material atoms/ molecules to vibrate (and rotate if not a solid sample) as the incident light strikes the substrate surface. The emitted Raman light can identify a material's optical, electrical and mechanical properties. Mechanical properties relate to the atomic mass and

bonding strength of a material, which shows in peak location. Quantity of defect and stress in a structure is shown through altered peak location and width. Raman spectroscopy influences phonon vibration by its incident beam as it collides with the material surface and depending on the surface, the incident light will reflect, absorb and scatter.

When using Raman spectroscopy on polyester fabric and fibre, caution must be taken, as laser power annealing can occur in the polymer based substrate. [47] The possibility of annealing, related to the polymer's bulk properties and structural amorphous and crystal content. The structural content in a polymer varies depending on the extrusion and production of the polymer, discussed in the *chapter 2 in section 2.6.*.

Raman spectroscopy requires different parts such as laser source, filters and optical lenses, detector, microscope and computer, which produced images and spectra as shown below (figure 3.4.). [48] The microscope has magnification option often of 100x, 50x and 20x, which influences the beam spot. The Raman measurement can either be static or dynamic, when static has fixed parameters and the scattered light is constant. On the other hand, dynamic means that parameters such as percentage of laser power, exposure time (seconds per measured time) and accumulation are altered for a number of repeats, which makes the scattered light change with time. [48]

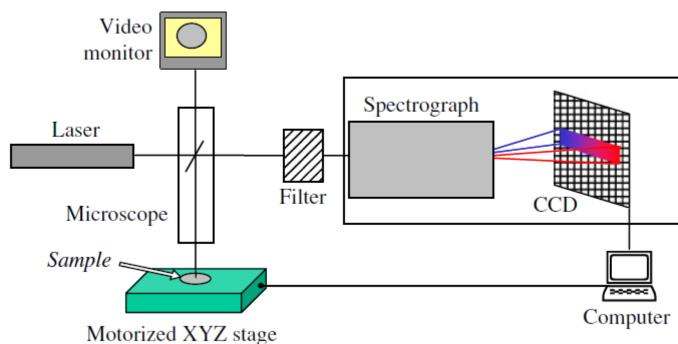

Figure 3.4. a typical Raman layout containing laser source, filtering equipment, detector, and sample stage and computer. [48]

There are many different laser options with common wavelengths of 333, 514, 633 and 785nm from UV to NiR depending on type of substrate to measure. Choice of wavelength will reflect on depth of penetration of the measurement. Longer wavelength

laser gives deeper penetration than shorter wavelengths. [48] Laser power is important in measurement of semiconductors, when powerful lasers can damage soft thin films by annealing and altering the structure content. Therefore, shorter wavelength is often applied to restrict deeper measurement and instead focus on surface properties of the substrate. Examples of depth penetration in relation with different wavelengths are found in table 3.1. [49], while figure 3.5. shows how the light travels through a material. [48]

Table 3.1. How beam penetration through a crystalline silicon material varies with different wavelengths of a laser-beam. [49]

Laser Wavelength (nm)	Penetration depth in Si (nm)
633	3000
514	762
488	569
457	313
325	~10
244	~6

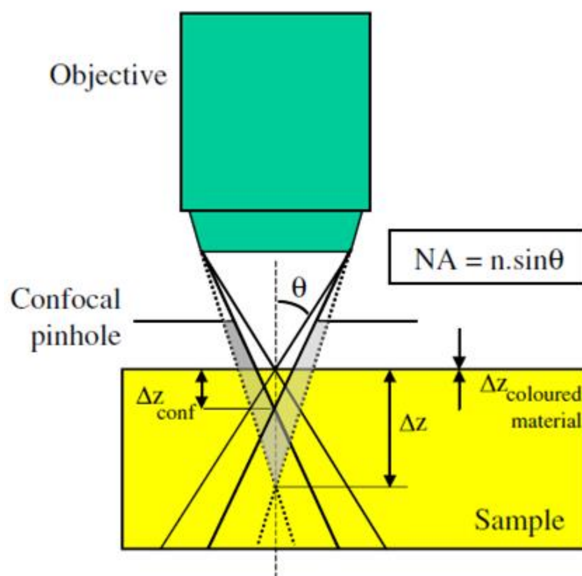

Figure 3.5. illustrates how the incident light penetrates through to a define focal depth in a sample by using confocal optics (pinholes). [48]

Depth of penetration in relation with Raman spectra and the transverse optical (TO) mode's peak location has been studied [50] by using the same type of substrate with different wavelengths. Surface measurement (top penetration) of nanocrystalline and crystal silicon gave a peak location at lower wavenumber (figure 3.6.) than deeper penetration, which gave a more significant transverse optical (TO) mode with increased phonon vibration. The beam changed in beam-width throughout the depth by the focal volume being of an oval shape in cross-section. [50]

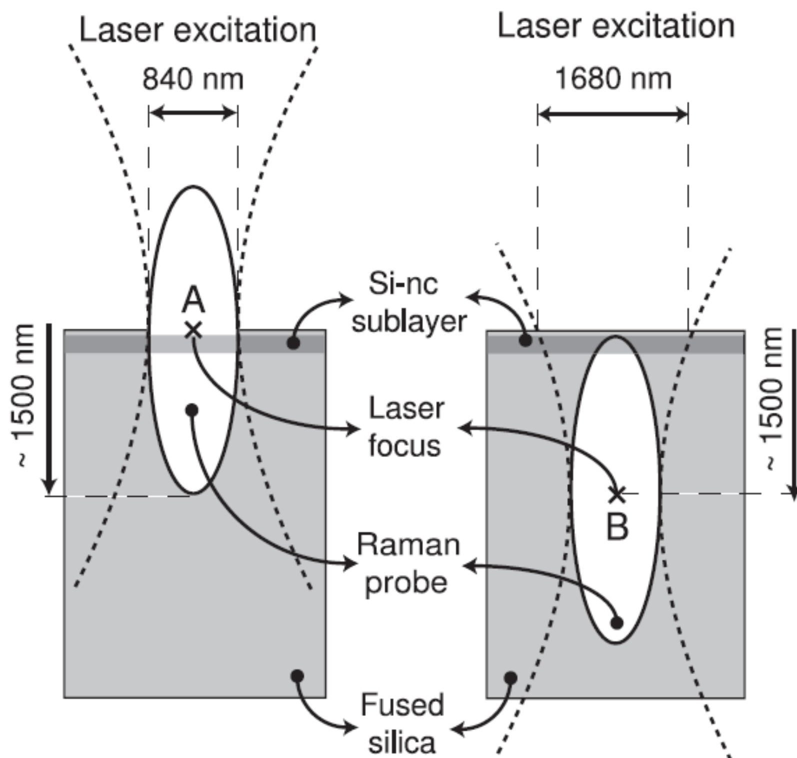

Figure 3.6. a comparison between laser sources of 840 and 1680nm and the penetration depth of the two light sources. [50]

The incident beam collides with the material surface and its photon energy, hv_0 makes the phonon change from ground state to become excited and then return as the photon energy, hv' is emitted. The returning light can either have the same or different angle to the incident light. Normal incident light reflected at 90° is elastic scattering (Rayleigh), and light reflected at different angle is inelastic scattering (Raman). [51] Scattered light returning from excited state to ground state transitions is the elastic component (Rayleigh), while scattered light returning from virtual excited states to new states will have a change in energy and is inelastic scattering (Raman). [52] Brillouin scattering is

similar to Raman scattering but involves longer wavelength phonons, and a transition from a ground state to an excited state and back again due to larger scale elastic behaviour, rather than scattering from individual atoms or molecules.

The altered energy of the returned light (inelastic) depends on a material's structural property such as molecular bonding and type of structure. The inelastically scattered light gives spectral bands shifted from the excitation energy and is often named differently depending on the scattered photon energy, with emitted photons having lost energy referred to as Stokes shifted and those having gained energy named as anti-Stokes shifted. [51,53] Vibrational energy produces a specific peak profile depending on stress, strain, defects and contamination in a material. [48,52] The peak-width can help to establish the amount of disorder or stress involved in a structure, when increased phonon vibrations result in a broader peak-width. [13,21,51,53]

Vibration can either be parallel or perpendicular to a plane, although more commonly vibrations are along both directions. The modes are longitudinal or transverse depending on how the atoms move in relation to the incident wave propagation (k), which is given by $k= 2\pi/ \lambda$ and illustrated below (figure 3.7.). [48,52] The single crystal silicon (Si-I) mode of 520cm^{-1} has a k-value of zero, whereas smaller crystallites deviate from the k-value of zero. The deviation of Si-I modes resulted in change of peak width and downshift from 520cm^{-1}. The 520cm^{-1} peak has often a full width of half maximum, FWHM of ~3cm^{-1}. [15,54] Smaller crystallites have larger differences in phonon vibration than large crystals. Wave propagation increases as the crystal gets smaller. [48]

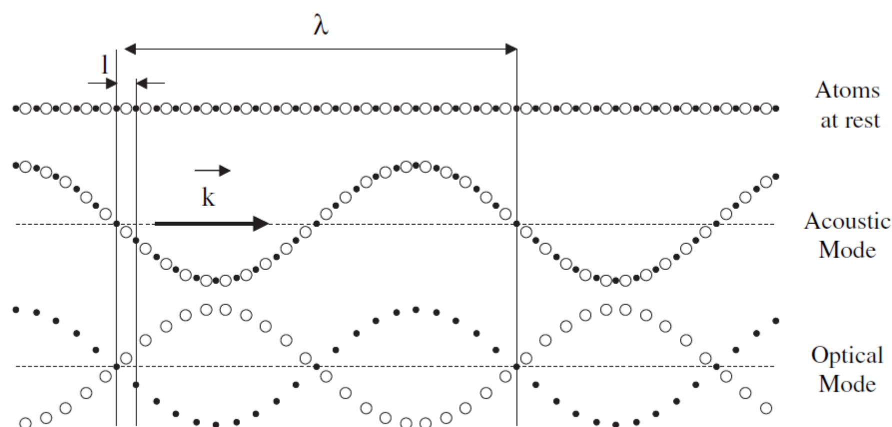

Figure 3.7. shows how atoms move during vibrations of either optical or acoustic modes. [48]

Vibrational modes for crystal and amorphous structures can be divided into two main types: acoustic (low energy in which adjacent atoms move approximately in phase) and optical (high energy in which adjacent atoms move out of phase). Within the acoustic and optical are transverse and longitudinal modes and with a second transverse mode, result in the acoustic having two transverse (TA and TA_2) and one longitudinal (LA) components and the optical having two transverse (TO and TO_2) and one longitudinal (LO). The modes are located in the spectra by TA being at the lowest wavenumber followed by LA, LO and TO (figure 3.8.). [17,25] The phonon vibrations and their strength change accordingly to crystal structure and size, producing particular spectral line positions and widths for the TO, LO, LA, and TA modes. [15,55,56] The peaks of TO, TA and LA became broader when the deposit contained small crystals, while larger crystals raised the structural stability and the peak width becomes reduced. [25,26,27,29,53,54,57,58,59,60,61] The different vibrational modes (TO, LO, TA and LA) and especially TO mode shifted location towards higher wavenumber with a narrower and more symmetric peak shape as the crystal size increased, while smaller crystals gave a broader peak at lower wavenumber.

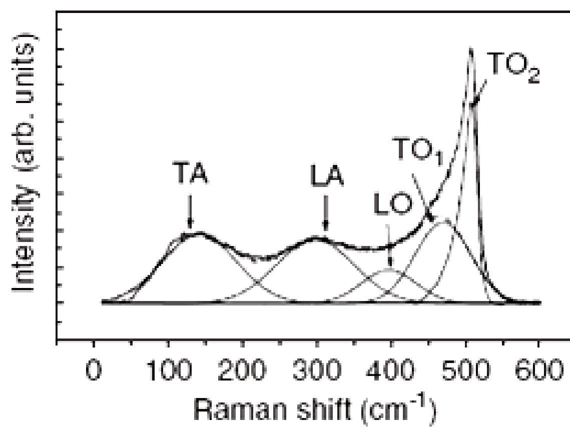

Figure 3.8. shows a typical graph for the four modes in crystalline Si. [29]

3.4. Raman spectrum for amorphous and crystal silicon

Peak locations were much dependent on structural content such as ratio of amorphous and crystal phases and the crystal size. Crystal growth in an amorphous matrix increased structural order, but introduced stress into the amorphous film. [34,62]

Crystal content influenced peak shape, when reduced crystal phase in an amorphous phase gave a broader peak shape due to less stress in the structure compared with increased crystal content, which led to lattice expansion. [62] Altered peak location and shape related to crystal size, when smaller crystals gave increased phonon vibration, which resulted in a more asymmetric peak shape with a broader peak at low wavenumber. [7,15,55,63] Larger crystals raised structural stability, which gave reduced peak width. The difference in peak shape and location in relation with crystal size is given in the Raman spectrum below (figure 3.9.). Silicon crystal (b) has a narrower and symmetric peak shape compared to spectrum (a) with nanocrystal growth, which peak is broad and asymmetric combined with several small peaks from the different phonon modes. [63]

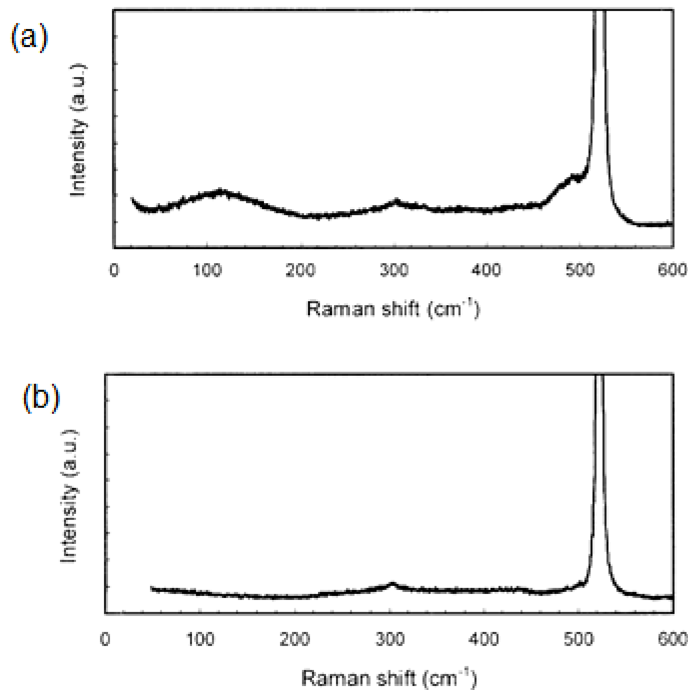

Figure 3.9. spectrum (a) refers to small crystals of Si and therewith an increased number of phonon vibrations, while spectrum (b) is from crystal silicon. [63]

The asymmetric peak shape related to an increase in phonon vibration in the nanocrystal structure. [26,52] However a change in phonon vibration can appear in crystals up to 12nm, but with a reduction in vibration towards a value of k=0. [15]
Determining crystal size from peak location became more accurate with larger crystals than small crystals due to a higher number of vibrations. [27,29,57] Frequency shift (figure 3.10.) was explained by softening in the phonon spectrum as the crystals

become smaller. Computer simulations of different crystal sizes helped to describe how reduced crystal size shifted the peak down from 520cm^{-1} by change in phonon density and vibrational mode, which was increased by smaller silicon crystals or clusters. [15]

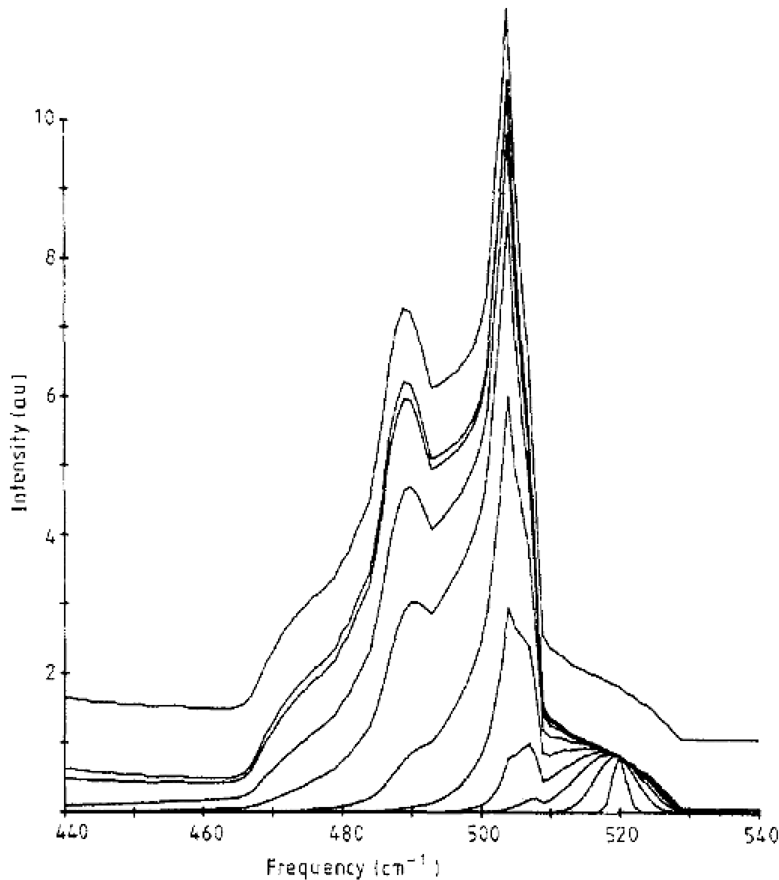

Figure 3.10. Increased crystal size changed the peak shape from being asymmetric to a more symmetric shape, while the peak location changed towards crystal silicon at 520cm^{-1}. [15]

3.4.1 Phonon modes for wurtzite silicon

The wurtzite structure has twelve possible phonon modes ($\Gamma_1^+ + \Gamma_2^- + \Gamma_3^+ + \Gamma_4^- + \Gamma_5^+ + \Gamma_5^- + \Gamma_6^+ + \Gamma_6^-$) according to theory and within this group, three ($\Gamma_1^+ + \Gamma_5^+$ and Γ_6^+) are Raman active. Two ($\Gamma_1^+ + \Gamma_6^+$) correspond to 520cm^{-1}, while the third (Γ_5^+) relates to a peak at 500cm^{-1}. The three active Raman modes have been variously labelled at 495cm^{-1}, 506.9cm^{-1} and 517.2cm^{-1} by using both theoretical and experimental results. [27,34,44] The mode of Γ_5 is distinctive for hexagonal structure and can appear from 496 to 512cm^{-1}. [18,39,44]

There are other phonon vibrations specific for semiconductors of hexagonal structure, which vibrate perpendicular to the plane direction and some of them are surface optical (SO) phonons, Fano and Boson effects. Surface optical (SO) phonon mode comes from phonon vibration between different materials such as in a multi-layered film, while Fano mode comes by structural disorder with crystal growth and Boson relates to the disorder of crystal growth in the amorphous structure. One of the more common defects related with the Fano effect is a twin defect, which appears from a mixture of wurtzite and zinc blende (cubic) phases. Fano effect is often related to quantum confinement, when some areas have higher energy than the bulk material. [64,65] Boson mode is the consequence of additional low-frequency vibrations caused by the disorder in the amorphous structure and was first discovered in glass, but later also in silicon film. [27,29,52,55,66] The crystals have to be of a few nm, whereas crystals larger than 4nm produce less phonon scatter. [67]

It has been suggested that doping (n- and p- type silicon) influences phonon vibrations after finding a relationship between concentration of doped material and strength of the Fano effect. [65,68] N-type doping of silicon proved a relation with Fano effect, when low quantity of n-dopant showed a small or no effect compared to larger quantity, which proved correlation. P-dopant did not influence phonon vibration. [69]

Choice of Raman power proved important to avoid altering the peak location and shape in a Raman spectrum due to changes in phonon vibration. [15,56] With applied beam-power small crystals respond with an increased lattice expansion due to increased phonon vibration, which is reversed with reduced power. Generally, the effect reversing to its original position meant that bulk-properties (microscopic) in a material were not irreversibly affected. In cases where the peak was not being 100% reversed, a small change in the macroscopic structure of the material took place. [70]

Altered peak location and shape with reverse effect was a typical feature of wurtzite and its Fano effect. High power excitation was observed to give a shift to low wavenumber with an asymmetric peak shape, while lower power gave an opposite effect with a symmetric and narrow peak at higher wavenumber. [27,29,55,56] Peak intensity changed too, when low power gave low peak intensity and vice versa. [15,71] This effect related to crystals less than 3nm in size due to these being thermodynamically unstable. [15]

3.4.2. How crystal size influences Raman spectra

The crystal size was estimated by comparing the TO Raman peak width with the Raman line of single crystal Si-I, which is constant at ~3cm^{-1}. [55,56,63] Development of crystals proved not to be exponential in their growth, when a crystal growth up to 4nm showed a clear change in peak location and shape, while crystals larger than 4nm had a reduced change in peak location and shape. [14,15,56,71,72] The peak shape became more symmetric and narrower as the crystallites got larger (figure 3.10.). [55,63] Both experimental and theoretical work have been carried out to try to match crystal size and formation with Raman peak locations and shapes [29,39,55,61] in comparison with cubic single crystal, Si-I at 520/ 521cm^{-1}.

Peak shift from 520cm^{-1} to lower wavenumber was due to crystal sizes less than 10nm. [15] The diagram below (figure 3.11.) illustrates how crystal size influenced peak location, width and shape, when increased crystal size produced a narrower and sharp peak compared to smaller crystals. [15] Crystal size less than 15nm contained both a crystal and amorphous content, while crystals larger than 15nm contained mainly crystal content and only a fraction of amorphous was left. [62] Larger surface of a crystal led to increased boundary area, which increased the disorder in the structure caused by crystal growth in the amorphous matrix. [73] Surface roughness of deposited films increased with the larger crystal sizes, when films with crystals between 4 and 12nm contained voids as the columnar shapes were formed. Crystals less than 4nm provided a smoother surface without voids. [9] Formation of crystals depended on crystal size, when 3nm appeared in a sphere compared with ~5nm, which occurred in a columnar shape. [29]

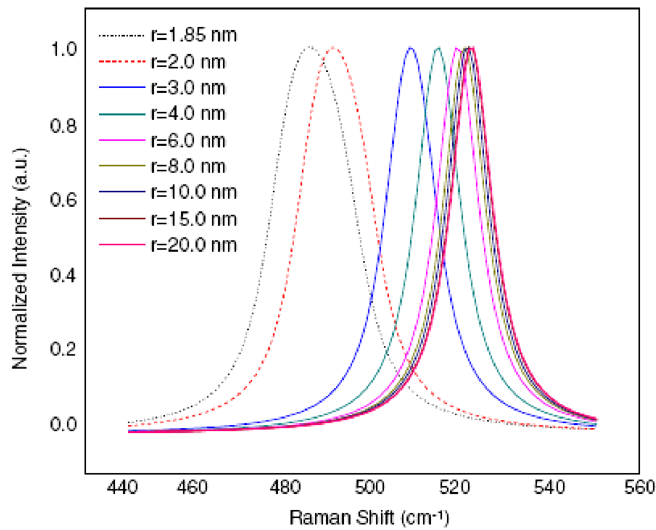

Figure 3.11. how the Raman peak changes in width and location by shifting from the crystal silicon peak at 520cm^{-1}. [55]

Different studies may be summed up as follows: a peak at 494-496cm^{-1} refers to ~1nm crystals [17,29,34,52] and a peak between 495 and 500cm^{-1} related to 1 to 2nm [31,72], whilst a peak at 504cm^{-1} had a crystal size calculated to be 2$\pm$0.5nm. [18,29,31,50] This was confirmed by a study calculating crystal sizes to be 1 to 2nm for peaks between 504 to 507cm^{-1} and 2 to 4nm for peaks between 508 to 512cm^{-1}, when a peak at 513.5cm^{-1} had a size of 4.7nm. [14,56] Structures containing crystals with a diameter less than 7nm can be considered as quantum dots with quantum confinement effect, which have an increased phonon wave vector compared with bulk silicon and a broader band-gap. [42,63]

Both Richter [74] and Campbell [75] have discussed a model to correlate peak shift, peak width and the crystal size. The focus is to understand how Raman spectra respond to different sizes of crystals in relation to single crystal silicon. The model considered phonon momentum, q and applicability to structures with crystal growth, when this effect becomes lost in an amorphous structure. The confinement value becomes lower as the crystal size becomes larger due to reduced phonon vibration compared with silicon crystal. [7,29,55,56,65,74,75] Quantum confinement was expressed by the frequency shift, $\Delta\omega$ (cm^{-1}) based on difference between given peak location $\omega(L)$ (cm^{-1}) for certain crystal size, L (Å) and the reference peak of crystal silicon at 520/ 521cm^{-1}, ω_0. Change in crystal size alters the lattice parameters such as lattice length (α) and cluster diameter/ crystal size, L (Å) [46,63] reflected in the quantum confinement parameter, γ. The quantum confinement, γ value depended on

crystal formation ($L^{-\gamma}$) such as crystal spheres ($L^{-1.44}$), crystallites ($L^{-1.39}$) and crystal columns ($L^{-1.08}$). [46,63] Quantum confinement effect can be expressed as:

$$\Delta\omega=\omega(L)-\omega_0=-A(a/L)^{\gamma} \quad (1)\ [46,63]$$

Richter [74] compared his work (figure 3.13.) with suggested [75] correlation between a crystal size (L), peak width (Γ) and the peak shift (Δω) from crystal silicon, at 520cm^{-1}.

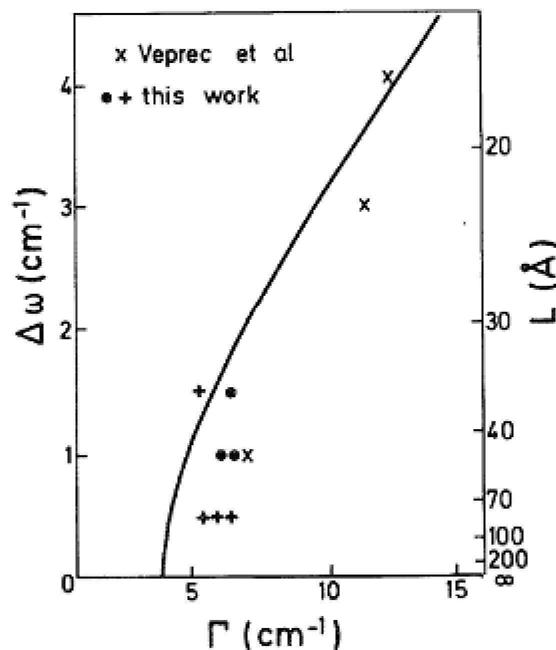

Figure 3.12. correlations between crystal size (L), peak shift (Δω) and peak width (Γ) in relation with peak shift from 520cm^{-1}. [74]

3.4.3. Raman peaks regarding nanocrystalline structure

Mixed structure of crystal and amorphous components including wurtzite structure, Si-IV phase, was recommended to give a peak fit with three Gaussian peaks at 480cm^{-1} (amorphous), 500/ 505cm^{-1} (nanocrystal) and 518/ 520cm^{-1} (crystal silicon) as in figure 3.13.. [24,60,76,77]

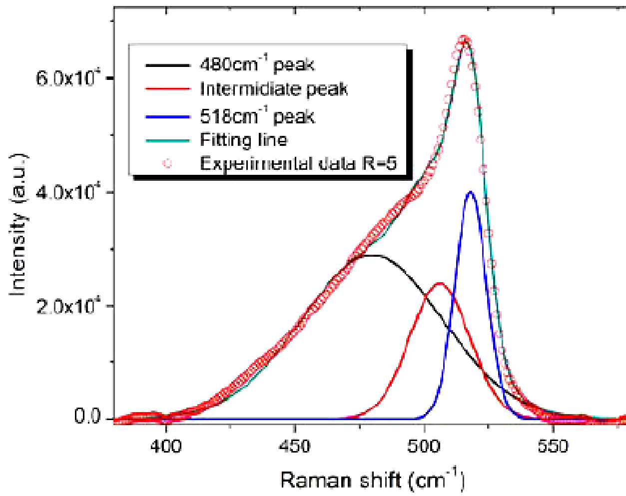

Figure 3.13. illustrates the typical peaks, location and shape of amorphous at 480cm^{-1}, nanocrystal at 500/ 505cm^{-1} and crystal at 520cm^{-1}. [61]

Peak location varied depending on crystal sizes in the structure, when two of the peaks at the higher wavenumbers were linked to the crystal content and the third peak referred to the amorphous matrix. Locations for the phonon modes such as TA (transverse optical), LA (longitudinal acoustic), LO (longitudinal optical) and TO (transverse optical) and the additional phonon vibrations such as twin defect (Fano) and surface optical (SO, common in doped material) and Boson (disorder) were changed by crystal size and content. [5,27,41,52,54,78,79] The Raman spectra in figure 3.14. show the complexity and the different ways to extract the peaks from a spectrum based on material with crystal growth in an amorphous matrix. [76]

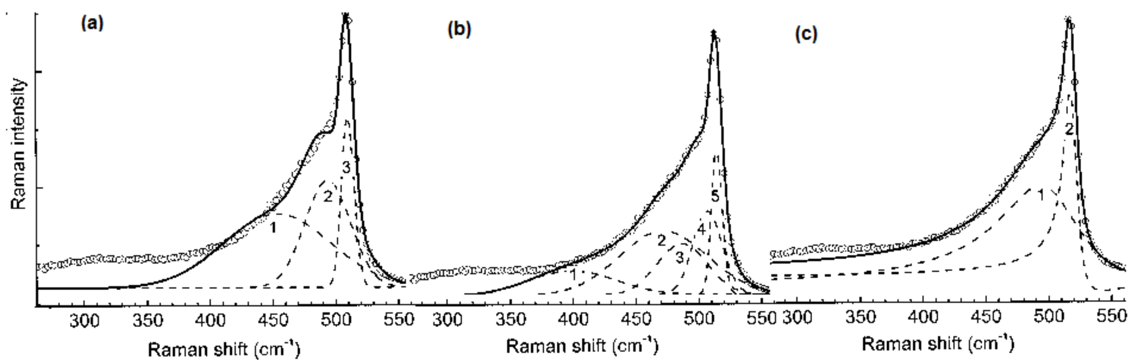

Figure 3.14. Peak locations depended on the number of peaks and type of peak fit used in a structure of mixed crystal growth in amorphous silicon. The example above shows how peak location and shape changed in microcrystal silicon by using (a) three Gaussian peaks (461, 501

and 517.5cm^{-1}) compared with (b) five Gaussian peaks (402, 475, 490, 510, 518cm^{-1}) and with (c) two Lorentzian peaks (501, 519.5cm^{-1}). [76]

The Si-IV phase was recognised by Raman peaks at a range from 499-512cm^{-1} [24,25,27,33,34,54,80], and 516& 518cm^{-1} [22,34,50] together with an amorphous peak at 480cm^{-1} or below. Other peaks typical for Si-IV was a peak at 290cm^{-1} known as the second TA peak, TA_2 and [21,22,32,34,80] the additional phonon vibrations such as surface optical (SO) phonons, Fano and Boson effects. Fano vibration causes an asymmetric peak shape and was found at ~495cm^{-1} between TO and LO modes, while the surface optical phonon peak was close to the Fano peak. The Boson peak often appears close to TA-mode, which appears in the range of 160cm^{-1} for pure amorphous to 210cm^{-1} with crystal content. These peaks' locations and intensities depend on structural disorder, where lower wavenumber arises from higher disorder and vice versa. The Boson interaction is produced by phonon scattering from acoustic phonons, which appear when small changes in the amorphous material occur such as crystal growth. Peak locations shift depending on quantity of disorder in the structure, when a low peak location comes from a high amorphous content [57], which shifts higher by increased crystal growth within the amorphous structure. [29,52,55,57,66,67] Additional infrared vibrational modes of phonons such as wagging at 630-650cm^{-1}, bending 830-880cm^{-1} and stretching at 2000-2200cm^{-1} are found too. [58,59,69,81]

With the onset of crystal nucleation, an initial peak from amorphous material at 480cm^{-1} showed an immediate effect by shifting upwards towards 485cm^{-1} and depending on crystal size could shift typically to ~512cm^{-1}. [2,8,31,34,52,58,80] However, initial peak location for crystal nucleation has been discussed when locations between 483 to 496cm^{-1} have been suggested. [8,26,71,80] The crystal peak located at 500/ 505cm^{-1} known as the "intermediate peak" moves upwards towards the boundary of nanocrystal and microcrystal peaks according to crystal size. Its location lies anywhere from the early intermediate region at 494cm^{-1} for smaller crystals, to 500/ 505cm^{-1} for larger crystals. [31,82]

As the crystals develop in size the two peaks move towards higher wavenumber and their locations depend on type of crystal structure, when nanocrystal gained two peaks in the intermediate region (between 494 and 512cm^{-1}), while a structure containing both nanocrystal and larger crystals (microcrystal) had a peak each in the intermediate and the microcrystal regions. The different crystal regions reflected on change in structure

in the amorphous content by having a hexagonal phase from small crystals, through a mixture of hexagonal and cubic phase, to a microcrystal with dominance of cubic phase. [18,24,28,39,44,55] The mixture of the two phases appears over a longer stretch of wavenumbers, when cubic phase starts forming during the nanocrystal growth and becomes more dominant as the crystal size increase. The hexagonal structure will still continue close to the boundary where an equilibrium between the phases is reached before cubic growth starts to dominate and its peak starts to appear in the microcrystal region. [25,34,50,61] A peak between 504cm^{-1} and 512cm^{-1} is suggested to be a combination of a mixture of hexagonal and cubic phase, while a peak located at 514- 517cm^{-1} is dominated by cubic phase. [18,39] The exact ratios of the two phases in relation with wavenumber are not completely known. [52,58] The boundary of nano- and micro- crystals is not agreed and suggestions such as ~510 to 514cm^{-1} [32] or 516cm^{-1} to 518cm^{-1} [34,50] where microcrystal dominates are still unclear. [18,29,52,54,58]

With crystal nucleation, the peak at 480cm^{-1} [5] is shifting up towards higher wavenumber and at same time an additional peak appears as “new” amorphous peak, which moved down in a typical range of 470-439cm^{-1}, although a peak at 420cm^{-1} was suggested by Kobiliska. [7,18,26,31,34] Locations of the amorphous peak related to the crystal size and typical peak combinations were suggested for both nanocrystal at 504cm^{-1} (446, 464, 477, 486cm^{-1}) and microcrystal at 515cm^{-1} (439, 462, 478, 486cm^{-1}). [31]

3.5. Properties of nanocrystal structure

The structure content has a great influence on optical and electrical properties of a material. An increased amorphous content in thin-film Si, the hydrogenated silicon, gave a higher light-degradation [1] with reduced electrical properties through the Staebler-Wronski effect [7,83], while integration of crystal phase would reduce the light-degradation [1] caused by the dangling bonds.

The electrical properties became improved by a mixed Si structure of crystals and amorphous, when the carrier transport took place preferentially through the crystal path. [2,4] An advantage was found with nanocrystal Si, that small crystals in the amorphous matrix increased the current flow by producing a bridging effect. [5]

Nanocrystals below 10nm, encouraged a quantum confinement effect (QCE) and provided a path for carrier transport through the crystallites. [5,6,84]

Film thickness was important too, when a thicker film was reported to reduce carrier mobility. [10] Correlation between thickness and electrical properties has been studied [5,18,83,85] by using film thickness between 10 and 200nm. It was experienced that the mobility increased with film thickness, but reached a maximum at 50nm as a thicker film had reduced current flow, which illustrates in figure 3.15.. Film thickness less than 30nm resulted in reduced electrical properties due to surface roughness of the substrate. [10] The same study [10] concluded how a film thickness of ~50nm was a good compromise between electrical and optical properties.

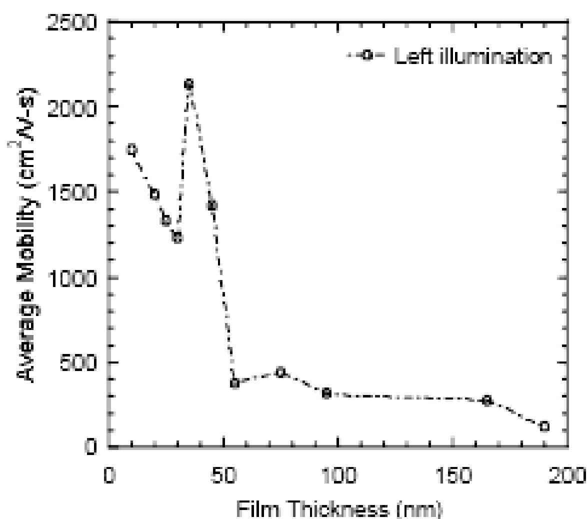

Figure 3.15. how increased silicon film thickness reduces the carrier mobility and increases loss in current flow. [10]

However, a material with some crystal content reduced the optical absorption compared with a pure amorphous material of same thickness. Therefore film thickness became important with mixed structure in relation to optical properties. The advantage with a mixed structure was the increased number of band-gap values, which improved optical absorption. The two band-gaps at 1.8 eV and below 1.6eV were associated with one for indirect transitions (nanocrystal) and one for direct transitions (amorphous), while indirect band-gap values changed depending on crystal size. [2,27] Indirect band-gap had higher absorption at long wavelength, when the amorphous structure with

direct band-gap absorbed at shorter wavelength. The band-gap energy was derived from a Tauc plot produced by using optical absorption data in form of $(ahv)^{1/2}$ against photon energy, hv, which is discussed in *chapter 5 section 5.3.5.*. [4]

3.6. Conclusion

Thin-film silicon was shown to have a complicated structure with more than one phase, including an unexpected hexagonal crystal phase, which could be identified by Raman spectroscopy. Crystal growth in the amorphous structure was reported to improve cell performance by avoiding light-degradation, which is a strong defect with the amorphous structure. [1] Crystal phase in the amorphous matrix improved both the electrical and optical properties. The small crystals produced a path for the current to flow, which gave better electrical properties. [2,4] Mixed structure contained two band-gap values, which improved the optical absorption. The crystal band-gap value decreased as the crystal content increased. [4] The higher band-gap of around 1.8eV referred to a direct band-gap of amorphous material, while the lower (less than 1.6eV) was indirect band-gap absorption from crystalline material. [2]

Fitting a Raman spectrum to thin film silicon was recommended with two or three Gaussian peaks at $480cm^{-1}$ (amorphous), 500/ $505cm^{-1}$ (intermediate) and $520cm^{-1}$ (crystal silicon) depending on the crystal size and content. [24,60,61,76,77] The third peak at 500/ $505cm^{-1}$ was applied in relation to nanocrystal structure, which was identified as hexagonal, wurtzite Si-IV. Location of the two crystal-related peaks varied due to crystal growth and size, when a content of small crystals would have both peaks at the intermediate region. This may be compared with larger crystal size, which gave peaks in the intermediate and microcrystal regions. The amorphous peak was developed with the initial nucleation of crystallites, when the original amorphous peak started to shift from $480cm^{-1}$ upwards to $485cm^{-1}$ together with the two crystal peaks. At the same time, a “new” amorphous peak occurred and shifted downwards, peak location depending on crystal growth and size. [2,31]

3.7. References

1 D.L. Staebler and C.R. Wronski, *Reversible conductivity changes in discharge-produced amorphous Si*, Appl. Phys. Lett. **31**, p.292-4 (1977)

2 B. Yan, G. Yue, X. Xu, J. Yang and S. Guha, *High efficiency amorphous and nanocrystalline silicon solar cells*, Phys. Status Solidi (a) **207** (3), p.671-7 (2010)

3 S. Klein, F. Finger, R. Carius, T. Dylla and J. Klomfass, *Relationship between the optical absorption and the density of deep gap states in microcrystalline silicon*, J. Appl. Phys. **102**, 103501 (2007)

4 B. Yan et al., *On the bandgap of hydrogenated nanocrystalline silicon thin films*, photovoltaic specialists conference (PVSC) **2010 35th** IEEE, p.003755-60 (2010)

5 G. Yue et al., *Material structure and metastability of hydrogenated nanocrystalline silicon solar cells,* Appl. Phys. Lett. **88**, (pp.3) (2006)

6 T.A. Burr, A.A. Seraphin, E. Werva and K.D. Kolenbrander, *Carrier transport in thin films of silicon nanoparticles*, Phys. Rev. B **56** (8), p.4818-24 (1997)

7 B. Yan, G. Yue, J.M. Owens, J. Yang and S. Guha, *Light induced metastability in hydrogenated nanocrystalline silicon solar cells*, Appl. Phys. Lett. **85** (11), (pp.3) (2004)

8 G. Viera, M. Mikikian, E. Bertran, P. Roca I Cabarrocas, L. Boufendi, *Atomic structure of the nanocrystalline Si particles appearing in nanostructured Si thin films produced in low-temperature radiofrequency plasmas*, J. Appl. Phys. **92** (8), p.4684-94 (2002)

9 D. Gracin et al., The structural ordering of thin silicon films at the amorphous to nano-crystalline phase transition by GISAXS and Raman spectroscopy, Renew. Energ. **33**, p326-30 (2008)

10 A.K. Sharma, R. Prinja and S.R.J. Brueck, *Effects of dimensional scaling on the electronic transport properties of silicon nanofilms and nanowires*, 5th IEEE conference on nanotechnology, Japan, (pp.4) (2005)

11 K. Ostrikov, *Colloquium: reactive plasmas as a versatile nanofabrication tool*, Rev. Mod. Phys. **77**, p.489-511 (2005)

12 H.B.T. Li, R.H. Franken, J.K. Rath and R.E.I. Schropp*, Structural defects caused by a rough substrate and their influence on the performance of hydrogenated nano-crystalline silicon n-i-p solar cells,* Sol. Energ. Mat. Sol. C. **93**, p.338-49 (2009)

13 D. Das, *Structural studies on Si:H network by micro- Raman, micro-photoluminescence, electron microscopy and ultraviolet ellipsometry: effect of Ar dilution to the SiH4-plasma*, Thin Solid Films **476**, p.237-45 (2005)

14 H.S. Mavi, A.K. Shukla, S.H. Abbi and K.P. Jain, *Raman study of amorphous to microcrystalline phase transition in cw laser annealed a- Si:H films*, J. Appl. Phys. **66** (11), p.5322-6 (1989)

15 Z. Iqbal and S. Veprek, *Raman scattering from hydrogenated microcrystalline and amorphous silicon*, J. Phys. C: Solid State Phys. **15**, p.377-92 (1982)

16 A. Chowdhury, S. Mukhopadhyay and S. Ray, *Fabrication of thin film nanocrystalline silicon solar cell with low light-induced degradation*, Sol. Energ. Mat. Sol. C. **93** (5), p.597-603 (2009)

17 J. Cain et al., *Reversible pressure-induced structural transitions between metastable phase silicon*, Phys. Rev. B **50** (17), p.13043-6 (1994)

18 K.U.M. Kumar and M.G. Krishna, *Chromium-induced nanocrystallisation of a-Si thin films into the wurtzite structure*, J. Nanomaterials **2008**, (pp.6) (2008)

19 K. Syassen, S. Bräuninger and U. Schwarz, *Crystal structure of silicon*, MPI/FKF, Stuttgart 1997/9, (pp.1)

20 A. Kailer, Y.G. Gogotsi and K.G. Nickel, *Phase transformations of silicon caused by contact loading*, J. Appl. Phys. **81** (7), p.3057-63 (1996)

21 Y. Gogotsi, C. Baek and F. Kirscht, *Raman microscopy study of processing-induced phase transformations and residual stress in silicon*, Semicond. Sci. Technol. **14**, p.936-44 (1999)

22 V. Domnich and Y.Gogotsi, *Phase transformation in silicon under contact loading*, Rev. Adv. Mat. Sci. **3**, p.1-36 (2002)

23 B. Wen, J. Zhao, M.J. Bucknum, P. Yao and T. Li, *First- principles studies of diamond Polytypes,* Diam. Relat. Mater. **17**, p.356-64 (2008)

24 Q. Cheng, S. Xu and K. Ostrikov, *Structural evolution of nanocrystalline silicon thin films synthesized in high-density, low- temperature reactive plasmas*, Nanotechnology **20**, 215606 (pp.8) (2009)

25 W. Wei, G. Xu, J. Wang and T. Wang, *Raman spectra of intrinsic and doped hydrogenated nanocrystalline silicon films*, Vacuum **81**, p.656-62 (2007)

26 K. Wu, X.Q. Yan and M.W. Chen, *In situ Raman characterisation of reversible phase transition in stress-induced amorphous silicon*, Appl. Phys. Lett. **91** (10) (pp.3) (2007)

27 J. Bandet, B. Despax and M. Caumont, *Vibrational and electronic properties of stabilized wurtzite- like silicon*, J. Phys. D. Appl. Phys. **35**, p.234-9 (2002)

28 Y. Zhang, Z. Iqbal, S. Vijayalakshmi and H. Grebel, *Stable hexagonal-wurtzite silicon phase by laser ablation*, Appl. Phys. Lett. **75** (18), p.2758-60 (1999)

29 G. Viera, S. Huet and L. Boufendi, *Crystal size and temperature measurements in nanostructured silicon using Raman spectroscopy*, J. Appl. Phys. **90** (8), p.4175-84 (2001)

30 H. Lind, J. Wilson and R. Mather, *Raman spectroscopy of thin-film silicon on woven polyester*, Phys. Status Solidi A **208** (12), p.2765-71 (2011)

31 X.L. Wu et al., *Raman scattering of alternating nanocrystalline silicon/ amorphous silicon multilayers*, Appl. Phys. Lett. **69** (4), p.523-5 (1996)

32 S.B. Concari and R.H. Buitrago, *Raman monitoring laser-induced phase transformation in microcrystalline silicon thin film prepared by PECVD,* Semicond. Sci. Technol. **18** (9), p.864-9 (2003)

33 J.M. Besson, R.H. Mokhtari, J. Gonzalez and G. Weill, *Electrical properties of semimetallic silicon III and semiconductive silicon IV at ambient pressure*, Phys. Rev. Lett. **59**, p.473-6 (1987)

34 R.J. Kobiliska and S.A. Solin, *Raman spectrum of wurtzite Silicon*, Phys. Rev. B **8** (8), p.3799-02 (1973)

35 A. Fontcuberta I Morral, J. Arbiol, J.D. Rades, A. Cirera and J.R. Morante, *Synthesis of Silicon Nanowires with Wurtzite Crystalline Structure by Using Standard Chemical Vapor Deposition*, Adv. Mater. **19**, p.1347-51 (2007)

36 F. Glas, J-C. Harman and G. Patriarche, *Why does wurtzite form in nanowires of III-V Zinc Blende semiconductors?*, Phys. Rev. Lett. **PRL 99**, 146101 (2007)

37 R. Zallen, R.M. Martin and V. Natoli, *Infrared activity in element crystals*, Phys. Rev. B **49** (10), p.7032-5 (1994)

38 F. Glas, *A simple calculation of energy changes upon stacking fault formation or local crystalline phase in semiconductors*, J. Appl. Phys.**104**, 093520-1 (pp.6) (2008)

39 J.D. Prades, J. Arbiol, A. Cirera, J.R. Morante and A.F.I. Morral, *Concerning the 506cm^{-1} band in the Raman spectrum of silicon nanowires,* Appl. Phys. Lett. **91** (12), (pp.3) (2007)

40 C-Y. Yeh, Z. W. Lu, S. Froyen and A. Zunger, *Zinc- blende- wurtzite polytypism in semiconductors*, Phys. Rev. B **46** (16), p.10086-97 (1992)

41 F.M. Davidson, D.C. Lee, D.D. Fanfair and B.A. Korgel, *Lamellar twinning semiconductor nanowires*, J. Phys. Chem. C. **111**, p.2929-35 (2006)

42 G. Conibeer et al., *Silicon nanostructures for third generation photovoltaic solar cells*, Thin solid films **511-512**, p.654-62 (2006)

43 X. Lui and D. Wang, *Kinetically- induced in chemically grown silicon nanowires*, Nano. Res. **2**, p.575-82 (2009)

44 F.J. Lopez, E.R. Hemesath and L.J. Lauhon, *Ordered stacking fault arrays in silicon nanowires,* Nano Lett. **9** (7), p.2774-9 (2009)

45 F. Glas, G. Patriarche and J.C. Harmand, *Growth, structure and phase transitions of epitaxial nanowires of III-V semiconductors*, J. Phys.: Conf. Ser. **209** (1), (pp.12) (2010)

46 J. Zi et al., *Raman shifts in Si nanocrystals*, Appl. Phys. Lett. **69** (2), p. 200-3 (1996)

47 H. Liem and L.J. Yeung, Segment self-orientational behaviour in shape memory polymer Thin films probed by Raman spectroscopy, J. Appl. Polym. Sci. **105** (2), p.765-70 (2007)

48 G. Gouadec and P. Colomban, *Raman spectroscopy of nanomaterials: How spectra relate to disorder, particle size and mechanical properties*, Prog. Cryst. Growth CH. **53**, p.1-57 (2007)

49 Horiba Jobin Yvon S.A.S., *Strain measurements of a Si cap layer deposited on a SiGe substrate determination of Ge content,* Semiconductors. **01**, p.1-3 www.Horiba.com

50 D. Barba, F. Martin and G.G. Ross, *Evidence of localized amorphous silicon clustering from Raman depth- probing of silicon nanocrystal in fused silica,* Nanotechnology **19**, 115707 (pp.5) (2008)

51 I. De Wolf, C. Jian, W. Merlijn van Spengen, *The investigation of microsystems using Raman spectroscopy,* Opt. Laser Eng. **36**, p.213-23 (2001)

52 I. Zardo, G. Abstreiter and A. Fontcuberta I Morral, *Raman spectroscopy on semiconductor nanowires*, chapter 12 Nanowires, edited by Paola Prete, ISBN 978-953-7619-79-4, p.227-54 (2010)

53 G. Weill, J.L. Mansot, G. Sagon, C. Carlone and J.M. Besson, *Characterisation of Si III and Si IV, metastable forms of silicon at ambient pressure*, Semicond. Sci. Tech. **4**, p.280-2 (1989)

54 D. Han, J.D. Lorentzen, J. Weinberg-Wolf and L.E. McNeil and Q. Wang, *Raman study of thin films of amorphous-to-microcrystalline silicon prepared by hot-wire chemical vapour deposition*, J. Appl. Phys. **94** (5), p.2930-6 (2003)

55 S.K. Gupta and P.K. Jha, *Modified phonon confinement model for size dependent Raman shift and linewidth of silicon nanocrystals,* Solid State Commun. **149**, p.1989-92 (2009)

56 Z. Sue, P.P. Leong, I.P. Herman, G.S. Higashi and H. Temkin, *Raman analysis of light-emitting porous silicon,* Appl. Phys. Lett. **60** (17), p.2086-8 (1992)

57 C. Laermans and M. Coeck, *Low-frequency Raman scattering in bulk neutron-disordered silicon*, Physica B **263-264**, p.152-5 (1999)

58 S. Zhang et al., *Silicon thin film prepared in the transition region and their use in solar cells*, Sol. Energ. Mat. Sol. C. **90**, p.3001-8 (2006)

59 Y. Xu el al., *Microstructure characterisation of transition films from amorphous to nanocrystalline silicon*, J. Cryst Growth **256**, p.27-32 (2003)

60 V. Lavrentiev, J. Vacik, V. Vorlicek and V. Vosecek, *Raman scattering in silicon disorder by gold ion implantation*, Phys. Status Solidi B **247** (8), p.2022-6 (2010)

61 T.Q. Trung et al., *The effects of hydrogen dilution on structure of Si:H thin films deposited by PECVD*, J. Phys.: Conf. Ser. **187**, 012035 (pp.6) (2009)

62 K. Bhattacharya and D. Das, *Nanocrystalline silicon films prepared from silane plasma in RF-PECVD, using helium dilution without hydrogen: structural and optical characterization*, Nanotechnology **18**, 415704 (pp.9) (2007)

63 G. Faraci, S. Gibilisco, P. Russo and A.R. Pennisi*, Modified Raman confinement model for Si nanocrystals,* Phys. Rev. B **73**, (pp.4) (2006)

64 R. Gupta, Q. Xiong, C.K. Adu, U.J. Kim and P.C. Eklund, *Laser induced Fano resonance scattering in silicon nanowires*, Nano Lett. **3** (5), p.627-31 (2003)

65 R. Kumar and A.K. Shukla, *Quantum interference in the Raman scattering from the silicon nanostructures*, Phys. Lett. A **373**, p.2882-6 (2009)

66 F. Finkemeier and W. Von Niessen, *Boson peak in amorphous silicon: A numerical study*, Phys. Rev. B **63**, p. 235204-1 (pp.6) (2001)

67 N.N. Ovsyk and V.N. Novikov*, Influence of structural disorder on Raman scattering in amorphous porous silicon*, Phys. Rev. B **57** (23), p.14615-8 (1998)

68 V. Magidson and R. Beserman, *Fano type interference in the Raman spectrum of photoexcited Si*, Phys. Rev. *B* **66** (19), (pp.6) (2002)

69 B.G. Burke et al., *Raman study of Fano interference in p-type doped silicon.* J. Raman Spectrosc. **41** (12), p.1759-64 (2010)

70 S. Khachadorian et al., *The morphology of silicon nanowire samples: A Raman study*, Phys. Stat. Sol. B **246** (11–12), p.2809–12 (2009)

71 R. Martins et al, *Nanostructured silicon and its application to solar cells, position*

sensor and thin film transistors, Philos. Mag. **89**, p.2699-721 (2009)

72 G. Faraci, S. Gibilisco, P. Russo and A.R. Pennisi, *Modified Raman confinement model for Si nanocrystals*, Phys. Rev. B **73**, p.033307-1 (pp.4) (2006)

73 J. Zi, H. Buscher, C. Falter, W. Ludwig, K. Zhang and X. Xie, *Raman shifts in Si nanocrystals*, Appl. Phys. Lett. **69** (2), p.200-2 (1996)

74 H. Richter, Z.P. Wang and L. Ley, *The one phonon Raman spectrum in microcrystalline silicon*, Solid State Commun. **39** (5), p.625-9 (1981)

75 I.H. Campbell and P.M. Fauchet, *The Effects of Microcrystal size and shape on the one phonon Raman spectra of crystalline semiconductors,* Solid State Commun. **58** (10), p.739-41 (1986)

76 C. Smit et al., *Determining the material structure of microcrystalline silicon from Raman spectra*, J. Appl. Phys. **94** (5), p.3582-8 (2003)

77 G. Yue, J.D. Lorentzen, J. Lin and D. Han, *Photoluminescence and Raman studies in thin-film materials: Transition from amorphous to microcrystalline silicon*, Appl. Phys. Lett. **75** (4), p.492-4 (1999)

78 C.C. Tsai, G.B. Anderson, R. Thompson and B. Wacker, *Control of silicon network structure in plasma deposition*, J. Non-Cryst. Solids **114**, p.151-3 (1989)

79 A.T. Voutsas, M.K. Hatalis, J. Boyce and A. Chiang, *Raman spectroscopy of amorphous and microcrystalline silicon films deposited by low- pressure chemical vapor deposition*, J. Appl. Phys. **78** (12), p. 6999-06 (1995)

80 S. Huet, G. Viera and L. Boufendi, *Effect of small crystal size and surface temperature on the Raman spectra of amorphous and nanostructured Si thin films deposited by radiofrequency plasmas*, Thin solid films **403-404**, p.193-6 (2002)

81 R. Singh, S. Prakash and N.N. Shukla and R. Prasad, *Sample dependence of the structural, vibrational, and electronic properties of a-Si:H: A density-functional-based tight- binding study*, Phys. Rev. B **70**, 115213 (pp.13) (2004)

82 P. Gogoi, P.N. Dixit and P. Agarwal, *Amorphous silicon films with high deposition rate prepared using argon and hydrogen diluted silane for stable solar cells*, Sol. Energ. Mat. Sol. C. **91**, p.1253-7 (2007)

83 G. Yue, B. Yan, C. Teplin, J. Yang and S. Guha, *Optimization and characterisation of 1/p buffer layer in hydrogenated nanocrystalline silicon solar cells*, J. Non-Cryst. Solids **354**, p.2440-4 (2008)

84 W.G.J.H.M. van Sark, A. Meijerink, R.E.I. Schropp, J.A.M. van Roosmalen and E.H. Lysen, *Enhancing solar cell efficiency by using spectral converters*, Sol. Energ. Mat.Sol. C. **87**, p.395-409 (2005)

85 B. Yan, G. Yue, J. Yang and S. Guha, *Hydrogen dilution profiling for hydrogenated microcrystalline silicon solar cells,* Appl. Phys. Lett. **85** (11), p.1995-7 (2004)

4. Environmental assessment & impact of silicon thin film on woven polyester

4.1. Introduction

In an attempt to avoid too big a change in the global environment, an agreement has been signed globally to cut energy use of non-renewable sources and emissions, especially of carbon dioxide, CO_2. The European community has, through set targets pushed for a drastic change in source of energy supply, where fossil fuel has to be replaced with renewable energy such as wind, hydro and photovoltaic. Non-renewable sourced energy comes from burned fossil fuel such as coal and oil, which has a very high contribution to carbon emission, CO_2 and greenhouse gases, GHG. Other environmental issues considered are energy payback time (EPBT), toxic emission, resources of raw material, health and safety risk. [1] Today, the renewable energy industry is relatively small-scale in most European countries, when the majority of energy source is still based on non-renewable sources such as fossil and nuclear power.

Manufacturers of renewable energy devices are facing a dilemma with most energy supplies being non-renewable sources, and this will increase the energy payback time (EPBT). A photovoltaic system manufactured by non-renewable energy faces difficulties to compete with PV-system manufactured by renewable energy, which gains low EPBT. Reduced use of non-renewable energy in supply of products and services has given less carbon emission and very low or no toxicity. [2] The energy supply has become in a country's interest, when this industry often targets an international market and therefore needs a low EPBT to get a strong position in the market of photovoltaic devices. With PV being one of the main options of renewable energy, a strong development has taken place to cut energy use in relation to this product and its manufacturing. Different studies have been carried out since 1990 to clarify the complexity with production and how the energy payback time, EPBT reflects on the PV-device. [3] The EPBT indicates performance by considering energy generated against energy used (primary energy) during a product's life-time. [4,5,6] The energy use regarding the total energy input (manufacture, installation and maintenance) divided by generated energy through a product's life-cycle gives EPBT= E_{input}/ $E_{generated}$. [2,5,7,8,9] Energy use regarding manufacturing relates to areas such as mining, treatment and

delivery of raw material; energy consumed during fabrication of a PV device and energy required to assemble the PV module. The energy payback time, EPBT is also expressed in numbers of years required to generate same amount of energy as used to manufacture a device. This is done by energy used divided by the sum of energy generated per year minus energy used for maintenance during a year, $EPBT= E_{input\ (material+\ fabrication+\ installation+\ recycling)} / E_{generated/\ year} - E_{(operation+\ maintenance)/\ year}$. The EPBT is often used as a method to measure performance of a photovoltaic device. [6]

Whether or not the energy payback time, EPBT is correct to use has been discussed [5,6] when options such as energy yield ratio, EYR [5] and electricity production efficiency, EPE [6] have been suggested as a more applicable way of expressing performance of a PV-system. Both energy yield ratio, EYR and electricity production efficiency, EPE are similar by including the maximum operational capacity of a PV-system, while EPBT has the disadvantage by using a set lifetime between 10 to 30 years [5], which becomes more like a guarantee for operational time than a PV-system's real capacity. The set lifetime is often much lower than a device can operate, whereas energy yield ratio, EYR and electricity production efficiency, EPE consider a device's total operational time by including enhanced time by additional maintenance and replaced parts. [5,6] EPBT does not include the energy generated after set time ends, which both EYR and EPE do. Energy return calculated with energy yield ratio, $EYR= E_{gen}L_{pv}/ E_{input}$ is given by energy generated, E_{gen} multiplied by the PV module's lifetime, L_{pv} divided by total energy used for the device, E_{input}. [5] Electricity production efficiency, EPE is based on same principles as EYR by using formulation $EPE= E_{gen}(lifetime)/ E_{mat}+ E_{fab}+ E_{ion}+ E_{elm}$, where energy generated during a life time is divided by energy used (material, fabrication, installation and end-life management) during a product's entire life. [5] Presently, energy payback ratio, EYR is used only by some [5], when most studies related to this work use energy payback time, EPBT. Therefore EPBT will be the method used in the discussion to follow.

Conventional silicon crystal solar cell with framed panel has a high EPBT due to high material and energy use, where the main reasons are framed module and large quantity of silicon. The processing of silicon wafers takes a large quantity of raw material to gain the high purity of silicon required, which increase the production time and higher energy use as a result. Thin film has proven a strong option with much lower material and energy use than crystalline silicon. [10,11] Introduction of silicon thin film has cut energy use and emission, which resulted in a lower EPBT. It was found [12] that silicon thin film with nanocrystal content had higher energy and gas use than a

cell design of triple-junction amorphous silicon, which related to the extended deposition time for the nanocrystal deposition. This proved the importance of having as high deposition rate as possible for nanocrystal thin film without damage the thin film quality. A life-cycle assessment for a photovoltaic device of amorphous silicon thin film requires the energy use from raw material, manufacturing and recycling and the transport during the process. The different areas such as material, manufacturing, and recycling contain several sub-groups such as raw material refining and production of the pure material, with manufacturing referring to fabrication and assembly of a device, and recycling referring to separately made devices and return of the material to its own industry and thence to a new one. [6] Development of these analytical tools has raised a question, how to consider the human factor and social life in relation to a product's life-cycle. This has been discussed in relation to people´s need of transport and the use of facilities during manufacturing and maintenance of a product. This is still in debate and no guidelines or standards have been introduced. [2]

The energy often considered in the assessments and calculation of energy input is primary energy, which relates to the energy used in direct relation with manufacture. Primary energy use is often given in megajoule (MJ), which relates to a device output power in kW over a period. [6,13] Relation between energy input in kWh (kiloWatthours) and MJ is 1kWh= 3.6MJ. [11] The quantity known as kWp is the maximum or "peak" power generated by a device operating at its highest efficiency. Payback time in years is given by dividing the total energy used with generated energy per device and years of operation. When calculating the total energy input, the BOS, balance of system can be included. BOS relates to components such as electrical connections, frame, mounting and installation of a PV-system. [6] The energy use for an amorphous thin film device refers to different areas such as fabrication of the module, BOS, frame and inverter which is illustrated in figure 4.1.. [2,11,14]

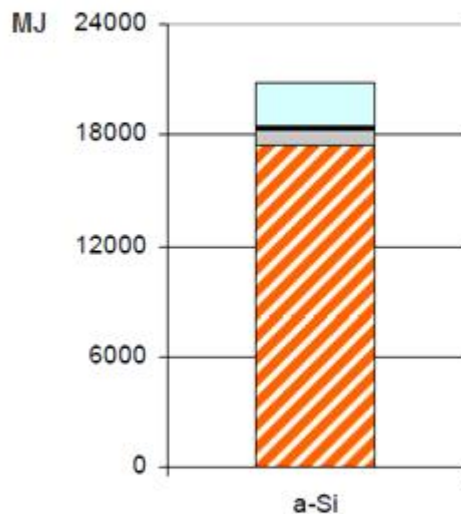

Figure 4.1. shows the total primary energy (MJ) input for amorphous silicon thin film per module kWp and the proportions the different areas have. The largest contribution is to process the thin film cell followed by energy for BOS, frame and inverter. This present work uses neither frame nor inverter, but can help to give an understanding of energy required for a process. [14]

Different photovoltaic designs and systems have been developed as a replacement of the traditional silicon crystal device due to its high silicon use and production cost. This work focuses on depositing a silicon thin film with amorphous structure and some crystal growth directly on a textile substrate of woven polyester. The energy emission related with this product has information collected both from the textile and semiconductor industries. The semiconductor industry has more information regarding the environmental management than the textile industry, although this information is not always applicable, when it is difficult to apply given information directly in connection with the product discussed in this work.

International Organisation for Standardisation, ISO has given guidelines through Life-cycle assessment, LCA [5,15,16] and its impact, LCI, which are tools to assess and evaluate material and energy use in a manufacturing process. Combination of Life-cycle assessment, LCA, and Life-cycle impact, LCI gives a systematic way of monitoring the input and output of energy and material use and quantifying the environmental impact during a product's life-cycle. [2,5,15] LCA helps in choice of process method, strategy and marketing of a product [2,15,16,17] and can be divided into four stages such as definition, analysis, impact and conclusion of the overall outcome. [2]

LCI is an environmental management tool with focus on the environmental impact and total energy use, which can quantify emission, toxicity and global warming. [2] Together with these two standards a third is applied, Life-cycle inventory that considers the financial aspect of used energy. [16,17] Mostly LCA and LCI (impact) are combined, which provide a good picture of the environmental burden for a product, but also a financial aspect. [10,18] A problem with LCA is not the assessment itself, but to collect the information required for the study, when the energy source is often difficult to define. The energy and material use regarding a LCA study is collected from different stages such as raw material, processes, transportation, manufacturing, use and waste management (figure 4.2.). [19] The assessments regarding the environmental management take time and mainly large companies have possibility to do them. [15]

LCA within the textile industry has proven more difficult, when same kind of industry can provide very different values regarding energy use related to a product and manufacturing. The difficulties can be due to many machines and processes within the textile industry being based on old methods, but also the quality of textile can vary from time to time in performance during manufacturing. [15,19,20,21] The textile industry has continuous pressure to reduce the energy use and emission, when this industry has a high production rate and a high quantity of chemicals, which results in high emission from solvents. Chemicals are found in most process stages such as wash, dye, coating and lamination etc. An increased awareness from the consumer wearing the garments close to the skin has pushed for use of fewer chemicals, which has led to a study [22] defining customer's requirements and how this refers to LCA and LCI (impact) and possible changes to process such as coating of woven polyester. The aim of the study was to address a coating method, which reduced the emission. [22]

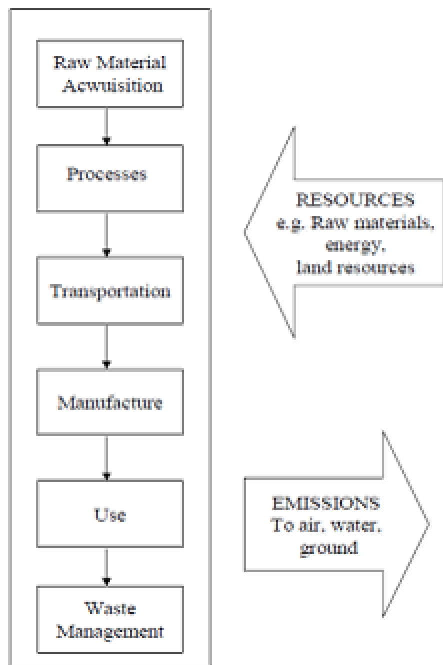

Figure 4.2. is a suggestion of a life-cycle model, which considers the material and energy input with waste and emission through the main production line. [19]

The semiconductor industry has applied LCA with the target of reducing EPBT and emission for photovoltaic devices. Recent development of silicon thin film has resulted in less EPBT and GHG (greenhouse gases) compared with conventional silicon crystal panel, even though thin film has lower efficiency than silicon crystal. The main reason for the low EPBT for thin film is the large reduction through the manufacturing of thin film such as raw material and process time. [23] A comparison with amorphous silicon thin film with 100% amorphous content and amorphous silicon thin film with nanocrystal growth, shows that the film with nanocrystal content had higher efficiency and allowed smaller module area than 100% amorphous content. [24]

Material for photovoltaic production is explained in stages from start to finish by material extraction, transport, manufacture supply service, and products for the main production line, assembly, installation, disassembly, deconstruction and/or decomposition. [2] From 1990 there has been concern about developing a recycling-route to most types of industries, when a good recycling route reduces the EPBT. [25] This route can either be partly or completely recycled back into its original industry. [19]

4.2. Standards and regulations

The International Organization for Standardization, ISO introduced in 1993 the first standard for environmental management (ISO/ TC 207), which later developed into ISO 9000. ISO/ TC 207 comes as a result from the meeting in Rio de Janeiro, 1992 where the world agreed to environmental changes and development of sustainability. [18] ISO 9000 regards Quality management and quality assurance, when ISO 14000 is known as environmental management. Both ISO 9000 and 14000 helped to evaluate a process and a product in relation to energy emission, efficiency and recovery time. With the two standards being analytical a third standard ISO 19000 was introduced, auditing environmental and/ or quality management. This standard helps recognize an evolution of a problem. [18] The three standards have together supported a more sustainable process and production within and surrounding environment. [18] These kinds of assessments are often applied in larger companies due to being very time consuming, when it covers from raw material to the exit of main production line. [5,16,19]

ISO 14000's LCA (assessment) and LCI (environmental impact) are often known as *PLAN-DO-CHECK-ACT, PDCA.* PDCA stands for Plan "how to implement it", Do "how to do the study and assessment", Check "the outcome of the assessment" and Act "documentation and declaration of the outcome". [18] The ISO 14000 is divided into sub-standards from ISO 14040 to 14044, where 14040 and 14041 refers to LCA with focus on material and energy use and emission, when 14042 and 14043 is LCI. [2,3,5,16] The standard 14040 helps to monitor and reduce the environmental impact from a product's process and service. [16,18] Recycling routes have been added into LCA in the later edition of ISO 14044. The European project TASK 12 has aimed "to quantify the environmental profile of electricity produced with PV system". [16]

LCI refers to the environmental impact of a product during its life-cycle, which includes process and maintenance. The main concern is to quantify the damage by expressing it in number of treatments required from a natural source such as water and air to return without damage or potential impact of climate change. [5,16] The impact is given in time to clear the damage either by a period of 100 years or infinite time. [2,16] With the photovoltaic process still using energy from non-renewable sources, the potential risk for Global warming, photochemical oxidation and acidification needs to be considered. [14]

Öko-/ oeko-Tex® Standard is a common certification within the textile industry and was developed by a request from the consumer. The first eco-labels on garments were the brand's own labels, which stated "ecologically produced". With increased number of eco-labels rose a need for a uniform system such as Öko-/ Oeko-Tex, which was introduced in 1990.

Oeko-Tex® Standard 100 was soon internationally recognized to address the risk of health for the public. This standard focused on identifying potential harmful substances in chemicals, production, process content and waste in relation to people's health. This standard was divided into four groups for textile application;
1st- children/ babies up to 3 years old,
2nd- textile, direct contact with skin,
3rd- textile, which is not intended to have direct contact with skin,
4th- textile for furnishing, floor and wall. [26]

Additional standards were later published, first Oeko-Tex® Standard plus100 and later Oeko-Tex® Standard 1000 with focus on the environment. Oeko-Tex® Standard plus100 aimed to show how the human and the environment responded to an increase of production capacity. Standard plus100 was divided into four parts:
1st- how production affected environment,
2nd- how textile and chemicals in a product or process affected human health,
3rd- how garments and textiles in use affected the environment.
4th- an ecological aspect regard recycling and recovery of disposed textile. [26]

Oeko-Tex® Standard 1000, the latest addition focuses on the environment around all process stages in a fabric and garment manufacture. This standard contains reduction of energy use, treatment and recycling of waste and air-pollution, safety at the workplace and no child-labour. Certification of Oeko-Tex® Standard 1000 is only given to companies, who have environmental management in use and are already certified to Oeko-Tex® Standard 100. [26]

4.3. Energy emission

4.3.1. Energy returns related to design of device and location

Energy payback time, EPBT reflects on design of a device, cell efficiency, location of manufacture and operational location. [23] The country where the PV-device is manufactured has a great influence on the EPBT, when some countries in Europe use renewable energy supply such as wind, hydro and photovoltaic, which gain lower EPBT compared with countries using conventional energy sources of fossil fuel. [3,17,27] Countries aiming to develop and manufacture renewable energy need to consider a grid supply of renewable energy to produce new renewable products, which are strong and competitive with a low EPBT. [17] Location of manufacture of PV-device is important in aspect of transport between manufacturer and sub-contractor, when this reflects on EPBT too.

Energy payback time, EPBT is based on energy use against generated electricity, G, G/m^2. Generated electricity is given by multiplying solar insolation (I), conversion efficiency (E) and performance ratio (PR), G=I x E x PR. Performance Ratio, PR is given by divide actual performance with the theoretical one. The performance ratio can change by temperature due to altered sunlight or shading or eventual defects in the device. Defaults/ performance value is suggested for different designs and locations. [17] Multiplying the generated electricity (G) by the expected life time (L) of a product will give the total electricity produced during a product's life time. [3] A product's life time is often based on either 20 [14] or 30 [3,11,16] years, but can be quoted as low as 10 years. [5] The life-time depends on the quality and efficiency of the cell. [15] Efficiency is defined as the ratio of light converted to electricity over the incident light. [23]

The EPBT is also influenced by location of operation, when solar irradiation and operational direction are considered. Three thin film solar cell structures (CIGS, a-Si and CdTe) in three different PV-designs were compared in aspect of operational location and both quality and design played a part, when roof fitted panels of amorphous silicon thin film gave the lowest EPBT. The same PV-design was evaluated at three locations such as solar belt, south and mid of Europe (see table 4.1.). Solar belt had the lowest EPBT, followed by the south of Europe with a slight increase and then mid Europe with highest EPBT. [14]

Table 4.1. explains how location and different PV-system reflects on the EPBT in years and the average EPBT in years for the different locations. [14]

Location	Application	EPBT a-Si	EPBT a-Si
Central Europe (Frankfurt)	Power modules (UCTE*)	2,6	2,3
	BIPV roof integrated (UCTE*)	1,8	
	Mobile (Diesel Generator*)	2,3	
Mediterranean area (Rome)	Power modules (UCTE*)	1,9	1,6
	BIPV roof integrated (UCTE*)	1,3	
	Mobile (Diesel Generator*)	1,6	
Solar belt	Power modules (UCTE*)	1,5	1,3
	BIPV roof integrated (UCTE*)	1,0	
	Mobile (Diesel Generator*)	1,3	

Both PV-design and location influence the EPBT, however the PV-design of thin film amorphous panels showed the greatest influence. The electricity provided (kWh) per design of the PV-system ($1m^2$) in relation to the location is given in table 4.2., while table 4.3. compares the panel system and their performance of generated electricity of $1m^2$ panel for 20 years. [14] Tables 4.2. and 4.3. show how location and PV-design influence the performance and the energy generated during a life-cycle. [14]

Table 4.2. electricity output in relation with device design and location per year. [14]

a-Si	$kWh/(m^2*y)$		
Installation	**Power plant**	**roof integrated**	**mobile**
Central Europe	61,4	59,6	57,8
Mediterranean	85,3	82,7	80,2
Solar belt	108,1	104,8	101,6

Table 4.3. energy generated during a period of 20 years. [14]

a-Si	20 Years $[MJ/m^2]$		
Installation	**Power plant**	**roof integrated**	**mobile**
Central Europe	4421	4291	4162
Mediterranean Area	6142	5954	5774
Solar Belt	7783	7546	7315

Other studies [10,13,14,16,27] looked at operational location and solar radiation and the effect of irradiation ($kWh/m^2/yr$) and irradiance (W/m^2), which reflected on cell

efficiency and indirect EPBT. An average value of solar irradiation for north, mid and south Europe and solar belt was suggested. The values given were 900kWh/m^2/yr for Scandinavia, 1200kWh/m^2/yr for Frankfurt, 1700kWh/m^2/yr for Rome and 2200kWh/m^2/yr for solar belt. [8,13,15] A value of 1000kWh/m^2/yr was suggested for mid Europe, which was lower than often quoted. [1] The EPBT was calculated for location of mid Europe being between 2.8 and 4.6 years and for south Europe from 1.7 to 2.7 years. [1,10,13,27]

4.3.2. Design of solar device and its manufacturing process

Product development of renewable energy needs a strict policy for material, energy use in relation with process, maintenance and recycling to meet stated requirements in the environmental management of ISO and Oeko-Tex. Developments of 2nd and 3rd generation PV are mainly thin film design with different cell content (figure 4.3.). The new PV-systems are often compared with conventional silicon crystal in relation to performance and environmental impact such as EPBT. Silicon thin film with amorphous structure has already proven to use less energy and has a low material cost compared with conventional silicon crystal cells. [11] This film has also reduced number of process stages and quantity of raw material compared with conventional solar cells. [10,17]

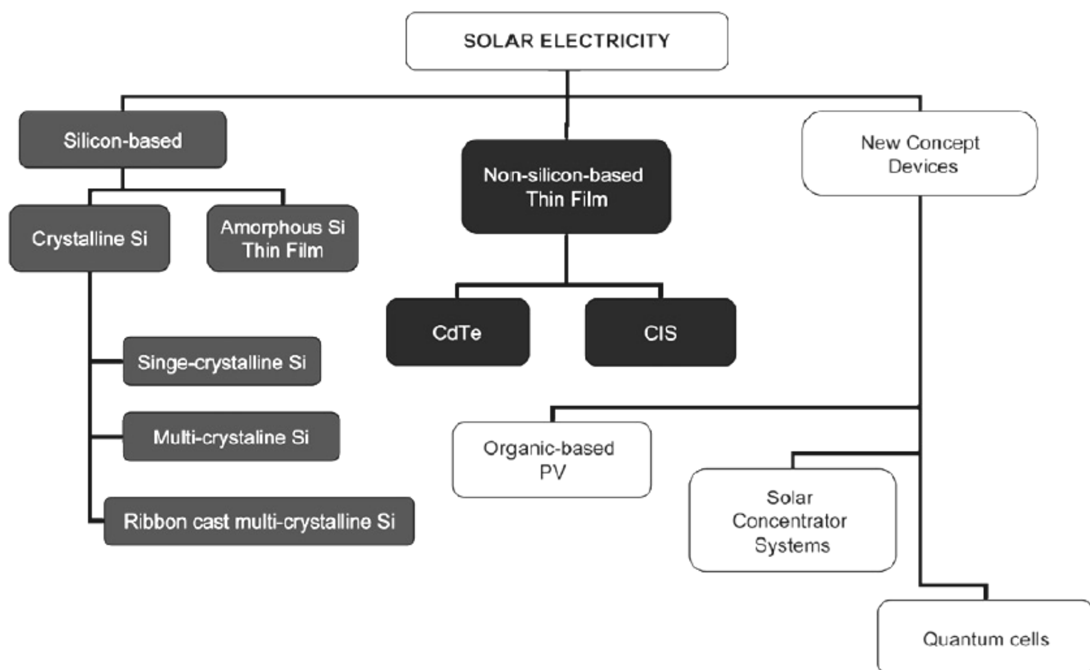

Figure 4.3. the different solar designs available today. [10]

The disadvantage with silicon crystal and wafer design is the large use and loss of material, which has encouraged developing of high purity silicon with reduced material and energy use. The manufacturing of silicon wafer starts with mining and refining to reduce the silica content and increase the purity of silicon. This is followed by the growth of crystalline ingots of silicon into high grade wafers which are polished and etched. Thereafter n-type dopant is incorporated for emitter formation. On the wafer there is a screen-printed back contact of aluminium and a metal grid front contact. The wafer is processed with plasma enhanced chemical vapor deposition, PECVD to modify its surface by a dielectric deposit for passivation and antireflection. Last is the assembly of the module such as encapsulation of the cell and the different process stages involved: energy and material use are shown below (figures 4.4. and 4.5.). [28] The handling of raw material such as preparation and process routes from mining to assembling of a PV-system is often the same for different designs of silicon solar cell. It was quoted that thin film needed only 10% of the silicon that is usually required for a silicon wafer. [11]

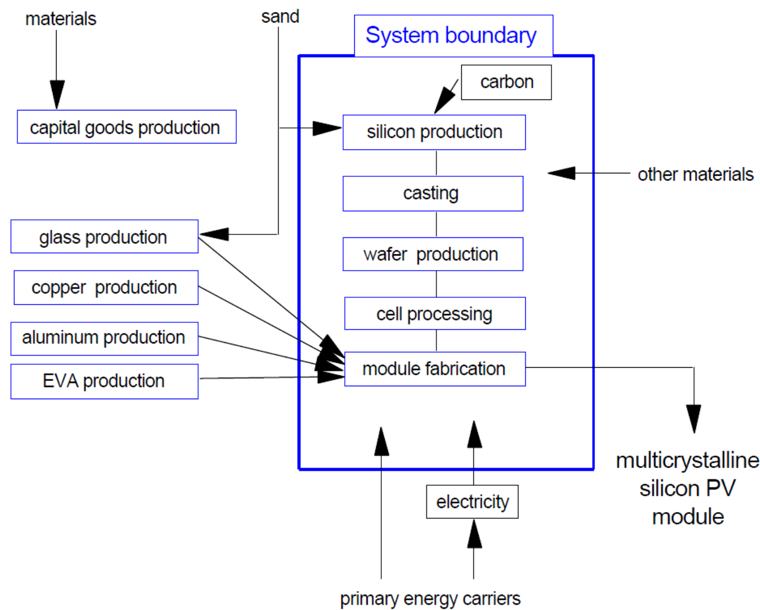

Figure 4.4. a process chart of silicon process of conventional solar cell and its material use. [28]

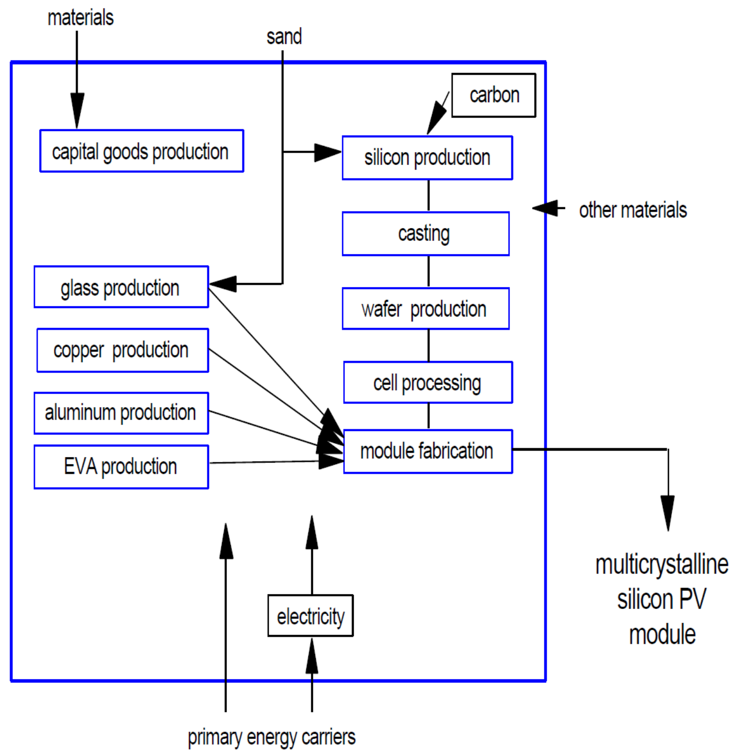

Figure 4.5. a process chart of silicon process of conventional solar cell and its energy use. [28]

4.3.3. Thin film process

Thin film semiconductor is much thinner than silicon crystal and has the advantage of being both light and flexible and can easily be integrated into different designs, while conventional crystal silicon is heavy, stiff and needs a frame. [23] A disadvantage with the amorphous silicon structure is increased light-degradation, which can be up to 30% during 1000 hours of use. [13,16] An attempt to reduce light-degradation has been by integrating crystal growth such as micro- or nano- crystals into the amorphous structure, although the optimum mixture is not known. The mixed structure has proven reduced light-degradation, by a more stable structure, which resulted in increased light absorption and higher efficiency. [12,24] Films with crystal growth in amorphous matrix are mainly under development, which means the EPBT, energy use and emission are mainly based on pilot runs. The drawback with nanocrystal growth is the high energy use required for the increased flow of hydrogen and extended process time required for the crystal formation. [12] Amorphous and nanocrystalline thin films were compared (table 4.4.), which showed how nanocrystalline thin films required a smaller module

area by having higher efficiency than amorphous silicon thin films, even though nanocrystalline structure has higher energy input. [24]

Table 4.4. gives an estimated value for growth rate for present and future designs of amorphous and nanocrystal thin film. High efficiency through high growth rate without increasing the energy use was possible by combining the right gas mixture. [12]

	a-Si, current	a-Si, future	nc-Si, current	nc-Si, future
Deposition rate (nm/s)	0.1–0.3	0.2–0.4	0.5–0.8	2–3
SiH_4 Concentration (%) in H_2	2	2	1	4
SiH_4 utilization (%)	20	20	20	80

Plasma enhanced chemical vapor deposition, PECVD is the most common process for silicon thin film. This process means environmental challenge, when increased energies are required for the process, but also the gases used for deposition and cleaning. [12,13] Most thin film processes of large scale are done by roll-to-roll method, which means constant power (kW), gas mixture and flow-rate and substrate temperature to provide a steady condition in- and out- side the chamber. A study [12] compared the energy use between two chambers powered by radio-frequency PECVD (table 4.5) and the sample size used was 5600mm x 400mm. [12] The averages of these values are given too, which can be compared against a single chamber used in this work.

Table 4.5. gives different values of energy use required for the two chambers, but also an average, which gives an approximation for plasma process in one chamber. [12]

Component[a]	Reactor 1 (%)	Reactor 2 (%)	Average
	Total = 6.8 kW	Total = 7.5 kW	7.15 kW
Heater	14.7	8.0	11.0
Vacuum pump	52.9	56.0	54.5
Plasma generation	8.8	18.7	13.5
RF generation for cleaning[b]	4.4	4.0	4.0
Water handling pump	13.2	NA	7.5
Miscellaneous	5.9	13.3	9.5

Life cycle analysis, LCA related to the semiconductor industry is not always consistent in the way of assessing different areas and stages in a product's life-cycle. The supply chain of a product has proven a great influence in a product's energy use and carbon emission. Calculating the impact is not always easy or straightforward, when the supplied energy source is often unknown, whether non- or renewable energy. Manufacturing semiconductors involves a large number of chemicals and most gases in the semiconductor industry use high purity. The work and process required to produce high purity gases will increase the energy and carbon emission. Silane gas of high purity increased carbon emission by ~25% compared with standard grade silane and the extra processes for high purity increased the total impact 10 times. Similar scenario was found for other common high purity gases such as argon. [29]

Production of amorphous silicon thin film has resulted in a global warming potential, GWP with high carbon emission, CO_2. The global warming potential is quantified by a gas in kg equivalent to a known gas such as carbon dioxide, CO_2. Green-house-gas (GHG) emission can be expressed in kg of CO_2 equivalent per kWh, but note that most CO_2 is given in gram.

Studies [30] have tried to link energy use from Energy payback time, EPBT to carbon emission, CO_2 and an EPBT of 3-6 years was equal to an emission of 39-110g CO_2 equiv/ kWh [3,5], when an EPBT of 1.7-2.7 years related to 30-45g CO_2 equiv/ kWh. [3,5,16] A study concludes, the lowest carbon emission of photovoltaic device per product life-time is the actual use, although an exact value of carbon emission during a product's life-cycle is very difficult to give. [29] A study [1] estimated that, the average PV device had a carbon emission, CO_2 of 25-32g/kWh. However the devices in the future will be reduced to 15g/kWh and classified as low-carbon devices. [1,13]

Instead of expressing the global warming potential, gwp in carbon emission, it can be converted to a photochemical oxidation potential, POCP (Ethylene), Acidification Potential, AP (Sulphur dioxide, SO_2) or Eutrophication Potential, EP (Phosphate), which all are given in kg. [14]

Gases for deposition of silicon thin film are silane, SiH_4, hydrogen, H_2 and dopants (phosphine and diborane). A study [31] was carried out to analyse exhaust gases and found how much of the silane did not react during deposition, which left non-reacted species coming through the exhaust system. With silane being toxic and flammable in

the air, it was important to dilute non-reacted species. Hydrogen dilution with silane is a common combination to provide a good deposition and crystal growth. To make gases such as silane and hydrogen less damaging, a recommendation was to bring the gases through a combustion system with cooling of either air or water before the emission was filtered from heavy metals. [11,31] Common cleaning gases for large plasma systems are SF_6 and NF_3, which have a high impact on climate change. NF_3 was 17200 times and SF_6 was 22800 times stronger than carbon emission based on a 100 years period. However, NF_3 had potentially higher effect on the greenhouse emission due to reduced cleaning effect of certain depositions such as amorphous structures. Due to SF_6 being related to fluoro-gases, restrictions are in place of use and instead NF_3 has been applied. The increase in use of NF_3 has reflected on the green-house effect by becoming seven times higher volume use from 1995 to 2008 due to high quantity of gas needed. [22,24,30,31]

4.4. Energy use and waste in textile and semiconductor process

4.4.1. Waste related to process of silicon thin film on to woven polyester

By having difficulties in finding sufficient information regarding carbon emission and energy use from a manufacturer producing the combination of silicon thin film deposited on textile, it was necessary to combine sources of data and guidelines from different textile and semiconductor industries to provide an estimation of energy use for silicon thin film on textile substrate. The different process stages, energy and material use are related to a textile wet-coating process such as polyaniline coated textile (figure 4.6.). [32]

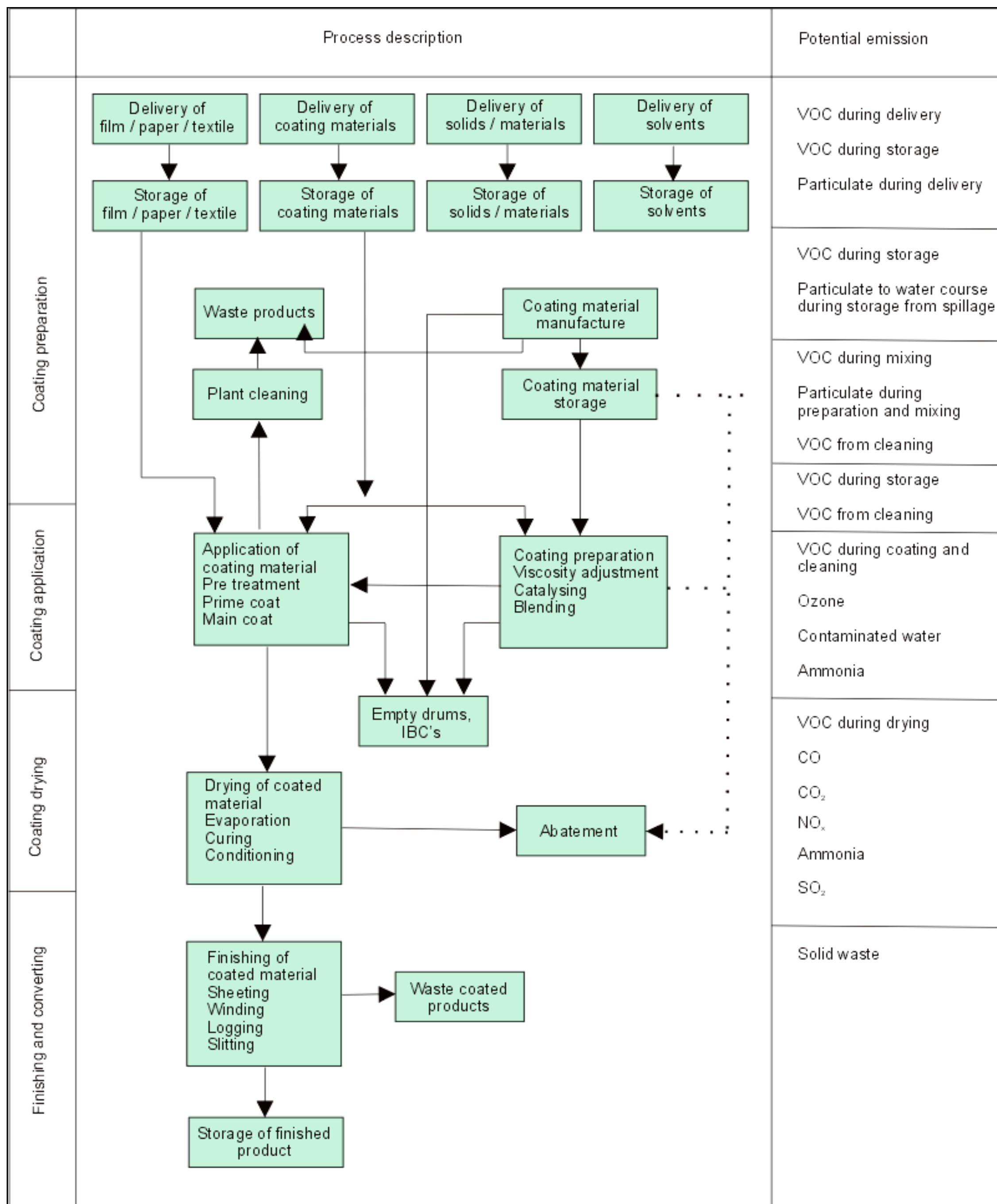

Figure 4.6. explains the process stages involved for wet-coat of textile. [32]

Information for waste and emission to air, land and water regarding textile coating with solvent based mix is described in an older edition from DEFRA [33], which also discusses waste management related to this process. Noise and odour has been ignored after being constant in this kind of process and industry. The tables below contain data for emission and waste related to the semiconductor and textile industry. The textile industry and its processes are defined by waste and emission more than the

semiconductor industry. Transport and handling of raw materials is considered as having the same environmental impact for the two manufactures. Table 4.6 gives a summary of process stages and the waste and emission considered for each stage and industry, while table 4.7 defines type of waste and emission considered in the process of silicon thin film on woven polyester. [32]

Table 4.6. summary of process stages and the waste and emission. [32]

STAGE	ACTION	RESULT IN	TEXTILE	SEMI-CONDUCTOR
Delivery	Incoming goods.		X	
Cleaning	Clean substrate with solvent or similar to incresae surface adhesion.	Emission& Waste	X	
Mixing/ Preprartion	Water based coat (polyaniline).	Waste	X	
Coating method	Direct coating, knife-on-roller.		X	
Drying/ Curing	Heat.	Emission	X	
finishing/ Inspection	Inspection of coated material before semiconductor process.		X	
Evaporation	Aluminium, back contact.	Waste		X
PECVD	Silicon layers, n-i-p.	Emission& Waste		X
RF-Sputter	Indium Tin Oxide, ITO, top contact.	Emission& Waste		X
Ink/ Print	Connect top and bottom contact and the cells.	Waste	X	
Coat/ Laminate	Encapsulation, Laminate a film or spray-coat. Laminate uses less energy.	Emission& Waste	X	X
Finishing/ Packaging	Inspection before despatch.	Waste	X	X

Table 4.7. waste and emission within process of silicon thin film on woven polyester. [32]

ACTION	ENERGY	AIR	WATER	WASTE	LAND
DELIVERY	NS	VOC	RoC	GRM	PR
CLEANING	NS	VOC	RoC, Metals	GRM	PR
MIXING/ PREPARATION	Large				
COATING APPLICATION	Large	VOC	PR	GRM	NS
DRYING/ CURING	Large	VOC	NS	NS	NS
FINISHING/ INSPECTION	25% of total	NS	NS	GRM	GRM
INK PRINTING	NS	NS	NS	GRM	NS
FINISH, INSPECTION & PACKAGE	NS	VOC	NS	GRM	NS

NS- No Significance/ RoC- Release of Contamination/ VOC- Volatile organic compound/ GRM- Generated Rejected Material/ PR- Possible Release.

4.4.2. Recycling of photovoltaic device

Recycling is important, when a correct recycling route reduces energy use and emission and the EPBT (figure 4.7.). No recycling or a wrong design of a recycling system will increase EPBT. Wrongly designed processes will often reflect on increased number of process stages, which add transport and energy use. [14] A way of reducing a product's EPBT is by using recycled material, which will reduce the EPBT. [6] There are two types of recycling, closed loop where the recycled product returns as raw material into its original production and open loop, when the recycled product ends up in a new process and product. [19,25]

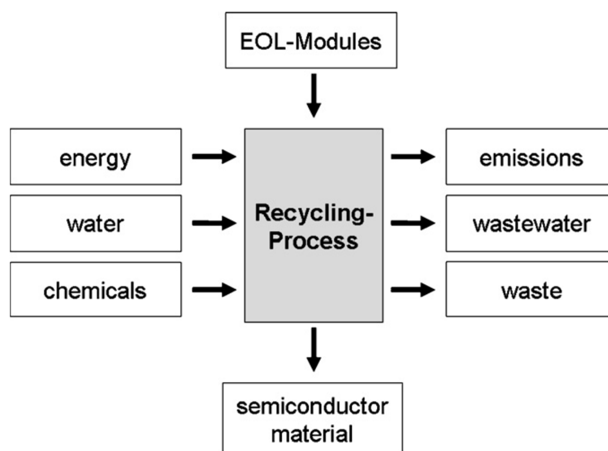

Figure 4.7. water during recycling process for material and energy use needs be considered. [25]

Different projects such as SENSE [14] and RESOLVED (www.resolved.bam.de) have looked at ways of developing the recycling of PV-systems, when recycling needs to be adjusted for different cell materials. Thin film of amorphous silicon needs fewer stages than crystal silicon with framed module. Recycling of PV-system can be divided into three main areas; separation of the PV-module, removing protective film/ sheet and semiconductor layer, and recovering metals from the frame. [14,25] The big challenge is to separate the different layers, when the frame has proven easier by being detached and recycled as solid waste. [6] Recycling of thin film is illustrated as two options (Figure 4.8), one (RS1) used for PV design which can be stripped down, while the other option (RS2) is partly separated, but needs to be crushed part of the recycling. Observe, the recycling route below is considered for CIS and CdTe, but for a-Si thin

film RS1 is applicable. The recycling shown on the other picture (Figure 4.9) is designed in agreement with an LCA study. [25]

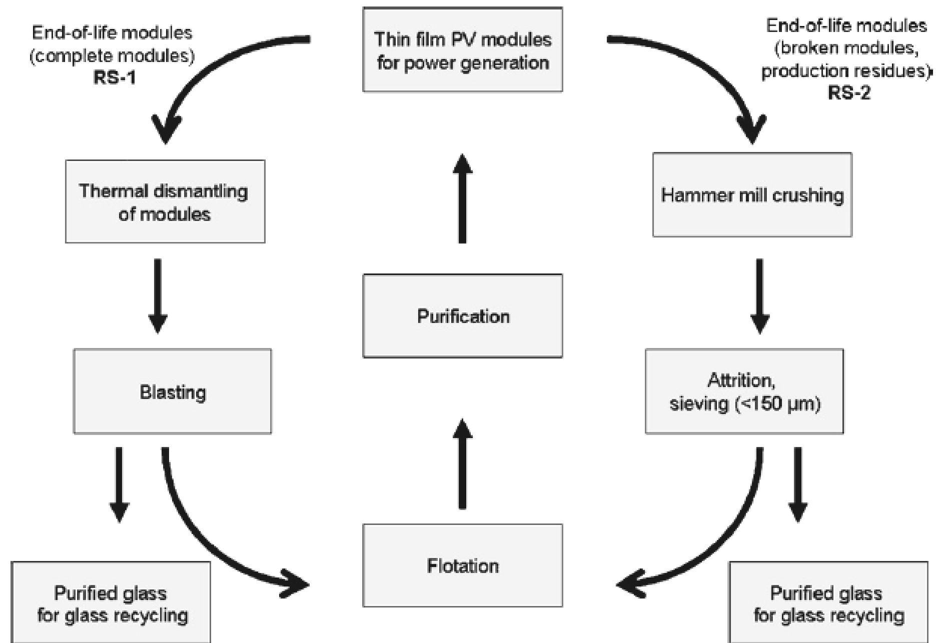

Figure 4.8. recycling of a complete PV- system and partly recycled, which requires parts being crushed. [25]

4.4.3. Energy use related to photovoltaic device

Energy consumption, the total energy use refers to all process stages in the main and sub-production. The energy use related to main production line is divided into sections such as material, E_{mtl}+ manufacturing, E_{mfg}+ installation/ maintenance, E_{use}+ recycling, end-of-life management, E_{elm}. All values of energy use are added, which gives the total energy input, E_{in} of a product's life-cycle ($E_{in}= E_{mtl}+ E_{mfg}+ E_{use}+ E_{elm}$). Each of the main process stages such as manufacture, operation (installation), end-of-life managements (recycling) can be divided into sub-groups. Electrical energy is often converted into primary thermal energy. [34]

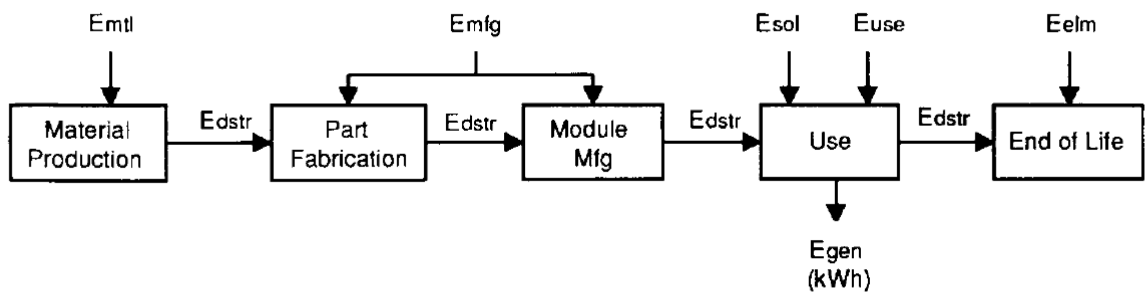

Figure 4.9. LCA diagram for a PV-system refers to energy use of a product's life-cycle with stages such as E_{mtl}- process of material, E_{mfg}- manufacturing, E_{sol}- insulation, E_{use}- required energy use, E_{elm}- end of life "recycling", E_{dstr}- distribution/ transport and E_{gen}- generated energy. [6,34]

Total energy output, E_{out} can be calculated either with or without Balance Of System, $E_{BOS\ loss}$, which refers to energy loss through transfer from a device to the grid. Energy output, E_{out} is energy gained from a PV-system, which is given by subtracting the Balance Of System, $E_{BOS\ loss}$ from generated energy, E_{gen}. Conversion efficiency, η of a PV-system is given by dividing total energy output, E_{out} with total energy input E_{in}. The ratio refers to the electricity gained from a cell. [34]

4.4.4. Manufacturing steps regarding silicon thin film on polyester weave

Most thin film studies are based on projects at development stage and not from an industrial scale and experience. This means much of the calculated data for a thin film

product's life-cycle contains error. [1] Therefore LCA data based on development work have been encouraged to introduce a default value of best and worst for the energy use. [23] Example of LCA for thin film process is given below (figure 4.10.). Thin film of amorphous silicon has low material use by being up to 100 times thinner than conventional silicon. [35]

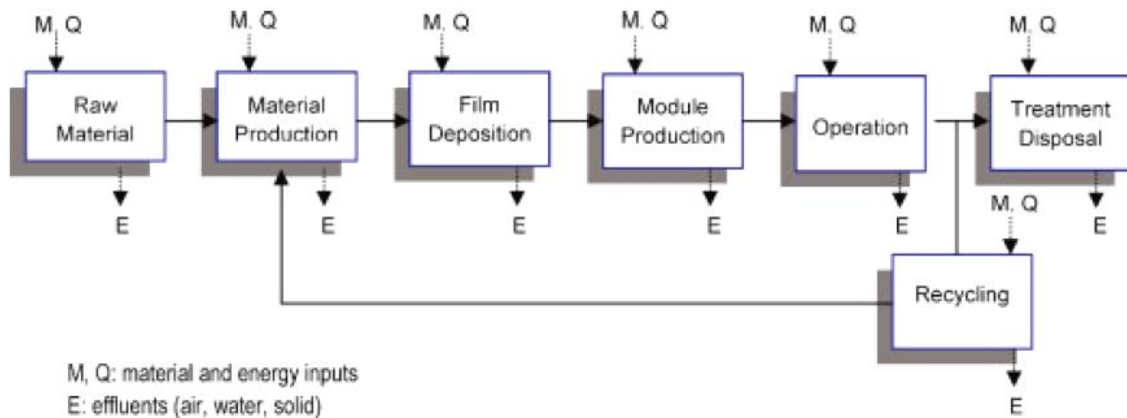

Figure 4.10. LCA with energy use for silicon thin film through its life-cycle. [12]

Standards Öko-/ Oeko- Tex® and ISO 14000 helped the textile industry to change process methods and reduce chemicals, waste water and energy use. Waste management helped address ways of cleaning and recycling the waste. Below is an example of process stages related to filament process (figure 4.11.) followed by process of and around weaving (figure 4.12.). [20] Polyester process has the option of having two monomers added either by using PAT, Purified Terephthalic Acid or DPT/ DMT, Dimethyl Terephthalate. The difference between the two monomers is the process route, when PAT is produced through a chemical process with Ethylene Glycol, EG added as a precursor. DPT/ DMT is instead produced in a condition with vacuum and heat, which refers to a higher energy consuming process and today less common than PAT. [36]

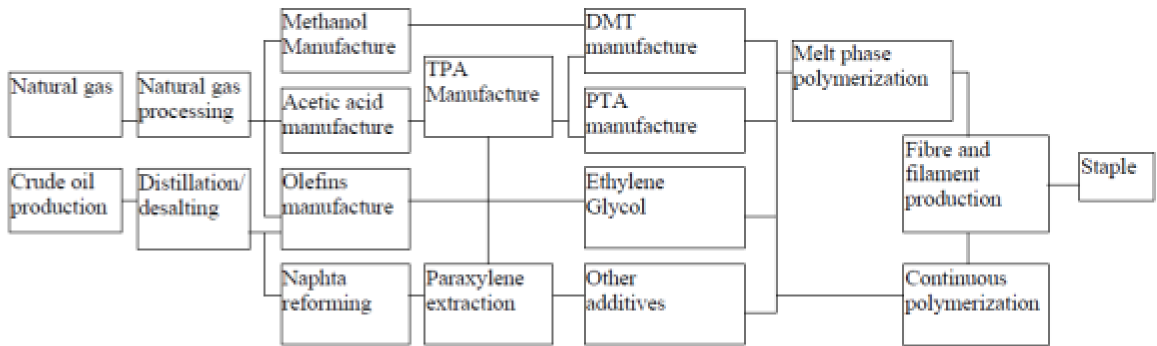

Figure 4.11. the different stages involved in extrusion of polyester filament, fibre. [20]

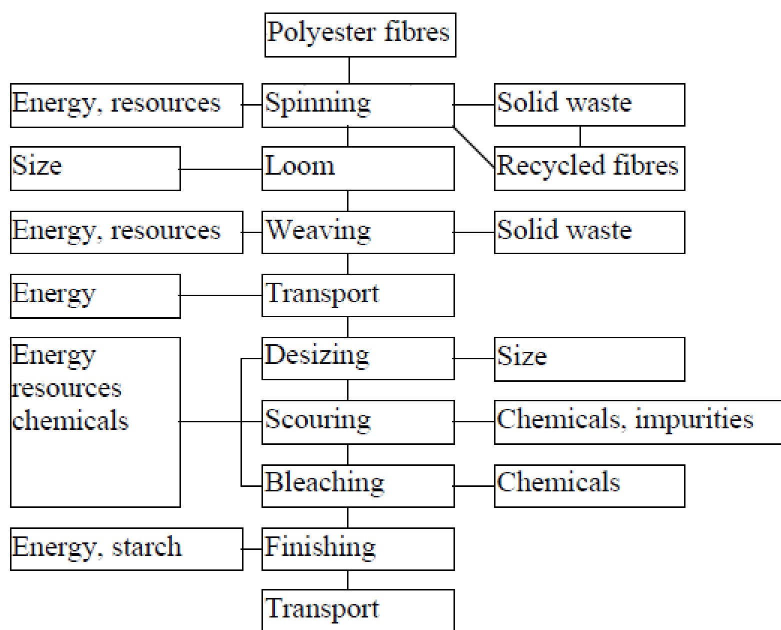

Figure 4.12. explains the stages involved in a weaving process. [20]

4.5. Energy use related to manufacturing silicon thin film onto woven polyester

The energy use related to this present work with silicon thin film on woven polyester includes processes from both textile and semiconductor industry (figure 4.13.). The processes related with the textile industry are from producing grains, to extruding polyester, through weaving to wet-coated textile. Thereafter an evaporated back contact is deposited onto the textile followed by required layers for a silicon thin film solar cell. The back contact does not necessarily have to be evaporated, instead a non-vacuum process such as wet-coat or printing can be used to apply a metallic back contact. Energy used in relation with semiconductor industry was easier to collect, although much of this data was based on studies regarding work on a pilot plant.

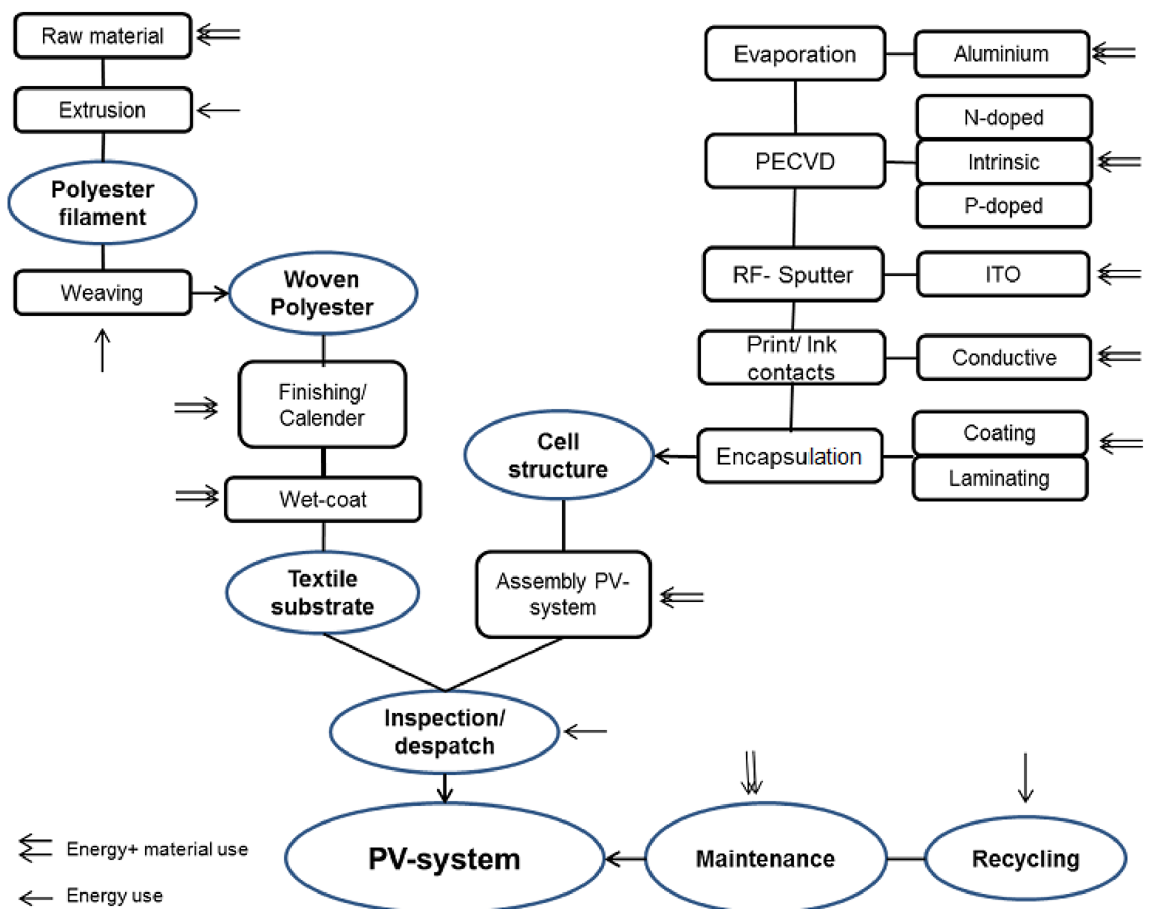

Figure 4.13. explains the different process stages, maintenance and recycling required for a life-cycle assessment for a photovoltaic device with silicon thin film deposited onto woven polyester.

With difficulties to get information regarding energy use for such specific production line as described in this work the given data from one source has not always been correlated with another one. Therefore estimation has been done to each process stage required, to give an approximate figure of the energy use applied. With the textile production having no complete LCA study published, information has been collected from different studies with certain focus on only parts of the process. The values given for the energy use related to textile process were often expressed as MJ/kg or MJ/Tonne and the information gained was based on non-renewable energy. [15]

4.5.1. Energy use required for woven polyester

The energy required to produce woven polyester is given below.

- Producing polyethylene terephthalate, PET grains needs 2MJ/kg (polyester). [15]
- Spinning of a fibre/ filament uses 94.7MJ/kg energy [15], when another study [21] gave energy use of 135MJ/kg to spin polyester.
- Weaving the polyester used 115.5MJ/kg. [15]

The textiles are often washed and dried after being woven to take off spin-finish, which often is applied onto a filament to make the spinning and weaving process easier. Drying of a textile after wash or finishing was quoted for hemp production, but helped to indicate the energy required to dry any fabric. Removing water mechanically from a hemp fibre was 2.3kg water/kg dried fibre. The drying of 1kg fibre (hemp) required an energy use of 3.6MJ/Tonne, which resulted in a use of 0.0036MJ/kg hemp. [21] Natural fibre has much higher capacity than a polymer based fibre such as polyester, although polyester today has been modified both in cross sectional design and its polymer chain to gain a higher moisture/ water uptake. A natural fibre such as hemp increases in diameter by ~45% compared to a polymer such as polyester with less than 5%. [37] These values helped to estimate the energy use required to dry polyester by knowing the energy (0.0036MJ) needed to dry one kilo hemp. To estimate polyester's swelling capacity a ratio with polyester against hemp (5/ 45) was multiplied with the energy use required to dry hemp (5/ 45x 0.0036MJ/kg), which gave the energy use required to dry polyester (0.0004MJ/kg).

4.5.2. Coating and deposition on textile substrate

Polyester weave

Polyester weave coated with water-based coat requires an energy use of 10.3MJ/m^2. The coated fabric increased by 20gram per m^2 due to shrinkage in the textile during cure and the extra coat weight gained by the two layers. Total energy use (10.3MJ/m^2) for coated textile (figure 4.6.) was divided into subsections such as textile material: 4.6MJ/m^2, electricity: 1.8MJ/m^2, fuel: 1.3MJ/m^2, chemicals: 1.9MJ/m^2 and transport/ packaging 0.7MJ/m^2. [38]

Plasma process

Plasma enhanced chemical vapor deposition, PECVD may be applied in roll-to-roll method to manufacture thin films commercially. [12] Earlier, table 4.5. gave energy use for plasma process and an average of the two chambers was calculated to be applicable to one process chamber, which is currently used for this work. This helped to estimate the total energy consumption of 7.15kW (kilowatt) and a percentage (%) of the different parts in the process using energy such as heater 11%, vacuum pump 54.5%, plasma deposition 13.5%, plasma clean 4%, water cooling/ pump 7.5% and miscellaneous 9.5%. However the frame is not included, as the thin film does not require this. [12] Frameless module was calculated for standard production of E_{mtl}+ E_{mfg}+ E_{dstr}, which gave a total energy use of 101.8kWh (366.6MJ). [34]

Energy use for the different depositions in a cell structure was estimated: [34]

Aluminium deposition,	30.3MJ/ module
Amorphous silicon deposition,	37.9MJ/ module
Transparent conducting oxide,	32.7MJ/ module
Encapsulation,	56.2MJ/ module

Estimation was based on module size of 119.4 x 34.3 x 3.8cm, which was converted into energy use per m^2:

Aluminium	73.93MJ/m^2	(30.3MJ/ [(1.194m x 0.343m) x 2.44])
Amorphous silicon	92.48MJ/m^2	(37.9MJ/ [(1.194m x 0.343m) x 2.44])
TCO	79.79MJ/m^2	(32.7MJ/ [(1.194m x 0.343m) x 2.44])
Encapsulation	137.1MJ/m^2	(56.2MJ/ [(1.194m x 0.343m) x 2.44])

The given values were used to calculate energy used for the device produced in this work:

- Aluminium, evaporated aluminium for back contact.
- Amorphous silicon, the n-i-p layers using phosphine, silane and diborane.
- TCO, transparent conductive oxide, sputtered indium tin oxide, ITO.
- Encapsulation (EVA), a polymer based encapsulation. [34]

By collecting and converting different information into correct units for energy use, it is possible to sum up a possible energy use for silicon thin film onto woven polyester. Energy used for different processes regarding this work is specified below.

Produce polyester filament,	94.4MJ/kg
Weaving the polyester fabric,	115.5MJ/kg
Drying the textile after wash,	0.0004MJ/kg
Wet-coat the textile,	10.3MJ/m^2
Evaporate Aluminium,	73.93MJ/m^2
PECVD of n-i-p layer	92.48MJ/m^2
RF-sputtered ITO	79.79MJ/m^2
Encapsulation, polymer	137.1MJ/m^2

The energy use regarding material construction is ~210MJ/kg, while the thin film cell needs 256.5MJ/ m^2 with encapsulation excluded.

Manufacturing of the woven polyester was converted into m^2 by multiplying the cloth (loomstate) weight of 0.250kg/m^2.

Polyester filament,	94.4MJ/kg x 0.250kg/m^2	=>23.6MJ/m^2
Polyester weave,	115.5MJ/kg x 0.250kg/m^2	=>28.9MJ/m^2
Total		52.5MJ/m^2

By converting the material to energy use/ m^2 gives as total of 309MJ/m^2, where 52.5MJ/m^2 relates to the material and 256.5MJ/m^2 to depositing the cell structures.

Estimated energy use of 309MJ/m^2 for amorphous silicon thin film on woven polyester can be considered in relation with Alsema [9], who evaluated amorphous silicon thin film by PECVD process with different substrates. Choice of substrate proved a great influence, when a combination of glass substrate and glass cover had higher energy use than a combination of glass and polymer film. The two samples with same cell

structure showed (table 4.8) how a combination of glass and polymer film gained a much lower EPBT. [9] Substrate choice of woven polyester (52.5MJ/m^2) is therefore shown to cut energy use in relation to conventional option such as glass substrate, which consumes energy of 150 to 200MJ/m^2. However the polymer based substrate has been estimated to an energy range of 20 to 50MJ/m^2, which means the maximum level of energy use is much the same as the polyester weave.

Table 4.8. the values show how energy input became less with a polymer layer replacing a glass sheet. [9]

	a-Si	
Depostion process	PECVD	
Encapsulation type	Glass/glass	Glass/polymer
Cell material	<40	<40
Substrate + encapsulation material	300–400	170–250
Processing direct	300–540	260–500
Processing ancillary	200–300	200–300
Capital equipment	100–200	100–200
Module Total (frameless)	940–1480	770–1290
Frame	50–500 MJ/m^2	

Used Energy in the table is based on primary energy and the MJ per m^2.

A LCA study regarding organic photovoltaics was considered too as a comparison to the more conventional silicon solar cells. The organic paper discussed how inorganic thin film and organic photovoltaics are similar by sharing much of the material and fabrication process. The thin film process has the advantage of using much less deposition. The energy use given for organic solar cell of 2800.79 MJ/m^2 was much higher than often given for inorganic device. Part of this energy use related to material 726.26 MJ/m^2. The value was based on a study at laboratory scale and at a scale up this value would be reduced. The carbon emission, CO_2 suggested was 21–37g/kWh, which is similar to suggested value for an inorganic device. [39]

4.6. Discussion and conclusion

Energy payback time, EPBT refers to energy used during manufacturing and installation of the device against the generated energy in a product's life cycle, which is often set between 10 and 30 years. [5] Cell efficiency, operational location, PV-design and film structure play a part in the energy payback time, EPBT. How to monitor energy use and its emission in relation to a product or service is described in an environmental management system ISO 14000 from The International Organization for Standardization, ISO.

The conventional crystal silicon requires high energy use to produce the high purity silicon required for the cell. However, crystal silicon is still attractive for the market with its high efficiency. Even though thin film based devices have less efficiency, their advantage of using less raw material and being processed in one line with reduced energy and gas emission, makes this option interesting. [12] Woven polyester was used as an option for a light and flexible substrate. Polymer materials regarded as an option for sustainable products needs to be considered, when the raw material of a polymer is based on oil and the polymer process involves high energy use. If polymer is compared with common substrates such as Silicon Wafer and glass, it has a relatively low energy use.

Poor correlation between the data of material and energy use from different studies within semiconductor and textile industries has led to an estimation of energy use related to this work. Calculating the energy use for silicon thin film on polyester weave has proven more difficult than first anticipated due to the poor correlation between the studies. This has led to uncertainty in relation to the calculation provided for silicon thin film on woven polyester. The estimated energy use for silicon thin film on woven polyester can be related to the calculations given in table 4.8.. [9] The estimation of silicon thin film on woven polyester resulted in an energy use of approximately 52.5MJ/m^2 to prepare the woven polyester and 256.5MJ/m^2 to deposit a working cell of silicon thin film. The total energy use for the photovoltaic device in this work ends approximately at 309MJ/m^2, while the estimated PV-device with glass substrate and polymer film was calculated to be between 770-1290MJ/m^2. This comparison suggests that silicon thin film on woven polyester can be a possible way forward in the aim of cutting energy use. The calculation for the polyester weave is applicable for Polyamide 6.6. too, when manufacturing of Nylon material involves similar energy use as polyester.

4.7. References

1 E.A. Alsema, M.J. de Wild-Scholten, V.M. Fthenakis, *Environmental impacts of PV electricity generation- a critical comparison of energy supply options,* 21st European Photovoltaic Solar energy conference, Dresden, (pp.7) (2006)

2 N.J. Mohr, A. Meijer, M.A.J. Huijbregts and L. Reijnders, *Environmental impact of thin-film GaInP/GaAs and multicrystalline silicon solar modules produced with solar electricity*, Int. J. Life Cycle Assess. **14** (3), p.225-35 (2009)

3 V.M. Fthenakis, H.C. Kim and E. Alsema, *Emission from photovoltaic life cycles,* Enviton. Sci. Technol. **42**, p.2168-74 (2008)

4 F. Riddoch, J.I.B. Wilson, *The energy cost of amorphous silicon solar cells*, J. Solar Cells, **2**, p.141-9 (1980)

5 B.S. Richards and M.E. Watt, *Permanently dispelling a myth of photovoltaics via the adoption of a new net energy indicator*, Renew. Sust. Energ. Rev. **11**, p.162-72 (2007)

6 G.M. Lewis and G.A. Keoleian*, Life cycle design of amorphous silicon photovoltaic modules*, United states Environmental Protection Agency, Research and development EPA/600/SR-97-081, (pp.6) (1997)

7 S.R. Allen and G.P. Hammond, *Thermodynamic and carbon analyses of micro-generators for UK households*, Energy **35** (5), p.2223-34 (2010)

8 V. Fthenakis, H.C. Kim, M. Held. M. Raugei and J. Krones, *Update payback times and life-cycle greenhouse gas emissions,* 24th European photovoltaic solar energy conference, p.4412-6 (2009)

9 E. Alsema, Energy requirements of thin film solar cell modules a review, Renew. Sust. Energ. Rev. **2**, p.387-415 (1998)

10 M. Raugei and P. Frankl, *Life cycle impacts and costs of photovoltaic systems: Current state of the art and future outlooks*, Energy **34**, p.392-9 (2009)

11 A. Blakers and K. Weber, The energy intensity of photovoltaics systems, Centre for sustainable energy systems, Australian National University, (pp.11) (2000)

12 H.C. Kim and V.M. Fthenakis, *Comparative life-cycle energy payback analysis of multi- junction a-SiGe and nanocrystalline/ a-Si modules*, Prog. Photovolt. Res. Appl. **19**, p.228-39 (2011)

13 E.A. Alsema and M.J. de Wild-Scholtzen *Environmental impacts of crystalline silicon Photovoltaic module production,* 13th CIRP intern. conf. on Life Cycle Engineering, Leuven, (pp.6) (2006)

14 Project coordinator: University of Stuttgart, SENSE, *Sustainability Evaluation of Solar Energy Systems, LCA Analysis,* Funded by 5th Framework between 1998- 2002 (revised 2008)

15 Y.S. Song, J.R. Youn and T.G. Gutowski*, Life cycle energy analysis of fibre-reinforced composites,* Compos. Part A **40**, p.1257-65 (2009)

16 E. Alsema et al., *Methodology guidelines on life cycle assessment of photovoltaic electricity,* IEP PVPS Task 12, Subtask 20, LCA Report IEA-PVPS T12-01:2009, (pp.16) (2009)

17 D. Beloin-Saint-Pierre et al., *Environmental impact of PV systems: effects of energy sources used in production of solar panels,* Proceedings of the 24th European Photovoltaic Solar Energy Conference, Germany, p.4517-20 (2009)

18 ISO Central secretariat, *Environmental management, The ISO 14000 family of international standards*, Geneva, Switzerland, ISBN 978-92-67-10500-0, (pp.12) (2009) www.ISO.org

19 L. Dahllöf, *Life cycle assessment (LCA) applied in the textile sector: the usefulness, limitations and methodological problems- a literature review*, *Environmental systems analysis*, ESA-report 2003:9, ISSN: 1404-8167, (pp.22) (2004)

20 E.M. Kalöiala and P. Nousiainen, Life cycle assessment environmental profile of cotton *and polyester-cotton fabrics*, AUTEX Research journal **1** (1), p.8-20 (1999)

21 N. Cherrrett, J. Barrett, A. Clemett, M. Chadwick and M.J. Chadwick, *Ecological footprint and water analysis of cotton, hemp and polyester,* Bio regional development group, ISBN 91 975238 2 8, (pp.45) (2005)

22 R.F. Wiss, J. Muhle, P.K. Salameh and C.M. Harth, *Nitrogen trifluoride in the global atmosphere,* Geophys. Res. Lett. **35**, L2082 (pp.3) (2008)

23 Ecoinvent, Ecoinvent report No. 6- part XII, www.ecoinvent.org

24 R. van der Meulen and E. Alsema, *Life-cycle greenhouse gas effects of introducing nanocrystalline materials in thin-film silicon solar cells*, Prog. Photovolt, Res. Appl. **19**, p.453-63 (2011)

25 W. Berger, F.-G. Simon, K. Weimann and E.A. Alsema, *A novel approach for the recycling of thin film photovoltaic modules*, Resources, conservation and recycling **54**, p.711-8 (2010)

26 Oeko-Tex® International, *Association for the assessment of environmentally friendly textiles*, Zurich, Switzerland. www.oeko-tex.com

27 K. Knapp and T. Jester, *Empirical investigation of the energy payback time for photovoltaic modules*, Solar Energy **71** (3), p.165-72 (2001)

28 G.J.M. Phylipsen and E.A. Alsema, *Environmental life-cycle assessment of multicrystalline silicon solar cell modules,* The Netherlands Agency for Energy and the Environment, NOVEM Report no. 95057, (pp.66) (1995)

29 T. Higgs, M. Cullen, M. Yao and S. Stewart, *Developing an overall CO_2 Footprint for semiconductor products,* Sustainable systems and technology, ISST 09, IEEE International Symposium, p.1-6 (2009)

30 M. Gillenwater, K. Saarinen and A-L.N. Ajavon, *Precursors and indirect emissions,* IPCC guidelines for National Greenhouse Gas Inventories, **Chapter 7**, p.7.2- 7.16 (2006)

31 M. Czerniak, *Safe gas handling,* Solar- A PV management magazine **1**, p.16-9 (2009) www.solar-pv-management.com

32 Defra, Department for Environment, Food, and Rural Affairs, *Integrated Pollution prevention and control, IPPC (IPPC SG 8),* Secretary of state's guidance for the A2 surface treatment using organic solvent sector, (pp.124) (2010)

33 Defra, Department for Environment, Food, and Rural Affairs, *Integrated Pollution prevention and control, IPPC (IPPC SG 8),* Secretary of state's guidance for the A2 surface treatment using solvent sector, (pp.120) (2008)

34 G.A. Keoleian and G. McD Lewis, *Application of life-cycle energy analysis to photovoltaic module design,* Prog. Photovolt. Res. Appl. **5** (4), p.287-300 (1997)

35 N. Jungbluth, *Part XII, Photovoltaics,* Swiss centre for life cycle- inventories, Ecoinvent data v.21, (pp.183) (2009)

36 R. Mather and R.H. Wardman, *The chemistry of textile fibres,* RSC Publishing, ISBN 978-1-84755-867-1, (pp.120) (2011)

37 K.L. Hatch, *Textile Science,* West Publishing, ISBN 0-314-90471-9, p.115-8 (1993)

38 S.M. Bidoki, R. Wittlinger, A.A. Alamdar and J. Burger, *Eco-efficiency analysis of textile coating materials*, J. Iran. Chem. Soc. **3** (4), p.351-9 (2006)

39 R. Garcia-Valverde, J. A. Cherni and A. Urbina, *Life cycle analysis of organic photovoltaic technologies,* Prog. Photovolt. Res. Appl. **18**, p.535-58 (2010)

5. Processes and parameters influencing the textile substrate

5.1. Introduction

Woven polyester was selected as the substrate of choice in this work to establish process methods to deposit silicon thin film on textile substrate. The thin film processes used to manufacture the solar cell design on more conventional substrates such as Silicon wafer or glass were addressed in an earlier PhD study. [1] Together with the conventional substrates a nonwoven substrate was also tried. [1]

The vacuum processes such as evaporation, plasma, and sputtering were processed separately in this work, whereas in large scale production these processes would be in a continuous production such as a roll-to-roll system. The process parameters used in previous work gave an amorphous silicon solar cell with good optical and electrical properties. The problems experienced using textile substrates made it necessary to change proven process parameters [1] to allow the textile to withstand the harsh plasma process. Therefore much of the research has been spent understanding how growth parameters influenced by textile substrate and the consequent effect on the film properties. The preparation of the substrate was done in the same manner as used in the textile industry to prepare fabric for coating or lamination, despite the combination of vacuum processes for thin films and textile substrates being less well understood.

5.1.1. Cell design

The structural design of the solar cell on the textile fabric contained several layers, shown in figure 5.1.. The first was a back contact of aluminium (marked as a conductive layer in figure 5.1.), which was evaporated directly onto the textile substrate. Thereafter the silicon thin film microstructure (n-i-p), was produced by a microwave plasma enhanced chemical vapour deposition, (MW-PECVD) followed by a transparent top-contact of RF-sputtered indium tin oxide (ITO). In later samples, an additional coat layer (conductive coat) was applied onto the textile substrate to even the textured surface and support the aluminium back-contact. Encapsulation of the cell and complete panel was suggested either by using lamination or coating/ deposition.

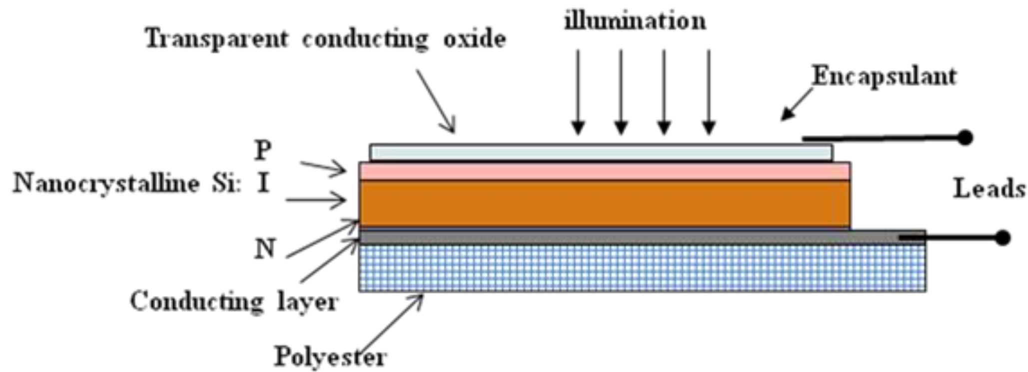

Figure 5.1. The cell structure on woven polyester containing deposition layers such as polyaniline (conducting coat), aluminium (back contact), phosphine doped silicon (n-layer), undoped silicon (i-layer), diborane doped silicon (p-layer) and Indium Tin Oxide (protective and top contact layer). [1]

5.1.2. Substrate

Polyester weave was chosen on the basis of being most common and commercialised filament and textile in the textile industry. Another advantage with polyester used in solar applications was its good environmental properties such as high moisture, bacterial and ultra-violet resistance. [2] The textile substrate of woven polyester was supplied by the Scottish weaver J&D Wilkie Ltd (Kirriemuir, Scotland, UK). Different weave structures such as plain and twill together with a thermal bonded nonwoven polyester web [1] and a polyester film (supplied by J&D Wilkie) were evaluated. The different substrates helped to address the importance of using the right textile to avoid unnecessary plasma penetration due to its mean-free-path, *chapter 2 section 2.6.*. [3,4] A plain weave had a more open and flat structure than twill and the plain structure was favoured for avoiding interaction with the plasma process and its deposition (*chapter 2 in section 2.4., 2.5. and 2.6.)*. Deposited thin films aimed to have the plasma on the substrate surface and avoid penetration through the structure, which led to the process parameters and values being carefully chosen. Throughout the work, both textile and aluminium substrates were used, which later (after the Taguchi model trials were completed) had microscope-slide glass added to observe eventual influence of the structure content and surface. Glass was chosen after being previously used as a common substrate for photovoltaic thin films and was used as a reference for other processes and results reported. The three substrates (textile, aluminium and microscope-slide glass) were similarly prepared.

5.1.3. Process methodology

The different polyester substrates, except the polyester film which was washed only, were prepared by washing, calendering and drying. Calendering of the textile substrate, helped flatten and smooth the substrate surface and increase the bonding properties. By previously observing the reduced conductivity of the aluminium layer when deposited on a textured substrate, a support layer was added in the form of a conductive wet-coat, which was applied by direct-coating (paste) onto the textile substrate. Different vacuum processes were used to encapsulate the cell, which remains a matter still to be fully addressed. The chart below (figure 5.2.) illustrates the order of the process techniques involved. Throughout this work it was found that the textile substrate needed to be dry to avoid unnecessary moisture interact with deposition of the contact coating and the silicon thin film.

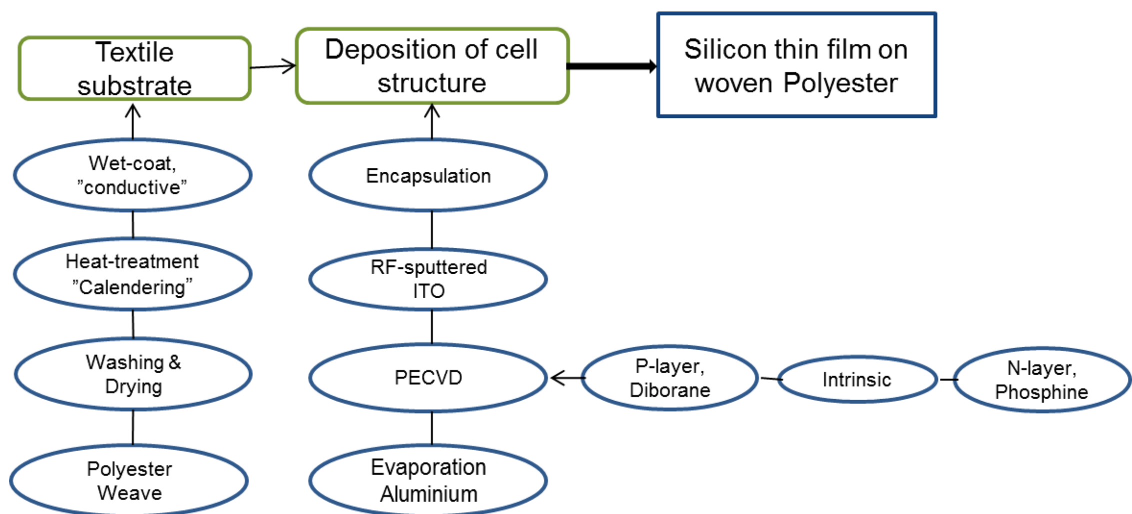

Figure 5.2. the chart explains the different stages in developing a solar device by silicon thin film onto woven polyester.

5.2. Experimental methodology for thin film on textile substrate

5.2.1. Preparation of textile substrate

The substrate was first washed to avoid impurities attaching to its surface, since these impurities would affect the bonding properties of the coated/ deposited layers. Since the textile had a textured appearance, a calender process was needed to flatten the fabric surface to avoid loose fibres and unevenness, which could result in delamination of the coating. A good preparation was important for the plasma process too, when impurities would influence both deposition and plasma conditions [5] through their lower surface energy and reduced adhesion, with inconsistencies in the coating/ deposition. [5] Cleaned samples were stored in a closed container between the different process stages to avoid samples being contaminated.

The deposition of silicon thin film solar cells onto a textile substrate involves several different types of deposition such as dry and wet coating. Dry refers to vacuum based depositions, whilst wet is based on a paste. Coating thickness was more accurate with vacuum based deposition (PECVD, evaporation and sputtering) as the thickness was measured in microns or nanometres compared with the wet-coat, which was quantified by weight, usually in grams per square-metre. [5]

Washing

The textile substrate was placed in a solution of 0,2ml detergent (Decon 90) and 200ml deionised water for 20 minutes in an ultrasonic bath. The sample was rinsed in deionised water before being dried by hot-air. Dried samples were then covered lightly with foil and stored on a laminar flow clean-bench overnight to avoid impurities being attached on the clean substrate surface and to allow the substrate to regain its natural moisture level before being calendering. If the polyester weave contained more moisture than its natural level of 0.4% [2], the substrate experienced a “steam effect” during the heat-treatment, which resulted in unwanted shrinkage, stiffer handle and damaged fabric.

Calendering (heat-treatment)

The purpose of the thermal-bonding process was to connect warp and weft yarn at their crossover points and flatten the substrate surface, which helped to increase the adhesion of coating and avoid breaks in the conducting layer. This method requires a careful balance between temperature, time and pressure and each fabric quality and structure requires its own particular settings to avoid damage to the substrate. Therefore each parameter required careful adjustment, in order to achieve a light bond without damaged handle or flex of the fabric.

Instrument and method

The fibre, filament and fabric surface become flattened by letting the fabric pass between two rollers, which can be either cold or hot depending on quality of substrate and the level of calender required for the specific textile and end-use. The two rollers can be adjusted for pressure applied onto the cloth, time related with speed and temperature and the principles of this technique are illustrated below in figure 5.3.. [6]

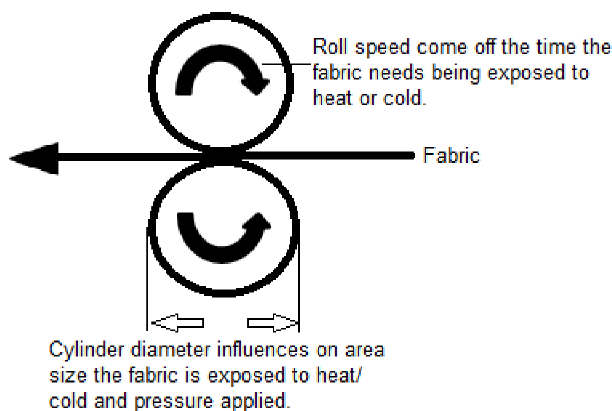

Figure 5.3. demonstrates the principle of calender process with the different parameters such as time, pressure and temperature, which will influence on the level of flatten the surface. [5]

The instrument used contained two heated plates, which the textile was placed between. The top lid had a weight of 4kg, which governed the pressure. The temperature for each plate was set individually, but for the work carried out had the same setting to provide a uniform calendering. To obtain a good bond the temperature

needed to be high enough to soften the polyester filament yarn without changing its bulk properties. Aluminium foil was placed on each side of the polyester substrate to avoid impurities being attached permanently onto the substrate surface during the softening process. The foil needs being placed flat against the substrate surface to avoid permanent marks on the textile.

Experimental

Combinations of time and temperature were tried to gain the correct bond without damaging or stiffening the fabric, table 5.1.. Consideration was given to the polyester's melting point, (T_m= 256°C) and glass transition temperature, (T_g ~70°C). An initial run was done at 150°C for 5 minutes, which led to a further test at higher temperature with reduced time (table 5.1.). Increased temperatures from 200°C to 230°C for 2 minutes were evaluated before foil was added (run 5) between the sample and the top and bottom plates to avoid impurity. With added foil, time was increased to 5 minutes. It was necessary to reduce the time with high temperature in an attempt to gain a quick flattening of the weave surface, but keep bulk properties of the substrate. All samples were evaluated by how the textile "handle" was affected.

Table 5.1. Process settings used to calender the textile substrate.

Trial run	**Temp., °C**	**Time, min.**
1	150	5
2	200	2
3	220	2
4	230	2
5 (foil)	220	5
6 (foil)	240	5
7 (foil)	260	5
8 (foil)	240	2
9 (foil)	230	1
10 (foil)	260	1
11 (foil)	240	1

5.2.2. Conductive backcontact and substrate

A support layer between the textile substrate and the evaporated aluminium was necessary after the observation that the thin layer of aluminium was not enough to fully cover the textured substrate, resulting in zero conductivity. The support layer was considered in two forms: by using a conductive substrate with evaporated aluminium (**1**) or the standard polyester weave with an extra coat layer (**2**) to provide a more uniform substrate before evaporation of the aluminium.

(**1**) Conductive substrate with evaporated aluminium;
The selection of conductive substrates included some woven, nonwoven, and strands (yarn), and a screen mesh of polyester with nickel areas (table 5.2.). The substrates were prepared in the same way as given for the woven polyester, except the woven copper material was not calendered due to being too thick. Most samples were tested both with and without calendering before the plasma process. The conductive samples considered and the settings such as time and temperature used were based on the experience from the woven polyester, see below:

1/ Amber Strand, Columbus, Ohio, USA, metal coated filament, a yarn of strand formation.

- AmberStrand®-Z-33-Ni, contains of Nickel clad polymer (Zylon® PBO) fibre with 33 filaments, untwisted.
- AmberStrand®-Z-166-Ag, contains of Silver clad polymer (Zylon ® PBO) Fibre, 166 filaments, untwisted.

2/ Kuraray trading Co. Ltd, Japan. Woven polyester 167dtex (plain weave) with antistatic fibre “Clarcarbo”.

- The antistatic fibres are polymer based with carbon distributed in four sections around the core
diameter of polyester, the weight of the weave was 280gsm.

3/ Technical Fibre products, Kendal, Cumbria, UK. Nonwoven web/ felt with Carbon.

- Carbon Veil 30gsm, product code 20303A.
- Carbon veil 80gsm, product code 20301A.

4/ Ugitech, Fibre department, France. Light and open (plain) weave named Sprintiss.

- Sprintiss of 300gsm is made by 100% AISI 316L.

5/ Neltec Ltd, UK. Polyester weave (plain weave), type screen mesh.

- Nickel etched areas onto the polyester mesh, 440gsm.

6/ Federal Mogul, system protective group, USA (+ France).

- Weave with polyester and twisted conductive yarn in the warp (DEW06090805) or both warp and weft (DEW 06090804), each 1320gsm. The conductive yarn contains of a thin twisted copper wire on the polyester yarn.

Table 5.2. Conductive material was tried as a replacement to the woven polyester.

Test run	Textile Supplier and quality	Calendering parameters	
		Time, min.	Temp., °C
1	AmberStrand®-Z-33-Ni	1	240
2	AmberStrand®-Z-166-Ag	1	240
3	Kuraray, Clarcarbo	1	240 and 220
4	Technical Fibre Products, Carbon veil 30gsm	--	--
5		1	220
6	Technical Fibre Products, Carbon veil 80gsm	--	--
7		1	220
8	Ugitech, Sprintiss	1	220
9	Neltec, nickel etched screen mesh	N/A	N/A
10	Federal Mogul, woven polyester with conductive yarn, DEW06090804.	--	--
11	Federal Mogul, woven polyester with conductive yarn, DEW06090805.	--	--

(**2**) Conductive coat on the standard polyester weave;

The extra coat layer between the non-conductive fabric and the evaporated aluminium was in the form of a paste/ coat of either Quick Drying Silver Paint (G3691, Aldrich) or polyaniline (Panipol OY) applied directly onto the textile substrate.

The silver paste was painted onto the textile substrate and cured in open air. Since silver paint proved not being a promising option for the plasma process, polyaniline coat was used instead.

Polyaniline mix, Panipol

The choice of Polyaniline (by Panipol OY) was based on its advantages of being water-based and already successfully tried on a textile substrate. [7] The conductive-coat was contained by the conductive solution Panstat W1-00-039.RD (*product data sheet, Appendix I*) and thickening agent Cognis DSX 3256 (*product data sheet, Appendix II*). The laboratory batch was often based on 5g with 10% of thickening agent in relation to total weight used of conductive solutions. The initial work was to establish a suitable viscosity of the wet-coat without reducing the conductivity, after the supplier advised to avoid adding too much water or thickening agent, which would reduce the conductivity.

The mixing procedure started by pouring Polyaniline, Panstat W into a beaker and stirring (using a magnetic stir) for 1.5 hours. The quantity used for the lab-coating was 5g. Thereafter was thickening agent, Cognis DSX 3256 of 0.5g added and the mix was stirred for further 1.5 hours before being left to rest for 2 hours. The lowest quantity of thickening agent was targeted by adding 10% of the Panstat W's weight. Before applying the coating, the mixture was stirred lightly by hand to avoid separation in the paste. Information regarding preparation of coating and the coating procedure is found in *Appendix III*.

Coating procedure for polyaniline

The Polyaniline coat was applied directly onto the textile substrate by a steel-blade, which was placed ~90° against the fabric surface. The blade was moved by hand in all four directions of the substrate. The coat paste was placed on same side of the blade as the travel direction and by applying pressure onto the paste, allowed certain amount of coat material to be evenly distributed on and into the textile surface. Spreading a thin and even coat onto the textile substrate helped improve the bonding between coat and substrate and resulted in a more durable product. Too little pressure would introduce pinholes and air-bubbles, while too much pressure stiffens the coated textile and affected the handle of coated substrate. No force or stress was applied onto the textile substrate during the coating, which resulted in a very small change in the textile during the cure. The coating procedure in the laboratory was slightly different to the principles of an industrial design of direct-coating (figure 5.4.), which is shown below. [6] Direct-coating is the most known coating method in the textile industry.

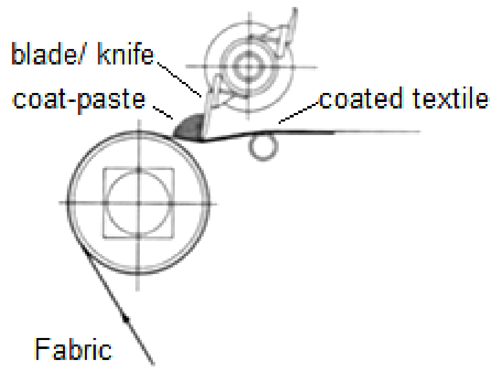

Figure 5.4. an image of direct coating used in an industrial scale and how the knife-blade and coat-paste is placed against the substrate. [6]

An industrial coating-machine contains of a coating-head (coat applied) followed by an oven, which blows hot-air from different directions in order to control a uniform cure. An even drying is important, when it affects the adhesion of the next layer. This may be compared with the hot-oven used here, which made it slightly more difficult to provide a uniform cure. A thermometer was placed through the oven top to monitor the temperature on the top-shelf. The oven was heated up for 3 hours prior to use, which allowed a more uniform and stable temperature and to avoid a sudden drop as the oven door was opened and samples were loaded. In case of temperature fluctuations, the curing time was altered to compensate for the deviation of temperature. Number of coats and thickness depended on performance required for the coated fabric, but often several coats were required. Most industrial machines have several coating-units (coating head and oven) placed in line.

Experimental

The aim was to build up a coat thickness by several layers to avoid poor adhesion and pinholes, which would reduce a coat's durability. Two coats with a total weight of ~15gsm were sufficient to cover and provide a smooth surface of the plain weave (247gsm).

The 1st coat layer was cured at 130$\pm$5°C for 10 minutes before the 2nd layer was repeated. The coated sample was covered lightly by foil and left overnight on the clean laminar flow bench to continue curing before being stored in a closed container, *Appendix III*.

The coated sample was measured by ohmmeter after being left for 24 hours to ensure the coat layer was cured and had sufficient thickness. Conductive measurements on the polyaniline were carried out for the different processes such as wet-coat, evaporation, PECVD and RF-sputter for possible change. The measurement was done at different distances across a sample of dimensions 5cm by 5cm and the locations of the probes were categorised by the distance between such as short <2cm and long >2cm. The measurement was carried out with a West meters model 169 multimeter on a scale of 200 ohm.

Metal contacts, aluminium

Evaporation contains of two main aspects, evaporation and deposition/ bonding of aluminium.

The evaporation was carried out by using an Edwards 360A, Edwards Vacuum Coater. [8] The chamber was constructed of glass in a cylindrical shape with vacuum seal on both sides, one towards the stainless steel lid and the other against the chamber floor. Pumping down the chamber was through the chamber floor. The evacuation of air was carried out by pumping first with a rotary pump, (roughing) and then with the diffusion pump to achieve high vacuum. The floor had in central position the evaporation source fitted with the sample holder placed ~20cm above. The distance between sample and source was adjustable, although in this work the sample was placed at the highest level possible.

The tungsten filament was fitted between two clamps, one to the AC supply and the other grounded. The aluminium source was three folded 1.5cm long 1mm diameter threads and lightly twisted several times to provide a more compact source, resulting in a more uniform glow and melt and an easier transfer onto the coil and evaporates. The substrate was placed above the aluminium source with the coat-side facing down towards the source. A shutter was placed between source and substrate and was closed during heating up of the coil to avoid early collection of impurity coming off the source and attaching to substrate surface. The shutter was not removed until aluminium was evenly distributed onto the coil.

The current required to melt and evaporate aluminium depended on resistance, which varied due to non-evaporated aluminium left on the filament. Current was first set at

20A to warm up and glow the coil and aluminium source before a further increase to 40A, which allowed evaporation of aluminium. Occasionally, a larger current of 60A was required, depending on the resistance build up in the filament and the source. It was important to increase the current flow slowly in order to get a uniform melt, transfer and distribution of aluminium onto the coil. A rapid increase gives a sudden melt and the aluminium falls off the coil. Evaporation of the back contact was recommended to take 5 minutes.

The coating thickness was estimated by the coating deposited onto the chamber wall window. When the desired thickness was reached without all the aluminium having been evaporated, the shutter was closed to allow the remaining aluminium to evaporate without irradiation or damage to the substrate. After the process was completed, the current was reduced slowly to zero and the coil was left to cool for ~10 minutes, since a rapid cooling down was found to make the coil brittle. Air was admitted and left for ~30 minutes to avoid force to break the vacuum seal of the chamber.

After releasing the sample, the chamber was wiped off to avoid aluminium deposition being built up and acting as an impurity in future depositions. The chamber was always kept in vacuum with or without new samples loaded. Due to the polyaniline coated textile containing high moisture content, it was necessary to pump the chamber overnight to reach a starting vacuum below ~5x 10^{-7}mbar, which increased to ~5x 10^{-5}mbar during the process. A poor vacuum pressure affects evaporation quality. Evaporation procedure is given in the *Appendix IV*.

A sputtered aluminium back contact was also evaluated in comparison to evaporated aluminium. The sputtering was produced by an RF-power of 70W for 10 minutes with a process pressure at 1x 10^{-3}mbar and the flow-rate of argon was set after a certain chamber pressure. Sputtering process is explained *in chapter 5 in section 5.2.4. and Appendix VI.*

A drying procedure of the substrate between evaporation and plasma process was later introduced to avoid trapped moisture in the textile substrate during vacuum processes. [5]

5.2.3. Plasma deposition

Plasma deposition with microwave and radio frequency powered source

In this work mainly microwave, MW powered plasma has been applied, although radio-frequency, RF based has been used for comparison. Microwave based plasma has the advantage of having a much faster deposition rate with a more excited plasma, which avoids ions impacting into the substrate. The different power source MW (2.45GHz) and RF (13.56MHz) does involve a change of electrode type and its location, which will influence where the plasma was located in relation to the substrate. Gas supplies for the process varied between the two types, RF-plasma is restricted to one inlet at the bottom of the chamber compared with microwave, which allows both top and bottom inlets. The machine procedures before and after the plasma run were the same for the two plasma systems. The operation procedure for plasma enhanced CVD is described below and additional information is given in the thesis from previous work [1,9] and *Appendix V*.

Preparation of process

In order to open the chamber and load samples, it was necessary to fill the chamber with argon to reach an atmospheric pressure, before breaking the seal between chamber and its lid. After the sample was in place, the chamber was pumped down initially by using a rotary pump, roughing to a pressure of 0.04Torr before use of high vacuum diffusion pump. A cleaning/ purging procedure of the chamber was always performed to load samples, heating up the chamber and after a process to avoid impurities in the chamber. The purges were carried out four times per cleaning procedure by filling the chamber with argon pressure of 1- 2Torr and then pumping the chamber out each time.

The chamber and substrate were heated up and cooled down before and after a process, and all gas-lines and regulators cleaned by purging them with argon six times. It was important to make sure the regulator and line was empty before the next purge of argon. Cleaning the regulators and lines was to avoid silane gas remaining in the pipes or reactants building up in the pipes and blocking a valve or pipe.

The substrate heater operated in a similar manner for the two plasma systems (Radio frequency and microwave), with the ceramic heater, fitted with a thermocouple, placed below the substrate plate. The temperature was controlled by a thermostat, which controlled the deviation from a set value and the response of feedback control was controlled by the PID settings. The voltage for the heater was supplied by mains voltage through a variable transformer which was set to a scale from zero to 100%. The heater was set to 40% during the heating, which allowed a substrate plate and textile temperature of ~200°C. During the microwave process, the power was reduced to 35% to avoid arcing, although the RF-plasma was at 40% without problem. With the microwave plasma it was necessary to increase to 40% during the changes of gas flow etc., when the temperature changes as the gases were altered.

When heating up, there are two options, either having a constant gas flow and pressure or having a vacuum in the chamber. Disadvantage with vacuum is when the substrate and its plate have reached process temperature the chamber compartment and walls are still cold. The advantage with constant argon flow and set pressure was that it gave a much more stable process temperature, with less fluctuation as the reactive gases were introduced and the plasma started. Fixed argon flow and chamber pressure was chosen as the project runs were prepared.

The chamber pressure was changed depending on power source, when RF-process had a higher (1.4Torr) pressure than microwave with 0.5Torr.

The rotary pump was always in operation throughout the process, and the diffusion pump was only used to achieve a base pressure, when the chamber went below a vacuum level of 0.04Torr. After the process was complete, the chamber was cooled down to 60°C or below to avoid a sudden cooling effect as argon, Ar was admitted (open the chamber), which could damage the deposited film.

Process parameters influencing a plasma process

Argon was used both as a cleaning and carrier gas during the run of reactive gases, eg silane (SiH_4); hydrogen (H_2); diborane (B_2H_6) and phosphine (PH_3), which all were required to process an n-i-p- layer. The doped n-layer was deposited with argon, silane and phosphine/ hydrogen, whilst the intrinsic (i-layer) used argon, silane and hydrogen, and the doped p-layer used argon, silane and diborane/ hydrogen. Argon was applied

in form of simple purges or with plasma to clean the substrate surface and chamber. The microwave power was altered depending on whether a doped or undoped layer was grown, when gas content and power showed an important relation.

Reactive gases such as silane, hydrogen and doped gases were introduced at the top of the chamber, whereas the carrier gas of argon was mostly introduced at the bottom inlet. Argon was used either as a cleaning or carrier-gas when the n-i-p- layers were deposited. Argon as top feed did cause strong temperature fluctuation, which was difficult to control and therefore the approach of top feed was discarded. The gases involved (silane, SiH_4; hydrogen, H_2; diborane, B_2H_6; phosphine, PH_3 and argon, Ar) each had their own cylinder, regulator, gas-line and flow-meter, which was specifically calibrated for the specific gas. In case a foreign gas needs access to a line, the flow-meter output rate needs to be calculated (a*ctual gas flow-rate= output reading x factor of new gas/ factor calibrated gas)*. The conversion factor for the gas concerned is given by gas or flow-meter supplier. An example of a calculation, argon (factor 1.4) requires an actual flow of 18sccm, which needs access through the hydrogen, H_2 (factor 1.01) line, which instead gives an output of ~13sccm (18sccm=? x 1.4/ 1.01=> 18/ 1.4= 12.86sccm).

Plasma enhanced CVD with Radio Frequency- RF

The radio-frequency, RF plasma had a different design compared with that used with the microwave run plasma. The main aspect was the power supply, which was connected through an impedance matching box to an electrode. The electrode was fitted through the chamber top (lid) and connected to the top plate of a parallel plate system, which was based on the same principles as below (figure 5.5.). The lower parallel plate was the earthed substrate holder and heater. Plasma strikes between the parallel plates and the matching box helped to tune the source to the chamber and avoid too much forward power being reflected.

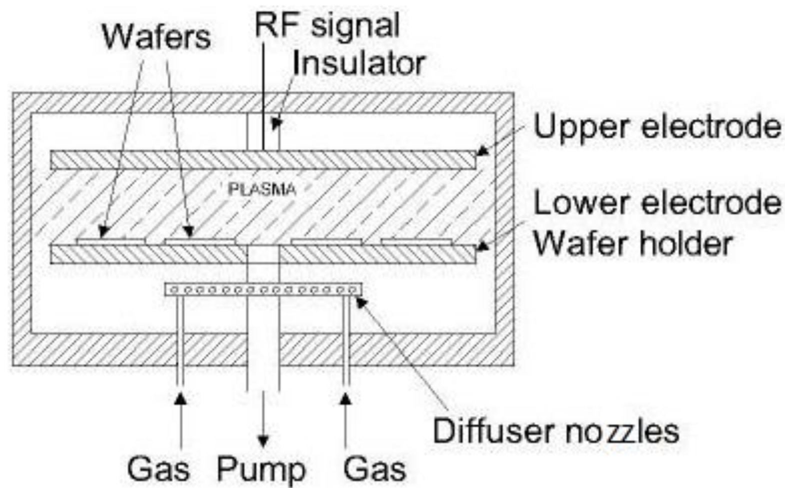

Figure 5.5. this layout shows the principles of a typical RF plasma process with parallel plate system. [10]

Another important aspect of plasma process is the distance between the parallel plates, which affects the plasma distribution and, indirectly, the quality of the deposited films. Initially a plate separation of 25mm was used, which was later reduced to 19mm in an attempt to increase the plasma intensity.

Plasma enhanced CVD with Microwave- MW

The microwave plasma machine was designed by Dilab Limited [11], and is a more complex system than the RF-parallel plate system. The microwave system had an additional chamber in the form of a quartz cylinder, which was attached to the chamber lid. The gas-inlet at the top of the chamber was via the stainless tube attached to the top of the quartz cylinder, which is illustrated in figure 5.6..

DC power entered the magnetron and was transformed into microwaves and then travelled through the waveguide and an impedance matching wedge. The wedge had a close fit to the stainless steel tube antenna (gas inside), which allowed the waves to travel along the tube towards the quartz cylinder. The quartz cylinder had antennae fingers fitted around the outside. The wedge needed a very close fit to the tube, since the smallest gap could lead to arcing and disturbance of the wave. Generally, all waveguide fittings for a microwave process have to be fitted tightly to avoid microwave leakage.

As power reached the end of the antennae fingers and the quartz cylinder was filled with reactive gases, the plasma was ignited by the electric field produced between the fingers. [1,11] The parameters of gas rate and mix, chamber pressure and microwave power had a direct influence on the concentration and location of the plasma. Microwave power was limited to a minimum of 200W depending on process parameters. The max was at 1000W, which was used for the doped layer in the work prior [1], but power was later reduced to 800W and below to avoid damage to the textile substrate.

A round substrate plate combined with a heater was located in a central position of the chamber and quartz. The height of the substrate plate could be altered from mid chamber height to half way up through the quartz. With the textile being more heat sensitive, the substrate plate was placed where the chamber and quartz meets. This location avoided too intense plasma conditions, but not too far off to receive active species from the plasma.

It was important that the substrate plate was placed in a central location, when a small move towards one side would attract the plasma with the narrow space. With the substrate plate being more close to the chamber wall, the narrow space between the wall and sample plate encouraged increased plasma activation and, occasionally, even a second plasma. Both plasma-effects resulted in an uneven deposit on the substrate. The picture below (figure 5.6.) explains the layout of the microwave unit and where and how the plasma was produced.

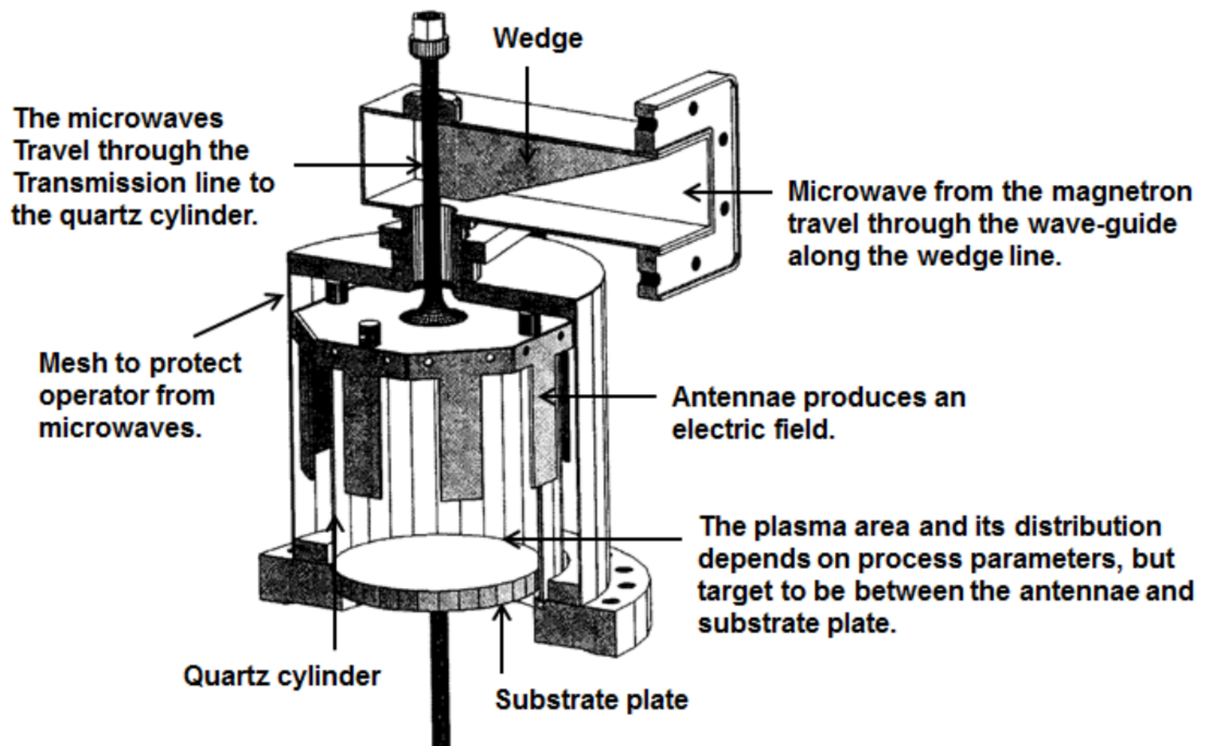

Figure 5.6.. explains the layout of the quartz cylinder where the plasma takes place in relation with the substrate plate. [1,11]

5.2.4. RF- sputter, ITO- Indium Tin Oxide

Transparent Conducting Oxide (TCO) was applied as a protective layer and top contact for the silicon thin film solar cell. For this solar cell design Indium Tin Oxide (ITO) was deposited by a radio frequency, RF powered sputter process. ITO is one of the more common top contacts used due to a broad absorption spectrum and good conductive properties. [12]

Magnetron sputter technology

The RF-sputter process was carried out with an Edwards AUTO 306 Vacuum Coater with Turbomolecular Pumping System [8], which was designed for both evaporation and sputtering. Operation of the machine was mainly automatic with the turbo-pump and very little to operate by hand, except adjusting gas flow and chamber pressure before, during and after the process. The sputter-process was controlled by RF-power and time.

The sputter-target of Indium Tin Oxide (ITO) was placed on a magnetic-plate and screwed in place. The sample was placed 10cm above the sputter target with the coated side facing the target below. Distance between sample and target was set depending on sample size and uniformity of coat required. A shutter between the sample and target controlled the coating thickness.

After samples were loaded and the chamber closed, the chamber was pumped down to a pressure below 1.3x 10^{-6}mbar. No supervision was required, when the turbo pump switched automatically from the rotary pump roughing to the high vacuum diffusion pump. In preparation of the process, argon was introduced and the flow-rate was adjusted by a needle valve fitted on the chamber lid. The gas-flow affected the chamber pressure and this was set to ~6x 10^{-3}mbar.

The process power was set and the shutter (fitted between sample and sputter-target) opened as the RF-plasma was switched on. The shutter was then closed immediately after the plasma ignited, which allowed the sputter surface to be cleaned without impurities being deposited onto the substrate surface. In the meantime, the chamber pressure was reduced to 1x 10^{-3}mbar. The quality and film thickness of deposited ITO film was determined by process time, which was controlled by the opening and closing of the shutter.

The plasma ignited by RF-power in the argon-flow provided electrons that were held close to the sputter target by the magnetic field. Electrons collide with the argon atoms which become ions and these bombard the sputter target and eject the desired species that travel toward the substrate surface above the target.

After the process, the argon-flow was stopped and the chamber pumped down for at least an hour. Nitrogen is used to open the chamber, but it also acts as a cleaning gas for the chamber and the exhaust system. The operation procedure of the RF-sputter process is given in *Appendix VI*.

Experimental

With no in-house work previously reported on Radio Frequency, RF-sputtered Indium Tin Oxide, ITO as the top contact/ protective layer of the cell, it was important to understand how the process parameters related to film thickness and its properties.

Some knowledge was gained from the industry, which used ITO coated glass before depositing the silicon thin film. However this present work applied the ITO last, which made the structure different due to uneven substrate and a silicon thin film coated on top. An ITO film thickness between 0.1 and 0.5µm was targeted as being sufficient to protect and result in good optical and electrical properties required for the silicon thin film.

RF-power and time were the two key parameters for the sputter process. Establishing the film thickness was done on ITO deposited on a microscope-slide glass with screen printed lines of photo-resistance material. The ITO coated print-lines were washed off in acetone, which left a sharp edge between the ITO coat and the exposed glass surface and the difference represented film thickness, which was measured by Dektak.

First trial run used RF-power of 70 Watt for 15 minutes, which later increased to 85W for 30 minutes.

5.2.5. Experimental design for N-I-P-layer

The plasma process was controlled by several parameters such as radio-frequency/ microwave power, gas mix and rate, process temperature, chamber pressure and process time, which influenced the thickness and quality of the deposited film. In the transfer from microwave settings to radio-frequency required process parameters being changed. In discussion to follow, the flow-rates given for silane, diborane and phosphine are the actual values, when these gases are heavily diluted with hydrogen. Discussion regarding thickness of deposition refers to the level of powder effect in a sample. This was estimated visual by the colour of the deposition, which occurred in a shade of white-beige-yellow.

Intrinsic silicon films with Microwave powered plasma

Using the previous project's recipe [1] (*hydrogen, H_2 20sccm, silane, SiH_4 1.02sccm, chamber pressure 0.3Torr, 800W, 20 minutes*) with a reduced sample temperature of 200°C, resulted in the textile substrate being damaged. The previous project had used this successfully on substrate such as glass, silicon-wafer and nonwoven.

After experiencing the textile being damaged, the focus was to establish a process condition suitable for textile substrates, which led to different combinations being tried.

- temperature (*from 150°C to 200°C*),
- process time (*10, 15 and 20 minutes*),
- hydrogen, H_2 (*2 and 20sccm*),
- silane, SiH_4 *(0.29, 0.49, 0.71, 0.82 and 1.14sccm*),
- power of *800W*
- process pressure at *0.3Torr*

The chamber pressure (*0.3, 0.5 and 0.75Torr*) was also evaluated, after difficulties were experienced in controlling the plasma process at 0.3Torr and pressure for continuous work became 0.5Torr.

Later it was found, that textile could withstand an argon-plasma (Ar *18.2sccm, 800W, 0.5Torr at 200°C and up to 30 minutes*), which became used as a reference plasma against the parameters below, which were added one by one.

- silane, SiH_4 from *0.29, 0.49, 0.71, 0.82 to 1.14sccm*,
- hydrogen, H_2 from *2 to 20sccm*,
- process temperature *from 150°C to 200°C*,
- process time of *10, 15 and 20 minutes*,
- microwave power of 4*00, 500 and 800W*,
- chamber pressure at *0.5Torr*.

An argon and silane mix (Ar 18.2sccm, SiH_4 0.82sccm) with a temperature of 200°C, power of 800W for 20 minutes was possible.

Different polyester substrates (supplier: J&D Wilkie Ltd, Scotland) such as plain and twill weave (both light and heavy weight), film and nonwoven were evaluated with this setting (*Ar 18.2sccm, SiH_4 0.82sccm, 200°C, 800W for 20 minutes at 0.5Torr*) to understand how the structure of the substrate influenced the performance during the plasma process. Fabric weight (247gm^2, 168gm^2, 86gm^2 and 68gm^2) together with yarn type (continuous filament, monofilament and spun staple fibre) were tried in different plain weave options. The fabric weight relates to yarn thickness, dtex and number of warp and weft threads/cm^2 (*chapter 2 in section 2.6.*).

To improve the deposition quality, time, temperature and power were altered against fixed argon- silane mixture (Ar 18.2sccm, SiH_4 0.82sccm) and pressure of 0.5Torr.

- time of *10, 20 and 30 minutes*,
- temperature of *200 and 210°C*,
- power of *600W, 700W and 800W*.

As occasional damage to the substrate was still experienced, other possible causes were considered such as temperature, impurity of substrate and chamber and how substrate structures influenced the plasma and its deposition. Alternative approaches were tried such as argon-plasma, melting-test and thermal temperature stickers.

- Argon plasma was used to clean the substrate before the plasma process of thin film (n-i-p- layers), to avoid the risk of having foreign particles on the substrate surface and in the chamber, which would react with the plasma condition and deposition. Argon, Ar (*18.2sccm*) plasma of 5 and 20 minutes was compared.

- Analysing thermal deformation of the textile substrate during the plasma process was done by using a hot-air-gun to reconstruct the heat-flow towards the textile substrate. The thermal test was done by reconstructing a similar arrangement the substrate experienced during the plasma process. The substrate was placed on a metal mesh instead of the substrate heater-plate in the plasma-chamber. The mesh allowed hot-air being applied from below (as in the case of heat coming from the substrate plate) and above (as in the case of heat coming off the plasma reaction) to learn about melt formation. The thermal test was done on various woven polyester samples, which vary in weight.

- Thermal temperature stickers were attached on the face side of the substrate to measure the maximum local surface temperature. The substrate controller displayed a temperature much lower than polyester's melting point at 256°C even when the substrate melted on numerous occasions. The temperature stickers used covered a range from 160°C to 190°C and from 204°C to 260°C.

The earlier trials were an attempt to avoid melting of the textile weave, but instead a powdery deposition and poor quality of deposited thin film was experienced. The necessity of additional hydrogen to the mix of hydrogen diluted silane and argon, led to use of an Orthogonal Statistical Design, Taguchi model [13,14], as an attempt to

introduce hydrogen, H_2 with varied values for argon, Ar, silane, SiH_4 and microwave power.

Taguchi model

This statistical design contained different silane rates (from *0.10 to 2.04sccm*), together with hydrogen introduced as a ratio against argon (hydrogen/ argon ratio *20/0, 17/3, 14/6 and 10/10sccm*) and the variable microwave power (*200 to 500W*) with fixed chamber pressure (0.5Torr), time (20 minutes) and temperature (200°C). The different parameters were changed in a repeated pattern as shown in table 5.3.. Both aluminium sheet and woven textile were used in each run to identify the eventual influence from the substrate surface and content.

Table 5.3. the different runs and their settings used in the Taguchi model.

No. of Runs	**Flow rate, sccm**		**Power, Watt**
	SiH_4	**H_2/ Ar**	
1	0.10	20/0	200
2	0.10	17/3	300
3	0.10	14/6	400
4	0.10	10/10	500
5	0.51	20/0	500
6	0.51	17/3	400
7	0.51	14/6	300
8	0.51	10/10	200
9	1.02	20/0	200
10	1.02	17/3	300
11	1.02	14/6	400
12	1.02	10/10	500
13	2.04	20/0	200
14	2.04	17/3	300
15	2.04	14/6	400
16	2.04	10/10	500

After the Taguchi trial, the fixed parameters such as time and temperature were considered with increased power. Run 16 (*silane, SiH_4 of 2.04sccm, hydrogen/ argon*

H_2/ Ar ratio of 10/10sccm, power of 500W) was used to evaluate process times of 5 and 30 minutes against the 20 minutes from the Taguchi run. The 30 minutes run was repeated by increasing the power to 600W and 700W. In addition, run 16 was replaced by the hydrogen/ argon, H_2/ Ar ratio of 17/3sccm (no. 10) and 14/6sccm (no. 11) from the Taguchi model.

- Run 10 (*silane, SiH_4 of 1.02sccm, H_2/ Ar ratio of 17/3sccm, power of 300W*)
- Run 11 (*silane, SiH_4 of 1.02sccm, H_2/ Ar ratio of 14/6sccm, power of 400W*).

Even though the two runs contained a higher rate of hydrogen, it was necessary to increase the power to target increasing the crystal content. The first attempt was by altering silane rate with increased power and altered process time of 20 and 30 minutes (table 5.4.).

Table 5.4. Silane rate, process time and increased power against H_2/ AR ratio of run 10 and 11 were applied.

SiH_4, (sccm)	**H_2/Ar, (sccm)**	**Pressure, (Torr)**	**Power, (Watt)**	**Temp., (°C)**	**Time, (min.)**
0.62	17/3 & 14/6	0.5	700	200	20 & 30
0.82	17/3 & 14/6	0.5	700	200	20 & 30
1.02	17/3 & 14/6	0.5	700	200	20 & 30

Silane rate of 0.82sccm resulted in a sufficient deposition rate, but it was necessary to reduce the process power to 600W with longer process time. This led to further combinations with power of 600W against time and temperature (table 5.5.). The trial had fixed parameters of silane, SiH_4 rate 0.82sccm, H_2/ Ar ratio 17/3sccm and process pressure at 0.5Torr.

Table 5.5. Explains the different combinations of temperature and time together with the fixed parameters of SiH_4 rate 0.82sccm, H_2/ Ar ratio 17/3sccm and 0.5Torr.

<table>
<tr><th>Power, W</th><th>Temp., °C</th><th>Time, min.</th><th>Temp., °C</th><th>Time, min.</th></tr>
<tr><td rowspan="4">600</td><td rowspan="4">200</td><td>20</td><td rowspan="4">205</td><td>20</td></tr>
<tr><td>30</td><td>30</td></tr>
<tr><td>40</td><td>40</td></tr>
<tr><td>60</td><td>60</td></tr>
</table>

Interface between n- and i-layer

With most focus being placed on the intrinsic layer at this point, it was found [15,16,17,18] that a clear break between the doped layer (prior to the intrinsic layer) and the intrinsic layer itself was very important to avoid dopant migration. Doped species in the intrinsic would act as impurities which would act as non-radiative recombination centres and reduce the overall cell efficiency. To produce the best clear break between the doped n-layer and the intrinsic layer, a standard n-layer recipe (*phosphine, PH_3 0.1sccm, argon, Ar 9.1sccm, silane, SiH_4 0.82sccm, 200°C and 800w for 5 minutes*) was combined with three intrinsic recipes. The actual flow value for the dopant was 1% of given rate, when the rest related to hydrogen. The intrinsic recipes used in this test were "normal", which was applied before the Taguchi model, and the two recipes (Taguchi run 10 and 11) with some of the parameters altered.

- Recipe 1: Normal (*argon, Ar 18.2sccm, silane, SiH_4 0.82sccm, 200°C and 800W for 20minutes*),
- Recipe 2: Run 10 (*silane, SiH_4 0.82sccm, hydrogen, H_2/ argon, Ar ratio of 17/ 3sccm, 200°C and 600W for 20 minutes*),
- Recipe 3: Run 11 (*silane, SiH_4 0.82sccm, hydrogen, H_2/ argon, Ar ratio of 14/6sccm, 200°C and 600W for 20 minutes*).

Six types of "cleaning" procedures were suggested for a clear break, which were combined with the intrinsic recipes (given above). The different cleaning procedures suggested between n- and i- layer.

Procedure **A**/ Standard procedure without a specific cleaning between n- and i-layer.
Procedure **B**/ Ar-plasma for 3 minutes before introducing the gases for i-layer.
Procedure **C**/ Ar-plasma for 3 minutes, followed by 2 minutes Ar+SiH_4 plasma followed by 18 minutes deposition plasma of Ar+SiH_4+H_2. The gases were added one by one without a break.
Procedure **D**/ The hydrogen, H_2 content in the plasma was reduced with ~5sccm/ 5 minute, which gave a flow-rate of 17-12-6-0sccm with recipe of run 10, while run 11 resulted in a flow-rate of 14-10-5-0sccm.
Procedure **E**/ Argon purges three times were applied between n- and i-layers.
Procedure **F**/ Argon purges six times were applied between n- and i-layers.

Due to the cleaning procedures C and D not applying to the Normal recipe (recipe 1), a total of 16 runs were carried out. In changing from processing n-layer to intrinsic layer, the plasma was switched off and the gases and flow-rates were altered and the plasma for intrinsic layer was not switched on until the chamber pressure was stable enough after changing gas mix and rates. The break could vary in time depending on type of cleaning procedure and the gases involved for intrinsic.

Table 5.6. the combinations used in the trial “clean break” between doped prior to the intrinsic layer.

Cleaning procedure	**Trial no.**	**Intrinsic recipe**
A	1	1
	2	2
	3	3
B	4	1
	5	2
	6	3
C	7	2
	8	3
D	9	2
	10	3
E	11	1
	12	2
	13	3
F	14	1
	15	2
	16	3

Doped layers

The first doped runs were based on previous work's recipes [1] for n-layer (*phosphine doped, PH_3 0.1sccm, argon, Ar 18.2sccm and silane, SiH_4 1.02sccm, 5 minutes and 200°C*) and p-layer (*diborane, B_2H_6 of 0.1sccm, argon, Ar 18.2sccm and silane, SiH_4 0.82sccm, 5 minutes and 205°C*). The power for the doped layers started at 700W after knowing the temperature restriction coming with a high quantity of hydrogen use, but soon, power was increased to 800W. The process temperature for diborane was reduced to 200°C as the power increased. The initial argon rate (18.2sccm) was soon reduced to 9.1sccm for the doped layers. The silane rate of 0.82sccm for the intrinsic became standard rate for n- and p- layer too. The two dopants used in this work, diborane, B_2H_6 and phosphine PH_3 are both heavily diluted with hydrogen, which means the actual flow value for the dopant was 1% of given rate, when the rest related to hydrogen.

Previous research showed [17,19,20], that n-layers did have a more crystalline nature while p-layer had an amorphous nature. [21,22] N-layer contained nanocrystal structure with a crystal size of 2-4nm, while diborane in case of crystal growth formed larger crystals (5nm) with a high amorphous content. [20] Due to many cell structures starting with a p-layer has focus been to introduce and increase the crystal content in the p-layer. Different process parameters such as temperature, time and dilution of boron with hydrogen and silane have been important and discussed. [23,24,25,26] A temperature study between 90°C to 270°C concluded, that 150°C or below resulted in the best crystal content and properties. [23,24] Dilution of diborane was considered too, when reduced diborane rate increased crystal content, while increased diborane supported an amorphous growth. [25,26]

N-layers with standard recipe (*phosphine, PH_3 0.1sccm, argon, Ar 9.1sccm and silane, SiH_4 0.82sccm, 200°C, 800W and 5 minutes*) showed, that extended proved deposition time to 10 minutes was sufficient.

P-layers (*diborane, B_2H_6 of 0.1sccm, argon, Ar 9.1sccm, silane, SiH_4 0.82sccm, 200°C, 800W and 5 minutes*) did require more work than just altering time and power, when the film still became powdery. However, reduced process temperature and diborane rate were suggested to increase crystal content. [21,24,27] When a drop in temperature from 200°C to 190°C showed a change in the structure content, further

reduction in temperature (table 5.7.) together with reduced diborane-rate, increased argon-rate and introduction of hydrogen were tried.

Run A/ Original setting: B_2H_6 had a flow-rate of 0.05sccm*.

Run B/ Reduced B_2H_6 flow-rate by half 0.025sccm.

Run C/ Increased by double the B_2H_6 rate of 0.1sccm.

Run D/ Double the argon rate (18.2sccm).

Run E/ Hydrogen, H_2 introduce as a ratio with argon, Ar/ H_2, 10/10sccm.

Run F/ Hydrogen, H_2 introduce as a ratio with argon, Ar/ H_2, 5/15sccm.

Run H/ Reduced process temperature at 180°C with best performing trial between run A to F.

* Original flow-rate of diborane had been reduced from 0.1 to 0.05sccm due to flow restriction in the diborane line.

Table 5.7. the table shows the different flow-rates used to optimise the p-layer deposition.

Trial run	Gas type and actual flow-rate sccm				Temp, °C	Time, min.	Power, W
	B_2H_6	**SiH_4**	**Ar**	**H_2**			
A	0.05	0.82	9.1	0	190	5	800
B	0.025	0.82	9.1	0	190	5	800
C	0.1	0.41	4.55	0	190	5	800
D	0.05	0.82	18.2	0	190	5	800
E	0.05	0.82	10	10	190	5	800
F	0.05	0.82	5	15	190	5	800
H	?	0.82	?	?	180	5	800

All runs were evaluated by Raman spectroscopy and optical transmission to determine crystalline content, and the run with the highest crystalline content was repeated at 180°C.

The trial above helped to address potential recipes to use for each the n- and the p-layer.

N- Layer: *Phosphine, PH_3 0.1sccm, argon, Ar 9.1sccm, silane, SiH_4 0.82sccm, 10 minutes, 200°C and 800W.*

P- Layer: *Diborane, B_2H_6 0.025sccm, argon, Ar 9.1sccm, silane, SiH_4 0.82sccm, 5 minutes, 190°C and 800W.*

N-I-P- layers, combinations

As the previous part mainly regards only single layers or stages in a complete cell, the following discussion refers to the deposition of the three layers (n-i-p-layer). Even if the individual process did not damage the textile substrate, occasionally a combination of the three layers damaged it. After this discovery, three layers were always processed, to check for damaged textile substrate, even after smallest modification to a single layer was made. This section highlights the single layers trials, which were used in combined version.

The process settings for initial trial (section **A** in table 5.8.) of three layers (n-i-p) had the power increased to 800W (section **B** in table 5.8.) for all three layers in an attempt to find the optimal process condition for non-powdery deposition with crystal growth. With introduction of an additional conductive layer such as conductive substrate or a conductive coat onto the textile substrate was necessary to reduce power for the intrinsic to 600W, while doped stayed on 800W (section **C** in table 5.8.). The intrinsic layer changed further with the knowledge from the Taguchi model by adding hydrogen through H_2/Ar ratio together with altered silane rate (section **D** in table 5.8.). Argon-purges of three and six were applied (section **D** in table 5.8.) to clean the interface and avoid doped species into the intrinsic layer. The doped layers were modified by time, temperature and flow-rate, while intrinsic was altered by time and temperature (section **E** in table 5.8.), when table 5.9 illustrate the different combinations in more detail. After further attempt to improve crystal growth in the p-layer was new settings suggested (section **F** in table 5.8.) at 180°C with added hydrogen (1) and with reduced diborane rate (2) combined with n- and i- layer.

Table 5.8. The settings for the n-i-p- layers.

N-I-P-Layer	Gas type and actual flow-rate, sccm					Temp, °C	Time, min.	Power, W	Sect. No.
	SiH_4	Ar	H_2	B_2H_6	PH_3				
N	0.82	9.1	0	0	0.1	200	5	700	A
I	0.82	18.2	0	0	0	200	20	700	
P	0.82	9.1	0	0.1	0	205	5	700	
N	0.82	9.1	0	0	0.1	200	5	800	B
I	0.82	18.2	0	0	0	200	20	800	
P	0.82	9.1	0	0.1	0	200	5	800	
N	0.82	9.1	0	0	0.1	200	5	800	C
I	0.82	18.2	0	0	0	200	20	600	
P	0.82	9.1	0	0.1	0	200	5	800	
N	0.82	9.1	0	0	0.1	200	5	800	D
Argon- purges three or six times in the interface of n- and i-layer									
I	0.82 (0.62/ 1.02)	17 (14)	3 (6)	0	0	200	20	600	
P	0.82	9.1	0	0.1	0	200	5	800	
N	0.82	9.1	0	0	0.1	200/ 205	10	800	E
I	0.82	17	3	0	0	200/ 205	30/ 40/ 60	600	
P	0.82	9.1	0	0.05	0	180/ 190	5	800	
N	0.82	9.1	0	0	0.1	200	10	800	F
I	0.82	3	17	0	0	200	20	600	
P:1	0.82	10	10	0.05	0	180	5	800	
P:2	0.82	9.1	10	0.025	0	180	5	800	

Table 5.9. the different combinations with altered time and temperature of n-i-p- layers were done in the order given below.

Process time, minutes			Process temperature, °C		
n- layer	**i- layer**	**p- layer**	**n- layer**	**i- layer**	**p- layer**
10	60	5	200	200	190
10	60	5	200	200	190
10	40	5	200	200	185
10	30	5	200	200	180
10	60	5	205	205	180
10	30	5	200	200	180
10	40	5	205	205	190
10	40	5	200	200	190
10	30	5	200	200	190

5.2.6. RF- powered plasma run

A small number of Radio Frequency, RF based plasma enhanced chemical vapour depositions, RF-PECVD were carried out to compare with the microwave PECVD processed samples. The RF-plasma processed an n-i-p- structure on textiles, aluminium sheets and microscope-slide glass. The recipes used (section **A** in table 5.10.) were parameters already established in previous projects [1,9], which focused on RF-based silicon thin films. Additional to the old recipe was a set of three argon-purges between n- and i- layers to avoid doping into the intrinsic.

The three layers (section **A** in table 5.10.) had several values in common such as RF-power, silane rate and temperature, when the deposition time was different for each layer. The actual gas rates used for n-layer, phosphine, PH_3 and p-layer, diborane, B_2H_6 were the same values applied in the microwave process.

After the initial runs the process parameters were altered as an aim to increase the crystal content. Same types of changes were made as observed with the microwave PECVD such as increased power, reduced silane rate for all three layers, altered process time for phosphine and reduced diborane rate in the last combination with reduced temperature (section **B** in table 5.10.).

Table 5.10. RF-powered trials

N-I-P-Layer	Gas and actual rate, sccm			Temp, °C	Time, min.	Power, W	Section no.
	SiH_4	B_2H_6	PH_3				
N	2.04	0	0.1	200	10	20 (30)	**A**
Argon purges three times							
I	2.04	0	0	200	30	20 (30)	
P	2.04	0.1	0	200	5& 10	20 (30)	
N	1.43	0	0.1	200	5&10	40	**B**
Argon purges three times							
I	1.43	0	0	200	30	40	
P	1.43	0.1	0	190	10	40	
		0.05		180			

5.3. Introduction to analytical instruments

The analysis of silicon thin films on textile substrate proved more difficult than first anticipated, since the polymer-based textile substrate incorporating the silicon thin films either charged up or was too textured and opaque to be measured routinely. The charging up was not always related to the textile substrate, since the same effect happened to the aluminium and microscope-slide glass. Therefore many of the known methods such as Scanning Electron Microscope, SEM, Atomic Force Microscope, AFM and Fourier Transform Infrared Spectroscopy, FTIR were not used. The textured surface of the textile proved difficult to measure the electrical and optical properties, when it gave too high a resistance and very scattered light. Instead Raman spectroscopy and optical transmission with microscope-slide glass became the main methods.

Raman Spectroscopy helped establish structure content, and optical transmission was measured on deposited thin film to calculate the band-gap energy. Raman spectroscopy technique is discussed in a separate *chapter 3 in section 3.3.*. Thermal analysis by Differential Scanning Calorimetry (DSC) was carried out too, which helped

establish changes in the polymer chains of the substrate during the different vacuum depositions required for the silicon thin film cell.

5.3.1. Scanning Electron Microscopy, SEM

Initially, scanning electron microscopy (SEM) had as its purpose to evaluate changes to the deposited textile, yarn and filament such as damage to the substrate by heating and melting. However, with problem of the textile substrate charging up during measurement this method was discarded. The charging up was experienced even after aluminium was deposited onto the textile. Sample preparation was required for SEM, to avoid the coated textile charging up. Even after a thin layer of gold was applied onto the textile substrate, the sample was still charging up, probably because the metal coatings were not continuous.

The instrument and method

The SEM image process was carried out in vacuum at 10^{-5} Torr and the sample was placed on a table which could be moved and tilted at different directions and angles to capture the best images of the filament surface. The details found on the sample were taken at different magnifications starting at 50x followed by 100x, 200x, 800x and 2000x to analyse the features of the surface. SEM gives detailed images with the characteristics of the surface which help to understand if the marks belong to an etch effect, coating or other causes affected by the process. At lower magnification of 50x, 100x and 200x information about the fabric appearance can be observed and whether specific effects are repeated or not. [28]

5.3.2. Raman spectroscopy

The instrument used was an inVia Raman Microscope from Renishaw, which helped identify how the crystalline structure altered with changing process parameters and plasma conditions. The parameters and procedure used to identify the structural content of deposited substrate are discussed below, whereas more analytical aspects of the Raman technique and its spectra are discussed in *chapter 3 in section 3.3.*.

Raman parameter's influence on thin film

With textiles not being a common substrate for Raman spectroscopy, the different parameters involved such as exposure, data accumulation, laser power and magnification were examined for potential thermal annealing effects. Heating can affect both the thin film and the polymer by increasing the crystal content due to crystallisation. All substrates were measured after the plasma process and depending on substrate and batch, each sample was measured at least twice. In case of large thickness variation in the film, the sample was measured between two and five times by analysing areas where a great contrast was observed between them. This helped to establish the film thickness and its variation. Sometimes, the sample had the measurement repeated in case the result did stand out from the other substrates (textile, aluminium and microscopic-slide glass).

Previously, a study [29] was made of Raman measurements on polymer fibre and the potential for changing the polymer content due to the heat generated by radiation from a laser beam. The different parameters used for Raman were altered to identify potential annealing effects in the substrate or the film. This change of crystal content would then be detected in the Raman spectra, by moving the peak towards higher wavenumber. The parameters such as number of scans, exposure time, magnification and laser power, with different values, were combined and the combinations given below.
Accumulation scans from 1- 20,
Exposure time, 1- 20seconds,
Magnification, 20x and 50x,
Laser power, 0.1- 100%.

The Raman settings used before and after the test were 50x magnification, 50% laser power, 10 seconds and 5 times exposure.

The Raman spectra were normalized to provide a good comparison between the runs and helped identify each parameter's influence on structural content. Normalisation of Raman results was carried out by converting peak intensity to a scale between 0 and 1, which made it easier to make a more accurate comparison of the batches and their peak intensities. Growth rate or thickness was related to peak intensity, where low intensity was from a thin film. However, each sample of aluminium and textile was analysed by Raman at least twice at different locations. The Raman spectra required

mainly a fit of three Gaussian peaks, unless clearly microcrystalline or amorphous structure, which needed only two peaks.

5.3.3. Thermal analysis, Differential Scanning Calorimetry, DSC

Potential change of the bulk properties was investigated by thermal analysis with the most known technique, Differential Scanning Calorimetry, DSC. This helped compare yarn and fabric, and coated and uncoated material. [30,31] The change in the bulk properties of a polymer reflects on the thermal properties such as glass transition T_g and melting temperature T_m. The heat capacity of a polymer will depend on its structural content such as percentage of amorphous and crystalline phase.

The instrument and method

The Differential Scanning Calorimetry system was supplied by Mettler Toledo, TA instrument DCS12E [30], which helped identify material properties during heating and cooling. Looking at the thermal transfer properties of a material during heating and cooling allowed the determination of the glass transition temperature, T_g, and the melting point, T_m, of a polymer.

DSC techniques can study a polymer change in relation to heating and cooling in two ways, either by a constant temperature known as isothermal or by a steady increase of a set heat-rate (°C/ minutes) known as dynamic isothermal. [30,31] The isothermal method has a limit to only one direction either by increasing or reducing the heat. Dynamic isothermal allows instead studying both heating and cooling in one measure. The heating and cooling curve depends on how a material absorbs and releases the heat energy. The measurement can be done in a temperature-range from -40°C to 400°C with a heat-rate set from 0.1 to 20°C/ minute between 0 and 999 minutes. [30]

The polymer properties on heating and cooling will reflect on the ratio of amorphous and crystal content. The heating properties of a polymer substrate can be established by a material's capability of absorbed heat, ΔH during a melting process. The enthalpy, H of a polymer refers to the heat capacity, C_p between a range of temperature, T. Thermal changes will depend on the structure stability and eventual impurity in the sample. The heat capacity will be very specific for a polymer, when the changes are

much related to its properties. [30,31] A polymer such as polyester (Polyethylene Terephthalate) has a glass transition, T_g at ~70C° and melting temperature T_m at 260+5C°. [32] Both T_g and T_m can vary depending on the crystal content. Polyester is commonly known as being semicrystalline, which has a content containing both amorphous and crystal structures.

A typical “energy” curve for a polymer with crystal content starts with a slow increase, which suddenly accelerates into an upwards peak known as endothermic before returning and dropping further. Steady rise is due to the heat being absorbed into a material and the first small peak, endothermic relates to glass transition, T_g. Reduced curve height is due to higher viscosity, which releases the heat absorbed. Continuous increase of heat will result in re-crystallisation taking place, which does give out heat (exothermic). Added heat is required to keep the substrate at same temperature, which leads to the melting point, T_m of a polymer. Sometimes a polymer shows steps with the peaks, which refer to a material having different content, structures and properties. [30,31]

The sample was placed in a pan, which was sealed by a lid and dented on the top to reduce the dead space in the pan. Most common material used for the pan (figure 5.7.a) is aluminium, although gold can be used for certain cases. It is important to avoid impurities in both sample and pan, as this will have a significant effect on the measurement. An empty reference pan was combined with the sample pan and the two pans (figure 5.7.b) each placed on a sensor plate (figure 5.7.c). The two pans were heated up by a furnace (figure 5.7.d), which provided a uniform heat-flow below the sample and reference pan. [30,31]

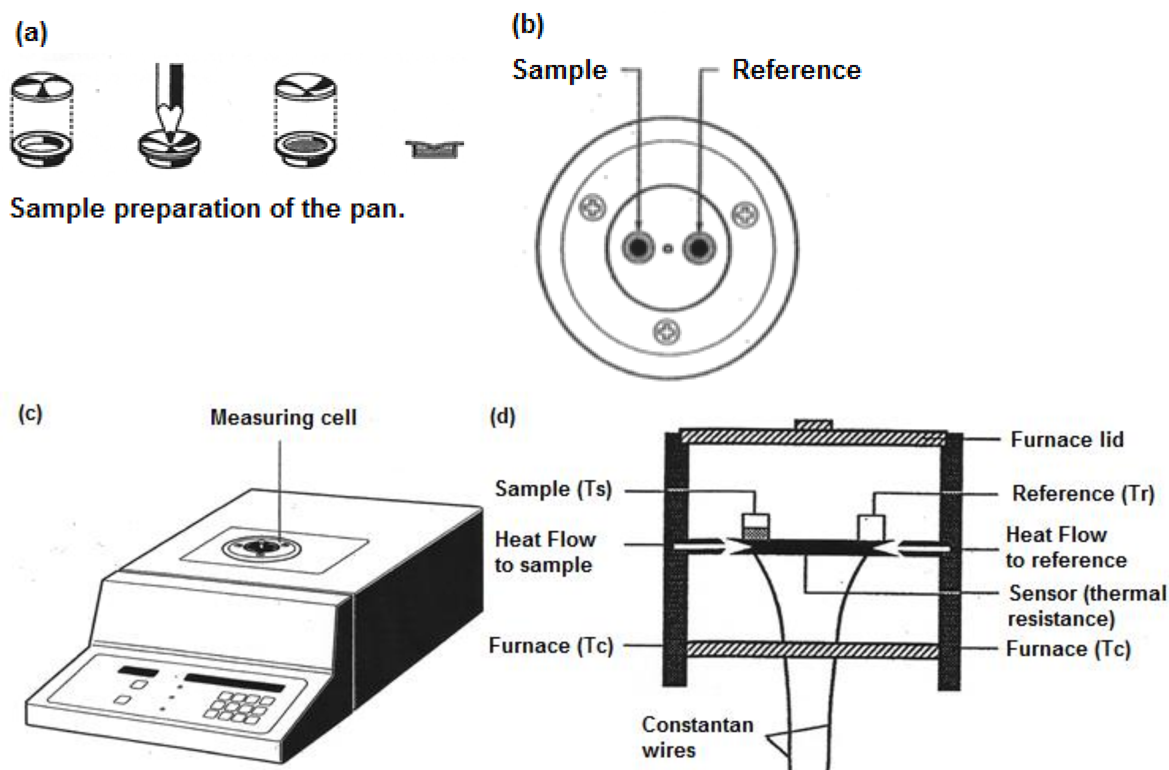

Figure 5.7. sample and reference to analyse in a DSC are prepared in each pan (a) and placed at the sample plate (b). The sample plate is accessed by lifting the furnace lid (d) at the top of the instrument (c) where the samples are placed and heated up (d). [30]

By comparing sample and reference pan, it was possible to calculate difference in heat, ΔQ and temperature, ΔT to get the heat capacity, C_p ($C_p = \Delta Q / \Delta T$) of the sample. The heat ΔH absorbed during the melting process and the heat released during crystallisation is proportional to the area between the curve and the baseline of the DSC. The peak area refers to the energy exchange (Enthalpy change, ΔH), which is measured by Joule per gram, J/g and the quantity of energy required to melt a sample will respond to the peak area. The enthalpy energy can be found by taking peak area divided by calorimetric sensitivity ($E = E_{In} x\ E_{rel}$) and sample weight (mg). [33,34]

The heat of fusion, ΔH_f was represented by the endothermic peak during melting and the heat loss during crystallisation, ΔH_c was given by the exothermic peak. The difference in ΔH_f- ΔH_c refers to the heat associated with the melting, which gives the percentage of crystal content by $(\Delta H_f-\Delta H_c)/ \Delta H_{100\%} x\ 100\%$. The $\Delta H_{100\%}$ value for polyester, PET is $166.5Jg^{-1}$. [35] The power (energy) required depends on the amount energy the material can absorb before melting.

Experimental

The samples measured were taken from each process stage such as uncoated with loomstate and calendered, conductive coat, evaporated aluminium, the plasma process of n-i-p-layers and sputtered ITO to compare and identify eventual change of the thermal properties. Both filaments and fabric were tested, the filaments were placed parallel in the pan. It is important that the samples have the same weight, as this affects the heating of the sample and the first targeted was ~8mg per sample. The second time of measurement the sample weight was reduced to 5±0.5mg, as less sample weight would provide a more detailed curve. Less sample weight was difficult when testing coated samples, which had higher weight than loomstate. Another crucial aspect was to place the sample at an identical position in the pan in order to not affect the melting procedure. The heating up was set to a step of 10°C/ minute with a temperature range from 50°C to 300°C.

5.3.4. Electrical properties

Current-voltage properties were measured by using I-V and four-point-probes. At the start of the project, these tests were the main ways of characterising the silicon thin films. The problem with the textured surface was the difficulty in placing the probe onto the surface without going through or sliding off a filament or yarn which was needed to make contact. Due to issues with the textured substrate and the measurement, this was soon stopped.

The instrument and method

The DC voltage source manufactured by Agilent Technologies (HP4140B) was used to carry out the I-V measurement. The four-point-probe was performed using a Keithley 224 current source and a 160B digital multimeter.

Measurement of I-V was carried out by two probes, one touching the back contact and the other the top contact. Top contact of the samples was often evaporated aluminium dots, but sputtered ITO is the top contact material used in the final cell device. The back contact was evaporated aluminium. Sometimes the measurement was instead

made between two top contacts to measure resistance related to the top part of the cell. The measurement of current flow was an indicator for resistance in the film. Altering the current flow direction between top and back contacts (changing between forward and reverse bias) helped determine the sample structure and resistance, R (R=V/ I). The probes for the current voltage measure could either produce a flow between the bottom and top contact (sandwich configuration) or between two top contacts (gap configuration).

As the deposited films were very soft, it was important to make sure the probes were placed on the surface and not penetrating through the film or substrate, which would then short circuit. Initially a sharp probe-needle was used, but soon exchanged to a flatter one, which helped to give a reliable measurement. Different designs of tips and larger probe diameters with springs were evaluated and a flat probe was chosen for future trials. The bigger and flatter probe tip helped avoid a breakage of the tip, scratching of the film or penetration through the film or substrate.

A more applicable test for surface resistance (sheet resistance) is a four-point-probe. Four-point-probe measurements consist of four probes in line with a small fixed distance between them (figure 5.8.). The disadvantage with four-point-probes was the necessity of being placed on the same horizontal surface for the probes to make contact between them, which was more difficult with a textured surface. [36,37] Therefore measuring textiles with textured surface has proven more difficult, which will generally increase the level of error in the measurement. Measurement on textile requires the probes being placed on same filament, yarn to avoid disruption or break in the connection. The conductive polymer coating on the textile gave a smoother and more uniform substrate surface, but still often too uneven to carry out an accurate four-point-probe measure.

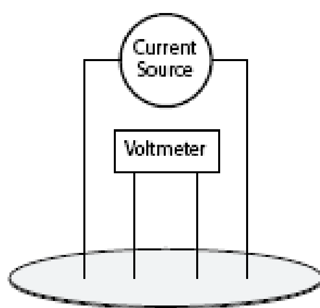

Figure 5.8. the configuration with four-point-probe. [37]

Experimental

The I-V measurement was carried out by altering the voltage direction and location of the two probes. Locations of the probes were done by back contact being at fixed location, while the top-contact was moved to different locations. Top-contact was often moved and measured at three different locations before the back contact changed location and the top-contact again measured at three locations. Measurement was carried out several times on each substrate. Aluminium and microscope-slide glass were measured along with the textile substrate. I-V was carried out by computer setting the voltage in a series of step increases and decreases and measuring the current at each step. Initial voltage range was from 0 to 1V with an increment of 0.1V, but soon the voltage range was increased from 0 to 10V with increments of 0.1 to 1V.

Some of the I-V measurement was done by heating up the sample between 35°C and 105°C, which helped characterise potential trapped charges and provide the thermal activation energy for conduction.

5.3.5. Optical properties

Optical spectroscopy measured light transmission and absorptance of a cell and the values were influenced by the structure content of the thin film. The transmission of the deposited thin film was measured on microscope-slide glass to satisfy the requirement of a transparent substrate. The disadvantage of using a non-textile substrate was the slight difference in the structure growth.

From the transmission data, the absorption coefficient was derived, which helped produce a Tauc plot and the band-gap energy. The optical band-gap was given by the intercept on the photon energy axis of the square root function of absorption times photon energy ("Tauc plot"). Cube root function was applied too, after Cardona [38] suggested this being a better fit for nanocrystal content.

The instrument and method

A Shimadzu UV 3100 dual-beam Spectrophotometer was used to measure the light transmission spectrum of deposited films on glass substrates. The light source contained both Deuterium and Halogen lamps, and a series of gratings which provided a spectral range from 190nm (UV) to 3200nm (NiR). The instrument also had a reflection attachment for the measurement of reflection spectra.

The sample compartment contained a sample and a reference position, which gave a choice of whether to exclude or include the influence of the glass-substrate. Before measurement, the instrument was calibrated against the wavelength range used and a sample at the reference holder was optional. Light transmission is performed by directing an incident light-beam towards a sample, which will result in the light being reflected, transmitted, diffused and absorbed (figure 5.9.). The total incident light is the same as the sum of transmitted, absorbed and reflected light. By examining the transmission spectrum, absorption can be expressed as weak, medium and strong (figure 5.10.). [39]

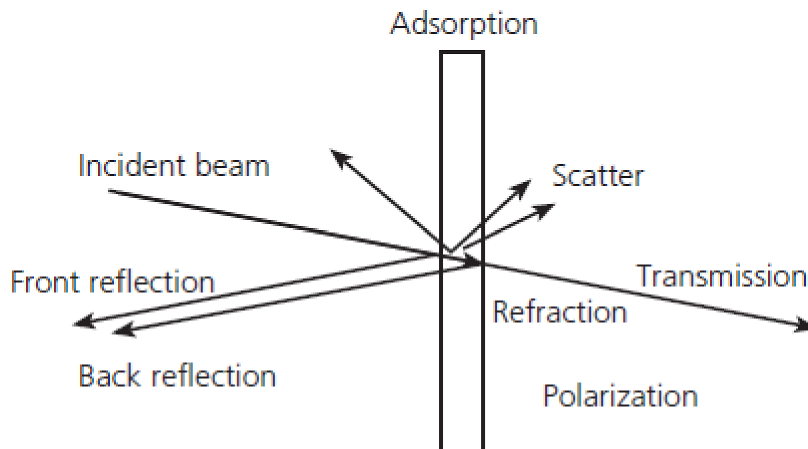

Figure 5.9. explains the change of incident light by it being split into different directions such as reflection and scattered light. [40]

Transmission comes by measuring the intensity of the incident light before (I_0) and after (I_1) passing through the substrate. The ratio (I_1/I_0) of the two values is known as transmittance and is given in percentage as Transmission, T= %/100. Optical

absorption can be calculated from the transmission, [log(1/T)]. The absorption coefficient, α is the absorption per unit thickness of material.

To determine absorption coefficient α(λ) of thin film, a transmission spectrum was measured in the visible and infrared region. Transmission was measured often from 350 to 900nm in wavelength, which contained at least one interference fringe with a second fringe starting to appear. The diagram below illustrates a typical example of the transmission spectrum of an amorphous silicon deposition. [39,41]

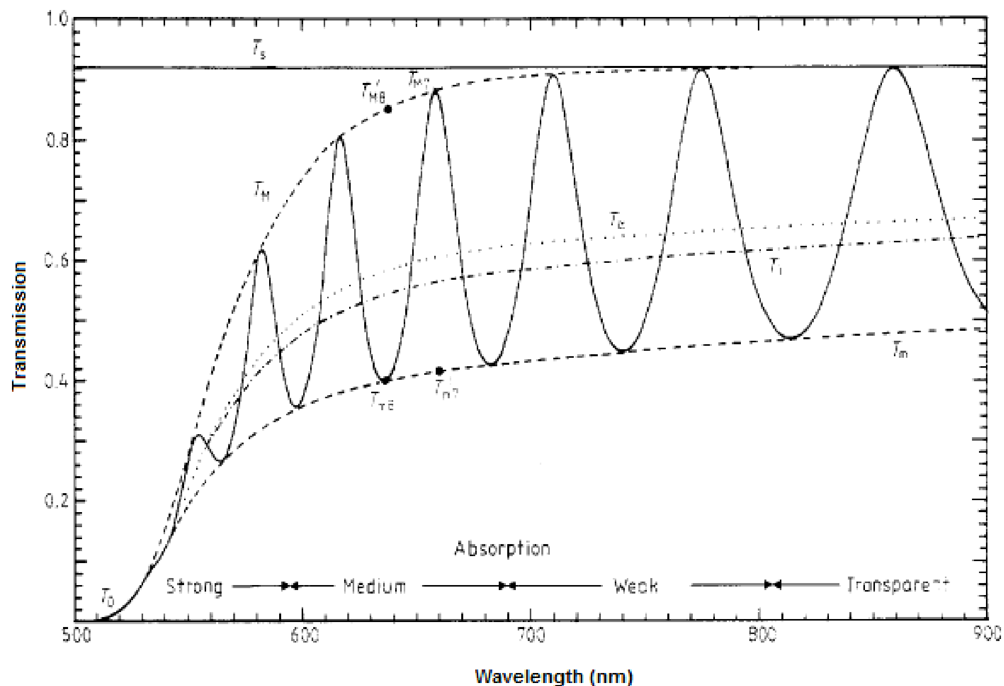

Figure 5.10. transmission spectrum and development of the interference fringes for an amorphous silicon film of 1μm. [39]

Several factors affect the transmission [T= function of (α, λ, n, n_s, n_0, d)] of thin films on glass substrate such as absorption (α), wavelength (λ), film thickness (d) and refractive index (n), refractive index of substrate (n_s) and the environment (usually air) (n_0). Film thickness, d is calculated [$d= \lambda_1 \lambda_2 / 2(\lambda_1 n_2 - \lambda_2 n_1)$] by taking refractive index and the wavelength at the lowest and highest transmission point on the shortest interference fringes. [39,41]

A Tauc plot helped to get the band-gap energy value from the absorption coefficient. By using a Tauc plot [$(\alpha hv)^{1/2} = \beta(E-E_g)$], which contains photon energy ($E=hv$) and a constant (β), the band-gap energy value can be obtained. Calculation of the absorption coefficient is often based on this square root dependence for amorphous silicon. [42,43] A combination of square root $(\alpha hv)^{1/2}$ and cube root $(\alpha hv)^{1/3}$ was necessary to get a linear fit and correct band-gap value for a mixed structure content such as crystal phase in amorphous matrix in a silicon thin film. [40,41] Cube root dependency for light transmission has been explained as caused by stress in the thin film structure. [38] Higher root number than cube root for nanocrystal content has been considered. Empirical attempts to gain a straight line with nanocrystal content used root values such as $\sqrt{}^{1/4}$ and $\sqrt{}^{1/5}$, which both gave a straighter line. [44] Root value of $\sqrt{}^{1/5}$ gave a band-gap value same as crystal silicon at 1.1eV, while a value of $\sqrt{}^{1/4}$ gave a higher value of 1.4eV.

Why the square root works for amorphous was explained by the optical transition between valence band and conduction band depending on the variation with energy of the "density of states" in each band, $_g(E) \sim (E_V-E)^{1/2}$ for valence band and $_g(E) \sim (E_V-E_c)^{1/2}$ for conduction band. The transition between valence and conduction bands in nanocrystal material was different due to the indirect band-gap of the small crystallites. Depending on the ratio of crystal to amorphous content, a higher percentage of crystallinity required rather $(\alpha hv)^{1/5}$ than $(\alpha hv)^{1/4}$. [44] It was experienced, that structures with two band-gap values (square and cube root) could receive a single band-gap energy value between 2 and 3eV. [42] The value above 2eV was explained as caused by very small and fine nanocrystals embedded in the amorphous structure like quantum dots. [44,45,46]

Two different band-gap values improve optical properties and the band-gap energy value reflects on the crystals size, when larger crystals such as microcrystalline has a band-gap value closer to amorphous (1.8eV), while smaller crystals such as nanocrystals have values toward 1.1eV (crystal silicon) (figure 5.11.). [42,47] The two values relate to quasi-direct band-gap at 1.8eV (amorphous) and indirect band-gap at 1.1eV (crystal) [48] with absorption below 1.1eV (0.6 to 0.8eV) related to the bandtail from thermal disorder and urbach bandtail from structural disorder. The thermal-disorder related absorption comes from the phonon states in the crystals in the amorphous structure. [49] These disorders/ defects are common in crystal growth with mixed structure and occur in the boundary area between crystal and amorphous area. [50,51,52,53] Absorption at low energy was much depending on the dangling bonds,

when absorption at high energy related to the amorphous phase. [54] The carrier transport was suggested [44,47] to go through the crystalline path at the boundary, which often contained small crystallites. Reduced band-gap energy value refers to increased crystal phase in the amorphous structure and the ratio of amorphous and crystal phases and crystal size determine the band-gap energy. [54,55]

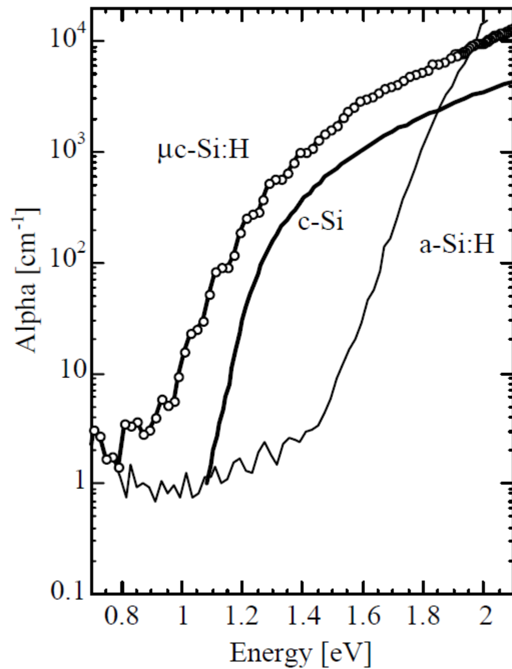

Figure 5.11. optical absorption and band-gap energy for the three silicon materials, amorphous, micro-crystal and crystal. A mixed structure crystal phase follows much of the crystal curve. [52]

The different plots of absorption coefficient against energy can be divided into three areas (figure 5.12.) such as extended states-to-extended states, tail states-to-extended states, and defect states-to-extended states. The extended-to-extended part refers to absorption at the highest energy, from excited electrons moving from valence band to conduction band. [43, 44,47] The band-gap value for thin film silicon will depend on structure content, when nanocrystal growth in the amorphous matrix will relate to a value between crystal silicon at 1.1eV and 1.8eV, when amorphous occur from 1.9 to 2.2eV. [56] A mixed structure containing different crystal size had often band-gap values such as 1.1eV (nano-sized) and 1.6eV (micro-sized) together with amorphous value at 1.8eV. The band-gap values for the crystal became closer towards the amorphous value as the crystal became larger. [51,55]

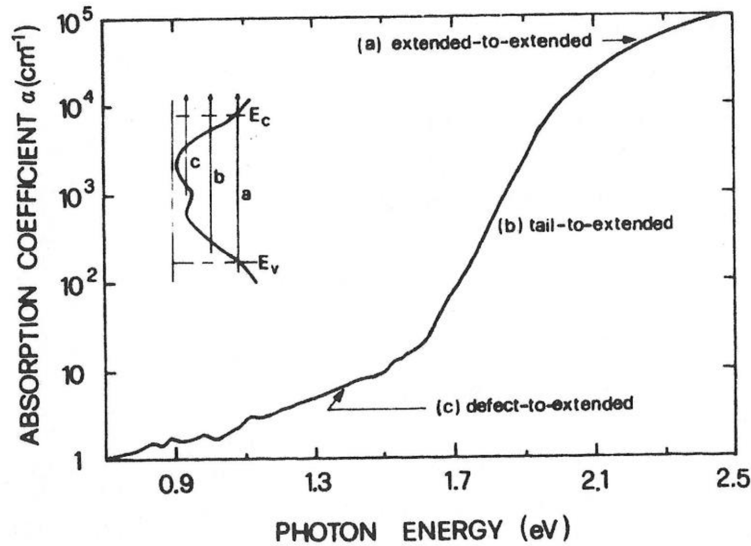

Figure 5.12. illustrates how optical absorption can be divided into three areas due to different states in the material. [43]

Experimental

Optical transmission was measured with a Shimadzu spectrometer at wavelengths between 900 and 300nm. The standard optical transmission spectrum measurements of the microscope-slide glass were done with the incident light normal to the plane of the substrate and with the sample orientated in one given direction. Some comparisons at other orientations were attempted and some changes in optical properties were observed.

5.4. Summary

A process route for silicon thin film on woven polyester was established by combining process methods from both the textile and the semiconductor industry. The preparation of the textile substrate was based on conventional methods in today's textile industry, while the thin film's deposition was based on methods from the semiconductor industry such as evaporation, plasma enhanced chemical vapor deposition and RF-sputtering. The vacuum based semiconductor processes were unknown for the textile substrate, which resulted in much time spent on establishing the process methods allowing textile substrate to be used.

In the work of depositing silicon thin films, with different modifications to the film structure, the process recipe has been determined to make it possible to use a textured substrate such as woven polyester. Changes took place in the intrinsic silicon, encouraging crystal growth in the amorphous structure. An Orthogonal Statistical Design “Taguchi model” was one of the methods to decide which parameters encourage crystal growth. The Taguchi model had as its aim to introduce hydrogen as an attempt to increase crystal content in a process with a temperature restricted at ~200°C. Other changes were introduced, such as a clean-break between the phosphorus-doped layer and the intrinsic layer, with altered process parameters of the three layers to encourage crystal growth in the intrinsic layer’s amorphous matrix. Doped layers had their parameters altered too, to increase the crystal content in each of the layers.

Analytical methods have been addressed for analysing silicon thin film deposition and its surface, structure, electrical and optical properties together with thermal analysis of the textile substrate.

5.5. References

1 S. Jardine, *Thin film silicon on textiles by microwave plasma chemical vapour deposition*, PhD Thesis, Heriot-Watt University, UK (2006)

2 K.L. Hatch, *Textile science*, West Publishing Company, ISBN: 0-314-90471-9 (pp.472) (1993)

3 H.U. Poll, U. Schladitz and S.Schreiter, *Penetration of plasma effects into textile structures*, Surf. Coat. Tech. **142-144**, p.489-93 (2001)

4 N. De Geyter, R. Morent and C Leys, *Penetration of a dielectric barrier discharge plasma into a textile structures at medium pressure*, Plasma sources Sci. T. **15**, p.78-84 (2006)

5 C. A. Bishop, *Vacuum Deposition onto Webs, Films and Foils*, Material Science and Process Technology Series, ISBN: 978-08155-1536-4, (pp.650) (2006)

6 Whitford, industrial coating guide by application of textile, www.whitfordww.com/industrial/app-textile.html (10/11-2012)

7 M. Skrifvars, W. Rehnby and M. Gustafsson, *Coating of textile fabrics with conductive polymers for smart textile applications*, Ambience **08**, Sweden, p.100-3 (2008)

8 BOC Edwards, Auto 306 Vacuum Coater with Turbomolecular Pumping System, E09-03-860, Issue G, Installation and maintenance Instructions 1, (pp.70) www.bocedwards.com

9 F. Ibrahim, *Photo-oxidation of amorphous silicon carbon alloys: preparation and mechanistics*, PhD Thesis, Heriot-Watt University, UK (1992)

10 MEMSnet- An information portal for the MEMS and Nanotechnology community, Dry etching-, when do I want to use dry etching, www.memsnet.org/mems/processes/etch.htlm (11/11/2012)

11 M.P. Bonnar et.al, *Hydrophobic fluorocarbon and organo-silicon condenser tube coatings deposited by Plasma enhanced CVD*, 12th International Symposium on Plasma Chemistry **1**, p.99-104 (1995)

12 Y.-H. Taka, K.-B. Kima, H.-G. Parka, K.-H. Leeb and J.-R. Leeb, *Criteria for ITO (indium–tin-oxide) thin film as the bottom electrode of an organic light emitting diode*, Thin Solid Films **411**, p.12–6 (2002)

13 G.Z. Yin and D.W. Jillie, *Orthogonal Design for Process Optimization and its application in Plasma etching*, Solid State Technology **May**, p.127-32 (1987),

14 R. Yang, *A Systematic Statistical Approach to polypropylene Fibre process technology*, PhD Thesis **1**, The School of Textiles, Galashiels, UK, p.64-90 (2000)

15 G. Yue, B. Yan, G. Ganguly, J. Yang, S. Guha and C.W. Teplin, *Material structure and metastability of hydrogenated nanocrystalline silicon solar Cells*, Appl. Phys. Lett. **88**, 263507 (pp.3) (2006)

16 X. Liao et al., *Impacts of nano-structures in p- and i-layer on the performances of amorphous silicon solar cells*, Phys. Status Solidi C **6** (3), p.696–9 (2009)

17 T. Söderström, F.-J. Haug, V. Terrazzoni-Daudrix and C. Ballif, *Optimization of amorphous silicon thin film solar cells for flexible photovoltaics*, J. of Appl. Phys. **103**, 114509 (pp.8) (2008)

18 X. Liao et. Al., Impacts of nano- structures in p- and i- layer on the performances of amorphous silicon solar cells, Phys. Status Solidi C **6** (3), p.696-9 (2009)

19 C. Voz, D. Peiro´, J. Bertomeu, D. Soler, M. Fonrodona and J. Andreu, *Optimisation of doped microcrystalline silicon films deposited at very low temperatures by hot-wire CVD*, Materials Science and Engineering **B69–70**, p.278–83 (2000)

20 W. Jin-Liang and W. Er-Xing, *Characterization of doped hydrogenated nanocrystalline silicon films prepared by plasma enhanced chemical vapour deposition*, Chinese Physics **16** (3), p.848-53 (2007)

21 A. Dussana, R.H. Buitragob and R.R. Koropeckib, *Microcrystalline silicon thin films: A Review of physical properties*, Microelectronics Journal **39**, p.1292–5 (2008)

22 R. Saleh and N.H. Nickel, *Raman spectroscopy of B-doped microcrystalline silicon films*, Thin Solid Films **427**, p.266–9 (2003)

23 L. Qing-Song el at., *Effect of substrate temperature on the growth and properties of boron-doped microcrystalline silicon films*, Chinese physics **15** (1), p. 213-8 (2006)

24 T. Saski at el., *Structural study of p-type µc-Si layer for solar cell application*, J Non-Cryst Solids **266-269**, p.171-5 (2000)

25 S. Minhji at el., *Boron-doped silicon film as a recombination layer in the tunnel junction of a tandem solar cell*, Journal of Semiconductors **30** (6), 063001 (pp.4) (2009)

26 Z. Li, X. Zhang and G. Han, *Electrical and optical properties of boron-doped Nanocrystalline silicon films deposited by PECVD*, Phys. Status Solidi A **207** (1), p.144-8 (2010)

27 M. Kondo, Y. Nasuno, H. Mase, T. Wada and A. Matsuda, *Low-temperature fabrication of microcrystalline silicon and its application to solar cells*, J Non-Cryst Solids **299–302**, p.108–12 (2002)

28 Scanning Electron Microscopy of Hitachi 2700, www.semservice.com/s2700.html (10/11-2012)

29 H. Liem and L.Y. Yeung, *Segment self-orientational behaviour in shape memory polymer thin films probed by Raman spectroscopy*, J. Appl Polymer Sci. **105**, p.765-70 (2007)

30 Mettler Toledo, *Mettler Toledo TA instrument DSC12E, Operating Instructions*, (pp.40) (1996) www.mt.com

31 C. Schick, *Differential scanning calorimetry (DSC) of semicrystalline polymers*, Anal Bioanal Chem **395** (6), p.1598-11 (2009)

32 J.M.G. Cowie, *Polymers: Chemistry & Physics of modern materials, 2nd edition*, Blackie Academic & Professional, (pp.436) (1991)

33 R.M. France and R.D. Short, *Plasma treatment of polymers, effects of energy transfer from argon plasma on the surface chemistry* of poly(styrene), low density poly(ethylene), poly(propylene)and poly(ethylene terephthalate), J. Chem. Soc. Faraday Trans. **93** (17), p.3173-8 (1997)

34 S. Badhra and D. Khastgir, Degradation and stability of polyaniline on exposure to electron beam irradiation (structure-property relationship), Polymer Degrad. Stabil. **92**, p.1824-32 (2007)

35 J.D. Menczel et al., *Differential Scanning Calorimetry (DSC), Thermal Analysis of polymers*, Fundamentals and Applications **Chapter 2**, John Wiley& Sons Ltd., ISBN:9780471769170 (p.7-239) (2009)

36 J.N. Zemel, *Nondestructive evaluation of semiconductor, Materials and Devices*, NATO advanced study institute series B, Phys. **46**, ISBN 9780306402937 (1979)

37 *Electrical Characterization of Photovoltaic Materials and Solar Cells with the Model 4200-SCS Semiconductor Characterization System I-V, C-V, C-f, DLCP, Pulsed I-V, Resistivity and Hall Voltage Measurements*, Keithly application note series No. 3026, (pp.16).

38 L.D. Laude, F.H. Pollak and M. Cardona, *Effects of Uniaxial Stress on the Indirect Exciton Spectrum of silicon*, Physical review B **3** (8), p.2623-36 (1971)

39 R.J. Swanepoel, determination of the thickness and optical constants of amorphous silicon, J. Phys. E. Sci. Instr. **16**, (pp.16) (1983)

40 C. Tams and N. Enjalbert, *The Use of UV/Vis/NIR Spectroscopy in the Development of* Photovoltaic Cells, application note PerkinElmer, Inc. and INES, Institut National de l'Energie Solaire, (pp.6) (2009) www.perkinelmer.com

41 A. Ganjoo and R. Golovchak, Computer program PARAV for calculating optical constants of thin films and bulk materials: Case study of amorphous semiconductors, J. Optoelectron. Adv. M. **10** (6), p.1328-32 (2008)

42 Q. Cheng, S. Xu K. Ostrikov, *Structural evolution of nanocrystalline silicon thin films synthesized in high-density, low-temperature reactive plasmas*, Nanotechnology **20**, 215606, (pp.8) (2009)

43 A. Frova and A. Selloni, *The optical threshold of hydrogenated amorphous silicon*, in Tetrahedrally-bonded amorphous semiconductors, eds D. Adler and H. Fritsche, Institute for Amorphous studies series, ISBN-0-306-42076-7, p.271-84 (1985)

44 B. Yan et al., *On the bandgap of hydrogenated nanocrystalline silicon thin films*, Photovoltaic Specialists Conference (PVSC) **35th IEEE**, p.003755-60 (2010)

45 A.A.D.T. Adikaari, J.D. Carey, V. Stolojan, J.L. Keddie and S.R.P. Silva, *Bandgap enhancement of layered nanocrystalline silicon from excimer laser crystalisation*, Nanotechnology **17**, p.5412-16 (2006)

46 D. Das, *Quantum confinement effects in nano-silicon thin films*, Solid State Commun. **108** (12), p.983-7 (1998)

47 B. Yan, G. Yue, X. Xu, J. Yang and S. Guha, *High efficiency amorphous and Nanocrystalline silicon solar cells*, Phys. Status Solidi A **207** (3), p.671-7 (2010)

48 S. Reynolds, *Carrier mobility, band tails and defects in microcrystalline silicon*, *16 ISCMP: Progress in solid state and molecular electronics, ionics and photonics*, J. of Phys.: Conf. Series **255**, (pp.12) (2010)

49 G.D. Cody, T. Tiedje, B. Abeles, B. Brookes and Y. Goldstein, *Disorder and the Optical- Absorption Edge of Hydrogenated Amorphous Silicon*, Phys. Rev. Lett. **47** (20), p.1480-3 (1981)

50 W.J. Soppe, C. Devilee, M. Geusebroek, J. Löffler and H-J. Muffler, *The effect of Argon dilution on deposition of microcrystalline silicon by microwave plasma enhanced chemical vapor deposition*, Thin solid films **515**, p.7490-4 (2007)

51 X. Deng and E.A. Schiff, *Amorphous Silicon Based Solar Cells*, edited by Antonio Luque and Steven Hegedus, Handbook of Photovoltaic Science and Engineering, John Wiley & Sons, UK, ISBN: 9780471491965, p.505–65 (2003)

52 A.V. Shah et al., *Material and solar cell research in microcrystalline silicon*, Sol. Energ. Mat.Sol. C. **78**, p.469-91 (2003)

53 W.G.J.H.M. van Sark, A. Meijerink, R.E.I. Schropp, J.A.M. van Roosmalen and E.H. Lysen, *Enhancing solar cell efficiency by using spectral converters*, Sol. Energ. Mat.Sol. C. **87**, p.395-409 (2005)

54 S. Klein, F. Finger, R. Carius, T. Dylla and J. Klomfass, *Relationship between the Optical absorption and the density of deep gap states in microcrystalline silicon*, J. Appl. Phys. **102**, 103501 (2007)

55 X. Xu, J. Yang, A. Banerjee, S. Guha, K. Vasanth and S. Wagner, *Band edge discontinuities between microcrystalline and amorphous hydrogenated silicon alloys and their effects on solar cell performance*, Appl. Phys. Lett. **67** (16), p.2323-5 (1995)

56 A. Gajovic et al., *Nanostructure of thin silicon films by combining HRTEM, XRD and Raman spectroscopy measurements and the implication to the optical properties*, Appl. Surf. Sci. **254**, p. 2748-54 (2008)

6. Results and discussion

6.1. Introduction

After experience, that woven polyester was damaged by using the process settings from a previous project, [1] much of the work became focussed on establishing process parameters, which allowed a textile substrate to be used and gain good properties for the silicon thin film. The aim was to produce a thin film with crystal content to gain a more durable structure, compared with the previous recipe which was amorphous content with potentially high light-degradation.

Several modifications to the original process settings were done, but also an additional conductive layer was applied as support to the back contact. Conductive substrates were considered combined with different weave structure of polyester.

Measurement of thin film properties on textile substrate proved more difficult than first anticipated due to the textured surface and the deposited coat charging up in scanning electron microscopy with usual beam power. Most standard analytical methods were discarded due to imaging or contacting difficulties. Electrical properties had first been pointed to be the main analytical tool, but soon discarded due to the much textured substrate. The textile was too uneven to provide a contact between the probes for I-V or four-point-probe measurement. The methods possible to use were Raman spectroscopy and light transmission, which became the standard techniques used to analyse the deposited silicon thin film.

6.2. Textile for plasma process

6.2.1. Introduction

The work prior [1] to this project worked with substrates such as glass, silicon wafer and nonwoven web (60gsm thermal bond random fibre direction), which gave no problem to the plasma process. Later the nonwoven sample was tried again combined with the woven polyester and a slight change by relaxation and curled edges on the

web were experienced. This helped to conclude how an open and light web becomes less influenced than a heavier and denser weave. This helped also to address the problem with heat being trapped in the substrate. Different substrates were evaluated to identify the cause why sometimes the substrate melted at a process temperature of 100°C below the polyester's melting point (~256°C). [2]

6.2.2. Different textile substrate

Different polyester substrates such as plain and twill weave, nonwoven and film were coated with an intrinsic silicon film (*silane, SiH_4 rate 0.82sccm, argon, Ar 18.2sccm at 200°C with a chamber pressure at 0.5Torr and Microwave power of 800Watts for 20 minutes*) to evaluate how different material structures, quality and yarn type affected the quality and structure of the deposited film. As many of the flexible thin films available on the market are based on polymer film [3,4,5], a polyester film (J&D Wilkie Ltd) was tried too.

Twill weave was found to melt easier than plain weave due to its denser structure, which easily trapped heat through an increased area for etch and deposition on the fibre, filament and structure. [6,7,8] Twill was discontinued and instead the focus was on plain weave, which reduced the plasma penetration through the structure and the yarn. [6,9,10] Depth of gas species travelling through the textile structure depended on the gas species mean-free path and the space between yarn and filament, discussed in *chapter 2, section 2.6*. Too deep plasma penetration changed the bulk properties of a polymer, which this work did not target. The aim was to deposit on the filament, yarn surface without changing the polymer's original bulk properties.
It was experienced that polyester film was more heat sensitive than the plain weave by being deformed and melting. The nonwoven substrate used in previous work [1] was compared too, which was less affected than woven polyester, but did still show some change at the edges where the fibres bonded or melted. However, the open nonwoven web was not suitable as a substrate for silicon thin film solar cell, where the fibre orientation was too random and open to produce a working solar cell.

Most of the different plain weaves (247gsm, 164gsm, 86gsm and 68gsm, supplied by J&D Wilkie Ltd) proved to be heat-sensitive by easily changing shape during the plasma process, while the original weave of 247gsm with 210 filaments in each warp and weft yarn proved to be the best option in relation to withstand the plasma process

without structural change. By comparing the different plain weaves (247gsm, 164gsm, 86gsm and 68gsm) knowledge was gained on how a fabric's weight and density influenced the fabric performance during the plasma treatment and the quality of the thin film deposition. Density was considered indirectly by the number of warp and weft yarns per centimetre; yarn thickness and structure, such as open or close weave, were considered. Fabric weight and yarn density proved not to have a major impact on the fabric performance during the plasma process or the properties of deposited film.

The weave of 247gsm containing 210 filaments in both warp and weft yarn was evaluated against same weave structure with different yarn quality such as monofilament and spun yarn (staple fibre). The spun yarn being more textured required calendering (heat-treatment) at higher temperature to gain a smooth yarn surface, which led to a stiffer handle. The monofilament instead was heat-sensitive and melted as a result during the plasma process. The first option of weave structure 247gsm with 210 filaments was still the best option, being the most stable.

A possible change of structure towards melting can often occur as a domino effect, when one yarn starts to relax due to higher heat and the yarn beside changes due to the extra heat from the first change, which continues. The extra energy encourages the effect to develop and the area becomes larger with increased speed as it develops.

6.2.3. Calendering of textile substrate

The calender process was controlled by temperature and time, whilst pressure was constant (the weight of the lid of 4kg). A flat fabric surface was necessary, to gain a good coat and lamination performance. A good calender is defined by providing a fabric with a good bond and flat surface of warp and weft yarn and still be able to flex the substrate without breaking the bonds. Too much heat and time would instead give a too flat and stiff fabric handle, which would restrict the flexibility and produce a brittle substrate. The handle of a treated fabric was evaluated by flexing to observe eventual stiffness or break of a fibre. Temperature and time were set carefully to receive a good handle and coating adhesion. Different temperatures against time were evaluated to find best combination, which provided a flat surface with good adhesion, allowing flexing without damage to the coated substrate (table 6.1.). After run four, foil (aluminium) was added between the sample and the top and bottom plates, to avoid impurity. Adding the foil required some extra runs to verify the settings, when the heat

in the sample increased and permanent crease-marks from the foil were experienced in the polyester weave. The foil had to be placed carefully on the plate and substrate to avoid crease marks in the substrate. With increased temperature of the foil it stuck to the fabric, which made it necessary to set temperature as high as possible with a short process time to avoid melt of sample or foil.

Table 6.1. Process settings used to calender the textile substrate.

Trial run	Temp., °C	Time, min.	Comments regarding outcome
1	150	5	Some fibres melted partly, but overall the sample became too stiff.
2	200	2	Neither smoothed the surface nor bonded at the cross of warp and weft yarn.
3	220	2	Neither smoothed the surface nor bonded at the cross of warp and weft yarn.
4	230	2	A slight stiffness due to a bond of warp and weft yarn, but still too soft.
5 (foil)	200	5	Too soft after not receiving enough bonding.
6 (foil)	220	5	Received a too stiff handle due to a good bond between warp and weft and partly melted. Foil stuck to the fabric.
7 (foil)	240	5	Melted completely. Foil stuck to the fabric.
8 (foil)	240	2	Stiff handle due to too well bonded between warp and weft and the foil stuck to fabric.
9 (foil)	230	1	The bond between warp and weft was not enough, which left a too soft and flexible fabric.
10 (foil)	260	1	Did melt the sample partly, but also too stiff handle.
11 (foil)	240	1	Bonding enough for providing a smooth surface and enough stability in the fabric to withstand the plasma.

Initial test at 150°C resulted in partly melting the textile, which led to reduced time with increased temperature to allow the calendering effect being on the fabric surface and not through the textile bulk. Process condition of 1 minute and 240°C gave a good bond (filament, yarn and fabric) allowing plasma process without damage to the substrate and a good handle to provide a flexible product. Calendering the standard polyester weave of 247gsm (210 filaments in each warp and weft) was established as 1 minute at 240°C.

6.2.4. Heat evaluation of textile substrate

With occasional damage of the substrate occurring during the plasma process, tests were carried out to understand the cause of a textile sometimes being partly or complete melted. These tests were devised, such as argon-clean before plasma process of n-i-p-layer deposition, heat-gun, temperature-sticker and drying procedure of sample before plasma process.

- Argon-plasma was used to clean the chamber and substrate. Plasma clean with hydrogen is common in the semiconductor industry, but due to problem with excessive hydrogen, argon plasma was used here. Argon-plasmas (Ar rate at 18.2sccm) of 5 and 20 minutes were compared and after no difference in quality was observed, 5 minutes was chosen. Subsequently, this was later discarded after no difference was noticed and a concern was raised, that traces of argon left in the substrate or in the chamber supported a growth of amorphous structure.

- Thermal test was an attempt to understand the cause to damaged textile during plasma process. Hot-air was applied onto the face and back of the woven polyester to reconstruct possible heat-flow in relation with the textile substrate during plasma process. This test made it possible to identify the direction of the heat-source in relation to the deformation and melt caused by the excessive substrate temperature. Heat from above pushed the sample down and produced craters and waves, when heat from behind raised the fabric as shown below (figure 6.1.). The deformation in a textile could be in certain areas or to the complete substrate (textile). A difference between light and heavy weave was experienced, when lighter weave was less stable and easier to change.

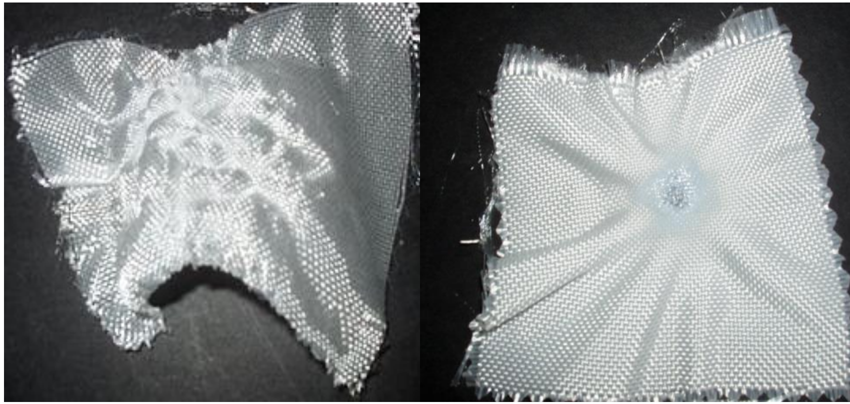

Figure 6.1. the left picture is hot-air applied from below, while right refers to heat applied above.

This helped to confirm the formation experienced during the plasma process (figure 6.2.). The excessive heat source from above was explained as being caused by a surface reaction, when the damage caused by heat from the back was more difficult to address.

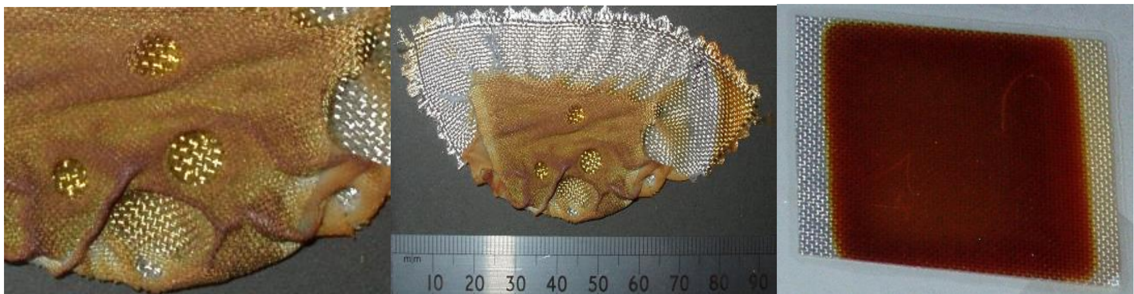

Figure 6.2. the two fabrics to left were damaged during a plasma process and had a typical combination with partly melted and untouched areas, while the right image is plasma treated textile without melt effect.

- Temperature-stickers were used to measure the temperature on the substrate surface, which helped establish the actual surface temperature. The temperature-sticker was placed on the substrate surface, which faced the plasma. Each sample had stickers in a temperature range from 150°C to 280°C to cover a large possible range of temperature. This test helped to establish that the front surface temperature was much higher than the displayed temperature from the thermocouple in the substrate-holder. It was found that a specific run with set and displayed temperature of 180°C had an actual surface temperature reaching ~240°C.

Several tests were carried out with the same conclusion, that the peak surface temperature was much higher than the displayed one. With the thermo-couple not registering this change, this indicated that the temperature change was locally on the surface and not in the substrate. The excessive heat experienced on the substrate surface was later explained as trapped moisture (surface facing substrate plate/ heater) and exposure to active hydrogen species (surface facing plasma). [11] Trapped moisture is a common problem [11] with textiles in vacuum processes. During evacuation of air from the chamber, the textile side facing the chamber has all moisture evaporated, whereas moisture at the back of a material was trapped between it and the substrate plate. The remaining moisture helped to increase the temperature, which caused the substrate to melt. The main issue with this work was caused by the natural moisture content of the textile, but also a contribution from the water-based conductive coat (polyaniline).

An attempt to avoid moisture in a sample was to implement a drying procedure between the metal evaporation and plasma processes. The sample was dried at ~100°C for 3 hours and thereafter stored in desiccators, which helped to minimise the risk of trapped moisture in the textile substrate and damage of the substrate during the plasma process.

6.3. Conductive option to support the back contact

6.3.1. Introduction

The evaporated aluminium proved too thin to provide a uniform cover on the rough surface of the textile substrate, which led to poor conductive properties. A thicker aluminium layer was not an option, as this would stiffen the substrate and introduce cracks during flexing of the substrate. To solve the problem different options were considered such as conductive substrates or additional coating layers.

6.3.2. Conductive substrate, material

The conductive substrates were prepared in the same way as plain polyester weave. The nickel etched mesh was an exception since it had already been treated prior to the

etch. The woven copper band (Federal Mogul) was too thick to calender. It was found that conductive substrates and especially woven ones were more heat-sensitive than polyester weave (240°C for 1 minute), which led to reduced temperature of 220°C for 1 minute (table 6.2.). The AmberStrand qualities withstood 240°C for 1 minute without being damaged, which can be due to the loose filament not being connected into a structure with trapped heat, which close weave experienced. Each quality was plasma treated twice, one sample with and without calender effect. All samples were plasma processed with same condition (*silane, SiH_4 rate 0.82sccm, argon, Ar 18.2sccm, 200°C, 700W, 20 minutes at 0.5Torr*). No difference between with or without calender were found, the sample performance were the same during the plasma process (table 6.3.).

Table 6.2. Calender parameters and performance for the conductive substrates which were evaluated.

Test run	Textile Supplier, quality	Fabric performance
1	AmberStrand®-Z-33-Ni	No visible change, slightly stiffer strand.
2	AmberStrand®-Z-166-Ag	No visible change, slightly stiffer strand.
3	Kuraray, Clarcarbo (280gsm)	240°C- too high, the sample got too stiff and (partly) melted. 220°C- the sample shrunk and got stiffer due to the uneven surface.
4	Technical Fibre Products, Carbon veil (30gsm)	With calender- slightly stiffer
5		Without calender- N/A
6	Technical Fibre Products, Carbon veil (80gsm)	With calender- slightly stiffer
7		Without calender- N/A
8	Ugitech, Sprintiss (300gsm)	Sample shrunk a lot due to a very open weave structure
9	Neltec, nickel etched screen mesh (440gsm)	N/A
10	Federal Mogul, woven polyester (1320gsm) with conductive yarn, DEW06090804.	N/A
11	Federal Mogul, woven polyester (1320gsm) with conductive yarn, DEW06090805.	N/A

Table 6.3. The conductive substrates during the plasma process.

Test run	Outcome from the Plasma process
1 & 2 AmberStrand	Possible to treat, but difficult to get a uniform tension of the strand attached to a microscopic-slide glass. The poor tension* of the strand on the slide resulted in poor deposition. The microwave power source had a high reflectivity of 38% during the process. This applied to the two qualities.
3 Kuraray	The weave shrunk even further during the plasma process, which led to a very uneven substrate. This quality was very sensitive towards heat, when it either changed shape, or melted partly or completely during the plasma process.
4- 7 Technical Fibre Products	No difference between with or without calender, except sample with had a slightly thinner deposition. No difference between the two weights was found or problem during the plasma process was experienced. A disadvantage, the surface contained loose fibres even after calender, which caused breaks in the deposit.
8 Ugitech	The weave structure was too open, which resulted in an unstable process and poor deposition quality. The open weave withstood the plasma process, but with too open weave structure to deposit a working solar cell. The microwave power source had a high reflectivity of 40% during the process.
9 Neltec	The screen-mesh with etched nickel (Neltec) melted completely during the plasma process, even when the process temperature was far below polyester's melting point.
10& 11 Federal mogul	The copper weave was possible to deposit. The problem was instead, with no calendered surface and very textured and open weave, this substrate was difficult to use.

None of the conductive materials were considered for future work.

6.3.3. Conductive substrate, coating

The other option was a conductive support layer to the non-conductive textile, which would smooth the textile surface and give conductive properties to the textile and enhance the thin aluminium layer. Many of the conductive products and coating methods used in the electronic/ semiconductor industry were not suitable for textile substrates.

The two options were considered:

- Quick Drying Silver Paint (G3691, Aldrich) by painting directly onto the textile;
- Polyaniline (Panipol OY) by "direct-coat" on the textile.

Silver paint was brushed onto the substrate and with a larger area to paint than the width of the brush resulted in a very non-uniform coat. Another disadvantage with the paint was recommendation of being air-cured, which led to moisture in the coat and melting during the plasma process. The moisture raised the substrate temperature and damaged the substrate. Silver paste was also considered to replace evaporated aluminium, but was discarded after experiencing trapped moisture and other problems occurring during the plasma process.

Even though polyaniline coat had high resistance ~200k Ohm, the conductivity in the coat was enough to support the evaporated aluminium. Polyaniline coated polyester weave (plain weave of 247gsm) with evaporated aluminium as a second coat was chosen for future runs. [12]

The recommendation was to minimise the use of water and thickening agent in the polyaniline mix, when these two ingredients reduce the conductive properties. The curing temperature and time were not to be above 124°C for more than ~20 minutes, when this would reduce the conductivity. However, no recommended combinations of temperature and time were given.

It was experienced in lab-scale that a batch of 5 or 10 grams was easier to mix with the recommended amount of thickening agent, 10% of a batch weight. Batch sizes larger than 10g became more difficult to mix, when the percentage of thickening agent required to be changed. Most batches mixed were based on 5g, which gave a good viscosity, coating performance and easy cure with a good conductivity.

The sample weight was checked from loomstate to coated substrate by using a sample by 5cm x 5cm: loomstate of 250gsm, washed and calendered at 356gsm and coated became 371.2gsm. The increase in weight during wash refers to the mechanical movement of the fabric and yarn, which make the fibres relax and shrink from earlier fixed position.

Coat by hand made it difficult to control the pressure applied onto the substrate and coat, which reflected on coat thickness and overall handle such as flex of coated

substrate. Too thick a coat resulted in a problem during the evaporation, when the samples become easily “burned”. Polyaniline (Panipol OY) in vacuum proved being more heat sensitive than the polyester weave. Changes in process parameters were required to avoid the polyaniline coated surface being damaged during exposure to thermal heat source during the plasma process or radiative source during the evaporation.

The resistance in coated samples (5 x 5cm) was measured by ohmmeter after the coated sample was left for 24 hours. Measurement was across the sample and categorised by the distances such as short <2cm and long >2cm and a common resistance was 60±10Ω for short distance and 110±10Ω for longer.

Evaporation

It was found that the polyaniline coated substrate was occasionally burned (figure 6.3.) during evaporation, which led to recommendation of reduced evaporation time from 5 to 3 minutes or less depending on coat thickness. With no instrument to measure the thickness of evaporated aluminium, thickness was estimated by observing the aluminium deposit on the chamber window. The “burned” areas on the coated aluminium appeared either as grey, black or soot patches which depended on the grade of damage. This was named as “carbonised” areas, which exhibited very high resistance with very little or no current flow.

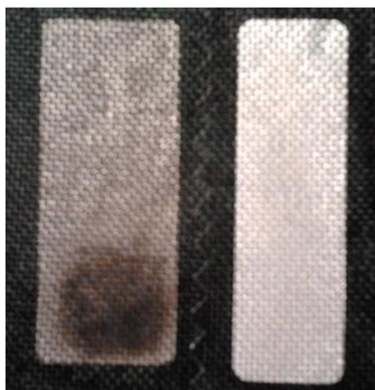

Figure 6.3. the left sample shows an example of burned area, which occasionally occurred with extended process time. This compared (right) with a non-damaged aluminium evaporation.

Plasma Process

Polyaniline coated textile showed problems with the plasma process by melting at a temperature and process parameters used previously for uncoated textiles. The process time and temperature required to deposit n-i-p-layers were much longer and higher than recommended for polyaniline. Conductivity was measured before and after the plasma process and it was found that polyaniline coated areas exposed to plasma activation became non-conductive. However, adjacent areas covered by evaporated aluminium were still conductive. Restriction of conductivity was turned to an advantage as it would increase the performance of adjacent cells by confining the current flow to the intended cell area.

6.4. Plasma process on textile substrate

6.4.1. Plasma process, chamber pressure

At the beginning of this project large fluctuations of temperature during the plasma process were experienced. These fluctuations were not removed by altering the different gas flows, so the chamber pressure was then considered. The initial chamber pressure was 0.3Torr, which was compared with 0.5Torr and 0.75Torr in an attempt to reduce reaction rate and control the temperature. At 0.3Torr, the reaction rate increased, and at 0.75Torr the numbers of excited species were reduced and resulted in too slow plasma environment. A chamber pressure of 0.5Torr gave a combination of excited plasma and sufficient control of substrate temperature. During the evaluation of chamber pressure it was found that 0.3Torr produced much stiffer substrate handle than 0.75Torr, which was softer. Hence, a pressure at 0.5Torr was used for the future runs.

6.4.2. Initial plasma process of intrinsic layer

After the initial plasma treatment with known settings (*hydrogen 20sccm, silane 1.02sccm, chamber pressure 0.3Torr, power 800W, 20 minutes, 200°C*) [1] resulted in damaged textile, the focus was to find settings to allow the polyester weave to be

plasma treated. The temperature of 200°C was set with consideration of the textile substrate. The different parameters were tried in different combination.

- process temperature (*from 150°C to 200°C*),
- process time (*10, 15 and 20 minutes*),
- hydrogen, (*2 and 20sccm*),
- silane, *(0.29, 0.49, 0.71, 0.82 and 1.14sccm*),
- power of *800W,*
- process pressure at *0.3Torr*.

Damaged substrate was still experienced with the different combinations. The breakthrough came after discovering the textile substrate withstood argon-plasma (Ar *18.2sccm, 800W, 0.5Torr for 5, 10, 20 and 30 minutes at 200°C*) without being damaged. The argon-plasma became used as reference plasma where each parameter of silane, hydrogen, power, chamber pressure and time was added separately to address the problem.

- silane from *0.29, 0.49, 0.71, 0.82 to 1.14sccm*,
- hydrogen from *2 to 20sccm*,
- process temperature *from 150°C to 200°C*,
- process time of *10, 15 and 20 minutes*,
- microwave power of *400, 500 and 800W*,
- chamber pressure at *0.5Torr*.

This helped to conclude, that:

- a combination with argon and silane rate up to 0.82sccm, temperature up to 200°C for a maximum time of 20 minutes with a power up to 800W did not damage the substrate.
- with increased silane rate of 1.14sccm, power was limited to 400 and 500W to avoid damage.
- additional hydrogen did cause damage to the substrate.

This meant that larger quantity of hydrogen damaged the textile. This resulted in argon replacing hydrogen in an attempt to reduce the hydrogen content to only that from decomposed silane and that from hydrogen diluted diborane (B_2H_6) and phosphine (PH_3) mixtures used for doped layers. Continuous work was run by a silane and argon mixture (Ar 18.2sccm, SiH_4 0.82sccm) with altered temperature (200°C and 210°C), time (10, 20 and 30 minutes) and power (600, 700 and 800W) to try to improve

deposition quality. The different settings with the silane and argon mixture helped conclude the following.

- extended process time to 30 minutes required a power at 600W or less to avoid the substrate being damaged.
- process temperature at 210°C was possible with a power of 700W or less without damaging the substrate.

A silane rate of 0.82sccm made it possible to process at 210°C for 30 minutes with 600W without damaging the substrate.

The earlier test was summed up in respect of not damaging the substrate.

- A "power barrier" between 700W and 800W was experienced, when 800W was restricted to use of very low silane flow and temperature whereas 700W permitted running with higher silane flow and temperature without damaging the substrate.
- Although 700W meant a restriction to 20 minutes in process time, 600W allowed extended time.

To avoid the substrate being damaged a combination of either:

- Low silane (<0.82sccm) with high power (>700W),
- High silane (>0.82sccm) with less power (<700W).

Reduced power allowed increased silane rate, extended process time and higher process temperature.

In respect to quality of deposition:
Low process temperatures (below 200°C) gave a high amorphous content with a powdery appearance, while increased process temperature (above 200°C) still contained amorphous silicon, but the powder was reduced. A silane rate of 0.82sccm combined with high temperature (above 200°C) and power (700W) gave less amorphous content, but increased the risk of damaged textile. The advantage of power at 700W or above was reduced powder deposition, but also a very thin film, whereas less power (700W) increased the risk of forming a powdery film.

A careful balance of silane rate according to the hydrogen quantity, power and temperature were required to allow the textile to be treated and to avoid a powdery deposition. The three parameters such as hydrogen content, temperature and power responded directly to a higher substrate temperature. Higher power and temperature

increased the number of active hydrogen species, which resulted in a higher surface activation such as dangling bonds and etching of the surface. Increased activity resulted in higher energy on the substrate surface followed by a higher substrate temperature.

An etch-effect is often related with hydrogen but was also experienced with argon. When the argon and silane mix was used, the presence of argon produced an etch-effect.

6.4.3. Plasma process, intrinsic layer, Taguchi model

Even after all modifications, a high amorphous content with a very powdery film was experienced. These runs proved how hydrogen was necessary to get crystal growth. The attempt to introduce hydrogen was through an Orthogonal Statistical Design, Taguchi model.

Taguchi model, process

Knowledge how power, temperature and hydrogen content influenced substrate and deposition helped to decide the values to use. With earlier experience of how temperature, time and power needed balancing, the power was kept low with a maximum of 500W. The Taguchi model was designed by introducing hydrogen as a ratio against argon, (hydrogen/ argon of *20/0, 17/3, 14/6 and 10/10sccm*) against silane rate (*0.10, 0.51, 1.02 and 2.04sccm*) and power (*200, 300, 400 and 500W*). These values were combined with fixed parameters such as substrate temperature at 200°C, deposition time of 20 minutes and chamber pressure at 0.5Torr/ 0.66mbar, which gave a total of 16 runs (table 6.4.).

Table 6.4. The Taguchi model and its parameters and settings combined with fixed temperature, time and pressure.

No. of Runs	Flow rate, sccm		Power, Watt
	SiH_4	H_2/ Ar	
1	0.10	20/0	200
2	0.10	17/3	300
3	0.10	14/6	400
4	0.10	10/10	500
5	0.51	20/0	500
6	0.51	17/3	400
7	0.51	14/6	300
8	0.51	10/10	200
9	1.02	20/0	200
10	1.02	17/3	300
11	1.02	14/6	400
12	1.02	10/10	500
13	2.04	20/0	200
14	2.04	17/3	300
15	2.04	14/6	400
16	2.04	10/10	500

During the growth programme, it was observed that a plasma power of 200W was too low to ignite the plasma. Run 8 (*SiH_4 0.51sccm, H_2/ Ar ratio 10/10sccm with 200W and fixed parameters*) was the only one to ignite, when run 1 (0.10, 20/0) needed 250W and run 9 (1.02, 20/0) and run 13 (2.04, 20/0) required 300W. This statistical design proved the possibility of processing with hydrogen and nucleating crystal growth into the amorphous matrix.

Substrate temperature was considered as an influence, but most Taguchi runs were processed at 200$\pm$2°C and further experimental runs were needed. Only a few runs experienced temperature fluctuation and unstable process condition and the parameters involved were SiH_4 rate of 1.02 and 2.04sccm, H_2/ Ar ratio of 20/0, 17/3 and 14/6sccm and power of 300 and 400W.

Analysis of the Taguchi thin film

Different methods were used to analyse the deposited film. Initially, all depositions were compared visually for thickness and uniformity by grouping them by appearance and process parameters. Raman spectroscopy was later used to identify the structure content on deposited substrates such as aluminium and textile. Generally, the textile had higher amorphous content than aluminium, which had higher crystallinity.

Different ways of analysis the Raman peaks were tried such as consider the recipes and the structure content in the two substrates.

Visual

The visual evaluation was by judging a sample by its appearance, such as powdery or etched, against parameters such as silane flow, H_2/ Ar ratio and power in an attempt to identify how the parameters influenced film properties such as the etch effect, thickness and powder.

Silane rate: Rate of 0.10sccm was too slow, giving very thin films, whereas 0.51sccm improved the film by being slightly thicker. Silane rates of 1.02sccm or more gave films that were too powdery. The different silane rates are compared in figure 6.4..
H_2/ Ar ratio: Ratios of 20/0 and 10/10sccm gave too high etch rate, whereas 17/3 and 14/6sccm showed dominance towards neither etch nor powder.
Power: Power showed an indirect influence for the bonding properties, which were improved by higher power.

Figure 6.4. Deposition visually changed in thickness with increased silane rate (0.10, 0.51, 1.02 and 2.04sccm), when image to the left (0.10sccm) has very thin deposition compared with the films to follow, which have higher silane rate (0.51, 1.02 and 2.04sccm moving to the right). All samples had H_2/ Ar ratio of 17/3sccm.

Raman spectroscopy

Deliberately no baseline was fitted, which allowed any background such as amorphous and vibrational modes related with nanocrystal structure to be considered. Both substrates of aluminium and fabric were analysed against silane rate (*0.10, 0.51, 1.02 and 2.04sccm*), hydrogen/ argon ratio (*20/0, 17/3, 14/6 and 10/10sccm*) and microwave power (*200, 300, 400 and 500W*) with aim of identifying parameters' influence on growth. Each of the samples (textile and aluminium) and runs were measured twice as a standard procedure, but in case of the measurement not showing a correlation further measurements were done.

Different analytical approaches were applied to try to understand the relation between 1st, 2nd and 3rd Raman peak and peak location, height and width in relation to process parameters used. On way was to use the data from the spectra for the 1st, 2nd and 3rd peak and plot both in 2D and 3D graphs to identify the parameters related to certain structural development such as amorphous or a strong growth of crystals. The 2D and 3D graphs did not provide a clear picture of structural content and process parameters. Instead, the ratios of crystallinity against amorphous were considered for the three main Gaussian peaks in the Raman spectra (table 6.5.). Both fabric and aluminium (table 6.5.) samples were considered and the amorphous and crystal fractions were based on an average of two readings per sample run and quality. The amorphous and crystal fractions against different parameters were plotted in the figures below (figure 6.5.; figure 6.6.; figure 6.7.; figure 6.8.; figure 6.9. and figure 6.10.).

The area of each peak against the total peak area was compared by using the formulation:

1st peak, amorphous= a/ (a+ C1+ C2)*100

2nd peak, intermediate= C1/ (a+ C1+ C2)*100

3rd peak, crystal= C2/ (a+ C1+ C2)*100

Table 6.5. Amorphous and crystal content for aluminium and textile substrates.

Sample run	Amorphous and crystal fraction, %					
	Aluminium			Textile		
	1st	2nd	3rd	1st	2nd	3rd
1	45	25	30	43	27	30
2	69	16	15	7	58	35
3	52	34	14	38	52	10
4	50	32	18	44	30	26
5	34	35	31	48	28	24
6	40	38	22	62	16	22
7	39	50	11	50	30	20
8	35	38	27	48	33	19
9	40	32	28	30	53	17
10	27	21	52	30	42	28
11	38	46	16	43	32	25
12	30	56	14	53	30	17
13	13	15	72	38	37	25
14	32	24	44	36	32	32
15	27	23	50	42	27	31
16	34	60	6	36	30	34

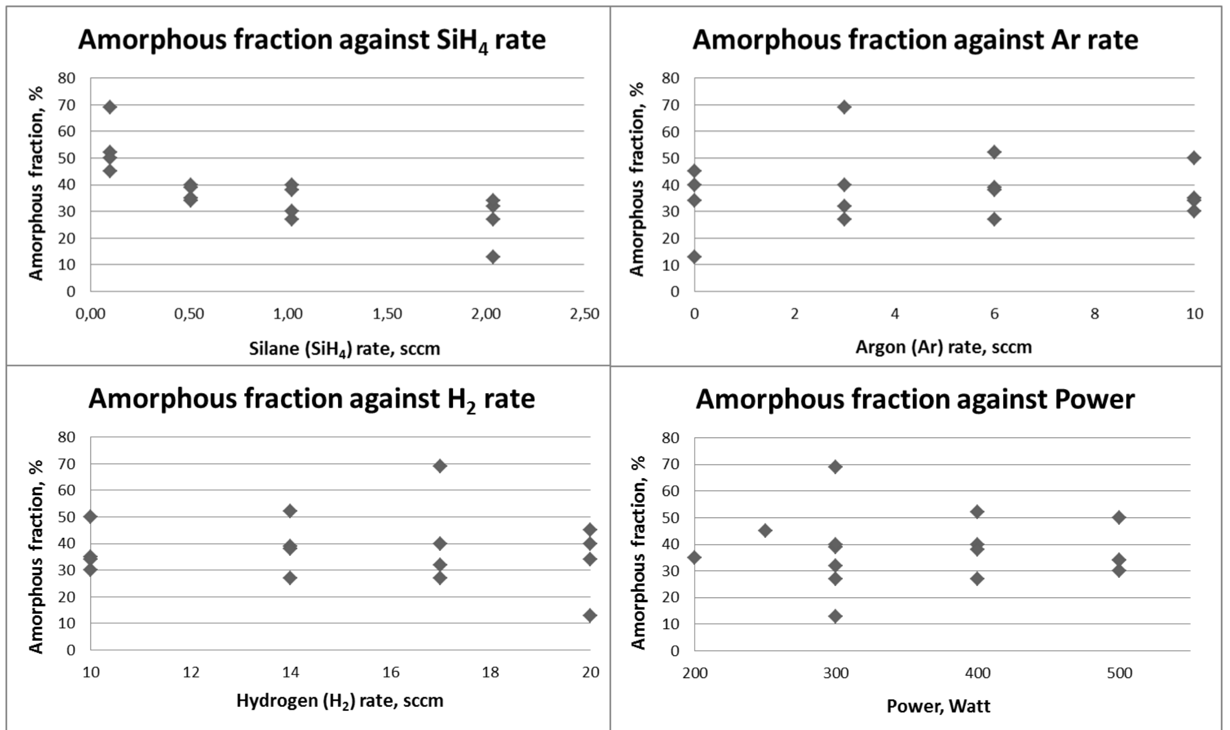

Figure 6.5. Amorphous fraction of deposited film on aluminium substrate.

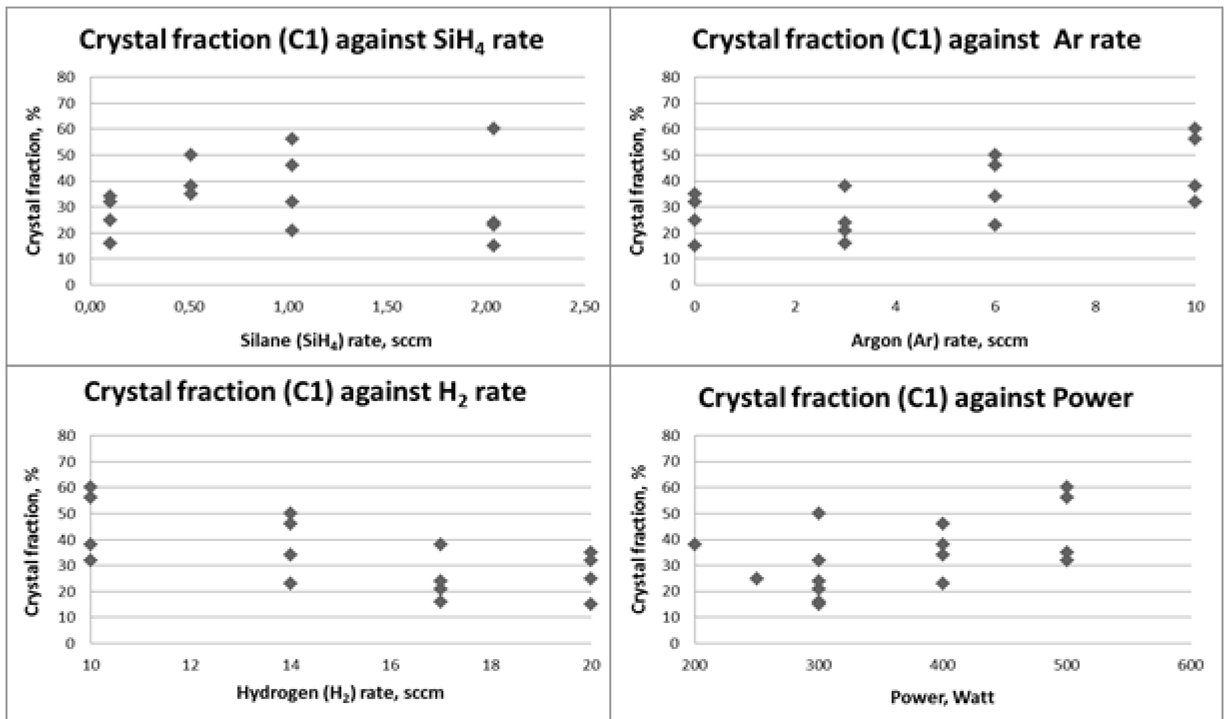

Figure 6.6. Crystal fraction regarding the intermediate peak (C1) of deposited film on aluminium substrate.

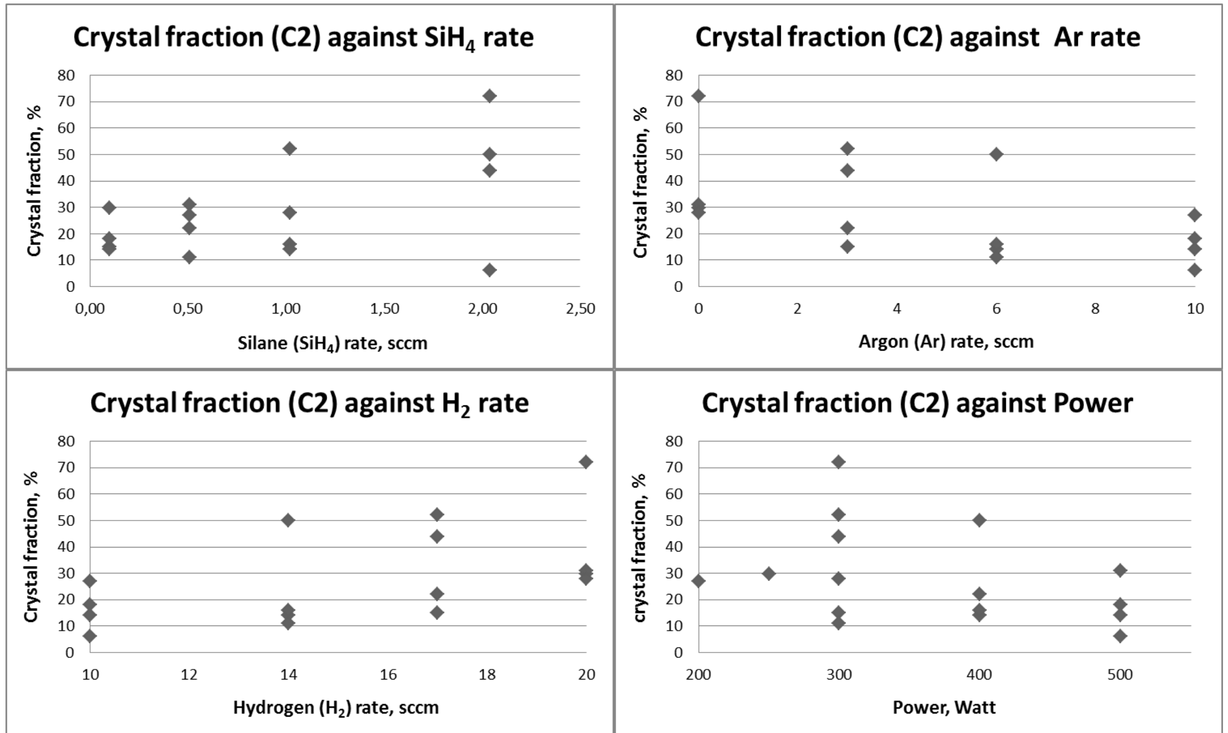

Figure 6.7. Crystal fraction regarding the crystal peak (C2) of deposited film on aluminium substrate.

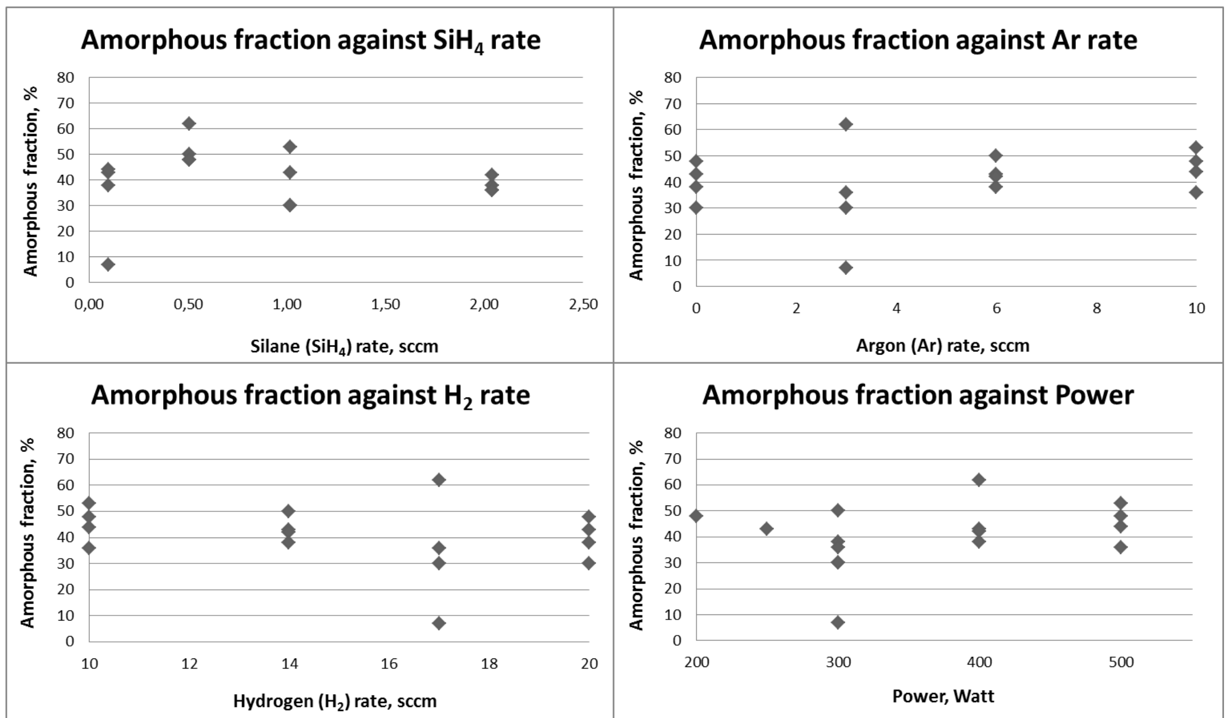

Figure 6.8. Amorphous fraction of deposited film on textile substrate.

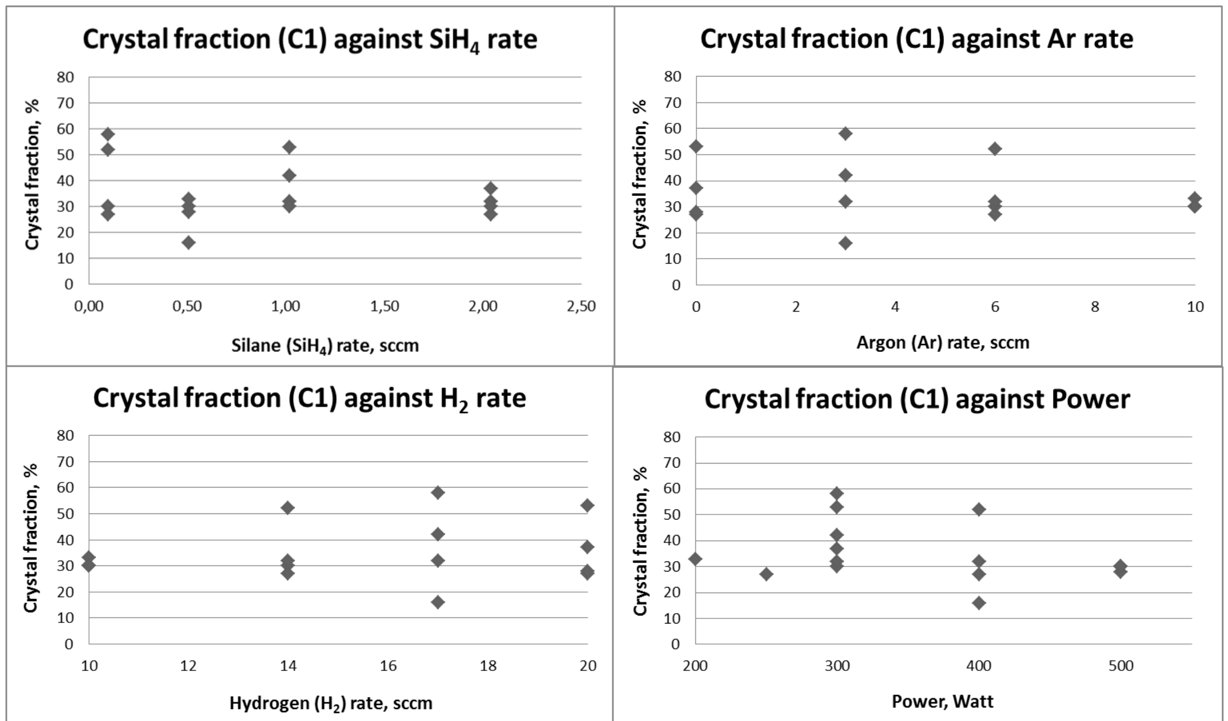

Figure 6.9. Crystal fraction regarding the intermediate peak (C1) of deposited film on textile substrate.

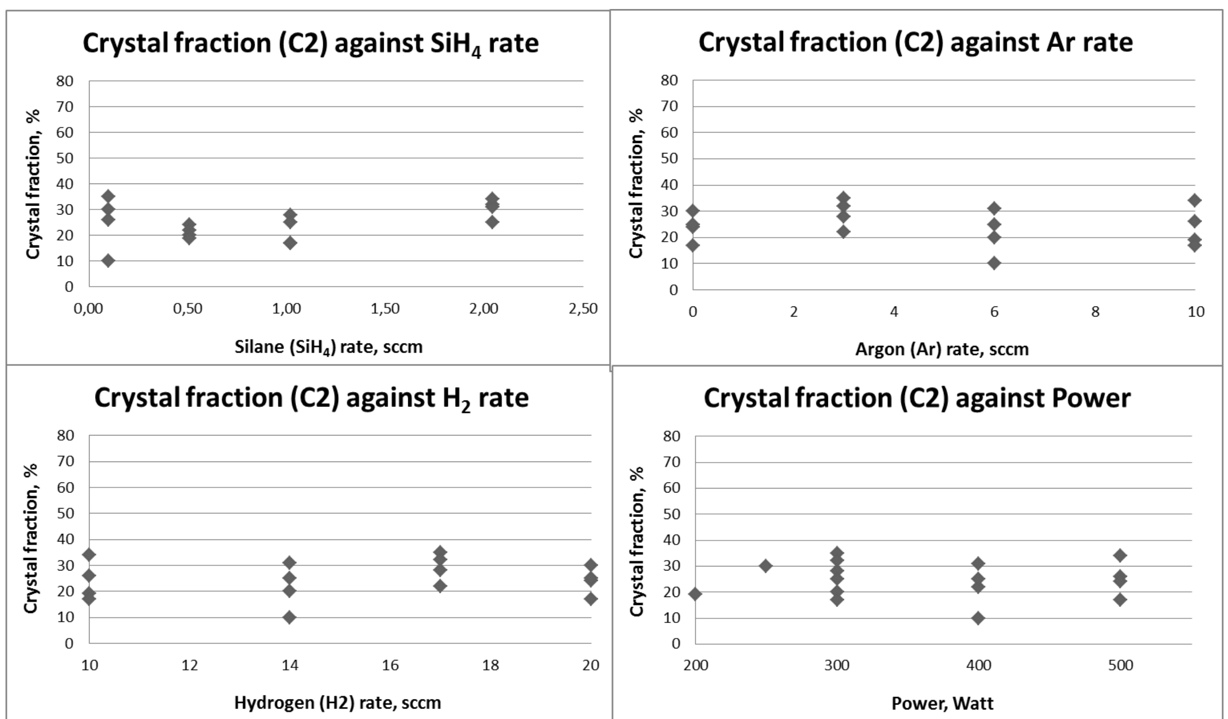

Figure 6.10. Crystal fraction regarding the crystal peak (C2) of deposited film on textile substrate.

A correlation between amorphous and crystal fractions against process settings (silane, hydrogen and argon rates, and power) was found in the aluminium sample, while textile substrates had limited correlations.

The intermediate peak (2nd peak, C1) of aluminium substrate had increased crystal growth with increased argon rate and power and reduced hydrogen. The 3rd peak (crystal peak, C2) of the aluminium substrate did have an opposite relation to the parameters, when reduced argon and power with increased hydrogen and silane gave a higher crystal fraction. In the aluminium samples, the amorphous content became reduced with increased flow-rate of silane.

Textile did show a small indication of reduced amorphous content by increasing the silane rate. The intermediate peak (2nd/ C1) showed that increased power did reduce the crystal content. However textile samples did contain less crystal fraction than the aluminium samples.

With focus on textile in this work and the aluminium performing differently from the textile, still little knowledge was gained regarding the parameters and their influence on crystal growth on the textile substrate. However, by putting all the Raman spectra against different process parameters to understand possible “trends” some conclusions were possible.

Raman peaks related with different process parameters

Links between silane flow-rate and peak location were found, when increased silane rate gave lower wavenumber peaks. This correlation was possible to establish by considering peak width, after previous trials with peak location, peak area (or intensity) gave no clear link to the parameters. However, a link between peak widths and their locations and silane rate was found too, when linked with other parameters such as hydrogen/ argon ratio and power were less clear.

Silane rate, less silane rate (0.10sccm) gave sharpest and most uniform crystalline peak whereas 0.51, 1.02 and 2.04sccm gave a broader peak with more amorphous content as the silane rate increased. (figure 6.11.)

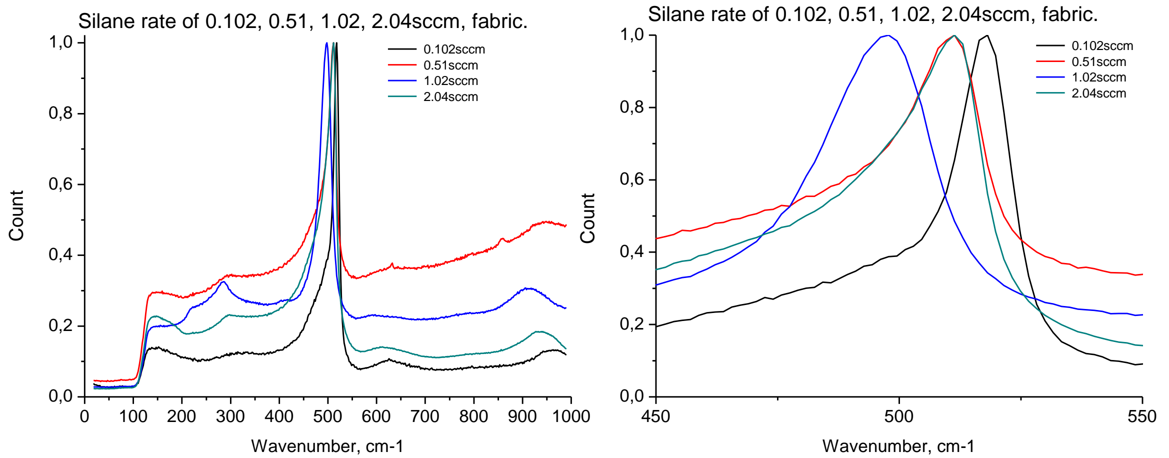

Figure 6.11. structure content and peak location for the different silane rates.

Silane rate was found to influence crystal structure and crystal size. A rate below 1.02sccm increased crystal content, when silane rate above 1.02sccm encouraged a larger crystal size. While a rate as low as 0.10sccm contained mainly nanocrystal structure. Low silane rate (0.10sccm) gave high etch effect and low growth rate with high power (400/ 500W).

Hydrogen/ argon ratio, ratio of 20/0 and 10/10sccm received a similar high amorphous content for both substrates (aluminium sheet and fabric) (figure 6.12.), while ratios of 14/6 and 17/3sccm showed a substrate dependence. The 14/6sccm ratio gave a higher peak location with aluminium than fabric, when 17/3sccm gave opposite effect (figure 6.12.).

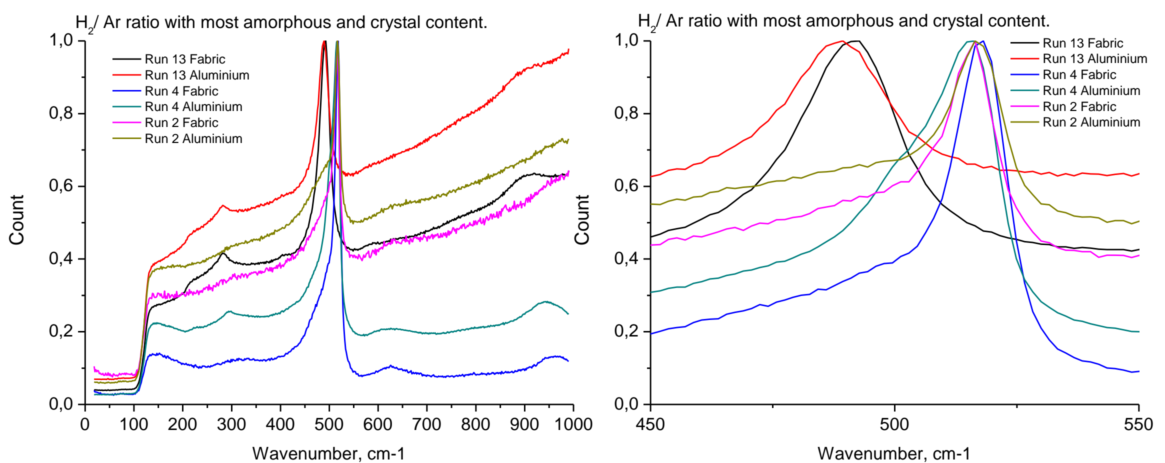

Figure 6.12. The runs which became most amorphous and most crystalline in relation to H_2/ Ar ratio. The parameters for each run are found in table 6.4.

Power, the influence of power was more difficult to define (figure 6.13.). However, a review of power helped to conclude, that powers of 200 and 300W gave a low peak intensity compared with 400 and 500W, likely to be a sample thickness effect. The vague trend of power could be due to the low maximum of 500W, when later trials with increased power (>500W) gave a stronger influence. Especially low power of 200W resulted in higher amorphous content with a textile substrate, while the diagram of crystal fraction (figure 6.9. and 6.10.) indicated that reduced power usually increased the crystal fraction. It was experienced how a high content of hydrogen compensated low power (200W) by still producing a crystalline structure.

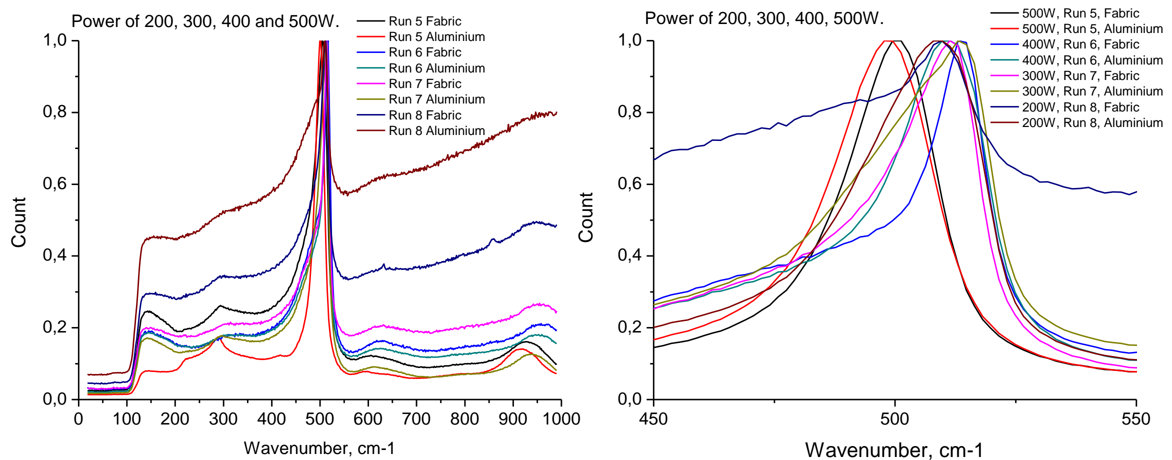

Figure 6.13. The effect of power in run 5 with 500W, run 6 with 400W, run 7 with 300W and run 8 with 200W. Highest power has not necessarily the highest peak location, which is due to influence of other parameters.

It was established, that aluminium and textile performed differently. Aluminium had most of the time, a higher silicon growth rate than textile, on which peak intensity was halved. Another distinction was how aluminium produced larger crystal growth with a higher rate of argon, when silicon on fabric instead becomes amorphous. However, run 5 (*SiH_4 0.51sccm, H_2/Ar ratio 20/0sccm and 500W*) resulted in very similar structure for both aluminium and fabric in figure 1, Appendix XIII.

Structure development

An attempt was made to compare and summarise the structural content for each sample and run. The samples (aluminium and textile) were grouped, by structural content such as amorphous (a), nanocrystal (ηc) and microcrystal (μc) against the process setting with silane rate (SiH_4), hydrogen flow (H_2) and power. This helped identify the parameters required for certain structural content.

The first summary (table 6.6.) was related to the samples (aluminium and textile) with same structural content. This helped to identify process parameters which had a more stable process condition, more uniform deposition and greater chance of repeatability. The recipes with higher crystal content were selected for further trials.

Table 6.6. Process parameters, which led to same structure content for the two substrates.

Process Parameter:	**Structure Development for both Aluminium and Textile**							
	a	a	a	a	a+ηc	a+ηc	ηc+μc	ηc+μc
SiH_4, sccm	1.02	1.02	2.04	2.04	0.51	0.51	0.102	0.102
H_2, sccm	20	20	10	20	20	14	17	20
Power, W	400	300	500	300	500	300	250	250

The second summary (table 6.7.), the samples containing two different structures were considered, which helped to understand possible ways of structural growth. These values were based on two measurements from each kind of sample (aluminium and textile). By adding the two structures, it was possible to understand the development route and different growth options.

Table 6.7. Process parameters from the Taguchi model resulting in different structural content.

Structure Development									
Fabric, plain polyester weave					Aluminium, plain sheet				
Structure	**SiH_4,** sccm	**H_2,** sccm	**Power,** W	**Structure**	**Structure**	**SiH_4,** sccm	**H_2,** sccm	**Power,** W	**Structure**
a	1.02	17	300	a+μc	a	1.02	17	300	a+ηc
a	1.02	14	400	a+ηc	a	2.04	14	400	a+ηc
a	2.04	17	300	a+ηc	a+ηc	0.51	14	300	ηc
a	2.04	10	500	a+ηc	a+ηc	1.02	14	400	ηc
a+ηc	0.10	20	250	ηc+ μc	ηc	0.51	10	300	a+ηc+μc
a+ηc	0.51	14	300	ηc+ μc	ηc	1.02	10	500	a+μc
a+ηc	1.02	10	500	ηc+ μc	ηc+ μc	0.10	17	300	a+ηc+μc
ηc+ μc	0.10	10	500	a+μc	μc	0.10	14	400	a+μc

The two earlier conclusions (table 6.6. and 6.7.) helped to predict a development of a structure and the parameters required for certain structures such as amorphous, nanocrystal and microcrystal structure. The summary helped to establish and explain how a growth started with amorphous and developed into nano/ ηc- or micro/ μc-crystal, shown
in table 6.8.. Microcrystal growth was suggested to develop either through a strong nanocrystal structure by annealing effect into larger crystals or forming larger crystals directly in the amorphous structure. All films started with an amorphous structure, which became less in its content as crystal growth started. Some process parameters led to the structure stopping at nanocrystalline.

Table 6.8. possible development routes for crystal growth in an amorphous matrix.

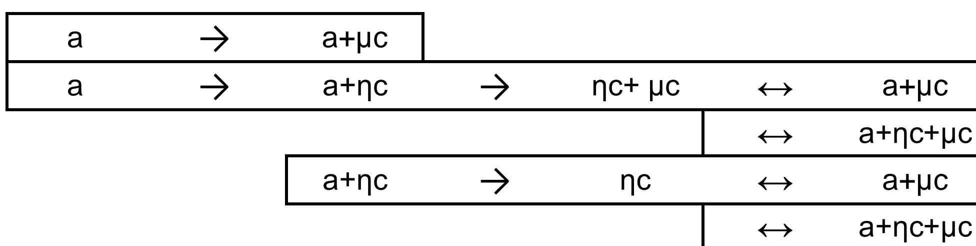

a	→	a+μc				
a	→	a+ηc	→	ηc+ μc	↔	a+μc
					↔	a+ηc+μc
		a+ηc	→	ηc	↔	a+μc
					↔	a+ηc+μc

Raman peak width

A narrow peak width would point towards a crystal structure with less stress and the most narrow peak width for aluminium was produced by 0.10sccm silane flow, whereas fabric had two similar peak-width values, with 0.51sccm as most narrow followed by 1.02sccm. This proved that textile had highest crystal growth between 0.51 and 1.02sccm silane flow-rates and confirmed what had been believed and practised earlier. The diagrams below (figures 6.14. and 6.15.) are based on average peak width and location for each silane rate (*0.10, 0.51, 1.02, 2.04sccm*).

Peak location and peak width are related in the manner of lower wavenumber tending to have broader peaks and vice versa. Changes in peak width are related to the amount of amorphous versus crystal content, when increased width is related to higher amorphous content and increased stress. For aluminium, stress did not reduce until the peak position reached 515cm^{-1}, which indicated larger crystals. Textile did not provide a simple trend, which indicated more parameters influenced the structural content and level of stress on this type of substrate.

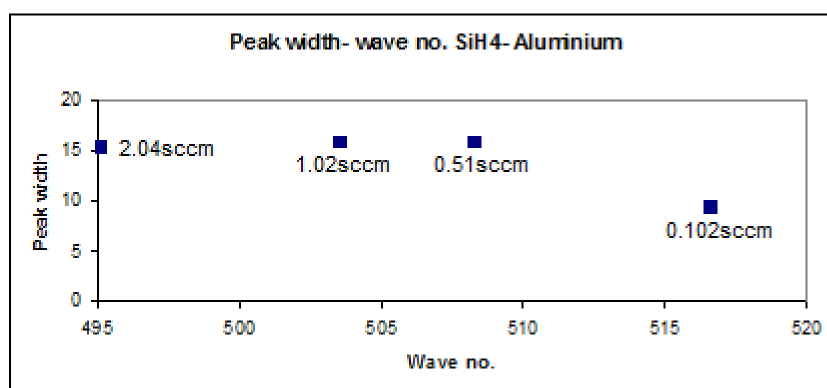

Figure 6.14. peak location and width related with silane rate for aluminium.

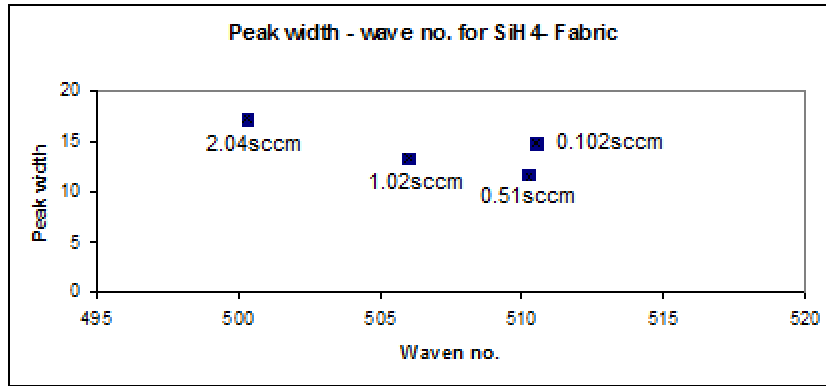

Figure 6.15. peak location and width related with silane rate for textile.

6.4.4. Plasma process, intrinsic silicon, after the Taguchi model

After establishing how the parameters of gas-rate and mixtures related with power and how they influenced film growth, the next step was to look at the fixed Taguchi parameters such as deposition time and substrate temperature.

Deposition time

Experiments done before the Taguchi set of silane/ hydrogen/ argon were based on an argon and silane mixture. Plasma process (silane/ argon) of 10 and 20 minutes had showed how peak location changed to higher wavenumber by enhanced deposition time. While plasma process based on silane/ hydrogen/ argon experienced an opposite effect by the peaks moving towards lower wavenumber with increased process time.

Deposition times of 5 and 30 minutes with run 16 conditions (*SiH_4 2.04sccm, H_2/ Ar ratio 10/10sccm, 500W, 200°C, 0.5Torr*) were processed and compared with the Taguchi run of 20 minutes to understand how time influenced structure growth. Raman spectroscopy helped to decide, that 5 minutes gained highest crystal content, while the other two runs behaved very similarly by getting a higher amorphous content in figure 2, Appendix XIII. Later further trials were carried out with a process time up to 60 minutes and depending on time and temperature the amorphous content was altered in figure 3, Appendix XIII. Due to the parameters of run 16 leaving a lot of powder deposition in the chamber after each run, this recipe was discarded for future runs. Instead the Taguchi ratios of 17/3sccm (run 10) and 14/6sccm (run 11) were used.

These two hydrogen/ argon ratios 17/3sccm (run 10) or 14/6sccm (run 11) were combined with different silane rates (*0.61, 0.82 and 1.02sccm*), process temperature at 200°C and a power of 700W for either 20 or 30 minutes as an attempt to optimise the crystal content on textile substrate (table 6.9.).

Table 6.9. silane rate and time were altered as a suggestion of increased crystal content. The outcome relates to fabric performance, if it withstood the plasma process without being damaged or not.

SiH_4, (sccm)	**H_2/Ar,** (sccm)	**Pressure,** (Torr)	**Power,** (Watt)	**Temp.,** (°C)	**Time,** (min.)	**Outcome**
0.61	17/3 & 14/6	0.5	700	200	20 & 30	20min- OK 30min- Not OK
0.82	17/3 & 14/6	0.5	700	200	20 & 30	20min- OK 30min- Not OK
1.02	17/3 & 14/6	0.5	700	200	20 & 30	20min- OK 30min- Not OK

The outcome of the two hydrogen/ argon ratios was much the same as the one using argon, before the Taguchi trial. The silane rate of 0.82sccm was found to be the best after getting neither too slow growth nor powdery film. The rate of 0.62sccm resulted in too low deposition rate, while 1.02sccm encouraged amorphous growth. This helped recognise, that power of 700W was not possible to run for more than 20 minutes, the textile became damaged by 30 minutes. A difference between the two H_2/ Ar ratios was found, with 17/3sccm (run 10) giving smaller crystals growth than 14/6sccm, which gave larger crystals. Smaller crystals were of more interest in the textured substrate, which led to more focus on settings of run 10.

Silane rate of 0.82sccm became the standard rate combined with Taguchi run 10 (*silane, SiH_4 of 0.82sccm, hydrogen/ argon H_2/ Ar ratio of 17/3sccm, 200°C*) and 11 (*silane, SiH_4 of 0.82sccm, hydrogen/ argon H_2/ Ar ratio of 14/6sccm, 200°C*) with a power of either 600W with a process time extended beyond 20 minutes or 700W with process time limited at 20 minutes.

With introduction of polyaniline coated textile it was necessary to reduce the power to 600W, when the conductive coated textile proved not to withstand a power above 600W due to the polyaniline being heat-sensitive and melting. With introduction of

polyaniline, the process settings were necessarily altered (table 6.10.) and the continuous trials were based on:
Run 10: (*silane, SiH_4 of 0.82sccm, hydrogen/ argon H_2/ Ar ratio of 17/3sccm, for 20 minutes, 200°C and 600W*)
Run 11: (*silane, SiH_4 of 0.82sccm, hydrogen/ argon H_2/ Ar ratio of 14/6sccm, for 20 minutes, 200°C and 600W*)

With power limited to 600W it was necessary to alter time and temperature in an attempt to improve the quality of deposition by avoiding a powdery film and encourage crystal growth (table 6.10.).

Table 6.10. time and temperature were altered in an attempt to compensate for the low power. The outcome relates to fabric performance, if it withstood the plasma process without being damaged or not.

SiH_4, (sccm)	**H_2/Ar,** (sccm)	**Pressure,** (Torr)	**Power,** (Watt)	**Temp.,** (°C)	**Time,** (min.)	**Outcome**
0.82	17/3	0.5	600	200	20 &30	20min- OK/ 30min- OK
				205		20min- OK/ 30min- OK
				200	40 & 60	40min- OK/ 60min- OK
				205		40min- OK/ 60min- OK

Reduced power (600W) allowed increased substrate temperature (205°C) and deposition time (60 minutes) without damage to the polyaniline coated substrate. The previous test was partly repeated to understand how a slight change in process condition would reflect on the result. Power of 500, 600 and 700W were tested against previous parameters (*silane, SiH_4 of 0.82sccm, hydrogen/ argon H_2/ Ar ratio of 17/3sccm, for 20, 30, 40 and 60 minutes, 200°C and 205°C at 0.5Torr*). (Table 6.11.).

Table 6.11. influence of power was evaluated against parameters from previous trial (table 6.10.).

Trial No.	**Power,** (Watt)	**Temp.,** (°C)	**Time,** (min.)	**Temp.,** (°C)	**Time,** (min.)
1	500	200	20, OK 30, OK	205	20, OK 30, OK
2	600	200	20, OK 30, OK	205	20, OK 30, OK
3	700	200	20, OK 30, Not OK	205	20, OK 30, Not OK
4	500	200	40, OK 60, OK	205	40, OK 60, OK
5	600	200	40, OK 60, OK	205	40, OK 60, OK
6	700	200	40, Not OK 60, Not OK	205	40, Not OK 60, Not OK

* Result related to the fabric performance, if the substrate melted or not, OK means the textile substrate withstood the plasma process without being damaged.

Power at or above 700W could be processed with a maximum time of 20 minutes to avoid damaged textile, as experienced during earlier trials with silane and argon mixture, while power at 600W could be run for 60 minutes without the weave being damaged. A great difference was found between using a power of 500W and 600W, when the peak intensity of Raman spectra doubled with a power of 600W, indicating a thicker film. Similar effect was found by using 205°C instead of 200°C, the small change gave a significant increase in crystal content with reduced amorphous content. There was no difference between running at 200°C or 205°C in relation to unstable process. However temperature and time together proved important, when right combination was necessary to avoid increased growth of amorphous content. The option of 60 minutes at 205°C and 40 minutes at 200°C encouraged amorphous growth, while shorter times had less amorphous content. Process time of 20 or 40 minutes at 200°C resulted in a higher nanocrystal content than 60 minutes at 200°C. (table 6.12.)

Table 6.12. how the structural content changed by being more amorphous by enhanced time and reduced temperature.

SiH_4, (sccm)	H_2/Ar, (sccm)	Pressure, (Torr)	Power, (Watt)	Temp., (°C)	Time, (min.)	Result, the film content. High →Low Amorphous
0.82	17/3	0.5	600	205	60.	High Amorphous content
0.82	17/3	0.5	600	200	40	Slightly reduced Amorphous
0.82	17/3	0.5	600	205	40	More reduced Amorphous
0.82	17/3	0.5	600	200	20	Low Amorphous content

This confirmed what earlier had been experienced with run 16, that amorphous content increased by longer deposition time. After the experiment of how time and temperature influenced the structural content was possible to narrow intrinsic recipe to be:
Silane rate, SiH_4: 0.82sccm
Hydrogen/ Argon ratio, H_2/Ar: 17/3 or 14/6sccm
Temperature: 200 or 205°C
Time: 20 minutes
Power: 600W
Pressure: 0.5Torr

6.4.5. Plasma process, interface between doped and undoped layers

Studies [13,14,15] have addressed the importance of a clear interface between n- and i- layer to avoid doped species affecting structural growth of the intrinsic layer and its performance. Different methods of cleaning procedure between n- and i- layers were suggested for the thin film structure in this work. Three intrinsic recipes (normal and two Taguchi runs) were used together with a standard n-layer (*phosphine, PH_3 0.1sccm, argon, Ar 9.1sccm, silane, SiH_4 0.82sccm, 200°C and 800W for 5 minutes*) to identify possible changes in the intrinsic structure content, Raman spectroscopy was used. Intrinsic recipes used:

- Recipe 1: Normal (*argon, Ar 18.2sccm, silane, SiH_4 0.82sccm, 200°C and 800W for 20minutes*),
- Recipe 2: Run 10 (*silane, SiH_4 0.82sccm, hydrogen, H_2 / argon, Ar ratio of 17/3sccm, 200°C and 600W for 20 minutes*),
- Recipe 3: Run 11 (*silane, SiH_4 0.82sccm, hydrogen, H_2 / argon, Ar ratio of 14/6sccm, 200°C and 600W for 20 minutes*).

The three intrinsic recipes were run against different procedures (table 6.13.):

A/ standard

B/ three minutes Ar- plasma

C/ **B**+ introduce intrinsic gases in stages

D/ hydrogen reduction, 5sccm/ 5minutes

E/ Ar- purges three times

F/ Ar- purges six times

Table 6.13. The combinations used in the trial "clean break" between doped and intrinsic layers.

Trial no.	Recipe	Procedure	Result
1	1	**A**	N/A
2	2		
3	3		
4	1	**B**	Nothing changed compared with procedure A.
5	2		
6	3		
7	2	**C**	Nothing changed compared with procedure A.
8	3		
9	2	**D**	Nothing changed compared with procedure A.
10	3		
11	1	**E**	Resulted in nanocrystal growth (aluminium substrate) by an intermediate peak at 503cm^{-1}
12	2		Resulted in nanocrystal content on fabric substrate. (peaks at 511, 500 and 462cm^{-1})
13	3		Resulted in microcrystal content on fabric substrate. (peaks at 514, 506 and 478cm^{-1})
14	1	**F**	Poor peak fit on fabric. Aluminium substrate had amorphous content with nucleation of crystal growth. (peaks at 482 and 490cm^{-1})
15	2		Resulted in nanocrystal content on fabric substrate. (peaks at 506, 490 and 447cm^{-1})
16	3		Resulted in microcrystal content on fabric substrate. (peaks at 515, 509 and 484cm^{-1})

Most of the suggested methods did not show a great difference from the original run. However argon-purges (three and six times) did stand out with influence on the

structure content of intrinsic silicon by altering the crystal content. The crystal growth became stronger with the two options (Run 10 and 11), although three and six times purges had a distinct difference between them. Raman spectra helped identify how the two argon-purges performed in relation to Run 10 and Run 11. With a clear difference in quality of deposition with either three or six argon purges against run 10 and 11 led to these runs being processed again with much the same outcome as the previous run.

This helped to conclude, that three purges with run 10 was ideal to use for a nanocrystal structure and six purges with run 11 for a microcrystal structure. The number of argon purges (three or six) was used in relation to the H_2/ Ar ratio, when three purges with 17/3sccm gave strongest nanocrystal growth and six purges with 14/6sccm supported a microcrystal structure (figure 6.16.).

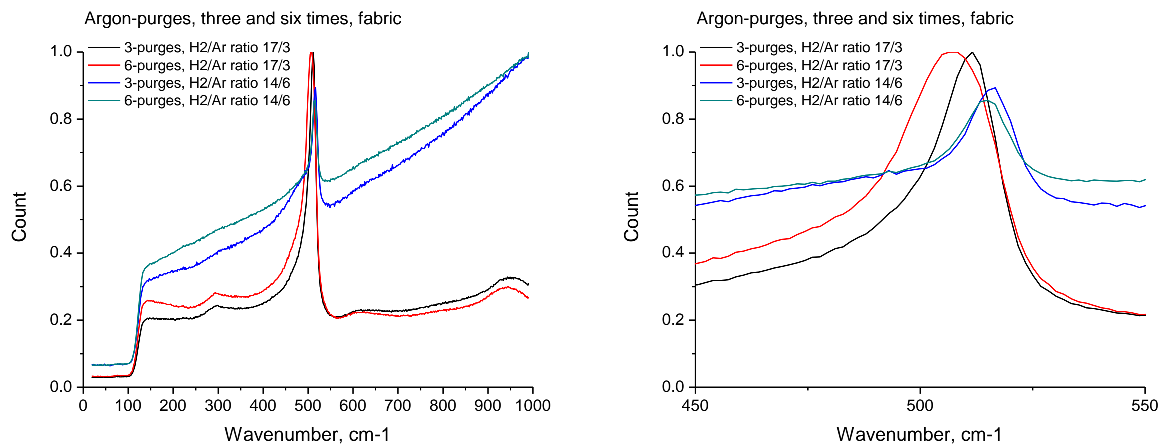

Figure 6.16. Explains how argon purges in relation with H_2/ Ar ratios of 17/3 and 14/6 influence the structure outcome.

That three purges produced smaller crystals than six purges was explained by the amount of argon left at the sample surface and in the chamber as the intrinsic deposition process started, when three argon purges left no argon to influence deposition and instead allowed the intrinsic gases to determine structure growth.

6.4.6. Plasma process, doped layers

With much work spent on addressing process parameters and a clear interface before the intrinsic layer, it was also important to consider crystal growth of doped layers to

enhance the overall cell efficiency. N-layers were known to be more crystalline than p-layers, which were known to have a strong amorphous growth. [16,17,18]

After the initial run of doped layers, the argon-rate was reduced by half from 18.2sccm to 9.1sccm. The previous p-layer recipe used an initial power of 1000W, but after experiencing how high power damaged the textile substrate during the work with intrinsic silicon, power was reduced to 700W. This gave a stable process without heat-fluctuation considering the larger quantity of hydrogen the dopant contained. The same happened to process temperature, which was reduced from 210°C to 205°C. N-layer's process parameters of power at 700W, temperature of 200°C required no change, except the process time, which was extended from 5 minutes.

Process time for doped layers was evaluated by using 5, 10 and 20 minutes, which resulted in changes with n-layer being extended to 10 minutes and p-layer reduced to 5 minutes. Advantage with reduced time for the p-layer was to avoid a too thick top layer, which would reduce the cell performance by trapped charges and undesirable optical absorption. Later, the power was increased for the two doped recipes from 700W to 800W to enhance crystal growth.

Process parameters for n-layer (*Ar 9.1sccm,* SiH_4 *0.82sccm and* PH_3 *0.1sccm at 200°C with 800W for 10 minutes*) were established, when reduced process time for p-layer (*Ar 9.1sccm,* SiH_4 *0.82sccm,* B_2H_6 *0.1sccm, 200°C, 800W for 5 minutes*) was not enough and further changes were required. The diborane rate was later reduced to 0.05sccm due to the flow-meter failing to deliver higher rates. The actual flow value for the dopant was 1% of given rate, when the rest related to hydrogen.

After establishing the conductive coated textile conditions, it was found that these selected conditions for doped layers damaged the textile substrate. P-layer could not be deposited directly onto the textile. Instead microscope-slide glass and aluminium sheet were used, when p-layer trials were carried out.

Plasma process, p-layer

Different process parameters such as temperature, time and dilution of boron with hydrogen and silane have been important. [19,20,21,22] Further changes to the p-layer were based on suggestions [19,20] of reduced process temperature from 200°C to

190°C to enhance crystal growth (as the Raman peak shifted towards higher wavenumbers). However, reduced temperatures were not enough to support a stronger crystal growth and additional changes such as altered gas rate and mix were done. [21,22] Argon, diborane and silane had their flow-rates and ratios altered together with hydrogen as an additional gas and the changes carried out are found in table 6.14.. All runs were processed for 5 minutes, at 800W with a temperature of 190°C, except run H and G processed at 180°C. The different runs in table 6.14. are values from measuring microscope-slide glass samples.

Table 6.14. Explains the flow-rates for each run and the Raman peak location for amorphous and crystal fractions together with the maximum intensity of the convoluted peak on microscopic-slide glass substrate.

Trial run	**Gas type and actual rate, sccm**				**Raman peak, cm^{-1} (glass substrate)**						**Peak intensity**
	B_2H_6	**SiH_4**	**Ar**	**H_2**	**1st**	**2nd**	**3rd**	**a**	**C1**	**C2**	
A	0.05	0.82	9.1	0	439	496	516	43	31	26	43780
B	0.025	0.82	9.1	0	460	503	513	32	28	40	110381
C	0.1	0.41	4.55	0	(419)	484	517	---	47	9	7468
D	0.05	0.82	18.2	0	435	490	513	39	46	16	25502
E	0.05	0.82	10	10	439	495	516	39	40	22	3899
F	0.05	0.82	5	15	455	499	516	40	35	27	6121
G	0.025	0.82	9.1	0	447	496	514	45	32	23	29406
H	0.05	0.82	10	10	473	500	510	34	49	19	163657

Conclusion of each run	
A	High amorphous content, with nanocrystal nucleation and growth of large sized crystals.
B	Well-developed crystal structure based on nano-sized crystals and the lowest content of amorphous phase.
C	Strongest amorphous growth with a small amount of large crystals. (With low peak intensity and high background in the Raman spectra indicated high amorphous content.)
D	High amorphous content with high content of crystals in nucleation stage and some larger crystals.
E	High amorphous content with high content of crystals in nucleation stage and larger crystals, slightly more than D.
F	High amorphous content with high content of crystals in nucleation, although less than run E, while the larger sized crystals had a higher content.
G	Good growth rate, strong crystal growth of nano-sized crystals.
H	Highest growth rate, dominated by nanocrystal growth with some larger crystals.

The runs with “old” recipe (C) and added hydrogen content (E and F) gave the lowest growth rates, probably due to high etch effect. While the present recipe (A) and the one with added argon (D) did have a slight increase in growth rate, run (B) with reduced diborane rate gave higher growth rate with process temperature at 190°C. Reduced diborane rate (G) with lower temperature (180°C) gave reduced deposition rate, while adding hydrogen (ratio 10/10) resulted in reduced amorphous content (E) and increased nanocrystal phase with highest growth rate (H). A comparison of the Raman spectra of the two options, run B and E, both at 180°C and 190°C for aluminium and microscopic-slide glass substrates is shown in figure 4, Appendix XIII. The diborane rate of 0.025sccm was a quarter of original flow rate of 0.1sccm. Added hydrogen through an argon ratio, H_2/ Ar showed reduced Raman peak intensity, which could either due to high etch rate or slow deposition rate. Overall performance, the runs with hydrogen content had reduced peak intensity, which could be 10 times less than without hydrogen. This helped to conclude the process settings for the p-layer, which should either be by reduced diborane rate (*B_2H_6 0.025sccm, SiH_4 0.82sccm, argon, Ar 9.1sccm*) processed at 190°C or added hydrogen, H_2/Ar ratio of 10/10 (*B_2H_6 0.05sccm, SiH_4 0.82sccm, argon, Ar 4.55sccm, hydrogen H_2 9.8sccm*) processed at 180°C (figure 6.17.).

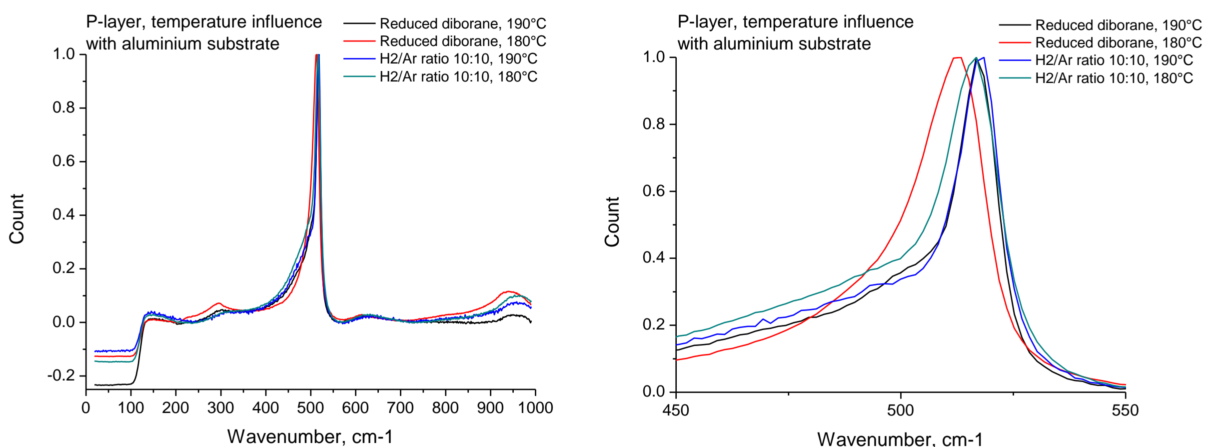

Figure 6.17. How the different temperatures influence the two options of reduced diborane rate and hydrogen/ argon ratio (10/10).

The two recipes adding hydrogen (H_2/ Ar 10:10) and reducing diborane rate (*B_2H_6 0.025sccm)* limited the amorphous growth but encouraged crystal growth so reduced diborane rate was chosen for all future runs. The choice was based on knowing how hydrogen caused temperature fluctuations and an unstable process condition. Another

aspect was to use 180°C, increasing the time of p-layer deposition, when intrinsic was run at 200/205°C. Future p-layer process was based on B_2H_6 0.025sccm, SiH_4 0.82sccm, Ar 9.1sccm for 5 minutes at 190°C with 800W.

6.4.7. N-I-P- layers, introduction

Earlier discussions regarded modification of single layers or inter-layer stages, whereas this section will discuss deposition of the three layers (n-i-p-layer) in a complete cell. Even if the individual processes did not damage the textile substrate, occasionally a combination of the three layers did. After this discovery, three layers were always processed, to check for damaged textile substrate, even after smallest modification to a single layer was made.

The initial three layers (section **A**, table 6.15.) used a power of 700W, which became increased to 800W (section **B**, table 6.15.) to reduce the high amorphous content and the powder effect. With introduction of the additional conductive layer Polyaniline coated directly onto the textile substrate, power was reduced to 600W for intrinsic silicon, while doped silicon stayed on 800W (section **C**, table 6.15.). The combination of reduced power and the silane and argon mixture gave increased amorphous content, which proved the necessity to use hydrogen. A Taguchi model was used to introduce the hydrogen, which resulted in work using a hydrogen/ argon ratios of 17/3sccm and 14/6sccm, which were evaluated against different silane rates (section **D**, table 6.15.). A silane rate of 0.82sccm was to be used and a cleaning procedure (section **D**) with argon purges was added. Further work such as altered process time (intrinsic) and temperature (n-i-p-layer) (section **E**, table 6.15.) was done without experiencing damaged substrate. However the overall structural content of the cell was not improved with extended time and instead 20 minutes was kept, with the temperature of 200°C (n-layer), 200°C (intrinsic) and 190°C (p-layer). Further attempt was to increase crystal growth in the p-layer (section **F**, table 6.15.) by running the new settings with added hydrogen (1) and with reduced diborane rate (2) at 180°C.

Table 6.15. This explains the different trials carried out in combinations of n-i-p-layers.

Layer	Gas type and actual flow-rate, sccm					Temp, (°C)	Time, (min.)	Power, (W)	Section No.
	SiH_4	Ar	H_2	B_2H_6	PH_3				
N	0.82	9.1	0	0	0.1	200	5	700	**A**
I	0.82	18.2	0	0	0	200	20	700	
P	0.82	9.1	0	0.1	0	205	5	700	
N	0.82	9.1	0	0	0.1	200	5	800	**B**
I	0.82	18.2	0	0	0	200	20	800	
P	0.82	9.1	0	0.1	0	200	5	800	
N	0.82	9.1	0	0	0.1	200	5	800	**C**
I	0.82	18.2	0	0	0	200	20	600	
P	0.82	9.1	0	0.1	0	200	5	800	
N	0.82	9.1	0	0	0.1	200	5	800	**D**
Argon- purges three or six times in the interface of n- and i-layer									
I	0.82 (0.62/ 1.02)	17 (14)	3 (6)	0	0	200	20	600	
P	0.82	9.1	0	0.1	0	200	5	800	
N	0.82	9.1	0	0	0.1	200/ 205	10	800	**E**
I	0.82	17	3	0	0	200/ 205	30/ 40/ 60	600	
P	0.82	9.1	0	0.05	0	180/ 190	5	800	
N	0.82	9.1	0	0	0.1	200	10	800	**F**
I	0.82	3	17	0	0	200	20	600	
P:1	0.82	10	10	0.05	0	180	5	800	
P:2	0.82	9.1	10	0.025	0	180	5	800	

The recipe to use for the three layers (n-i-p):

- N-layer (phosphine doped): *argon, Ar 9.1sccm, silane, SiH_4 0.82sccm, phosphine, PH_3 0.1sccm, 200°C, 800W for 10 minutes.*
- I-layer (intrinsic, undoped): *silane, SiH_4 0.82sccm, H2/Ar ratio of 17/3 or 14/6sccm, 200 or 205°C, 600W for 20 minutes.*
- P-layer (diborane doped): *argon, Ar 9.1sccm, silane, SiH_4 0.82sccm, diborane, B_2H_6 0.025sccm, 190°C, 800W for 5 minutes.*

6.4.8. Radio frequency powered plasma

Radio Frequency plasma was compared with the microwave based process, which was mainly used in this work. The RF-processes were based on earlier project's [1,23] plasma settings for n-i-p- layer, which were altered in the same way as the microwave trials were done, which is explained above. Parameters such as silane and diborane rate were reduced, when power was increased and the temperature of the p-layer was reduced.

The process time of n-i-p- layers was similar with 5 minutes for p-layer and 10 minutes for n-layer and 30 minutes for intrinsic. Gas mix and rates and chamber pressure were taken from previous RF-projects [1,23], although the diborane rate was reduced, three argon purges for the interface were used and reduced silane rate with the temperature established during the microwave work (*chapter 5, section 5.3., table 5.10., section **A**.*) Continuous RF- trials (*chapter 5, section 5.3., table 5.10., section **B**.*) were carried out as an aim of encouraging crystal content. Changes such as increased power of 40W and reduced silane (SiH_4 1.43sccm) for all three layers took place. For doped layers changes such as reduced diborane rate (B_2H_6 0.05sccm) with lower process temperature (180°C) and process time of 5 and 10 minutes for n-layer were evaluated.

There was no big difference between the RF-runs, when all depositions became amorphous with no or very small amount of crystal content (figure 5, Appendix XIII).

The conclusion was that more work was required to produce increased crystal content with the RF-plasma. The textile substrate was easier to process with RF-plasma than with microwave plasma, as this did not excite the hydrogen species to the same extent as microwave-plasma and therefore there was no risk of damaged substrates.

6.5. Results from the analytical instruments

6.5.1. Raman spectroscopy

Raman spectroscopy helped address how changes of deposition parameters and process condition affected the structure content of silicon thin films. This helped to recognise the parameters required to reduce the amorphous content and encourage crystal growth.

Raman spectra from wurtzite silicon structure

The Raman spectra were fitted by using three Gaussian peaks, unless a clear microcrystal or amorphous structure, which required only two peaks. Often, the Raman spectra had a baseline fitted with the focus on the spectral region between 400cm^{-1} and 600cm^{-1}. Peak locations in spectra containing crystalline growth in an amorphous matrix are discussed [24,25,26] often as lying at 480cm^{-1} (amorphous), 505cm^{-1} (intermediate) and 518cm^{-1} (crystal) (figure 6.18.).

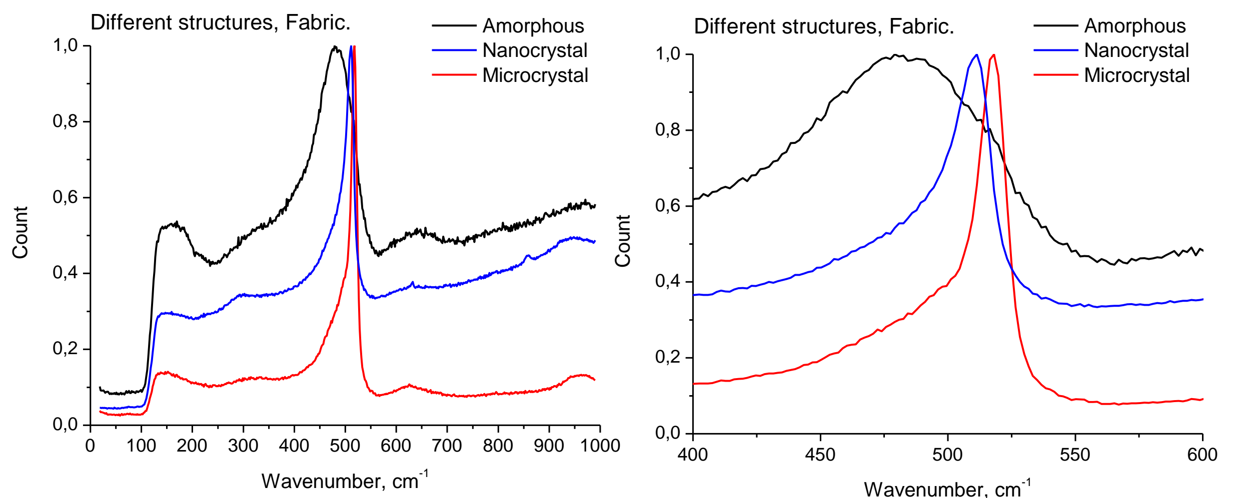

Figure 6.18. the three different structures such as amorphous, micro- and nano- crystal refer to different Taguchi run such as run 3- amorphous, run 4- microcrystal and run 8- nanocrystal.

Together with the three peaks of TO-mode (amorphous, intermediate, crystal), additional vibration modes such as Fano, Surface Optical (SO) and Boson peak were found in the Raman spectra, which are typical for wurtzite structure. To identify these

vibration modes no baseline was fitted and the wavenumber range was extended to be between 0 and 2000cm^{-1}. The Raman signals for the vibrational modes were stronger for the textile substrate than aluminium (or microscope-slide glass), which due to the textile surface got a higher nanocrystal content and in particular the wurtzite structure. The enhanced growth of wurtzite on textile was explained [27] to be due to its textured and uneven surface, which resulted in an increased energy field (*chapter 3, section 3.2.*). Other typical vibration modes for wurtzite structure are wagging at 630-650cm^{-1}, bending at 830-880cm^{-1} and stretching at 2000-2200cm^{-1}. [28,29,30,31]

An example of spectra with the different modes and peaks for nanocrystal silicon on fabric is given in figure 6.19., while aluminium is found in figure 6, Appendix XIII.

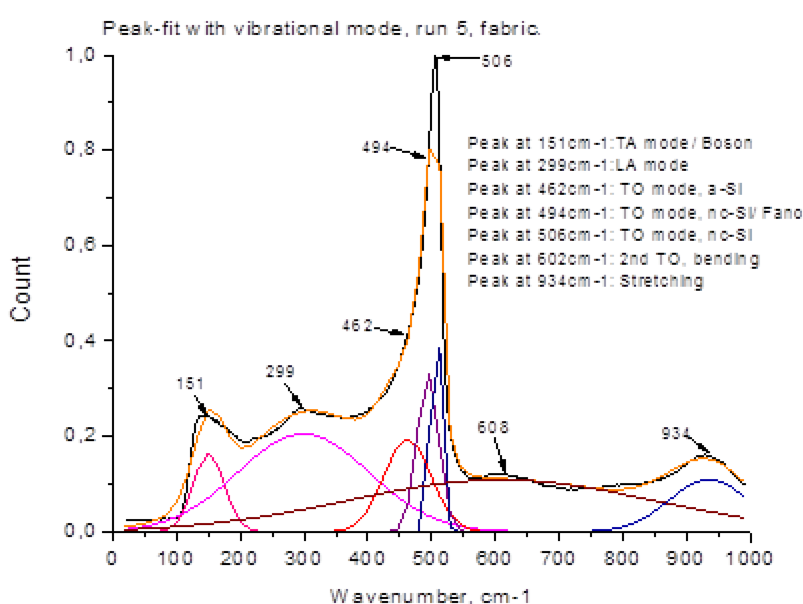

Figure 6.19. an example of different vibration modes possible in a Raman spectra of wurtzite structure on fabric.

Raman spectroscopy and its laser power

The different parameters such as accumulation scans, exposure time and magnification used for Raman spectroscopy were altered and combined to identify potential annealing effects in the substrate or the film. Neither accumulation, nor exposure time or magnification caused structural changes. Laser power was first considered after a report [32] discussed possible changes to surface properties of polymer substrate. A test was carried by evaluating the laser power from 0.1 to 100%.

The power was narrowed down to a comparison of 10% and 50%, when power below 10% and above 50% behaved the same as each of these. Due to the Raman instrument and its settings of power, there were no options between 10% and 50% laser power. Laser powers of 10% and 50% were measured at the same spot with different sequences to identify a potential annealing effect or not.

- 10% and 50%, 50% and 10%,
- 10%-50%-10% and 50%-10%-50%

No permanent changes were found, although power did influence peak location and its intensity, when 10% after exposure of 50% showed a slight change in peak shape by becoming sharper and narrower. By using 10% laser power, the peak location increased in wavenumber towards the microcrystalline region at 516-518cm^{-1}, while 50% produced a peak location in the nanocrystal region at 500-512cm^{-1}. The spectral measurements with cycles of 10%-50%-10% (figure 6.20.) laser power settings returned to the same wavenumber location as shown below, whereas cycles of 50%-10%-50% (figure 6.21.) did not quite return the spectra to the original values.

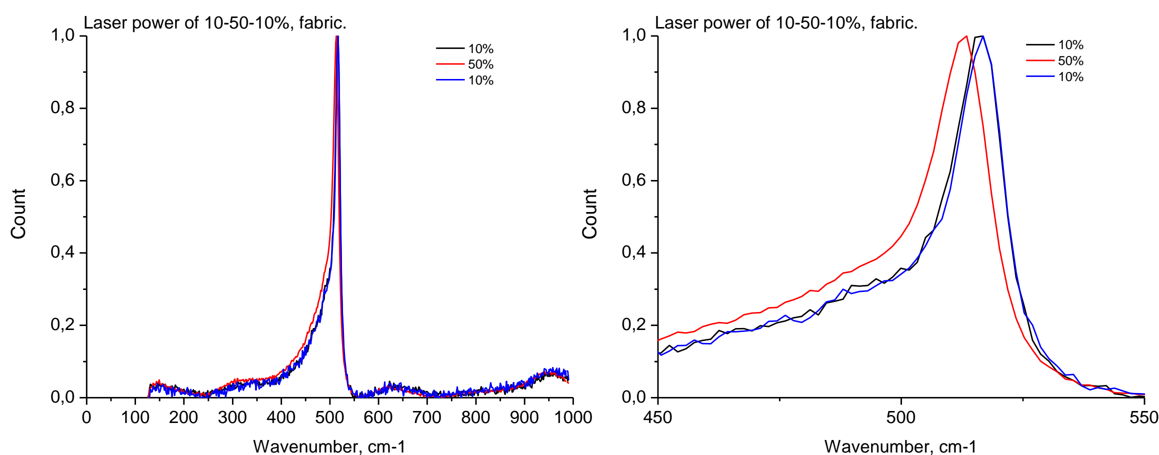

Figure 6.20. Raman spectra with laser power cycle of 10%-50%-10%.

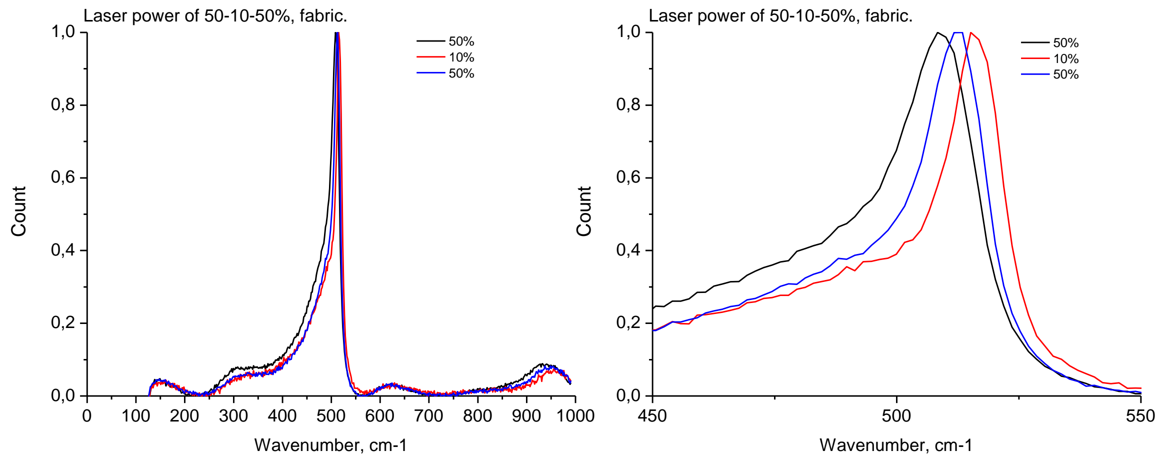

Figure 6.21. Raman spectra with laser power cycle of 50%-10%-50%.

The laser power proved to cause annealing, but in reverse of what had been published. [24,33,34] It was often stated that higher laser power tended to give a peak towards the ~520cm^{-1}, when opposite was experienced in this work by 50% power resulting in a peak in the nanocrystalline region. Change towards lower wavenumber due to 50% power was by heating up the sample. The increased temperature resulted in higher vibrations, which gave a more asymmetric peak shape and caused the down shift. This behaviour was common for nanocrystal content with a hexagonal structure. [24]

6.6. Optical properties

Optical transmission measurements helped to establish the band-gap energy which was a parameter that changed with structure type. These band-gap energy values were supported by data from the Raman spectroscopy, when both measurements gave information regarding the structure content of the deposited film. The extraction of the band-gap energy from optical absorption is often based on a square root function against photon energy, but in case of nanocrystal growth in an amorphous structure this can give a poor linear fit and instead a cube function is to be considered. [35,36]

6.6.1. Transmission measurement

In these measurements, a transmission range from 300nm to 900nm in wavelength was selected. Most samples reached zero transmission at ~350nm and a maximum transmission of ~70% at ~800nm. The transmission data was deconvoluted into absorption and square- or cube- root functions against the photon energy known as Tauc plots. A poor linear fit with square root suggested two band-gap values, one for nanocrystal and the other for amorphous structures. The most accurate method to use has never been clear, but it has been observed that the cube root produces lower values for the band-gap energy compared to the square root. A mixed structure in most samples made it difficult to tell whether square- or cube- root was to be applied. A common practice is that both graphs are produced to decide the most appropriate fit. These two alternative fits are derived from the theory for the type of transition between valence and conduction bands (e.g. allowed or forbidden, direct or indirect band-gap).

It was observed that the line became straighter as the film increased in thickness and with higher nanocrystal content. The figure below (figure 6.22.) shows how increased film thickness resulted in a straighter line such as sample C with increased time (60 minutes) and temperature (205°) and the thickest deposition, compared with thinner sample A with less deposition. A cube root function was more applicable as the nanocrystal structure became increased in the amorphous matrix.

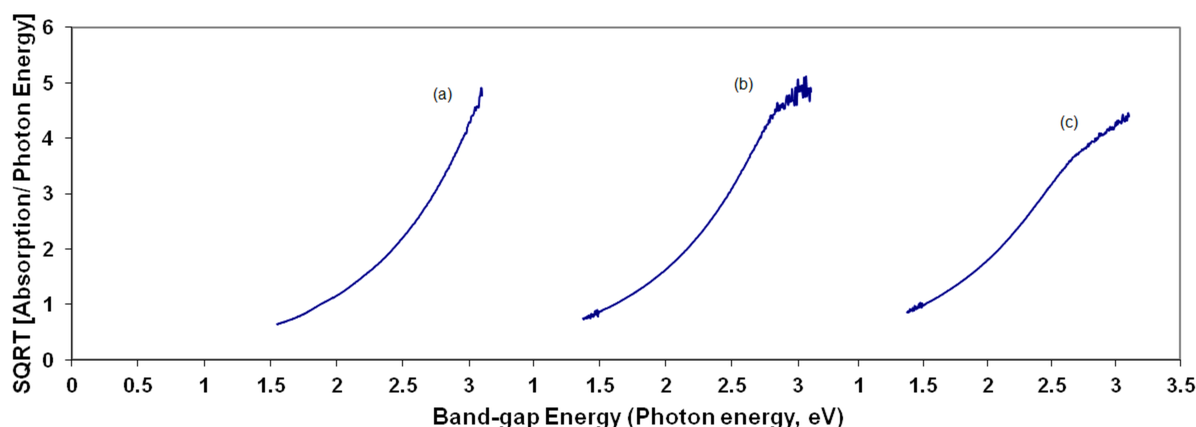

Figure 6.22. How absorption was influenced by process time and temperature by comparing three different settings of 200°C for 40min (a), 205°C for 40min (b) and 205° for 60min (c).

The band-gap value for thin film silicon will depend on structure content, when crystal growth in the amorphous matrix will relate to a value between crystal silicon at 1.1eV and amorphous silicon at 1.8eV. [37] Band-gap values above 1.9eV to 2.5eV were experienced and were explained to refer to very small and fine nanocrystals embedded in the amorphous structure like quantum dots. [37,38] The best combination with mixed structure was to use the square root to fit the band-gap value for amorphous combined with cube root for crystal to get a linear fit and correct band-gap value for the crystal phase. [36] By using a combination (square and cube root) often band-gap values in the region of 1.1eV regarding nano-sized crystal, 1.5eV for micro-sized crystal and a value at 1.8eV for the amorphous phase were obtained.

The introduction of argon-purges in combination with the H_2/ Ar ratios gave a clear picture of how band-gap values were changed by structure (table 6.16.). Three argon-purges with H_2/ Ar ratio of 17/3 (run 10) gave two band-gap values, one at the crystal region and one at the amorphous. Six argon purges with H_2/ Ar ratio of 14/6 (run 11), obtained a value of 1.8eV for amorphous material.

Table 6.16. explains how argon purges in relation with H_2/Ar ratio of 17/3 and 14/6 influences the structure outcome.

Trial No.	**Process parameters**						
	Actual rate, sccm			**Power**	**Temp.**	**Time,**	**Ar-purges**
	SiH_4	**H_2**	**Ar**	**W**	**°C**	**Min.**	
A	0.82	17	3	600	200	20	3
B							6
C		14	6				3
D							6

Trial No.	**Band- gap energy values**				**The values from square and power fitted phases such as:**		
	SQUARE		**POWER**				
	1st	**2nd**	**1st**	**2nd**	**ηc**	**μc**	**a**
A	1.3	1.8	1	1.25	1	1.3	1.8
B	1.4	1.8	1	1.5	1	1.4/1.5	1.8
C	1.1	1.8	1.4	1.9	1.1	1.4	1.8/1.9
D	1.5	2	1	1.5	1	1.5	2

The band-gap energy values showed how nano-sized crystals were developed in the amorphous phase in the chosen process runs E and F from the interface trial (table 6.13.). The chosen procedures resulted in a structure content of both nano- and micro-sized crystals in the amorphous matrix. Optical absorption of run 10 and 11 with three argon purges shows how run 10 has a straighter line towards the value of 1.1eV (crystal silicon). The two runs are compared (figure 6.23.) both by using a square and a cube root, which shows how the line became straighter with cube root due to the content of nano-sized crystals responding to cube root calculation.

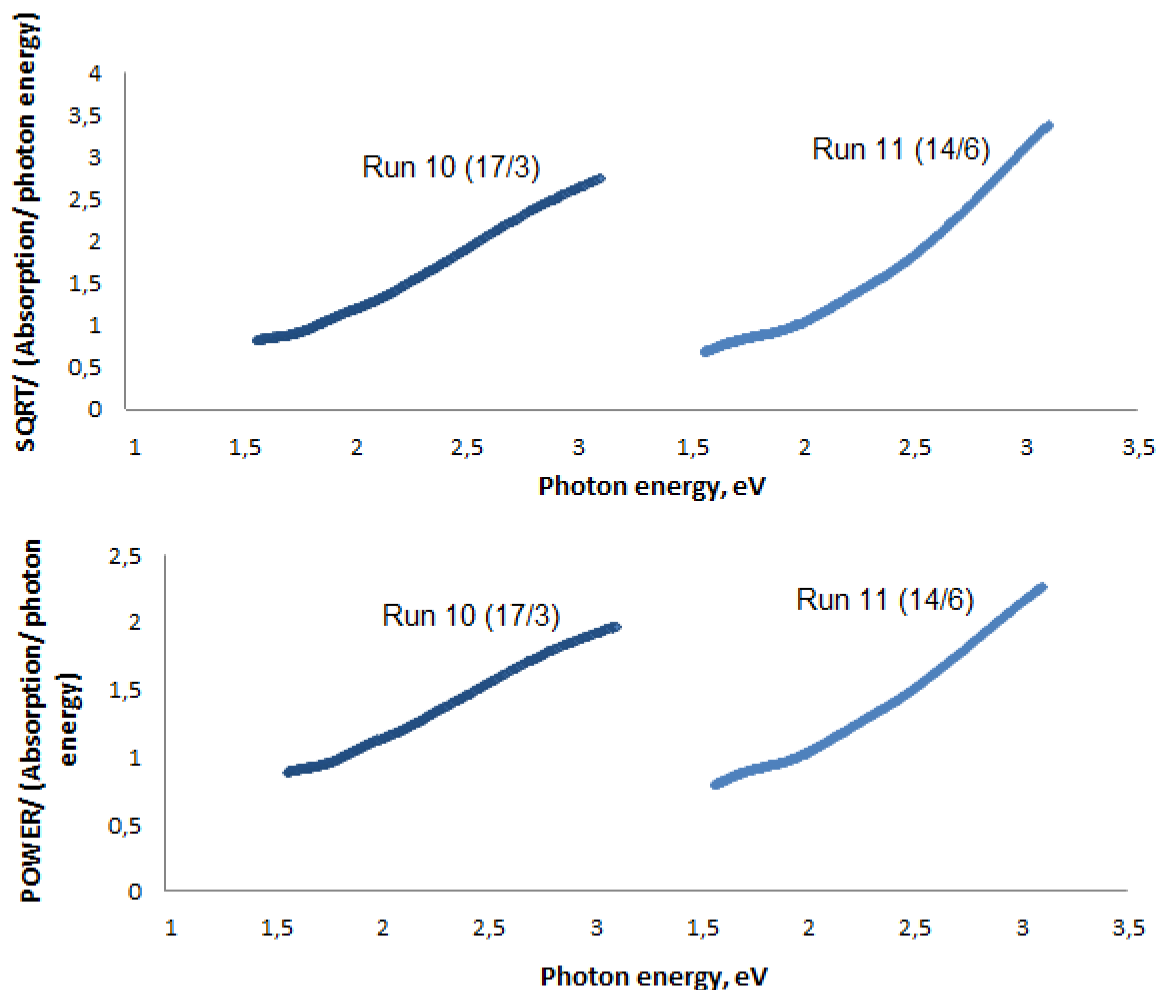

Figure 6.23. comparison between run 10 and 11 and the difference by using square root (upper plots) and cube root (lower plots) calculations.

The p-layer work involved altered process parameters and added hydrogen (table 6.17.) against fixed temperature, time and pressure. The structural changes regarding

Raman spectrum (table 6.14) were related in most of the runs to optical transmission data (table 6.18.).

Table 6.17. the process parameters used in the p-layer trial.

Trial run	Gas type and actual rate, sccm				Trial run	Gas type and actual rate, sccm			
	B_2H_6	**SiH_4**	**Ar**	**H_2**		**B_2H_6**	**SiH_4**	**Ar**	**H_2**
A	0.05	0.82	9.1	0	**E**	0.05	0.82	10	10
B	0.025	0.82	9.1	0	**F**	0.05	0.82	5	15
C	0.1	0.41	4.55	0	**G**	0.025	0.82	9.1	0
D	0.05	0.82	18.2	0	**H**	0.05	0.82	10	10

Table 6.18. p-layer changes and their band-gap values in relation to a structural phase.

Trial run	Band- gap energy values				The values from square and power fitted phases such as:		
	SQUARE ROOT		**POWER**				
	1st	**2nd**	**1st**	**2nd**	**ηc**	**µc**	**a**
A	1.5	1.9	1.1	1.5	1.1	1.5	1.9
B	1.55	2.1	1	1.5	1	1.6	2.1
C	1.45	2	1	1.5	1	1.5	2
D	1.45	2	1	1.45	1	1.4	2
E	1.2	1.9	1	1.4	1 /1.2	1.4	1.9
F	1.2	1.9	0.8	1.45	0.8/ 1.2	1.4	1.9
G	1.9	2.15	1	1.8	1		1.8/ 2.2
H	1.9	2.25	1.25	1.6	1.2	1.6	1.9/ 2.2

Initially, a visual analysis of the interference fringes of the deposited film was suggested to estimate the film thickness.

6.7. Electrical properties

Initially, measurement of electrical properties was intended as one of the main approaches to characterise the development of silicon thin films on textile substrates. However, this was soon found to be impossible due to the thin films on textile substrates being too uneven to measure the electrical properties reproducibly by the usual methods.

Electrical properties were not determined for films on textile substrates because of the rough surfaces.

6.7.1. I-V & four-point probe

The unevenness in the textile substrate comes from both warp and weft yarns (210 filaments in each yarn) making the surface on a microscopic scale very textured. With the textile being too textured, calendaring was applied to smooth the filament and yarn surface and bond them together to support the current flow. Still the textile was too textured for the thin aluminium film to cover the substrate surface sufficiently. A conductive support layer in form of a wet-coat of polyaniline was applied directly onto the woven polyester, which made it possible to measure current flow by I-V measurement. However, the thin film on textile contained still too much resistance, which resulted in too low flow of current for the I-V measurement to be applicable as a future test. The conductive coat made it possible to use four-point probe, which made it possible to measure the resistance accurately, even though the measured resistance was very high and the measurement was difficult to repeat due to probe positions changing with regard to particular filaments. Four-point-probe measurements on polyaniline coated substrates have been carried out in two individual projects related to this thesis (D. Walton, E. Baker, both physics undergraduates at HWU).

Both aluminium sheet and coated microscope-slide glass were measured, which resulted in a very low or no current flow. The high resistance was a result of poor film quality, which helped to highlight the importance of improving the deposited film quality. One solution was to introduce crystal content into the amorphous matrix, which would support improvements in the electrical and optical properties.

6.8. RF- sputtering of ITO and analysis

Radio Frequency, RF-sputtering was used to deposit top contacts and a protective layer on the cell structure of n-i-p-layer. The material sputtered was Indium Tin Oxide (ITO) the properties of which could be controlled by RF-power and process time. Since the textile substrate contained moisture, it was necessary to have the coating system to pump out overnight to obtain the required vacuum pressure. Microscope-slide glass was used to determine the film thickness. Thickness was measured by screen-printing lines of photoresist paste onto a microscope-slide glass after depositing ITO, and cleaning the slide with acetone which removed the printed tracks. This left ITO coated areas with a sharp edge, from which the ITO film thickness could be measured using the Dektak apparatus.

Initial runs were set at an RF-power of 70Watts for 15 minutes, on the basis of previous experience with different substrates. However, using these growth parameters, the film had a growth rate of ~13nm/ minute, which was too thin to protect and operate as a functional top contact on a solar cell. Consequently, the RF-power was increased to 85Watts for 30 minutes. Although this thickness was not measured by a Dektak, a visual judgement was made, that the film was probably thick enough to protect the cell.

RF-sputtered aluminium was considered as an alternative to evaporated aluminium (due to the problem of occasionally causing overheating of exposed polyester), but the quality proved to be unsuitable using the present sputter unit. Sputtered aluminium was produced by a RF-power of 70Watts for 10 minutes, which resulted in a growth rate of 10nm/ minute.

An optical microscope was used to evaluate the difference between sputtered and evaporated aluminium by comparing the distribution of the aluminium material. After microscope analysis, sputtered aluminium appeared to exhibit the same problems as evaporated aluminium by producing an uneven coating distribution on the textile surface, which led to the conductive properties being interrupted, resulting in a non-working back contact. Another disadvantage with sputtered aluminium was the larger aluminium particles that were randomly attached to the filament and yarn. Hence a decision was taken to continue to use evaporated aluminium in combination with a conductive organic material such as the polyaniline coated direct onto the textile substrate.

6.9. Thermal properties and analysis

6.9.1. Differential Scanning Calorimetry, DSC

When measuring a substrate's thermal properties, it is important to consider a low sample weight, consistent for all samples, to gain an accurate comparison between the samples. The sample weight influences the quantity of absorbed energy required to melt the sample and as low sample weight as possible is preferred. Another important factor is the set heat-rate (°C/ minute), when it influences the melting of a material and its energy curve. Good measurement was obtained by using sample weight less than 10mg and a temperature change of 10°C/ minute. [39,40]

Samples from each process-stage such as loomstate, calendered and after each process (evaporated aluminium, polyaniline, polyaniline coated with aluminium and silicon) as a single layer and combined cell structure were tested, to establish possible changes in the bulk properties of the polyester. Both fabric and filament were tested in case heat and melting curves became different, but no great difference was experienced in relation to glass transition and the melting point(s). The sample weight varied between 2.36 and 7.46mg, but did not show a great influence in the energy absorbed in the samples.

Tested samples were compared by considering the largest peak area and its temperature in relation to known melting point of polyester at 256°C. [2,41] Some of the samples had one melting point, although most samples contained two peaks, which pointed towards the substrate containing two types of polymers. The cause of the multiple melting points;_melting, recrystallisation and remelting is still unsolved, but a possible cause is that the polymer used contained different crystal formations. Peaks occurring below 200°C were suggested to come off melting- recrystallisation and remelting, while peaks above were due to melt of the crystal formation in the specific polymer. [40] By comparing all process stages it was possible to address a change in the bulk properties of the polyester, which was determined by the peak location changed to higher melting temperature and the biggest change was after silicon deposition. An increased melting point could either due to a higher percentage of crystallinity or the bulk material of the polymer being modified. A study discussed [42] possible change of bulk properties in a polymer during argon plasma at 0.025mbar with RF-powered plasma and the most likely cause was a break in the backbone of the polymer known as chain-scission. By comparing the peaks and their shape it was

possible to identify a more uniform, straight and narrow peak on samples with silicon, which meant plasma treatment resulted in crystal formation in the polymer. Crystal content has a more uniform melt than an amorphous content.

The peak area did reflect on the energy required to reach the melting point of the polymer substrate. A difference in the energy absorption was found between the different process stages:

- *Loomstate* had a melting point at 256°C, while *calendering loomstate* got an even melt divided into two peaks at 250°C (1st peak) and 257±1°C (2nd peak).
- *Polyaniline coated textile* (calendered loomstate) received several peaks (figure 6.24.), but the last two main peaks were 1°C (1st peak) and 1- 2°C (2nd peak) above those peaks from previous process-stage.

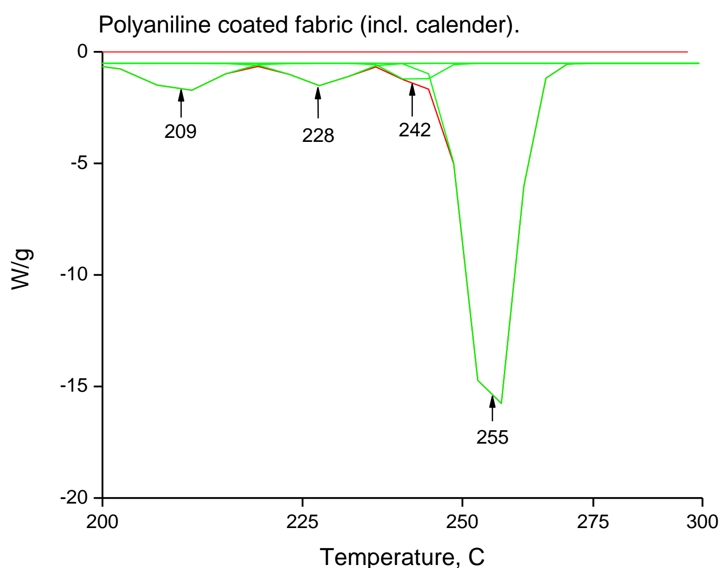

Figure 6.24. polyaniline coated textile produced different peaks as discussed in reference [43] in relation with DSC analysis and the diagram below shows the different peak values in more detail.

The increased number of peaks with polyaniline was reported (figure 6.25.) by another study [43], which reported how polyaniline gave several peaks due to moisture loss, re-crystallisation, loss of bonded water, loss of dopant, melting of the crystalline phase. The increased melting point after the plasma process did support a modification of the polymer chain, while calendaring, polyaniline and aluminium did not change the bulk

properties in the polyester.

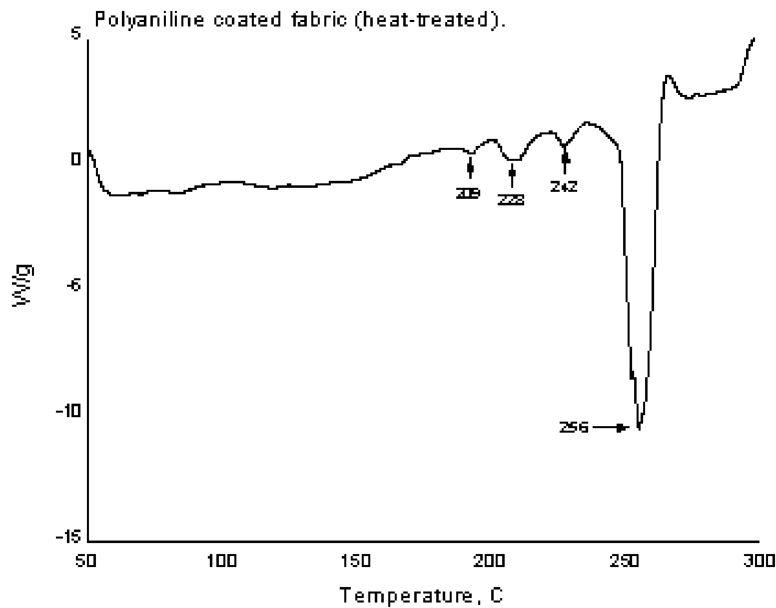

Figure 6.25. increased number of peaks with polyaniline coated due to loss of moisture and recrystallisation number of times.

- *Polyaniline coated textile with evaporated aluminium* (figure 6.26.) got peaks at 254°C (1st peak) and 259°C (2nd peak).

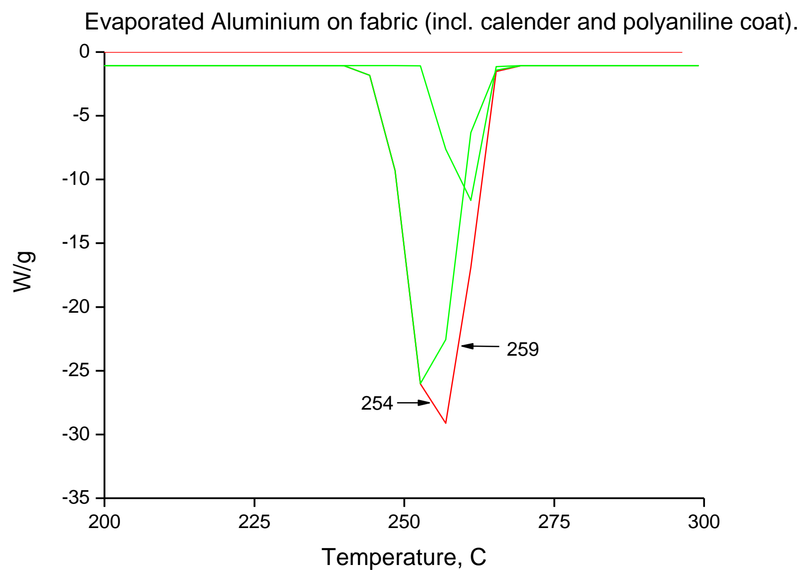

Figure 6.26. the increased numbers of peaks for polyaniline coated substrate become reduced after evaporating aluminium onto the substrate, when one peak contained two peaks at 254°C and 259°C.

- The great difference was found *after the plasma process of silicon thin film on textile* (figure 6.27.), when the peaks moved down to 243+2°C (1st peak) and up to 265-6°C (2nd peak).

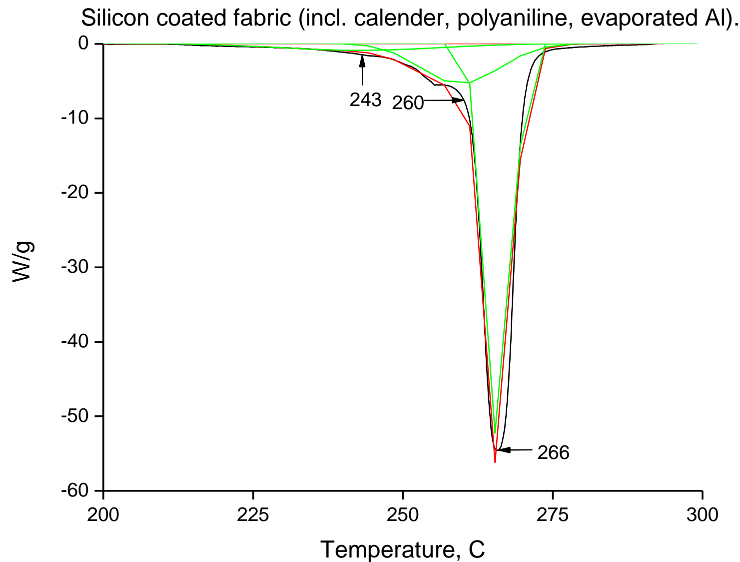

Figure 6.27. the melting point after plasma deposition of silicon increases by 10°C compared with polyester's melting point at 256°C.

6.10. Summary

After woven polyester was damaged by the initial process settings [1] for plasma enhanced chemical vapour deposition, much time was spent on finding settings which allow good quality silicon thin films to be deposited onto a textile substrate. With help of an argon-plasma, it was established that larger quantities of hydrogen, including from high silane flow rates, caused damage to the textile. After different changes were made to the argon (replacement of hydrogen) and silane (lower rate) mixture against parameters such as process time, temperature (limit to max 200°C due to textile melt), pressure and power, the deposited silicon still gained a high amorphous content and a powdery form. This proved that some hydrogen was necessary to avoid these effects.

Introduction of hydrogen was through a Taguchi model (table 6.4.), which helped to define two useful hydrogen/ argon ratios of 17/3 and 14/6sccm. These ratios were combined with different settings of silane-rate, temperature, time and microwave-power, which resulted in crystal growth of two kinds namely nano- and micro-

crystalline. As the textile responded better to the 17/3 ratio by increased crystalline growth rate, this ratio was focussed upon. The crystal structure experienced is commonly known as the hexagonal wurtzite structure.

Although there was much focus on intrinsic silicon, other aspects were investigated such as a clear break after the doped layer prior to the intrinsic layer and a change of doped recipes to increase the crystal content. A cleaning procedure with either three or six argon-purges proved to have a great influence on structure content of the intrinsic layer, when three purges together with a silane/hydrogen flow ratio of 17/3sccm encouraged nanocrystal growth while a ratio of 14/6sccm gave a microcrystal growth. Increased crystal content in the n-layer was gained by increasing process time, while p-layer still required more work such as reduced boron rate, process temperature and time.

An additional conductive layer was added as a support layer for the evaporated aluminium, which proved too thin for the textured surface of textiles. The conductive coat (Polyaniline) was applied directly onto the textile by wet-coating. By polyaniline being heat sensitive, it became necessary to reduce aluminium evaporation time from 5minutes to 3 minutes.

The process route to apply a complete cell structure directly onto a textile substrate was thus defined as:
Preparation- cleaning off impurity and drying the woven polyester before calendering (240°C for 1 minute) stabilised and flattened the yarn and structure without damaging properties such as flex and bend.
Back contact- evaporated aluminium needed a support layer of polyaniline, which was applied by direct coating onto the textile before evaporate aluminium for 3 minutes.
Semiconductor layers (n-i-p) were processed by the following settings:
N-layer, (*Ar 9.1sccm, SiH_4 0.82sccm, PH_3 0.1sccm, 200°C, 800W and 10 minutes*),
I-layer, (*H_2/Ar 17/3 or 14/6sccm, SiH_4 0.82sccm, 200 or 205°C, 600W and 20 minutes*). Longer process time of 30, 40 and 60 minutes is still to be considered.
P-layer, (*Ar 9.1sccm, SiH_4 0.82sccm, B_2H_6 0.025sccm, 190°C, 800W and 5 minutes*)
(N.B. PH_3 and B_2H_6 are presently supplied as 1% mixtures in hydrogen.)
Front contact- conducting, protective layer of RF sputtered indium tin oxide (ITO) required RF-power of 85W for 30 minutes to give enough thickness.

Electrical properties were initially targeted as the main analytical approach, but soon discarded due to poor electrical contact between the probes and the textured textile. Therefore during the establishment of process parameters and methods, analytical techniques of Raman spectroscopy and optical transmission were applied, which did complement each other in the evaluation of structural content. In analysis of the nanocrystal structure three Gaussian Raman peaks (amorphous at 480cm^{-1}, intermediate 500/ 505cm^{-1} and crystal silicon at 518/ 520cm^{-1}) were required. The third intermediate peak was a fingerprint for growth of an unexpected hexagonal wurtzite structure in the usual amorphous phase.

Optical absorption gave two band-gap values, one value (1.8eV) coming from a square root calculation and related to amorphous phase. The other band-gap value was calculated by cube root fit and was close to crystal silicon (1.1eV), which confirmed small crystals in the amorphous structure. The crystal size determined the value, when the band-gap for larger microcrystals was found closer to amorphous silicon at ~1.5eV, while smaller crystals moved it towards 1.1eV.

6.11. References

1 S. Jardine, *Thin Film Silicon on Textiles by Microwave Plasma Chemical Vapour Deposition*, PhD thesis, Heriot-Watt University, UK (2006)

2 K.L. Hatch, Textile science, West Publishing Company, ISBN: 0-314-90471-9 (pp.472) (1993)

3 Konarka Technologies Inc., www.konarka.com (09/10/2012)

4 Flexcell Technology, www.flexcell.com (09/10/2012)

5 PowerFilm Inc., www.powerfilmsolar.com (09/10/2012)

6 H.U. Poll, U. Schladitz and S. Schreiter, *Penetration of plasma effects into textile structures*, Surf. Coat. Tech. **142-144**, p.489-93 (2001)

7 J. Verschuren and P. Kiekens, *Gas Flow Around and Through Textile Structures during Plasma Treatment*, AUTEX Research Journal **5** (3), p.154-61 (2005)

8 N. De Geyter, R Morent and C Leys, *Penetration of Dielectric Barrier Discharge Plasma into textile Structures at medium Pressure*, Plasma Sources Sci. T. **15**, p.78-84 (2006)

9 J. Verschuren, P. Kiekens and C. Leys, *Textile- specific Properties that Influence Plasma Treatment, Effect Creation and Effect Characterization*, Tex. Res. J. **77** (10), p.727–33 (2007)

10 G. Buyle, *Nanoscale finishing of textiles via plasma treatment*, Mater. Technol. **24** (1), p.46-51 (2009)

11 C. A. Bishop, *Vacuum Deposition onto Webs, Films and Foils*, Material Science and Process Technology Series, ISBN: 978-08155-1536-4 (pp.650) (2006)

12 M. Skrifvars, W. Rehnby and M. Gustafsson, *Coating of textile fabrics with conductive polymers for smart textile applications*, Ambience **08**, Sweden, p.100-3 (2008)

13 M. Kondo, Y. Nasuno, H. Mase, T. Wada and A. Matsuda, *Low-temperature fabrication of microcrystalline silicon and its application to solar cells*, J. Non-Cryst. Solids **299-302**, p.108-12 (2002)

14 X. Liao et al., *Impacts of nano-structures in p- and i-layer on the performances of amorphous silicon solar cells*, Phys. Status Solidi C **6** (3), p.696-9 (2009)

15 G. Yue et al., *Material structure and metastibility of hydrogenated nanocrystalline silicon solar cells*, Appl. Phys. Lett. **88** (26), 263507 (pp.3) (2006)

16 R. Saleh and N.H. Nickel, *Raman spectroscopy of B-doped microcrystalline silicon films*, Thin solid films **427** (1-2), p.266-9 (2003)

17 R. Saleh and N.H. Nickel, *The influence of boron concentrations on structural properties in disorder silicon thin films,* Appl. Surf. Sci. **254**, p.580-5 (2007)

18 W. Jin-Liang and W. Er-Xing, *Characterization of doped hydrogenated nanocrystalline silicon films prepared by plasma enhanced chemical vapour deposition*, Chinese Phys. **16** (3), p.848-53 (2007)

19 L. Qing-Song et al., *Effect of substrate temperature on the growth and properties of boron- doped microcrystalline silicon films*, Chinese Phys. **15** (1), p.213-8 (2006)

20 T. Sasaki et al., *Structural study of p-type µc-Si layer for solar cell application*, J. Non-Cryst. Solids **266-269**, p.171-5 (2000)

21 S. Mingji et al., *Boron-doped silicon film as a recombination layer in the tunnel junction of a tandem solar cell*, J. Semicond. **30** (6), p.063001 (pp.4) (2009)

22 Z. Li, X. Zhang and G. Han, *Electrical and optical properties of boron-doped nanocrystalline silicon films deposited by PECVD*, Phys. Status Solidi A **207** (1), p.144-8 (2010)

23 F. Ibrahim, Photo-oxidation of amorphous silicon carbon alloys: preparation and mechanistics, PhD Thesis, Heriot-Watt University, UK (1992)

24 Q. Cheng, S. Xu and K. Ostrikov, *Structural evolution on nanocrystalline silicon thin films synthesized in high- density, low- temperature reactive plasmas*, Nanotechnology **20**, 215606 (pp.8) (2009)

25 W.J. Soppe, C. Devilee, M. Geusebroek, J. Löffler and H.-J. Muffler, *The effect of argon dilution on deposition of microcrystalline silicon by microwave plasma enhanced chemical vapor deposition*, Thin Solid Films **515**, p.7490-4 (2007)

26 T.Q. Trung et al., *The effects of hydrogen dilution on structure of Si:H thin films deposited by PECVD*, J. Phys. Conf. Ser. **187** (1), 012035 (pp.6) (2009)

27 G. Viera, S. Huet and L. Buofendi, *Crystal size and temperature measurement in nanostructured silicon using Raman spectroscopy*, J. Appl Phys **90**, p.4175-83 (2001)

28 S. Zhang et al., *Silicon thin film prepared in the transition region and their use in solar cells*, Sol. Energ. Mat. Sol. C. **90** (18-19), p.3001-8 (2006)

29 Y. Xu et al., *Microstructure characterisation of transition films from amorphous to nanocrystalline silicon*, J. Cryst. Growth **256**, p.27-32 (2003)

30 D. Das, *A novel approach towards silicon nanotechnology*, J. Phys. D: Appl. Phys. **36** (19), p. 2335-46 (2003)

31 M.H. Brodsky, M. Cardona and J.J. Cuomo, *Infrared and Raman spectra of the silicon-hydrogen bonds in amorphous silicon prepared by glow discharge and sputtering*, Phys. Rev. B **16** (8), p.3556-71 (1977)

32 R. Gupta, Q. Xiong, C.K. Adu, U.J. Kim and P.C. Eklund, *Laser induced Fano resonance scattering in silicon nanowires*, Nano Lett. **3** (5), p.627-31 (2003)

33 W. Wei, G. Xu, J. Wang and T. Wang, *Raman spectra of intrinsic and doped hydrogenated nanocrystalline silicon films*, Vacuum **81**, p.656-62 (2007)

34 V. Magidson and R. Beserman, *Fano type interference in the Raman spectrum of photoexcited Si*, Phys. Rev. B **66**, 195206 (pp.6) (2002)

35 L.D. Laude, F.H. Pollak and M. Cadrona, *Effects on Uniaxial stress on the Indirect Exciton Spectrum of Silicon*, Phys. Rev. B **3** (8), p.2623-36 (1971)

36 A. Frova and A. Selloni, *The optical threshold of hydrogenated amorphous silicon*, Tetrahedrally- Bonded Amorphous Semiconductors, ISBN 0-306-42076-7, p.271-84 (1985)

37 A. Gajovic et al., *Nanostructure of thin silicon films by combining HRTEM, XRD and Raman spectroscopy measurements and the implication to the optical properties*, Appl. Surf. Sci. **254**, p. 2748-54 (2008)

38 B. Yan et al., *On the bandgap of hydrogenated nanocrystalline silicon thin films*, Photovoltaic Specialists Conference (PVSC) **35th IEEE**, p.003755-60 (2010)

39 Mettler Toledo, *Mettler Toledo TA instrument DSC12E,* Operating Instructions, (pp.40) (1996) www.mt.com

40 C. Schick, *Differential scanning calorimetry (DSC) of semicrystalline polymers*, Anal Bioanal. Chem. **395** (6), p.1598-11 (2009)

41 J.M.G. Cowie, *Polymers: Chemistry & Physics of modern materials, 2nd edition*, Blackie Academic & Professional, (pp.436) (1991)

42 R.M. France and R.D. Short, *Plasma treatment of polymers, effects of energy transfer from argon plasma on the surface chemistry* of poly(styrene), low density poly(ethylene), poly(propylene)and poly(ethylene terephthalate), J. Chem. Soc. Faraday Trans. **93** (17), p.3173-8 (1997)

43 S. Badhra and D. Khastgir, *Degradation and stability of polyaniline on exposure to electron beam irradiation (structure-property relationship)*, Polymer Degrad. Stabil. **92**, p.1824-32 (2007)

7. Summary and conclusion

7.1. Amorphous structure, silicon thin film

The most common thin film silicon content is amorphous, but soon after producing the first amorphous silicon solar cell structure, experience was how this design did not reach expected performance due to its disadvantage of light-degradation known as "Staebler-Wronski" effect. [1] Mixed structure with a crystal growth in the amorphous phase helped to reduce light-degradation, but also improved the overall cell performance such as optical properties with increased absorption. A thin film cell contains between top and bottom contacts, three semiconductor layers (n-i-p). The semiconductor layers are often processed by plasma enhanced chemical vapor deposition, PECVD either in atmospheric or vacuum condition powered by radio-frequency or microwave source, although microwave is less common. The back contact of aluminium was usually evaporated, while the top contact of indium tin oxide was RF-sputtered.

7.2. Silicon thin film on woven polyester

This work has reported a procedure of how to overcome the difficulties of depositing a silicon thin film directly onto woven polyester. The plasma process of producing semiconductor layers contained a combination of reactive gases and vacuum condition, which is not common for textile material. The process conditions required for a thin film cell proved to be a challenge due to damaged weave. Different polyester substrates such as film, nonwoven and weave were compared, while different weave qualities such as structure (plain and twill), cloth weight and filament type (spun-, mono- and multi-) were evaluated. The original plain polyester weave of 247gsm with 210 filaments (warp and weft) was chosen after being the most stable quality during the plasma process.

7.2.1. Textile substrate and preparation

Woven polyester was more textured than conventional substrates such as silicon wafer or glass commonly used in the semiconductor industry. A flatter textile surface helped to improve adhesion properties of the film and coating. Calendering (heat-treatment) was applied to flatten the fibre and fabric surface, a process commonly used in the textile industry. Different combinations of temperature and time were tried, before a setting at 240°C for 1 minute was approved.

The less textured sample after being calendered was still too uneven for the evaporated back contact of aluminium, which resulted in a non-uniform distribution with poor or no conductivity. A support layer in the form of a conductive coat (Polyaniline) was addressed. Polyaniline had the advantage of being applied directly onto the substrate by wet-coat and already successfully used on textiles. The disadvantage with polyaniline, it was heat-sensitivity and required altered process parameters to avoid exposure from thermal sources and irradiation. The evaporation time of aluminium film had to be reduced from 5 minutes to 3 minutes to avoid the textile being damaged, but still to gain a good film thickness. The power for the plasma process had to be reduced too, from 800W to 600W, to avoid melting the coated substrate. Occasional damage was still experienced, later the cause was understood to be moisture left in the substrate. A drying procedure was introduced for the coated substrate prior to the plasma process to remove trapped moisture in the substrate and coating.

7.2.2. Process settings for silicon thin film on woven polyester

Much of the experimental time has been used to focus on process parameters for the plasma enhanced chemical vapour deposition by altering settings such as chamber pressure, microwave power, gas mix and flow-rate, temperature and time. This helped to address a way of processing textile substrates in vacuum without damage to the substrate and to be able to deposit silicon thin film with mixed structure of either nano- or micro- crystal growth in the amorphous structure.

To understand the cause of damaged textile, different approaches were used such as a reference plasma of argon. The different parameters and their values for the reference intrinsic silicon recipe were added one by one to the argon plasma, which helped to

address that larger quantity of hydrogen damaged the textile. After this knowledge hydrogen was restricted to a low rate in the diluted silane in the intrinsic recipe. Argon replaced hydrogen and together with low silane rate (0.82sccm) the recipe was used to deposit intrinsic silicon. Even with altered process power, temperature and time the deposited film was too powdery with a high amorphous content, which proved the importance of adding some hydrogen into the intrinsic recipe. An Orthogonal Statistical Design "Taguchi model" (*chapter 5, table 5.3*) was used, which helped to find a possible way of using hydrogen combined with a larger quantity of silane without damaging the textile substrate. Initially the run 16 (*SiH_4 2.04sccm, H_2/ Ar ratio 10/10sccm with 500W at 0.5Torr, 200°C, 20 minutes*) was first favoured by its high deposition rate. Run 16 was later discarded due to a high amount of deposition (silicon) left in the chamber after each run. Instead the Taguchi runs 10 (*SiH_4 1.02sccm, H_2/ Ar ratio 17/3sccm with 300W at 0.5Torr, 200°C, 20 minutes*) and 11 (*SiH_4 1.02sccm, H_2/ Ar ratio 14/6sccm with 400W at 0.5Torr, 200°C, 20 minutes*) were considered, after indicating crystal growth in the amorphous matrix on textile substrate. More work on the two Taguchi recipes was necessary by altering process power, time and temperature to encourage crystal growth without damaging the substrate. Silane rate was considered too by evaluating different values such as 0.62, 0.82 and 1.02sccm.

The two H_2/ Ar ratios indicated different crystal growth, when ratio of 17/3sccm produced smaller crystals, while 14/6sccm gave larger ones. The two ratios supported crystal growth differently depending on type of substrate, when 17/3 supported crystal growth on textile, while 14/6 helped aluminium. The difference became more obvious with the new settings for intrinsic silicon (*H_2/ Ar 17/3 or 14/6sccm, SiH_4 0.82sccm, 20 minutes, 200°C or 205°C and 600W*) and argon-purges (six or three times), when numbers of purges did influence the crystal growth combined with the specific hydrogen/ argon ratio. Three argon-purges with ratio of 17/3sccm gave nano-sized crystals compared with six argon-purges and 14/6sccm, which resulted in micro-sized crystals. Argon purges were introduced to avoid doped species moving into the intrinsic layer from the underlying n-type layer.

Increased power (from 500W to 600W) made a difference in film thickness, which was revealed by the Raman peak intensity becoming doubled.

After gaining an increased crystal content in the intrinsic layer, doped layers came in focus for increased crystal content. N-layers had a natural crystal growth compared with p-layers, which had an amorphous structure. Increased process time (from 5 to 10

minutes) was the only change required for n-layers (*Ar 9.1sccm, SiH_4 0.82sccm, PH_3 0.1sccm, 200°C, 10 minutes, 800W*). P-layers required changes such as altered gas rate and mix, process temperature and time, which led to reduced diborane rate, temperature and time (*Ar 9.1sccm, SiH_4 0.82sccm, B_2H_6 0.025sccm, 190°C, 5 minutes, 800W*).

7.3. Evaluation of deposited silicon thin film on woven polyester

Analytical methods to use on silicon thin film on woven polyester were limited due to the problem experienced with a textured surface and the charging up during the electron microscopy analysis. Raman spectroscopy and optical transmission were used, which helped identify structural content of deposited thin film and how the content changed by altering the process parameters.

The Raman spectra were often fitted with three Gaussian peaks, indicating three types of silicon structures such as 480cm^{-1} for amorphous silicon, 500/ 505cm^{-1} regarding "intermediate" nanocrystal structure and crystal silicon at 518/ 520cm^{-1}. In some cases two Raman peaks were fitted in films with strong amorphous or microcrystal growth without nano-sized crystal. The intermediate peak was identified with a typical fingerprint for wurtzite structure (Si-IV) with nanocrystal growth in a hexagonal formation. The process settings for intrinsic silicon on the uneven textile surface (*H_2/ Ar 17/3sccm, SiH_4 0.82sccm, 20 minutes, 200°C or 205°C and 600W*) favoured this hexagonal nanocrystal structure. A correlation between Raman peak width and peak location was found, which confirmed how the peak width became reduced with increased wavenumber. Reduction in width was due to less stress in the structure as the crystal content increased. Nanocrystal growth of wurtzite type gave a peak which became broader on the side towards the amorphous peak position, due to a vibrational mode named twin effect, typical for wurtzite. Silane flow-rate was linked to peak location, when higher amorphous content correlated with increased silane rate.

Optical transmission shown as a Tauc plot often revealed at least two band-gap values as a result of crystal growth in the amorphous matrix. Mixed structure had both square- and cube- root dependencies on the absorption, when square-root was applied for the amorphous content, while cube-root was used to fit crystal phase. The band-gap values referred to amorphous phase at 1.8eV and the crystal phase with a value

towards crystal silicon at 1.1eV. Band-gap energy value of crystal phase depended on crystal size, as the smallest crystals (nano-sized) got closer to crystal silicon at 1.1eV, while larger crystal (micro-sized) got value towards 1.6eV. With increasing film thickness and structural development, the curved shape of the Tauc plot became much straighter.

Differential Scanning Calorimetry, DSC was used after experiencing the substrate melting during the plasma process at a much lower temperature than polyester's melting point at 256°C. The woven polyester was tested after each process stage with focus on eventual changes in the bulk properties. Small changes in the temperature curve were found after heat-treatment, wet-coating and evaporation, but no change in bulk properties was experienced. However plasma treated samples did prove to change, when the melting point increased to ~265°C, which confirmed a change in the bulk properties.

Combination with different process parameters and values (such as gas rate and mixture, process power, temperature and deposition time) and continuous analysis with Raman spectroscopy and optical transmission have helped to establish process parameters possible to deposit silicon thin film onto textile substrate. The settings for the semiconductor layers (n-i-p) have resulted in a silicon thin film with crystal growth in an amorphous matrix deposited onto woven polyester without the substrate being damaged. The actual flow value for each dopant was 1% of the given rate, when the rest of the mixture contained hydrogen. The recipe to use for each layer is suggested as follows:

Phosphine doped, n- layer: (*Ar 9.1sccm, SiH_4 0.82sccm, PH_3 0.1sccm, 200°C, 10 minutes, 800W*).

Undoped intrinsic, i- layer: (*H_2/ Ar 17/3 or 14/6sccm, SiH_4 0.82sccm, 200°C or 205°C, 20 minutes, 600W*).

Diborane doped, p- layer: (*Ar 9.1sccm, SiH_4 0.82sccm, B_2H_6 0.025sccm, 190°C, 5 minutes, 800W*)

7.4. Environmental assessment regarding energy use

Manufacturers of photovoltaic systems often calculate the energy payback time, EPBT to understand the time it takes for a device/ system to generate the same amount of energy used during manufacturing and installation of the device. The payback time of a device will depend on its efficiency, location of operation etc.

Environmental management (ISO 14000) contains guidelines in how to assess energy use regarding a product and a service. An attempt to make such an assessment was done for silicon thin film on woven polyester by calculating the total energy use, which ends at 309MJ/ m^2 (52.5MJ/ m^2 for substrate and 256.5MJ/ m^2 for the cell). This design level stood well against silicon thin film on conventional substrate such as silicon wafer or a combination of glass and polymer film, which was quoted between 770MJ/m^2 and 1290MJ/m^2 (glass substrate and polymer film).

7.5. Future thoughts

Most of the work in this project has been to address process parameters for crystal growth of either nano- or micro- sized crystal in the amorphous matrix. The process settings established are guidelines, which still require adjustment to optimise the crystal content and the structural growth against photovoltaic properties such as electrical and optical performance. Light transmission has proven that optical properties have been improved with crystal growth in the amorphous structure by increasing the absorption spectrum, smaller crystals giving a wider absorption range due to their band-gap value being close to crystal silicon of 1.1eV together with the amorphous value at 1.8eV. Electrical performance of the silicon thin film was discounted at an early stage of this project due to problems in measuring films on textile due to being too textured. By introducing a smoother substrate surface and a conductive support layer the next step can be to introduce electrical measurements.

The disadvantage with the process of the silicon thin film cell on textile was the exposure to air between some of the process stages, which can allow moisture and air being trapped in the film and substrate. Moisture trapped in substrate or coat can cause an unnecessary increase in substrate temperature during plasma processing, which can damage the textile during the process, while oxygen trapped into the

substrate and deposit can damage the cell performance. The risk of thin film having its properties altered by exposure to air was discussed [2] as a higher risk with film deposited by microwave plasma enhanced CVD at low temperature (175-300°C). It was reported, that no changes in either structural or optical properties were experienced, but electrical properties did change.

Work still to be done to optimise the cell performance can address areas such as encapsulation, higher dtex and flatter yarn structure than plain weave, and altered wet-coat options:

- *Encapsulation*

Different coatings and lamination methods are available, but an important aspect in the choice is to protect the cell without damaging it or the flexibility of the panel. This device requires encapsulation on both sides, when the woven polyester allows moisture, impurity etc. coming through the structure if a protective layer was only applied on the face side of the panel. A fine spray coat such as polypyrrole (PPy) has been considered, but a problem can be to provide a full coverage protective layer due to the deposited thin film and textile being much textured. Vacuum lamination can be an option with a film applied on both sides of the textile, although a very light film will be required as a lamination will stiffen the overall flexibility of the product.

- *Flatter yarn*

After using a multifilament yarn with 210 filaments, a monofilament was considered in an attempt to gain a flatter surface. However the monofilament yarn in a plain weave did result in an increased substrate temperature during plasma deposition and as a result damage of the textile. A suggestion is to use a straw-like yarn in a plain weave structure, as for example used in the construction of tarpaulin fabrics, which allows a more uniform deposition of thin film by being less textured surface, increased bonding area and gaining a smoother transfer between the warp and weft yarn. Still the quality should either be of polyester or of polyamide, when these have a higher melting point than most polymer fabrics used in textile manufacturing.

- *Wet-coat*

A support layer for evaporated metal back-contact was necessary to improve the conductive properties in the layer. The support layer contained a conductive-coat of polyaniline applied by wet coating. Instead of a conductive-coat, a non-conductive coat was suggested to smoothen the textile surface, which should be enough support for evaporated aluminium to gain the conductivity properties required for a functional cell. A non-conductive coat has the advantage of being easier to apply, cheaper and having properties and performance more similar to the polymer based substrate. In comparison, the conductive-coat proved more sensitive to heat from processes such as evaporation, plasma enhanced CVD and RF-sputtering.

7.6. Final conclusion

Preparation, process methods and settings were established for woven polyester, to allow depositing silicon thin film onto the textile surface. Analytical methods such as Raman spectroscopy and light transmission helped confirm process recipes, which resulted in a dominance of either nano- or micro- crystal growth in the amorphous phase. Electrical properties were discarded due to a too textured surface, when neither I-V nor four-point probe gave readings. An assessment regarding the environmental impact of the product was done in connection with the production-route for thin film solar cells on woven polyester. It was concluded that a thin-film silicon solar cell on textile had a lower impact than conventional solar cells and flexible cells based on polymer-film.

7.7. References

1 D.L. Staebler and C.R. Wronski, *Reversible conductivity changes in discharge-produced Amorphous Si*, Appl. Phys. Lett. **31** (4), p.292-4 (1977)

2 D. Gracin et al., *The structural ordering of thin silicon films at the amorphous to nano-crystalline phase transition by GISAXS and Raman spectroscopy*, Renew. Energ. **33**, p.326-30 (2008)